Study of perforated liners for aeronautics

Robin Billard

DOCTORAT BRETAGNE LOIRE SCIENCES POUR L'INGENIEUR

Le Mans Université

THESE DE DOCTORAT DE

LE MANS UNIVERSITE

ECOLE DOCTORALE N° 602
Sciences pour l'Ingénieur
Spécialité : Aéro-acoustique

Par

Robin Billard

Study of perforated liners for aeronautics

Thèse présentée et soutenue au Mans, le 14 avril 2021
Unité de recherche : LAUM – UMR CRNS 6613
Thèse N° : 2021LEMA1012

Rapporteurs avant soutenance :

Marie-Annick Galland	Professeure des Universités à l'École Centrale de Lyon
Mabrouk Ben Tahar	Professeur des Universités à l'Université de Technologie de Compiègne

Composition du Jury :

Président :	Yves Aurégan	Directeur de recherche au CNRS
Examinateurs :	Estelle Piot	Maître de recherche ONERA
	David Marx	Chargé de recherche à l'Institut Pprime
Dir. de thèse :	Gwénaël Gabard	Professeur des Universités à l'Université du Mans
Co-dir. de thèse :	Gilles Tissot	Chargé de recherche à l'INRIA Rennes

Invité

Marc Versaevel	Ingénieur à Safran Nacelles

Acknowledgements

Merci au Centre de Transfert de Technologie du Mans pour avoir réalisé les mesures avec écoulement sur la veine *In Situ*. Je remercie en particulier Eric Portier et Joachim Golliard d'avoir pris le temps de m'expliquer les détails techniques du dispositif expérimental.

Merci aux membres du Jury d'avoir accepter d'évaluer mon travail de thèse et les échanges que nous avons pu avoir après ma présentation. Merci à l'ensemble des personnes qui ont assisté à ma soutenance de thèse et pour vos messages d'encouragements. Je remercie les trois personnes qui m'ont encadré et soutenu pendant ces trois années. Gilles, j'ai apprécié ton optimisme et ta bonne humeur même dans les situations de stress. Merci pour ton implication dans ma thèse et pour ta pédagogie. Gwénaël, j'ai beaucoup appris sous ta direction. Merci d'avoir été un encadrant curieux. Tu m'as posé des questions auxquelles je n'avais souvent pas la réponse, sûrement celles qui m'ont le plus fait progresser. Marc, merci pour ton professionnalisme et les discussions que nous avons pu avoir. Je souhaite aussi remercier Jean-Philippe Groby, Olivier Dazel, Guillaume Penelet, et Nicolas Joly pour avoir accepter de m'aider au début de ma thèse.

La thèse est une période difficile et je n'y serais peut-être pas arriver sans mes amis, Charlotte et Valentin. À tous les deux, un grand merci. Théo, merci d'avoir été mon colocataire et de m'avoir supporté pendant tout ce temps. Merci pour ces sessions passées à déboguer mes codes sous Matlab et à faire des belles figures Tikz. Je salue ton altruisme, ta passion pour la science et pour Counter Strike. Marguerite, merci pour tes encouragements et ton soutien jusqu'à la soutenance. Merci de m'avoir empêcher de répéter la veille de ma soutenance. Robin, merci d'être un ami fidèle depuis les bancs du lycée et pour ton soutien quand j'en avais besoin. Merci à mes parents, qui habitent à l'autre bout de la planète et qui m'ont toujours encouragé pour aller jusqu'au bout. Julien, j'ai apprécié nos sessions de sports dans la montagne et nos week-ends entre frères. Merci d'avoir été présent pour représenter les Billard le jour de la soutenance. Merci Bonne Maman pour ton soutien et tes encouragements depuis le début de ma thèse. À mes amis Gaël et Théo P., merci pour les week-ends en Bretagne qui m'ont permis de décompresser et d'échanger sur nos vies. À mes collègues du bureau 81, Thomas, Théo C., Théo T. et Jean, merci pour les discussions et surtout pour les vendredis après-midi où l'on oubliait nos thèses l'espace de cinq minutes, voire deux heures. Je remercie aussi le bureau 79, Mathieu, Élie, Valentin. Vous m'avez appris à ne surtout pas sous-estimer les pauses café en tant qu'outil de travail. Remerciement spécial à Thomas pour nos discussions philosophiques sur la vie et la thèse.

Contents

Acknowledgements **i**

Résumé en français **1**

Introduction **7**

1 Impedance models in the linear regime without flow **11**
1.1 Introduction . . . 11
1.1.1 General description . . . 11
1.1.2 Visco-thermal effects . . . 12
1.1.3 Radiation effect . . . 13
1.1.4 Interaction effect . . . 13
1.1.5 Back-plate reflection . . . 14
1.1.6 Viscous edge effects . . . 14
1.2 Guess impedance model . . . 16
1.3 Mode-matching model . . . 17
1.4 Impedance tube measurements . . . 19
1.5 Discussion . . . 21
1.5.1 Comparison with measurements . . . 21
1.5.2 Impact of the number of modes on the impedance . . . 24
1.6 Conclusion . . . 26

2 Numerical models in the linear regime **27**
2.1 Introduction . . . 27
2.2 Numerical models . . . 28
2.2.1 Linearized Navier–Stokes equations . . . 29
2.2.2 Helmholtz with losses model . . . 31
2.3 Numerical method . . . 32
2.4 Comparison with measurements . . . 33
2.5 Analysis of the rate of dissipation . . . 36
2.6 Convergence of the numerical models . . . 38
2.7 Conclusion . . . 40

3 Impedance model in the non-linear regime **43**
3.1 Introduction . . . 43
3.2 The Guess model in the non-linear regime . . . 44
3.3 Equivalent fluid model in the non-linear regime . . . 47
3.4 Computation of the acoustic velocity . . . 49
3.5 Comparisons with impedance tube measurements . . . 49
3.5.1 Sine-swept source . . . 50
3.5.2 White noise source . . . 57

3.6 Comparisons with impedance measurements with a grazing incidence 61
3.7 Conclusion 62

4 Impact of the grazing flow on the impedance **67**
4.1 Introduction 67
4.2 Semi-empirical impedance models with grazing flow 68
4.2.1 Guess model with flow 68
4.2.2 Impedance correction proposed by Meng *et al.* (2019) 69
4.3 Experimental set-up 71
4.4 Perforated plates 73
4.5 Eduction of the empirical parameters from measurements 74
4.6 Discussion on the empirical parameters k_{Guess} and ς_{Meng} 76
4.7 Conclusion 85

5 Sensitivity analysis in the presence of non-linear effects and grazing flow **89**
5.1 Introduction 89
5.2 Resolvent analysis for a simple mechanical system 90
5.3 Definition of the problem and frequency response 91
5.3.1 Linearized Navier-Stokes equations and impedance definition 91
5.3.2 Frequency response to a plane wave with and without flow 95
5.4 Sensitivity and response computation with and without flow 96
5.4.1 Sensitivity 96
5.4.2 Response to a non-linear optimal forcing 98
5.5 Case study without flow 101
5.6 Case study with flow 107
5.7 Choice of another line to define the impedance with flow 116
5.8 Perspectives with an iterative procedure 117
5.9 Conclusion 119

Conclusion **121**

A Details of the mode-matching formulation **125**
A.1 Pressure continuity 125
A.1.1 Interface between the neck and the exterior 125
A.1.2 Interface between the neck and the cavity 126
A.2 Axial velocity continuity 126
A.2.1 Interface between the neck and the exterior 126
A.2.2 Interface between the neck and the cavity 127
A.3 Linear system 127

B Weak formulations of the numerical models **129**
B.1 LNSE plane wave derivations 129
B.2 LNSE weak formulations 130
B.2.1 Mass equation 130
B.2.2 Momentum equation 130
B.2.3 Energy equation 130
B.3 Weak formulation of the Helmholtz model 131

C Details on the measured samples in the non-linear regime **133**

D Results at $L_p = 130\,\text{dB}$ **135**

E Example of triadic interaction **139**

Bibliography **141**

List of Symbols

c_0	sound speed in air	$\mathrm{m} \cdot \mathrm{s}^{-1}$
k_0	wave number in air	m^{-1}
L_p	sound pressure level	dB
L	cavity height	m
h	plate thickness	m
R_{neck}	radius of perforation	m
R_{cav}	radius of the cavity	m
R_{ext}	radius of the exterior domain	m
c_p	specific heat capacity at constant pressure	$\mathrm{J} \cdot \mathrm{m}^{-1}$
C_p	heat capacity at constant pressure per unit mass	$\mathrm{J} \cdot \mathrm{m}^{-1} \cdot \mathrm{kg}^{-1}$
c_v	specific heat capacity at constant volume	$\mathrm{J} \cdot \mathrm{m}^{-1}$
T	temperature	K
p	acoustic pressure	Pa
v_{neck}	axial velocity in a perforation	$\mathrm{m} \cdot \mathrm{s}^{-1}$
v	velocity in the perforations due to a turbulent boundary layer	$\mathrm{m} \cdot \mathrm{s}^{-1}$
e	specific internal energy	J
z	acoustic impedance	$\mathrm{kg} \cdot \mathrm{m}^{-2} \cdot \mathrm{s}^{-1}$
Z	normalized acoustic impedance	
St	Strouhal number	
Sh	shear number	
Pr	Prandlt number	
Re_a	acoustic Reynolds number	
M_0	acoustic Mach number in a perforation	
M	Mach number of the grazing flow	
ω	angular frequency	rad
λ	wavelength	m
ρ_0	air density	$\mathrm{kg} \cdot \mathrm{m}^{-3}$
μ	dynamic viscosity	$\mathrm{Pa} \cdot \mathrm{s}$
μ_B	bulk viscosity	$\mathrm{Pa} \cdot \mathrm{s}$
ν	kinematic viscosity	$\mathrm{m}^2 \cdot \mathrm{s}^{-1}$
κ	thermal conductivity	$\mathrm{W} \cdot \mathrm{m}^{-1} \cdot \mathrm{K}^{-1}$
β_T	iso-thermal compressibility	Pa^{-1}
α_p	coefficient of thermal expansion	K^{-1}
δ_V	acoustic viscous boundary layer thickness	m
δ_T	acoustic thermal boundary layer thickness	m
δ_{bl}	grazing flow boundary layer thickness	m
δ^*	grazing flow boundary layer displacement thickness	m
δ	end correction	m
$\varsigma_{\mathrm{Meng}}$	convection speed of vorticity above a perforation	$\mathrm{m} \cdot \mathrm{s}^{-1}$
Φ_{shear}	dissipation rate due to viscous shear effects	$\mathrm{Pa} \cdot \mathrm{s}$
Φ_{bulk}	dissipation rate due to viscous bulk effects	$\mathrm{Pa} \cdot \mathrm{s}$
ω_t	vorticity	s^{-1}

Θ	acoustic resistance	$\mathrm{kg} \cdot \mathrm{m}^{-2} \cdot \mathrm{s}^{-1}$
χ	acoustic reactance	$\mathrm{kg} \cdot \mathrm{m}^{-2} \cdot \mathrm{s}^{-1}$
γ	heat capacity ratio	
α	absorption coefficient	
σ	porosity	

Résumé en français

Le principe du résonateur de Helmholtz, par sa simplicité et son efficacité, est la technologie la plus répandue pour jouer le rôle d'absorbant acoustique dans l'aéronautique. Les revêtements perforés, composés d'une plaque rigide, d'une cavité en nid d'abeille et d'une plaque perforée, sont un moyen simple de fabriquer et d'intégrer ces résonateurs à l'échelle industrielle. Dans cette thèse, nous nous intéressons aux traitements perforés intégrés dans les turboréacteurs afin de réduire leurs émissions sonores.

La fréquence pour laquelle l'absorption de ces revêtements est maximum, c'est à dire la fréquence de résonance, dépend principalement de la hauteur de cavité. Certains revêtements sont composés de plusieurs cavités empilées afin d'obtenir plusieurs résonances. Le nombre de ces cavités détermine le nombre de degré de liberté du traitement. Des photographies montrant des revêtements perforés à un et deux degrés de liberté sont présentées sur la figure 1.

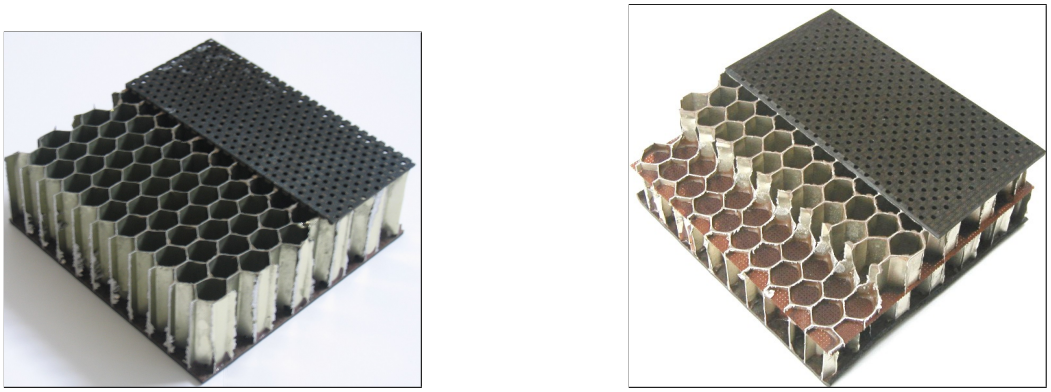

FIGURE 1: Photographies de revêtements perforés un avec un degré de liberté (gauche) et deux degrés de liberté (droite).

La nacelle est une structure qui entoure le moteur. Cette dernière à plusieurs fonctions. Le positionnement des revêtements acoustiques proche des sources sonores du turboréacteur en fait partie. Sur la figure 2, les traitements sont indiqués par des hachures. Ces derniers sont exposés à un écoulement rasant dont la vitesse dépend largement de la position du traitement et du régime du moteur. En conséquence de leur rugosité de surface, les revêtements sont des sources de pertes aérodynamiques.

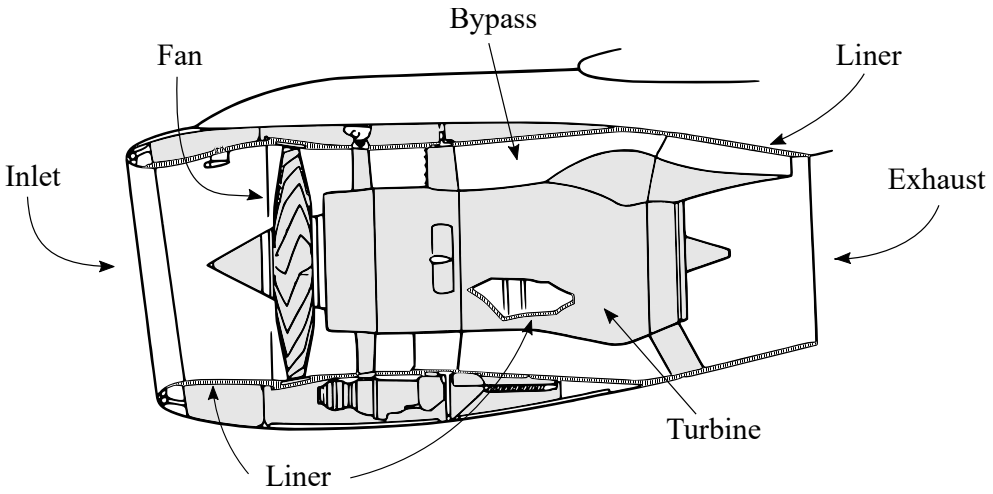

FIGURE 2: Vue en coupe d'un moteur et de sa nacelle par Spillere (2017). Les rayures indiquent la position des revêtements perforés

Ces pertes peuvent être minimisées en réduisant la rugosité des traitements, qui dépend notamment du diamètre des perforations et du taux de surface ouverte (ou porosité) de la plaque perforée. Cela est illustré par la figure 3 issue de l'étude expérimentale de Roberts (1977). L'utilisation de revêtements micro-perforés, avec un diamètre de perforation inférieur au millimètre, est donc une solution intéressante pour réduire la trainée aérodynamique des revêtements.

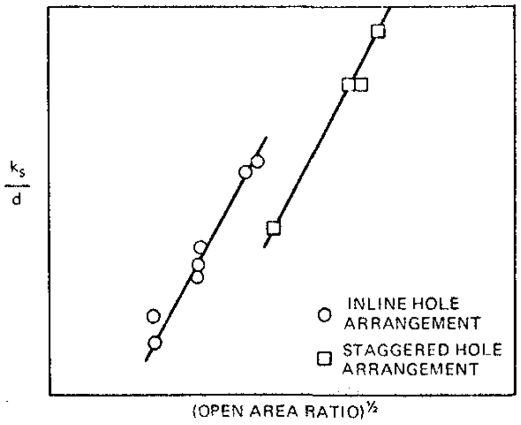

FIGURE 3: Rugosité de grain de sable équivalente en fonction de la porosité du revêtement et de l'agencement des perforations par Roberts (1977).

Un modèle d'impédance acoustique permet de caractériser le milieu dans lequel se propage une onde acoustique. L'impédance de surface d'un matériau correspond au rapport de la pression incidente par la vitesse normale rentrante dans le matériaux. Cette relation est valable seulement pour des ondes planes. Les modèles d'impédance disponibles dans la littérature ne sont pas adaptés pour les traitements micro-perforés, en particulier lorsqu'un écoulement tangentiel est présent. L'objectif principal de cette thèse est d'évaluer et d'enrichir ces modèles pour étendre leur domaine de validité aux micro-perforés. On distingue également les revêtements macro-perforés, ayant un diamètre de perforation supérieur au millimètre. Ce manuscrit est composé de 5 chapitres, dans lequel on tente d'affiner la compréhension des phénomènes physiques avec une complexité croissante.

Dans les chapitres 1 et 2, le régime linéaire sans écoulement est étudié, ce dernier a suscité un intérêt scientifique important depuis Kirchhoff (1868) qui a réalisé des développements théoriques afin de de modéliser les pertes visco-thermiques dans les tubes. Cette théorie a été simplifié par

Zwikker *et al.* (1949) en appliquant l'hypothèse de tube court. Stinson (1991) a consolidé le modèle de Zwikker *et al.* (1949) en apportant des justifications supplémentaires à leurs hypothèses. Rayleigh (1878) a proposé une correction de longueur de tube analytique prenant en compte l'effet de rayonnement à l'entrée d'une perforation. Plus récemment, des corrections de la conductivité de Rayleigh on été proposées par Laurens *et al.* (2013) pour des trous coniques. En parallèle à cela, les modèles numériques pour l'acoustique visco-thermique se sont développées pour être plus efficaces et précis avec par exemple Malinen *et al.* (2004), Kampinga *et al.* (2011) et Joly *et al.* (2006).

Les mécanismes physiques linéaires sont récapitulés dans le chapitre 1 et un modèle relâchant une approximation commune : l'hypothèse de tube court, est proposé. La méthode de raccordement modal est utilisée et les résultats sont comparés à des mesures en tube à impédance et au modèle de Guess (1975). On montre que le rayonnement et que l'interaction entre les perforations peuvent être pris en compte en utilisant des modes évanescents. Une perspective importante de ce chapitre est d'intégrer les effets de bords visqueux pour obtenir des prédictions de résistance acoustique précise. Cela pourrait être réalisé en utilisant des modes visqueux d'ordres élevés.

Deux modèles numériques sont développés dans le chapitre 2. Le premier modèle résout les équations de Navier-Stokes compressible linéarisées (LNSE) et inclu une liste exhaustive de phénomènes physiques, mais à un coût de calcul élevé. Une analyse du taux dissipation lié à la viscosité basé sur la solution des LNSE est proposée. La figure 4 montre le taux dissipation pour deux configurations macro-perforées (a et b) et deux configurations micro-perforées (c et d). On constate que la répartition de la dissipation est significativement différente lorsque l'on passe du cas macro au cas micro. Le second modèle résout l'équation de Helmholtz avec une condition limite visco-thermique développée par Berggren *et al.* (2018). Il est montré que ce modèle est précis pour les revêtements micro- et macro-perforés avec un coût de calcul bien inférieur au modèle LNSE. Ici, une perspective intéressante serait d'utiliser ce modèle simplifié pour des géométries complexes, cela a notamment été réalisé pour des matériaux poreux dans Cops *et al.* (2020) ou dans Tissot *et al.* (2020) pour optimiser la forme de cavité d'un résonateur de Helmholtz.

Lorsque le niveau sonore devient important à la surface du revêtement, l'impédance varie selon une loi non-linéaire en fonction de la vitesse acoustique dans les perforations (Komkin *et al.*, 2020). De plus, l'apparition de tourbillons générés aux coins des perforations induit des pertes supplémentaires. Cet effet est mis évidence numériquement par Tam *et al.* (2001), Zhang *et al.* (2012) ou encore par Roche *et al.* (2009). Dans ce régime non-linéaire, des générations d'harmoniques apparaissent. Cela signifie que plusieurs fréquences contribuent à la vitesse acoustique dans les perforations. Ingard (1953) a mis évidence cet effet expérimentalement dans le domaine temporel et a montré que la première harmonique était dominante, permettant ainsi de modéliser l'impédance dans le domaine fréquentiel de manière simplifiée.

Dans le chapitre 3, l'impédance des revêtements perforés dans le régime non-linéaire est étudiée. Le modèle de Guess (1975) est modifié avec une procédure itérative permettant de prédire la vitesse acoustique dans les perforations et une correction d'impédance non-linéaire. Ce modèle est comparé au modèle de Laly *et al.* (2018b), incluant également une procédure itérative. Les deux modèles sont comparés à des mesures réalisées en tube à impédance pour des niveaux de pression sonore élevés. Des sources sonores en sinus glissant et en bruit blanc sont utilisées. La procédure itérative est adaptable au type de source. Les résultats sont aussi comparés à des mesures faites avec une onde ayant une incidence rasante au traitement perforé. Des prédictions d'impédance raisonnables voire très précises sont obtenues avec les deux modèles. On montre que les itérations sont essentielles pour modéliser l'impédance dans le régime non-linéaire de manière précise. Le modèle de Guess modifié est utilisé dans le chapitre 4 dans lequel des mesures avec écoulement sont étudiées. L'impact de l'écoulement rasant sur l'impédance d'un revêtement perforé est significatif. Un nombre important d'études ont montrées que lorsque le nombre de Mach augmente, la partie réelle de l'impédance augmente et sa partie imaginaire diminue. Ces tendances ont été confirmées notamment par le travail expérimental dans Groeneweg (1969) et Tam *et al.* (2014) ou l'approche théorique de Howe (1979). Des études numériques sont aussi disponibles avec Roche

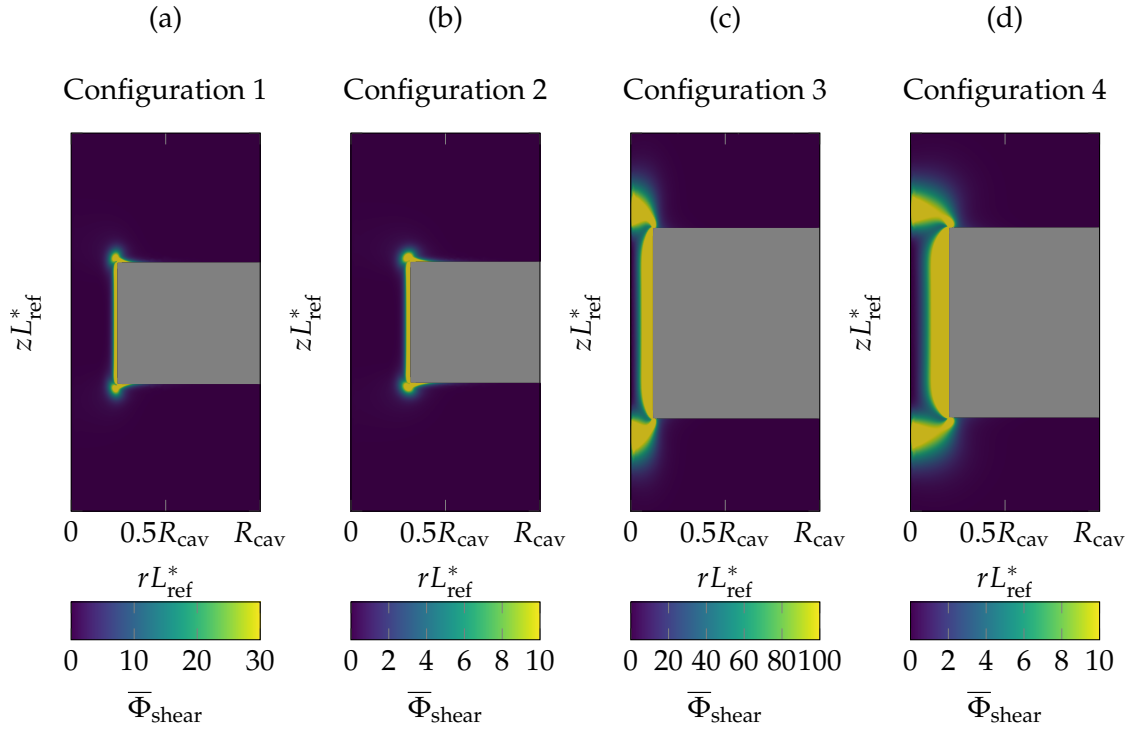

FIGURE 4: Valeur moyenne du taux de dissipation lié aux effets de cisaillement à la fréquence de résonance de la configuration 1 à $Sh = 13.4$ (a), configuration 2 à $Sh = 15$ (b), configuration 3 à $Sh = 2.2$ (c) et configuration 4 à $Sh = 2.9$ (d).

et al. (2010), Zhang *et al.* (2016), Avallone *et al.* (2019) et Wu *et al.* (2019) pour des revêtements perforés. Cependant, la compréhension actuelle des phénomènes physiques n'est pas suffisante pour prédire l'impédance des traitements soumis à un écoulement rasant. L'impédance dépend des paramètres géométriques de la plaque perforée, du nombre de Mach et de l'épaisseur de couche limite de l'écoulement cisaillé (Jing *et al.*, 2001). Ingard (1968) a proposé une correction de la résistance fondée sur un paramètre expérimental utilisé dans les modèles de Guess (1975), Yu *et al.* (2008) et Allam *et al.* (2011). Une correction d'impédance est aussi disponible dans Meng *et al.* (2019), déterminée à partir de la continuité de vitesse dans la couche limite. Ce dernier modèle dépend également d'un paramètre empirique déduit d'une résistance mesurée.

Le modèle de Guess (1975) prenant en compte les effets non-linéaires (utilisés dans le chapitre 3) est modifié pour prendre en compte l'effet de l'écoulement rasant. Les corrections d'impédance proposées par Guess (1975) et Meng *et al.* (2019) sont utilisées. Ces deux corrections utilisent un paramètre expérimental. Ces paramètres sont déduits des mesures récemment réalisées par le Laboratoire d'Acoustique de l'Université du Mans (LAUM) pour plusieurs épaisseurs de couche limite et configurations de plaque perforée. Une tendance claire des paramètres empiriques est identifiée. Ces derniers décroissent en fonction de l'épaisseur de couche limite de manière cohérente avec les résultats expérimentaux de Meng *et al.* (2019) et Yu *et al.* (2008). À la suite de cela, une recommandation des paramètres expérimentaux et proposée suivie par une discussion des résultats et des perspectives de modélisation.

Dans le dernier chapitre, une méthode fondée sur l'analyse résolvante introduite par Schmid *et al.* (2001) est présentée. Cette dernière permet d'identifier les forçages d'un système dynamique pour lesquels l'amplitude de la réponse est maximale. Dans notre cas, on s'intéresse à la sensibilité de l'impédance d'une perforation à des sources non-linéaires en présence d'écoulement rasant à partir des équations linéarisées de Navier-Stokes. De plus, la réponse du système à un terme non-linéaire est calculée et comparée à la réponse à un terme linéaire. Cette méthode permet

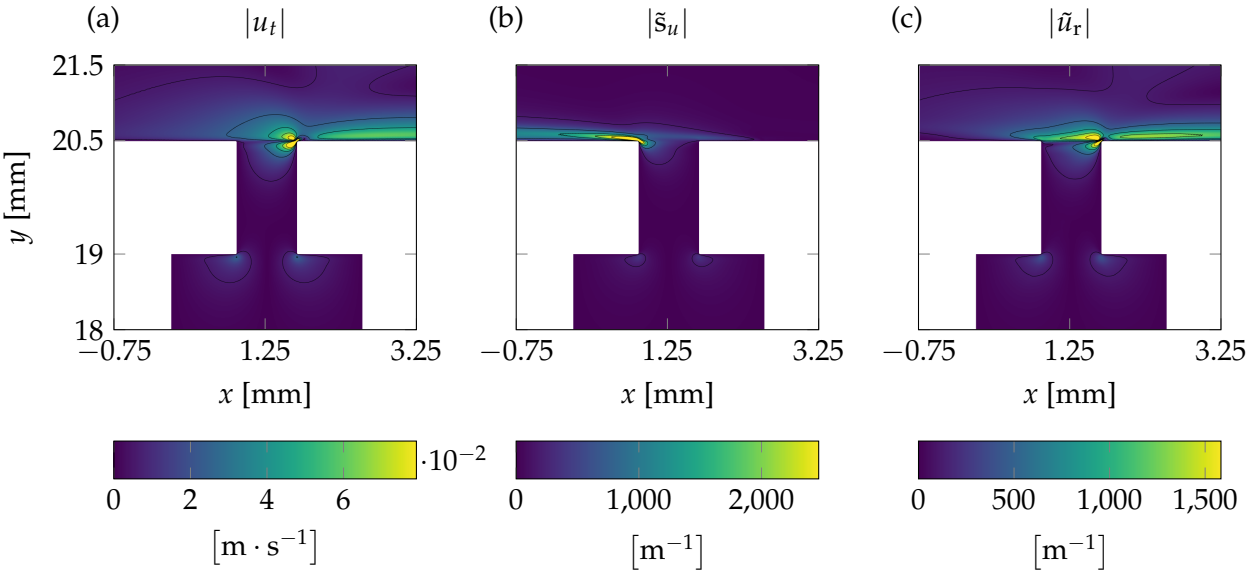

FIGURE 5: Vitesse tangentielle à une plaque perforée. (a) Réponse à une onde plane. (b) Sensibilité de l'impédance à une source non-linéaire. (c) Réponse à un terme non-linéaire.

de mettre en évidence les quantités effectives impactant le plus l'impédance. Un exemple pour la vitesse tangentielle au traitement est montré sur la figure 5. La réponse à un terme linéaire est montrée à gauche (a), le champ de sensibilité est montré au centre (b) et la réponse à un terme non-linéaire est montrée à droite (c) pour la vitesse tangentielle au traitement. Ici, une interprétation de la sensibilité est que l'impédance serait très impactée par une perturbation en amont de la perforation, et que la réponse à cette perturbation serait importante en aval de la perforation.

Perspectives globales Dans cette thèse, plusieurs méthodes ont été utilisées pour modéliser l'impédance des revêtements perforés du régime linéaire au régime non-linéaire avec écoulement. Dans les régimes linéaires et non-linéaires, les prédictions d'impédance obtenues avec les modèles présentés sont correctes. En présence d'un écoulement rasant, les prédictions présentées dans le chapitre 4 ont montrées que les modèles existants restaient perfectibles, en particulier pour les traitements micro-perforés. Il semble nécessaire d'améliorer la compréhension des phénomènes physiques impactant l'impédance d'un perforé soumis à un écoulement rasant pour obtenir des prédictions précises. L'analyse de sensibilité présentée dans le chapitre 5 s'avère être un outil adapté à cette objectif. Des perspectives d'améliorations pouvant rendre cette technique prédictive ont été présentées en conclusion du dernier chapitre. Ces perspectives constitueraient une suite cohérente à ce travail de thèse. De plus, les travaux présentés pourraient être adaptés pour des perforations présentant des formes coniques ou inclinées.

Introduction

The Helmholtz resonator principle, through its simplicity and its efficiency, is the most widespread technology employed in acoustic treatments in aeronautics. The perforated liners, composed of a rigid plate, a honeycomb cavity and a perforated plate, are a simple way to manufacture and integrate these resonators at an industrial scale. In this thesis we focus our interest on the perforated liners integrated on turbofan engines to reduce their noise emissions.

It can be noted that the resonance frequency is mainly determined by the cavity height. A common practice to increase the attenuation frequency range is to stack honeycomb cavities of different heights separated by a wire mesh or a micro-perforated sheet, named septum, to obtain a dual resonant liner. The number of cavities stages determines the number of degrees of freedom of the treatment. On figure 6, photographs showing perforated liners with a Single Degree of Freedom (SDOF) and Double Degrees of Freedom (DDOF) are presented.

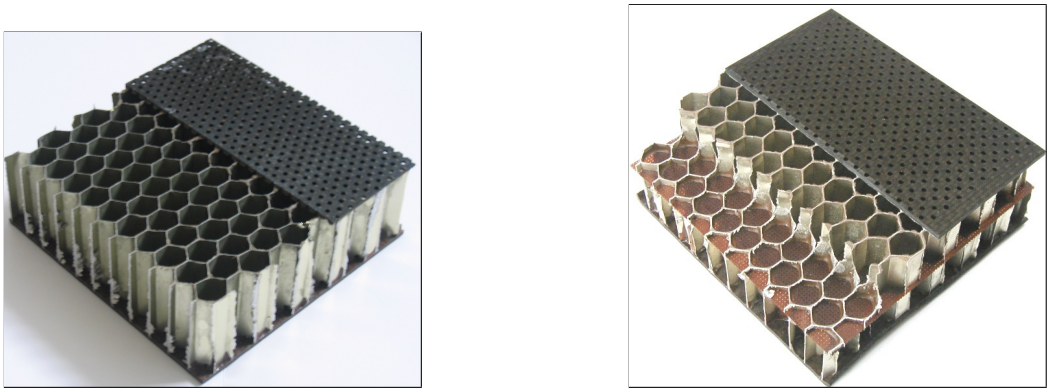

FIGURE 6: Photographs of perforated liners with a single degree of freedom (left) and double degrees of freedom (right).

The nacelle is a structure surrounding the jet engine which has several functions. One of them is to damp the noise radiated by the turbofan. On figure 8, the liners are indicated by the stripes. They are exposed to a grazing flow whose velocity depends greatly on the position of the treatment and the power rating. Consequently, these liners are a source of aerodynamic losses due to their surface roughness. Such friction losses can be minimized by reducing the surface roughness of the liners, which, as shown experimentally by Roberts (1977), is a function of the plate porosity and the perforation diameter. On figure 7 we can see that the roughness of a perforated plate increases with growing porosity.

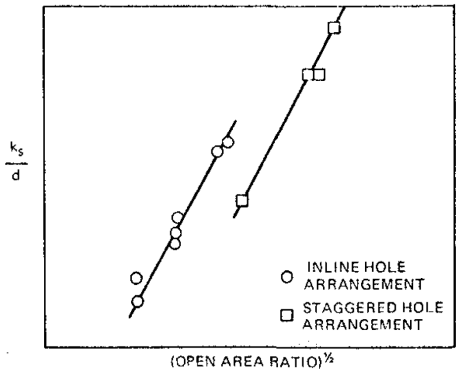

FIGURE 7: Sand-grain grain roughness of perforated plates depending on the porosity by Roberts (1977).

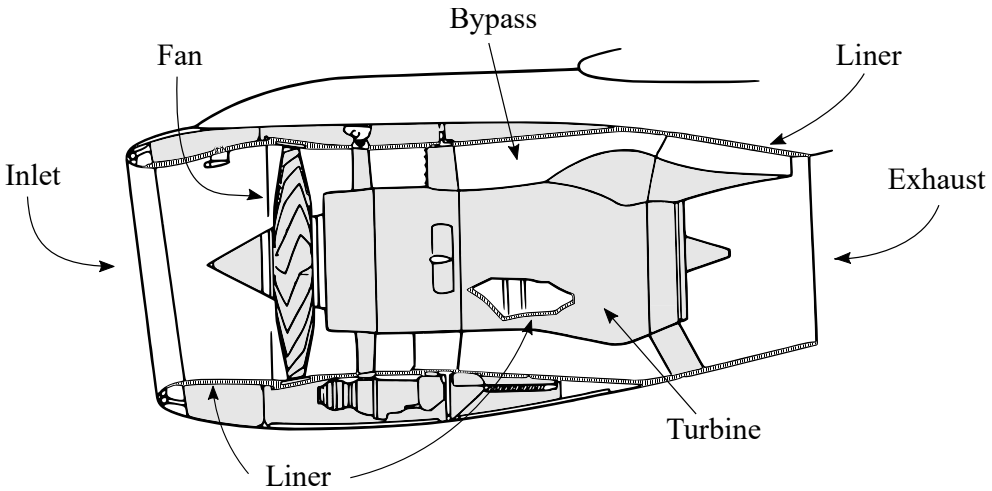

FIGURE 8: Sectional view of a jet engine and its nacelle from Spillere (2017). The stripes indicate the position of the perforated liners.

Hence, using micro-perforated plates (MPP), with a perforation diameter below 1 mm, has become of interest to reduce the flow drag due to the liners. In this thesis, we also consider the macro-perforated liners, with a perforation diameter above 1 mm. A considerable number of studies have been carried on cylindrical perforations and adapted to macro- and micro-perforated liners. However, the existing impedance models perform poorly for micro-perforates in the presence of grazing flow. One of the purposes of the present work is to evaluate and enhance these models in the case of micro-perforated liners.

In the linear regime without flow, Kirchhoff (1868) initiated theoretical developments to model the viscous and thermal losses in tubes. This theory was later simplified by Zwikker *et al.* (1949) with the short tube approximation. Stinson (1991) consolidated the model from Zwikker *et al.* (1949) with additional justifications of its main assumptions. Rayleigh (1878) also contributed an analytic correction to account for the radiation effect at the entrance of a tube. More recently, corrections of the Rayleigh conductivity were proposed in Laurens *et al.* (2013) for conical shape perforations. Meanwhile, numerical methods for visco-thermal acoustics have been developed to be computationally efficient and accurate with, for instance, the work from Malinen *et al.* (2004), Kampinga *et al.* (2010), Kampinga *et al.* (2011) and Joly (2010).

When the acoustic sound pressure levels at the surface of the liner is high, the impedance has a non-linear dependence with the acoustic velocity in the perforations (Komkin *et al.*, 2020). Furthermore, additional dissipation appears due to the shedding vortices from the corners of the perforations. This is highlighted with numerical methods in a number of article, for instance Tam

et al. (2001), Zhang *et al.* (2012) or Roche *et al.* (2009). In this non-linear regime, harmonic distortion is known to occur, as highlighted in Ingard *et al.* (1967). Ingard *et al.* (1967) showed experimentally that in the time domain, the first harmonic is dominating, which allows to define a simplified effective velocity impacting the impedance at a given frequency. A non-linear impedance correction was derived from the latter approach and is used in the semi-empirical models from Guess (1975) and Allam *et al.* (2011).

The impact of a grazing flow on the impedance of perforated liners is significant. A number of studies have shown that with increasing experimetal Mach number, the real part of the impedance increases and its imaginary part decreases. These trends are confirmed by the experimental work in Groeneweg (1969), Howe (1979) or Tam *et al.* (2014). Numerical investigations are also available in Roche *et al.* (2010), Zhang *et al.* (2016), Avallone *et al.* (2019) and in Wu *et al.* (2019) for perforated plates. However, the current understanding of the underlying physics is not sufficient to accurately predict the impedance under grazing flow, which depends on the geometrical parameters of the perforated plate, the Mach number and the shear flow boundary layer thickness (Jing *et al.*, 2001). Ingard (1968) proposed a grazing flow correction of the resistance relying on an empirical parameter which is used by the models from Guess (1975), Yu *et al.* (2008) and Allam *et al.* (2011). A correction of the impedance is also available in Meng *et al.* (2019) based on the continuity of velocity across the boundary layer but also relies on an empirical parameter. For the moment, the amount of data is not sufficient to provide a recommendation of the latter empirical parameters based on a chosen configuration.

In the five chapters composing this manuscript, we attempt to understand the physical behavior of perforated liners under different circumstances. The main purpose is to model the impedance of the treatments in order to optimize their design. The thesis begins with the introduction of a simple model in the linear regime and follows a plan with increasing levels of complexity. In the first chapter, the linear regime is treated, and in the last chapters the impact on the impedance of the grazing flow combined to non-linearities is studied.

In chapters 1 and 2, the framework is focused on the linear regime without flow, which has already received a significant attention from the community. In chapter 1, the linear physical mechanisms are reviewed and a model releasing a common hypothesis is proposed. The mode-matching method is used. In chapter 2, two numerical models are developed. The first model solves the compressible linearized Navier-Stokes equations (LNSE), hence it is able to account for an exhaustive list of physical mechanisms but it is computationally costly. An analysis of the viscous dissipation based on the solution of the LNSE is presented. The second model is based on the Helmholtz equation with a boundary condition accounting for visco-thermal losses. The latter approach is found to be accurate and numerically cheap for both macro- and micro-perforated liners.

In chapter 3, the impedance of perforated liners under high sound pressure level, *i.e.* in the non-linear regime, is studied. The model from Guess (1975) is modified with an iteration procedure to predict the non-linear impedance and the acoustic velocity in the perforations. The results are compared with a more recent model by Laly *et al.* (2018b) and to impedance tube measurements performed for macro- and micro-perforated plates. In addition, measurements are carried out with a grazing incidence to the plate and considered for comparison. A good agreement is obtained with the Guess model and the iteration procedure is shown to be primordial to obtain accurate predictions in the non-linear regime. This serves as a basis for chapter 4, in which the impact of the grazing flow is accounted for.

The impedance corrections accounting for the grazing flow either from Guess (1975) or from Meng *et al.* (2019) are considered. Both corrections are based on empirical parameters. These parameters are educed from measurements recently performed at the *Laboratoire d'Acoustique de l'Université du Mans* (LAUM) for several flow boundary layer thicknesses and perforated plate configurations. The trends of the empirical parameters are found to depend on the geometry of the liner, the boundary layer thickness and the Mach number of the flow. A recommendation of

the empirical parameters is proposed, which is shown to enhance the impedance predictions for micro-perforated liners. A perspective to this chapter would be to understand which physical quantity has the most impact on the impedance of liners under grazing flow. This would be helpful to derive a grazing flow impedance correction. For that purpose, a sensitivity analysis is performed in the last chapter.

In the last chapter, a method based on the resolvent analysis (Schmid *et al.*, 2001) is introduced. It allows the identification the non-linear forcings for which the harmonic response of a dynamical system has the highest amplitude. In our case, we study the sensitivity of the impedance to non-linearities in the presence of a grazing flow based on the compressible linearized Navier-Stokes equations. Additionally, the response to a non-linear forcing is computed and compared to the response to a linear forcing, here, a plane wave with a normal incidence to the plate. This method is shown to highlight the relevant physical mechanisms impacting the impedance. Without flow, our results are consistent with the literature. With flow, upstream/downstream behaviors are observed. A conclusion summarizes the key findings in this thesis and provides a number of perspectives for future work.

Chapter 1

Impedance models in the linear regime without flow

In this chapter, we provide a review regarding the modeling of the impedance of perforated plate liners in the linear regime without flow. An exhaustive and standard semi-empirical model of the physical mechanisms occurring in the linear regime without flow is described: the model from Guess (1975). Thereafter, we propose to model the impedance by removing the very common short-tube approximation and to describe the radiation and aperture interaction effects using higher order modes. A mode-matching model is introduced to this end. The discussion revolves around the comparison of the mode-matching model and the mentioned semi-empirical model, and the comparison of both these models with impedance tube measurements. The impact of the number of modes on the impedance is also discussed. Finally, research perspectives are discussed in the conclusion.

1.1 Introduction

In the linear regime without flow, the impedance modeling of cylindrical tubes has already been widely discussed in the literature. Several physical mechanisms have been identified, including the acoustic viscous and thermal effects, the radiation and the edges effects. We propose in this section to detail these mechanisms separately, and to show a review of some proposed modeling strategies.

1.1.1 General description

If one considers a perforated liner as illustrated by figure 1.1, which is composed by a plate with multiple cylindrical perforations, a cavity and a back plate, two more physical effects are introduced: the orifice interaction and the back plate reflection. The perforated liners can be viewed as a periodic arrangement of Helmholtz resonators and an analogy can be made with a mass-spring system. The mass would correspond to the air oscillating in the perforations, and the spring would correspond to the air in the cavity.

The visco-thermal losses are caused by the presence of an acoustic viscous boundary layer and an acoustic thermal boundary layer appearing on the rigid boundaries. Their respective thicknesses are defined as follows (Rienstra *et al.*, 2018)

$$\delta_V = \sqrt{\frac{2\nu}{\omega}} \quad \delta_T = \sqrt{\frac{2\kappa}{\rho_0 c_p \omega}}$$

where ν is the kinematic viscosity, κ is the thermal conductivity, c_p is the heat capacity at constant pressure, ρ_0 is the density and ω is the angular frequency. At a given frequency, δ_V and δ_T are of the same order of magnitude but the thermal boundary layer is always slightly thicker than the viscous boundary layer. For the remainder of this thesis, an $e^{j\omega t}$ time dependence is used. In

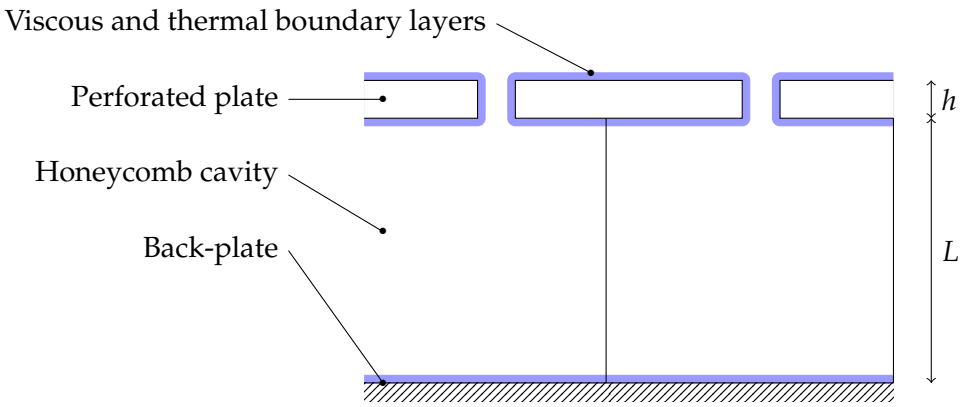

FIGURE 1.1: Schematic of a perforated plate liner.

the following, the radius of the perforations is denoted R_{neck} and the porosity of the plate, which corresponds to the Percent of Open Area (POA), is denoted σ. We also introduce the shear number Sh such that

$$Sh = \frac{R_{\text{neck}}}{\delta_V}. \tag{1.1}$$

Sh is large when the viscous boundary layer is thin compared to the tube radius and conversely. Its value plays an important role in the visco-thermal dissipation mechanisms and allows to distinguish the macro-perforated liners (large value of Sh) for which $R_{\text{neck}} > 0.5\,\text{mm}$ from the micro-perforated liners (low value of Sh), with $R_{\text{neck}} < 0.5\,\text{mm}$.

1.1.2 Visco-thermal effects

We focus our interest on the visco-thermal losses. Kirchhoff (1868) was the first to provide a general description of these phenomena in cylindrical tubes. His model has been simplified (Allard *et al.*, 2009) by Zwikker *et al.* (1949) which addressed the viscous and thermal effects distinctly for a circular apertures. Among others, the Zwikker and Kosten model has further been justified by Stinson (1991). Besides, in his semi-empirical model, Guess (1975) and Maa (1998) use the impedance of a single tube Z_ν derived by Crandall (1926) making the short-tube approximation. This hypothesis can also be found in Kinsler *et al.* (1950) and is very common in semi-empirical models.

In the following, we recall a brief derivation of Z_ν and introduce the short-tube approximation. We begin by writing the expression of the axial velocity in the neck v_{neck}, which can be found in Zwikker *et al.* (1949),

$$v_{\text{neck}}(r,z) = \frac{\partial p}{\partial z}\frac{1}{\mathrm{j}\rho_0\omega}\left[\frac{\mathrm{J}_0(Kr)}{\mathrm{J}_0(KR_{\text{neck}})} - 1\right], \tag{1.2}$$

where $K^2 = -\mathrm{j}\omega/\nu$ is the square of the Stokes acoustic wave number, ω is the angular frequency, p is the pressure and r is the radial coordinate. J_i is the ith-order Bessel function of the first kind.

According to Stinson (1991), the pressure is constant over the cross section of the tube, consequence of the parallel streamlines in the perforations. Therefore, after some derivations, the axial velocity averaged over the cross section of the neck reads

$$\overline{v}_{\text{neck}} = \frac{\partial p}{\partial z}\frac{1}{\mathrm{j}\rho_0\omega}\left[\frac{2\mathrm{J}_1(KR_{\text{neck}})}{KR_{\text{neck}}\mathrm{J}_0(KR_{\text{neck}})} - 1\right]. \tag{1.3}$$

For $h \ll \lambda$ with h the length of the tube and $\lambda = 2\pi c_0/\omega$ the wavelength, c_0 is the sound speed, the pressure gradient along the axial direction is considered to be constant such that

$$\frac{\partial p}{\partial z} = \frac{p_c - p_o}{h}, \tag{1.4}$$

where p_c is the pressure in the cavity and p_o is the outside pressure. Hence, the impedance resulting from viscous and inertia of a small tube is

$$Z_\nu = \frac{p_c - p_0}{\overline{v}_{\text{neck}}} = \mathrm{j}\omega\rho_0 h \left[\frac{2\mathrm{J}_1\left(KR_{\text{neck}}\right)}{KR_{\text{neck}}\mathrm{J}_0\left(KR_{\text{neck}}\right)} - 1\right]^{-1}. \tag{1.5}$$

1.1.3 Radiation effect

We now consider the radiation effects occurring at the entrance and the exit of the tube. Ingard *et al.* (1967) derived the radiation impedance Z_r of a single baffled cylindrical aperture in a infinite plane from the Rayleigh integral (Rayleigh, 1878) such that

$$Z_\mathrm{r} = \rho_0 c_0 \left[\left(1 - \frac{2}{\eta}\mathrm{J}_1\left(\eta\right)\right) + \mathrm{j}\mathrm{H}_1\left(\eta\right)\right], \tag{1.6}$$

where H_1 is the Struve function of first-order and $\eta = 2\omega R_{\text{neck}}/c_0$. Using the first-order expansions for J_1 and H_1 for small η (Pierce, 1981), we find

$$Z_\mathrm{r} = \rho_0 c_0 \left[\frac{\pi^2}{2}\left(\frac{2R_{\text{neck}}}{\lambda}\right)^2 + \mathrm{j}\frac{\omega}{c_0}\delta_0\right], \text{ for } \eta < 1/2, \tag{1.7}$$

where $\delta_0 = 16R_{\text{neck}}/(3\pi)$ is considered as an end correction which, as explained by Crandall (1926), can be interpreted as an added length of the tube due to the added mass of the medium outside the cylinder. As the radiation impedance depends on the radius of the neck, the approximation (1.7) is supposed to be better for micro-perforated liners.

1.1.4 Interaction effect

The interaction effect between the perforations of a plate was modeled by Fok (1941) and Ingard (1953) for an infinitely thin plate and further discussed by Melling (1973). Melling describes this effect both on the resistance and the reactance when the distance separating two perforations is small enough. On the reactance, the attached mass of both perforations interacts, while on the resistance the shear region between the perforations is disturbed.

In Ingard (1953), the main steps to determine analytically the end correction $\delta_{12} = \mathrm{z}_{12}/\left(-\mathrm{j}\omega\rho_0\right)$ corresponding to the interaction impedance z_{12} between two circular apertures are as follows. First, the end correction δ_{11} for a single eccentric circular aperture of radius R_{neck} in a circular tube of radius R_{tube} is determined neglecting the viscosity and using the Bessel addition theorem. This end correction is expressed as a function of the distance between the axis of the aperture and the axis of the tube and the ratio $\epsilon = R_{\text{neck}}/R_{\text{tube}}$. Secondly, an aperture of same radius is added at the same distance from the axis of the tube. Finally, the interaction impedance z_{12}, which involves the integral of a corrective pressure term taking into account the effect of the second perforation, is derived by considering a uniform velocity in both apertures.

In Guess (1975), this mechanism is accounted for by multplying the end correction δ_0 by $1 - 0.7\sqrt{\sigma}$ which accounts for the interaction effect on both sides of the perforation. This multiplying factor, which only depends on the porosity of the plate, is derived from the earlier work from Ingard (1953).

In Fok (1941), an analytic solution to account for the acoustic interaction effect is derived in the case of an infinitely thin plate. Unfortunately, the paper from Fok can hardly be found and is written in Russian. Therefore, we don't have access to much details on the derivation performed by Fok and we rely on the paper from Melling (1973), which briefly describes the results from Fok (1941). The attached conductance from Fok is $K = 2R_{\text{neck}}F(\epsilon)$ with

$$F(\epsilon) = 1 - 1.4092\epsilon + 0.33818\epsilon^3 + 0.06793\epsilon^5 - 0.02287\epsilon^6 + 0.03015\epsilon^7 - 0.01641\epsilon^8. \tag{1.8}$$

Equation (1.8) is commonly called the Fok function.

1.1.5 Back-plate reflection

Honeycomb cells are used in the cavity, forbidding any propagation in the transverse direction, hence the liner can be considered to be locally reacting. This means that the propagation in the cavity is normal to the plate, even if the incident wave has a non-normal incidence to the perforated plate.

Furthermore, the tangential velocity to the viscous boundary layer along the cavity walls is low, thus the viscous losses are negligible. The thermal effects are also known to be negligible (Ingard, 1953) in most liner application. Therefore, the cavity is assumed to be purely reactive and its normalized impedance is the one of a perfectly reflecting back-plate

$$z_b = -\cot(k_0 L), \tag{1.9}$$

where $k_0 = \omega/c_0$ is the wave number and L is the cavity height.

1.1.6 Viscous edge effects

In this section, we discuss the so-called *viscous edge effects* which occur at both end of the perforation. These dissipative effects play an important role on the resistance of a liner and are commonly accounted for by using a correction to the length of the tube. This approach is very practical and only requires to consider a longer tube when calculating the viscous term of the resistance. For a Helmholtz resonator, Ingard (1953) determined through theory that the end correction accounting for the viscous effects on both sides of the plate perpendicular to the aperture is R_{neck}. However, this correction is not sufficient to account for the complete edge effects which was yet to be fully understood. Indeed, the corners of the perforation and a *jet* extending from the neck also contribute to the viscous edge effects (Roche, 2011). This is highlighted in a detailed numerical analysis in chapter 2.

Ingard rectified the R_{neck} end correction through experiments to fit resistance measurements and found that the end correction is close to $2R_{\text{neck}}$. In doing so, Ingard accounts for the remaining contribution of the viscous edges effects, *i.e.* the corners and the jet.

His procedure is briefly recalled in what follows. Ingard (1953) starts by defining the dissipation due to viscosity W_ν through the integral

$$W_\nu = \frac{1}{2}\int_S R_S |U_S|^2 \, dS, \tag{1.10}$$

in which U_S is the tangential velocity amplitude at any surface S calculated neglecting the viscosity. R_S is an approximation of the so-called "surface resistance" of an infinite plane surface submitted to a tangential oscillatory flow and reads

$$R_S = \frac{1}{2}\sqrt{2\mu\rho_0\omega}, \tag{1.11}$$

in which μ is the dynamic viscosity. Hence, this approximation is supposed to remain valid inside the neck if R_{neck} is large compared to δ_V, *i.e.* for large Sh.

Ingard applies equation (1.10) to the neck and the plate of a Helmholtz resonator. He derives the acoustic specific normalized resistance Θ_i of the resonator as a function of the thickness of the plate and the aperture radius, separating the contributions from the surface of the neck and the surfaces of the parallel walls of the plate such that

$$\Theta_i = \Theta_{\text{neck}} + \Theta_{\text{plate}} = \frac{2R_S}{\rho_0 c_0} \frac{1}{R_{\text{neck}}} \left(h + R_{\text{neck}}\right), \tag{1.12}$$

where $\Theta_{\text{neck}} = 2R_s h / \left(\rho_0 c_0 R_{\text{neck}}\right)$ is the normalized resistance contribution of the neck and $\Theta_{\text{plate}} = 2R_S / \left(\rho_0 c_0\right)$ is the normalized resistance contribution of the plate on both sides. Thus, the resistance contribution from the plate can be interpreted as a resistance end correction (taking only the walls of the plate into account) equal to the radius of the aperture R_{neck}. However, when performing comparisons with measurements, Ingard finds that the end correction is closer to $2R_{\text{neck}}$ than R_{neck} to fit the measured resistance.

A possible explanation, given by Ingard, is the fact that the corners of the perforation have a radius smaller than the acoustic viscous boundary layer thickness, making approximation (1.11) inapplicable. Furthermore, the amplitude of the velocity tangential to the viscous boundary layer is expected to be large at the corners. We recall that in equation (1.10), the viscosity is neglected when calculating the amplitude of the tangential velocity, hence this approximation is flawed at the corners of the aperture. This explanation is confirmed by the numerical study in chapter 2 which highlights that the dissipation is strong at the corners of the perforation in the case of a macro-perforated liner.

It is noteworthy that this early work from Ingard (1953) is done for resonators with a perforation diameter greater than 3.6 mm. Therefore, its resulting end correction shall be used with care when considering micro-perforated liners. In fact Temiz *et al.* (2015) proposed end corrections to the acoustic resistance based on numerical simulations of perforated plate liners, including macro- and micro-perforated configurations. These end corrections translate in a multiplying factor to the surface resistance R_S used by Ingard.

Popie (2016) numerically determined an end correction to the acoustic resistance by considering a flat plate using the integral equations method. However, his correction is estimated to be between $0.81R_{\text{neck}}$ and $0.89R_{\text{neck}}$. This estimation is of the same order of magnitude that the end correction determined by Ingard through theory (R_{neck}). Popie suggests that this correction underestimation is induced by the corners region, in which a flat plate hypothesis cannot be assumed and where a corner field shall be considered.

From this brief review, it is clear that determining a reliable expression of the viscous edges effects end correction without measurements is challenging. The end correction determined experimentally by Ingard (1953) is shown to be accurate for both macro- and micro-perforated liners in section 1.4, although the Sh considered in Ingard's measurements is between 17 and 48 and the Sh considered in the measurements presented in this thesis is between 2 and 18.5.

The objective of this chapter is to (i) further investigate the visco-thermal losses modeling in the neck by not making the short-tube approximation and (ii) to model the radiation and interaction effects without using a length correction, but by using evanescent modes. A mode-matching (MM) model is introduced in section 1.3 to this end. The mode-matching model is compared, in section 1.5, to a semi-empirical model accounting for all the effects listed above: the Guess (1975) model, described in section 1.2.

1.2 Guess impedance model

Guess (1975) is one of the most well-known semi-empirical model including all physical mechanisms mentioned above. It is therefore a sound basis to assess the performance of the mode-matching model introduced in section 1.3. The losses in the neck are modeled using equation (1.5), which provides the impedance of a single tube, the flow rate conservation is used to obtain the non-dimensional impedance of a perforated plate z_ν such that

$$\mathrm{z}_\nu = \frac{\mathrm{Z}_\nu}{\sigma \rho_0 c_0}. \tag{1.13}$$

However, Guess approximates equation (1.13) and accounts for viscous edges effects for the high and low frequency regimes separately. For $Sh > 7.07$, *i.e.* for the high frequency regime, we have

$$\mathrm{z}_\nu \simeq \mathrm{z}_{\nu,\mathrm{H}} = \frac{\sqrt{2\nu\omega}h'}{\sigma c_0 R_{\mathrm{neck}}} + \mathrm{j}\left(\frac{\omega h}{\sigma c_0} + \frac{\sqrt{2\nu\omega}h'}{\sigma c_0 R_{\mathrm{neck}}}\right). \tag{1.14}$$

Here, $h' = h + 2R_{\mathrm{neck}}$ is a corrected length accounting for the viscous effects occurring at both entrances of the perforation based on the earlier work of Ingard (1953). This equation is suitable for macro-perforated liner, when the boundary layer thickness is thin compared to the perforation radius. In the low frequency regime, for $Sh < 0.71$, the approximation is

$$\mathrm{z}_\nu \simeq \mathrm{z}_{\nu,\mathrm{L}} = \frac{8\nu h'}{\sigma c_0 (R_{\mathrm{neck}})^2} + \mathrm{j}\frac{4\omega h}{3\sigma c_0}. \tag{1.15}$$

It is possible to directly compute the impedance from equation (1.5) instead of using the high and low frequency approximations, yet it is important to note that the h' correction is not applied on the mass inertance term $\omega h/(\sigma c_0)$. Hence, it would not be strictly equivalent to replace h by h' in equation (1.5).

In addition, approximations (1.14) and (1.15) are not valid for the micro-perforated configurations studied further below, for which $0.71 < Sh < 7.07$. Lack of information is given to model the impedance in this range of parameters in Guess (1975). Therefore, in this set of parameters, the model is completed in this thesis by implementing the following linear interpolation:

$$\mathrm{z}_\nu \simeq \mathrm{z}_{\nu,\mathrm{M}} = \mathrm{z}_{\nu,\mathrm{L}}(\omega_\mathrm{L}) + \frac{\mathrm{z}_{\nu,\mathrm{H}}(\omega_\mathrm{H}) - \mathrm{z}_{\nu,\mathrm{L}}(\omega_\mathrm{L})}{\omega_\mathrm{H} - \omega_\mathrm{L}}\omega, \tag{1.16}$$

where $\omega_\mathrm{H} = 100\nu/R_{\mathrm{neck}}^2$ and $\omega_\mathrm{L} = \nu/R_{\mathrm{neck}}^2$. This choice of interpolation is shown to provide accurate prediction for $2 < Sh < 3.5$ when compared to measurement in section 1.4.

Adding the remaining effects, namely the radiation, interaction and back-plate reflection, we get the explicit normalized impedance expression provided by Guess

$$\mathrm{z}_{\mathrm{Guess}} = \mathrm{z}_\nu + \frac{2\pi^2}{\sigma}\left(\frac{R_{\mathrm{neck}}}{\lambda}\right)^2 + \mathrm{j}\left(\frac{\omega\delta_1}{\sigma c_0} - \cot\left(k_0 L\right)\right). \tag{1.17}$$

The $\omega\delta_1/(\sigma c_0)$ term is a correction to the mass inertance to account for the radiation and interaction effect with the following end correction:

$$\delta_1 = \delta_0\left(1 - 0.7\sqrt{\sigma}\right). \tag{1.18}$$

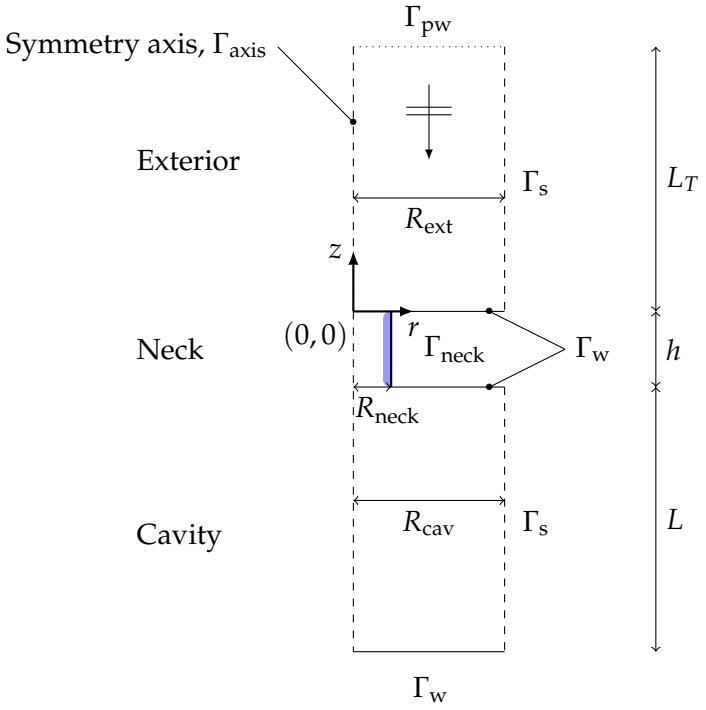

FIGURE 1.2: Axi-symmetric domain used for the mode-matching model.

1.3 Mode-matching model

The mode-matching model consists in coupling models of connected domains by matching in a weak sense the boundary conditions. The purpose of this model is to remove the short-tube approximation by accounting for the velocity profile in the neck (equation (1.2)). Another of its objectives is to account for the radiation and interaction effects explicitly through evanescent modes. In our problem, we consider three circular domains: the exterior, which is semi-infinite, the neck and the cavity. A unit plane wave with a normal incidence to the plate is considered. In the following, we consider a single perforation and further simplify the geometry to an axi-symmetric domain as illustrated in figure 1.2.

In the following the radius of the cavity and the exterior are respectively denoted R_{cav} and R_{ext} ($R_{cav} = R_{ext}$), the height of the cavity is L and the thickness of the plate is h. L_T is the distance between the surface of the plate and the surface for which the plane wave's phase equals zero.

To ensure that this non-pavable single-hole model is representative of a periodic arrangement of perforations, the porosity must correspond to that of the actual perforated plate. The cavity radius R_{cav}, which is equal to the exterior radius, is chosen to achieve the target plate porosity σ such that

$$\sigma = \left(\frac{R_{neck}}{R_{cav}}\right)^2. \tag{1.19}$$

Γ_s corresponds to the boundary of fictional ducts in the exterior and cavity domains.

One of the purposes of the mode-matching model is to release the short-tube approximation. Therefore, in the neck, the normal velocity profile is imposed according to equation (1.2). The pressure in the neck corresponds to a plane wave such that

$$p_{neck} = A_{neck} e^{-jk_{neck}(z+h)} + B_{neck} e^{jk_{neck}z}, \tag{1.20}$$

where A_{neck} and B_{neck} are the amplitudes of the waves propagating towards the positive and negative z, respectively. k_{neck} is a complex wave number defined by an equivalent complex density

$\rho(\omega)$ and a complex compressibility $C(\omega)$ (Stinson, 1991) such that

$$k_{\text{neck}} = \omega\sqrt{\rho(\omega)\, C(\omega)}. \tag{1.21}$$

The respective expressions of $\rho(\omega)$ and $C(\omega)$ are given in appendix A. The expression of the axial viscosity in the neck is

$$v_{\text{neck}} = -\frac{1}{\mathrm{j}\omega\rho_0}\left(1 - \frac{\mathrm{J}_0(Kr)}{\mathrm{J}_0(KR_{\text{neck}})}\right)\frac{\partial p_{\text{neck}}}{\partial z}. \tag{1.22}$$

Sound propagation in the exterior and the cavity is modeled using the classical Helmholtz equation in the absence of background flow

$$\nabla^2 p + k_0^2 p = 0, \tag{1.23}$$

and using a free-slip boundary condition such that

$$\frac{\partial p}{\partial n} = 0 \text{ on } \Gamma_{\text{axis}},\ \Gamma_{\text{w}} \text{ and } \Gamma_{\text{s}}. \tag{1.24}$$

Boundary condition (1.24) translates in the fact that there is no mass flux on the sides and the axis of the domain. Indeed, there is no flux through the fictional cylinder delimited by Γ_{s}. On the parallel wall of the plate and the back-plate, the viscosity is not accounted for, hence we use the latter free-slip boundary condition on Γ_{w}. On the wall of the neck, we impose a rigid wall boundary condition on the velocity $\mathbf{u} = (u, v)^{\mathrm{T}}$ such that:

$$\mathbf{u}_{\text{neck}} = \mathbf{0} \text{ on } \Gamma_{\text{neck}}. \tag{1.25}$$

Hence, the pressure solution to the Helmholtz equation in the (r, z) plane in the exterior and the cavity is an infinite sum of modes (Bruneau *et al.*, 2006), such that

$$p_i = \sum_{m=0}^{\infty}\left(A_i^m \mathrm{e}^{-\mathrm{j}k_i^{z,m}z} + B_i^m \mathrm{e}^{\mathrm{j}k_i^{z,m}z}\right)\Phi_i^m(r), \text{ with } i = \{\text{ext}, \text{cav}\}, \tag{1.26}$$

where A_i^m and B_i^m are the amplitudes of the waves propagating in the positive and negative z respectively. m is the mode index and $\Phi_i^m = \mathrm{J}_0\left(k_i^{r,m}r\right)$ is the mode shape function. The radial wave number $k_i^{r,m}$ and the axial wave number $k_i^{z,m}$ are related by the dispersion relation

$$\left(k_i^{z,m}\right)^2 = k_0^2 - \left(k_i^{r,m}\right)^2, \tag{1.27}$$

with $k_i^{r,m} = \gamma^{0,m}/R_i$ and $\gamma^{0,m}$ being solutions of $\mathrm{J}_0'\left(\gamma^{0,m}\right) = 0$.

The velocity in the cavity and the exterior are determined using the linearized Euler equation

$$v_i = -\frac{1}{\mathrm{j}\rho_0\omega}\frac{\partial p_i}{\partial n}. \tag{1.28}$$

The number of modes in the cavity and the exterior domains is truncated to $N+1$ (taking into account the mode 0). When modes are added on both sides of the plate, the coupling between the air present in the neck with the air in the exterior and the cavity is described by the mode-matching model. This coupling is commonly called the radiation effect.

The streamline confinement induced by the periodic layout of the perforations, also known as the interaction effect, is described by accounting for the radial velocity in the exterior and cavity domains. Due to the fact that some streamlines run along the parallel wall of the plate, several modes are needed to describe their confinement correctly. It is noteworthy that the interaction effect is implicitly depicted by adjusting R_{ext} and R_{cav} to fit the plate porosity.

The mode-matching method is implemented by enforcing the continuity of pressure and normal velocity at both the interface between the neck and the exterior and the neck and the cavity. More details on the continuity expressions can be found in the thesis from Sergent (1996). When matching the exterior and the neck domain, the weak formulation for the pressure continuity can be expressed as

$$\int_{S_{\text{neck}}} p_{\text{neck}} \Psi_{\text{neck}} \mathrm{d}S_{\text{neck}} = \int_{S_{\text{neck}}} p_{\text{ext}} \Psi_{\text{neck}} \mathrm{d}S_{\text{neck}}, \tag{1.29}$$

with p_{neck} the pressure field in the neck, p_{ext} the pressure field in the exterior domain and Ψ_{neck} the test function corresponding to the neck modal basis (see equation (A.2)). Here, S_{neck} is the neck cross section. The pressure continuity is further detailed in appendix A.1. The normal velocity continuity condition

$$v_{\text{ext}}(z=0) = v_{\text{neck}}(z=0) \text{ for } r \in [0; R_{\text{neck}}] \tag{1.30}$$

and

$$v_{\text{ext}}(z=0) = 0 \text{ for } r \in [R_{\text{neck}}; R_{\text{ext}}]. \tag{1.31}$$

The corresponding weak formulation is expressed as

$$\forall l \in \mathbb{N} \quad \int_{S_{\text{ext}}} v_{\text{ext}} \Psi^l_{\text{ext}} \mathrm{d}S_{\text{ext}} = \int_{S_{\text{neck}}} v_{\text{neck}} \Psi^l_{\text{ext}} \mathrm{d}S_{\text{neck}}, \tag{1.32}$$

with v_{ext} the axial velocity field in the exterior domain, v_{neck} the axial velocity field in the neck and Ψ^l_{ext} the l^{th} test function corresponding to the exterior modal basis. S_{ext} is the exterior cross section. The normal velocity continuity is further discussed in appendix A.2. The same equations are used when matching the cavity and the neck domains. As mentioned above, a plane wave is implemented in the exterior domain. The ingoing plane wave with amplitude $B^0_{\text{ext}} = 1$ is implemented as

$$\frac{\partial p_{\text{ext}}}{\partial n} = 2\mathrm{j}k_0 B^0_{\text{ext}} \mathrm{e}^{-\mathrm{j}k_0 L_T} + \mathrm{j}k_0 p_{\text{ext}} \text{ on } \Gamma_{\text{pw}}. \tag{1.33}$$

Using the rigid boundary condition on the back cover, a linear system is formed, giving access to the modal amplitudes A^m_{ext} and B^m_{ext}. Thus, the reflection coefficient is derived as $R = A^0_{\text{ext}}/B^0_{\text{ext}}$. The linear system is detailed in appendix A.3. Finally, the normalized impedance is determined using

$$\mathrm{z}_{\text{mm}} = \frac{R+1}{R-1}. \tag{1.34}$$

1.4 Impedance tube measurements

In order to assess the validity of Guess (1975) model and the mode-matching model, measurements are carried out in accordance with the NF EN ISO 10534-2 standard method. The measurements are performed for a frequency range between 400 Hz and 6400 Hz but the comparisons in the next section are done between 850 Hz and 2600 Hz. Outside this range, the measurements are considered to be too noisy. The diameter of the tube is 29 mm. The cut-on frequency of the first non plane mode is 6932 Hz. Two 1/4" microphones with a 20 mm spacing are used to determine the surface impedance of the liners. The distance between the sample and the closest microphone is 45.2 mm. The cavity height is $L = 29$ mm. Four perforated liners are considered for measurements to investigate the impact of the liner's geometry on the impedance. Although this measurement method is known to be robust, the sample mounting repeatability is tested. The sample's impedance is measured four times. Between each measurements the perforated plate is remounted. In the following, the mean quantity over the four measurements is plotted. The blue zone surrounding each plot is delimited by the curves corresponding to, respectively, the mean

Configuration	σ (%)	R_{neck} (mm)	R_{cav} (mm)	h (mm)
1 (macro)	6	0.8	3.27	1.5
2 (macro)	10	0.8	2.53	1.5
3 (micro)	1.4	0.15	1.27	0.6
4 (micro)	4.2	0.15	0.73	0.6

TABLE 1.1: Perforated plate configurations.

FIGURE 1.3: Cross-sectional view of a perforated plate with $R_{\text{neck}} = 0.9\,\text{mm}$. Note that this view does not intersect with both of the perforations axes.

minus and plus the standard deviation. The red zone is delimited by the minimum and maximum values of the impedance.

The chosen parameters are summarized in Table 1.1. Configuration 1 and 2 correspond to macro-perforated plates with a low and high porosity respectively. Configuration 3 and 4 are micro-perforated plates with a low and high porosity. The neck radius is kept constant in the macro- and micro-perforated cases. The perforated plates are manufactured by mechanical drilling. More details on the accuracy of this manufacturing process can be found in Drevon (2004). Figure 1.3 shows a photography of a perforated plate cut to assess the sharpness of the corners. From a macroscopic point of view, the corners appear to be very sharp, however, dedicated measurements would be necessary to completely characterize their geometry. The corners are known to have an important impact on the real part of the impedance (Temiz *et al.*, 2015) and could explain discrepancies between the measurements and the predictions in the next section.

The diameter of the perforations is known within $\pm 0.01\,\text{mm}$, which provides a good accuracy on the overall porosity of the plate. In the macro-perforated case, the maximum relative error on the porosity is 1.3 % while for the micro-perforated case it is 6.8 %. The Sound Pressure Level (SPL) is set to 105 dB at the plate surface with a white noise source.

We introduce the Strouhal number

$$St = \frac{2\omega R_{\text{neck}}}{|\sqrt{2}u_p|} \tag{1.35}$$

in which $|u_p|$ is the Root Mean Square (RMS) value of the acoustic velocity through a perforation. In order to remain in the linear regime, the condition $St > 1$ must be verified according to Temiz *et al.* (2016). If this condition is respected, the particle displacement is smaller than the diameter of the perforation and non-linear effects are unlikely to appear. Since we are using a white noise source, this velocity $|u_p|$ can be defined at least in two ways. Firstly, we can consider that the perforation is submitted to the acoustic velocity associated with each frequency independently. Secondly, we can use the root mean square velocity calculated over the complete frequency range. This is defined as follows

$$u_p = \sqrt{\sum_i u_{p,i}^2} \tag{1.36}$$

in which $u_{p,i}$ is the acoustic velocity at each frequency. The latter u_p is supposed to be the effective velocity at the surface of the plate and is formed with the contribution from each frequency. In the linear regime, using a sine-swept source instead of a white noise source makes no difference as the impedance does not depend on the effective velocity in the neck. However, in the non-linear

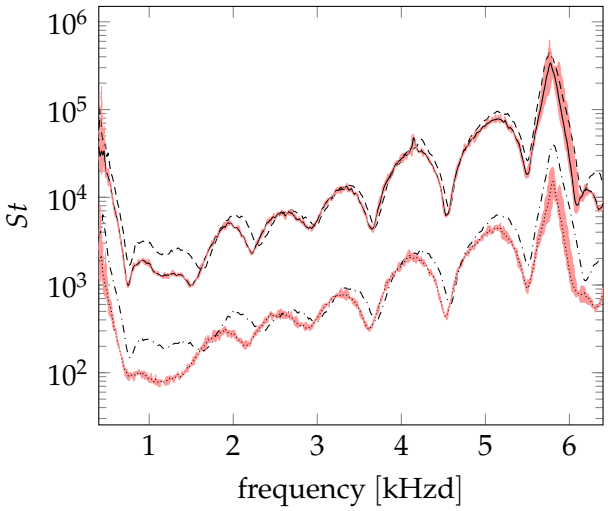

FIGURE 1.4: Mean value of the Strouhal number measured for the 4 configurations. The red zone is delimited by the minimum and maximum measured values for configuration 1 and 3.

regime, significant differences can be observed, especially on the resistance (this is discussed in details in chapter 3).

It is necessary to check that $St > 1$ using both definitions of the velocity $|u_p|$. Figure 1.4 shows the Strouhal number based on the acoustic velocity at each frequency. We can observe that the repeatability of these measurements is satisfactory. The lowest value observed between 850 Hz and 2600 Hz is $St = 79.8$ at 1120 Hz for configuration 3.

When using the root mean square velocity calculated between 400 Hz and 6400 Hz, *i.e.* the complete frequency range used during the measurement, we see that its lowest value is $St = 3.3$. As a consequence, it can be considered that we remain in the linear regime in the whole considered frequency range.

1.5 Discussion

The impedance obtained from the mode-matching and Guess models are now compared with the impedance obtained through measurements. The difference between both predictions are highlighted and their validity range is assessed.

1.5.1 Comparison with measurements

The comparison between calculations and measurements is operated between 850 Hz and 2600 Hz. The normalized impedance is defined by $\mathrm{z} = \mathrm{Z}/(\rho_0 c_0)$. The normalized resistance $\mathrm{Re}(\mathrm{z})$ and the normalized plate reactance $\mathrm{Im}(\mathrm{z}) + \cot(k_0 L)$ are plotted as functions of the frequency. The normalized plate reactance is determined by removing the cavity reactance $-\cot(k_0 L)$ from the total normalized reactance. This is done to better see the difference between the predictions and the measurements, as the cavity reactance dominates the total reactance.

Figures 1.5 and 1.6 correspond the macro- and micro-perforated cases respectively. We can observe that the mounting repeatability of the measurements is good for every samples.

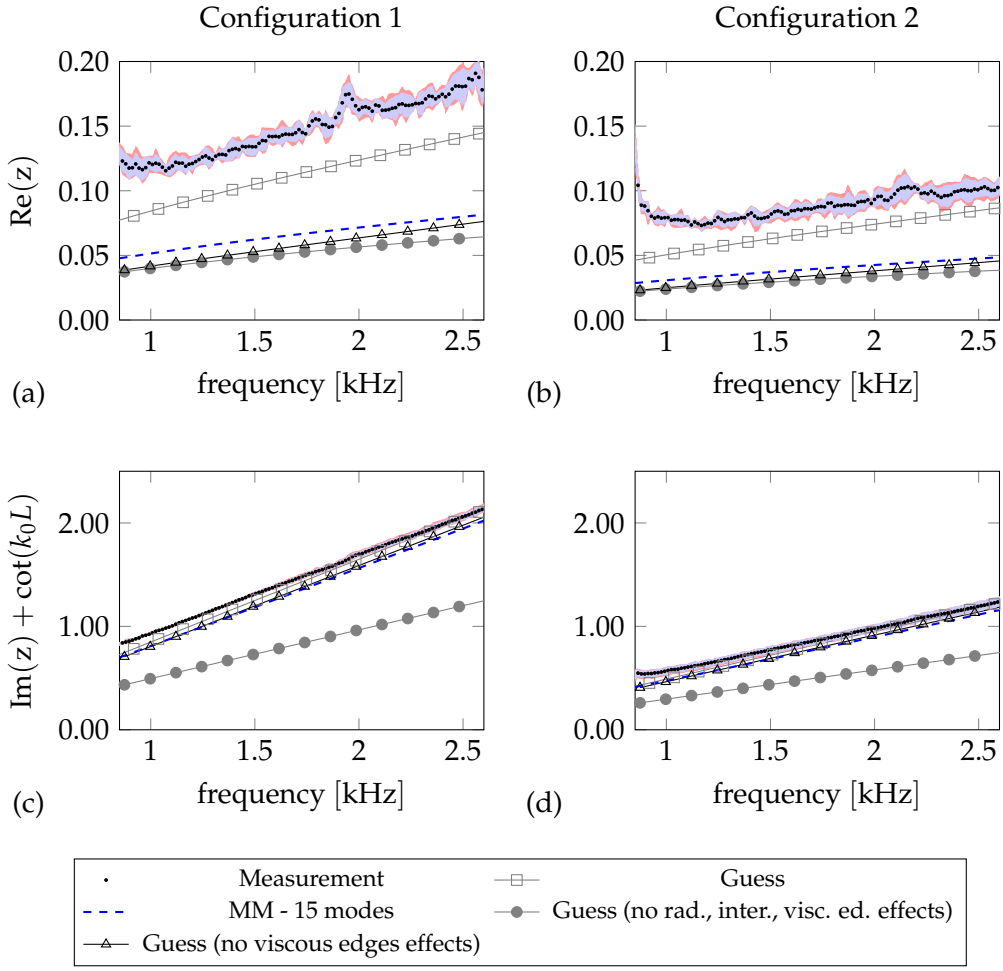

FIGURE 1.5: Left: Normalized resistance (a), and normalized plate reactance (c) for configuration 1: a macro-perforated liner with a low porosity. Right: Normalized resistance (b), and normalized plate reactance (d) for configuration 2: a macro-perforated liner with high porosity.

The measurement (·), the full Guess model (—□—), the Guess model without edges effects (—△—), the Guess model without radiation, interaction and edges effects (—●—) and the mode-matching model using 15 modes (- - -) are compared. In the case of the macro-perforated configurations 1 & 2, we have $10.6 < Sh < 18.5$. For the micro-perforated configurations 3 & 4 we have $2 < Sh < 3.5$. This change of shear number regime allows to assess the validity of the models.

First, we observe that the mode-matching model underestimates the measured resistance for configuration 1 to 4. On the other hand, the full Guess model provides good resistance prediction. When using the Guess model without viscous edges effects (—△—), we find resistance values comparable to those given by the MM model (- - -). It shows that the mode-matching model does not account for viscous edges effects. A possible explanation to this is the fact that we consider non-viscous modes outside the aperture and that we do not account for the thermo-viscous losses on the wall of the plate. Furthermore, the corners velocity and pressure fields are not handled explicitly in the MM formulation.

We now focus on minor discrepancy between the mode-matching and the Guess models. We compute the impedance using the Guess model without radiation, interaction and viscous edges effects (—●—). It is noteworthy that the correction associated to the interaction effect has only an impact on the imaginary part of the impedance.

According to figures 1.5 (a) and (b), the radiation has a minor impact on the real part of the

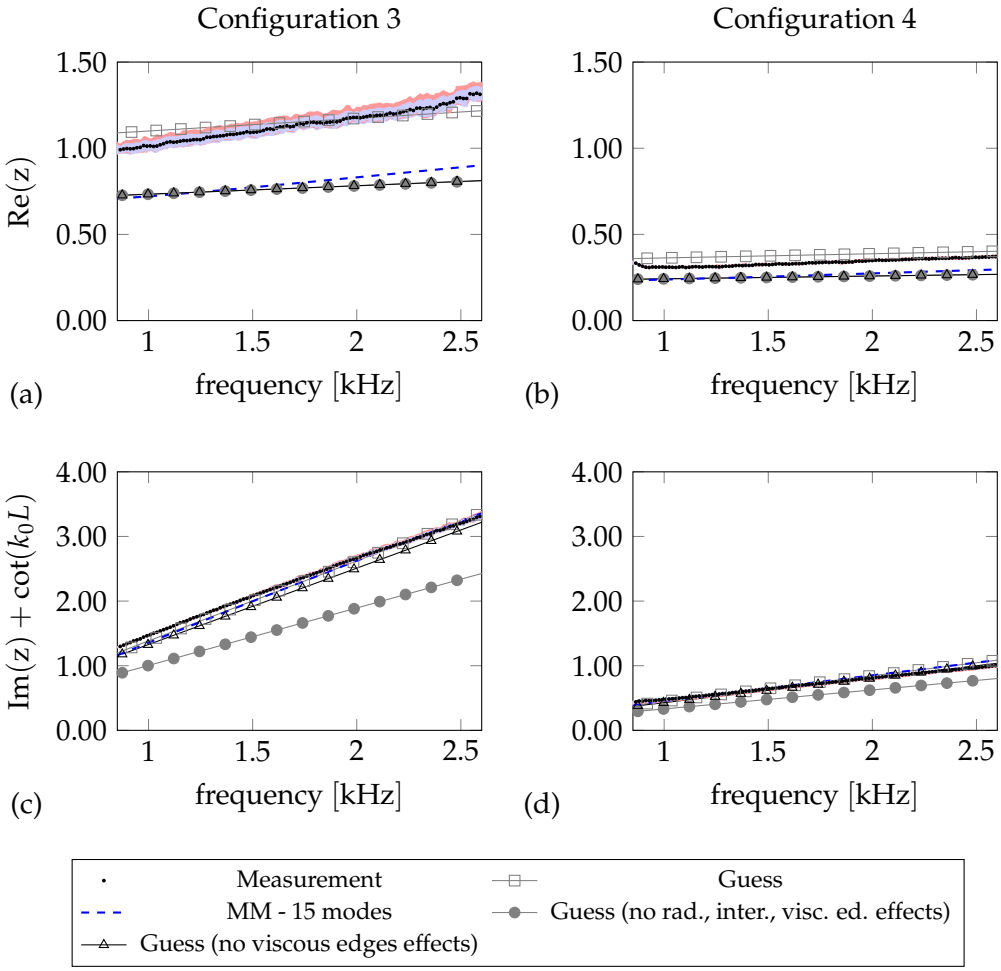

FIGURE 1.6: Left: Normalized resistance (a), and normalized plate reactance (c) for configuration 3: a micro-perforated liner with a low porosity. Right: Normalized resistance (b), and normalized plate reactance (d) for configuration 4: a micro-perforated liner with a high porosity.

impedance of the macro-perforated configurations and close to no influence when considering the micro-perforated configurations (figures 1.6 (a) and (b)), as far as Guess model is concerned. In figures 1.5 (a) and (b) the resistance provided by the mode-matching model (- - -) is close to the resistance predicted by the Guess model without viscous edges effects (—△—), which suggests that the MM model captures correctly the real part of the radiation impedance.

The resistance computed with the mode-matching model (- - -) is slightly higher than the Guess model without viscous edges effects (—△—) in figures 1.6 (a) and (b) (micro-perforated configurations) and figures 1.5 (a) and (b) (macro-perforated configurations). This might indicate that the MM model is able to represent a subtle dissipative effect that is not accounted for the Guess model. This difference could be related to

- the fact that we take into account the velocity profile in the neck,
- the thermal losses that are taken into account in the expression of k_{neck}, which are neglected in the Guess model,
- or the interaction and radiation effect that are approximated more precisely in the mode-matching model. Indeed, in the Guess model, these effects are modeled by first order series approximation.

In Guess (—□—) (figures 1.5 (c), (d) and 1.6 (c), (d)), the viscous edges effects have a limited impact on the imaginary part the impedance. On the contrary, the radiation and interaction effects have a meaningful influence on the plate reactance of the macro-perforated configurations 1 and 2. The plate reactance predicted by the mode-matching model (- - -) is close to those computed with the full Guess model (—□—), which indicates that both the radiation and interaction effects are correctly described by the MM model when considering both macro- and micro-perforated plates.

1.5.2 Impact of the number of modes on the impedance

In the previous section 1.4, the Guess model was compared with the mode-matching model with $N = 15$ modes. In the present section, we justify this choice of value for N.

First, we inspect how the velocity in the neck is approximated at the interfaces for respectively 5, 15, 30 and 50 modes. In figure 1.7, we plot the modulus of the velocity profile in the neck and the exterior domain at the surface of the plate for $z = 0$ for the 4 configurations close to their resonance frequency, *i.e.* when the reactance is zero. The axial velocity profile in the neck from Zwikker *et al.* (1949) is compared to the exterior velocity approximated for different numbers of modes.

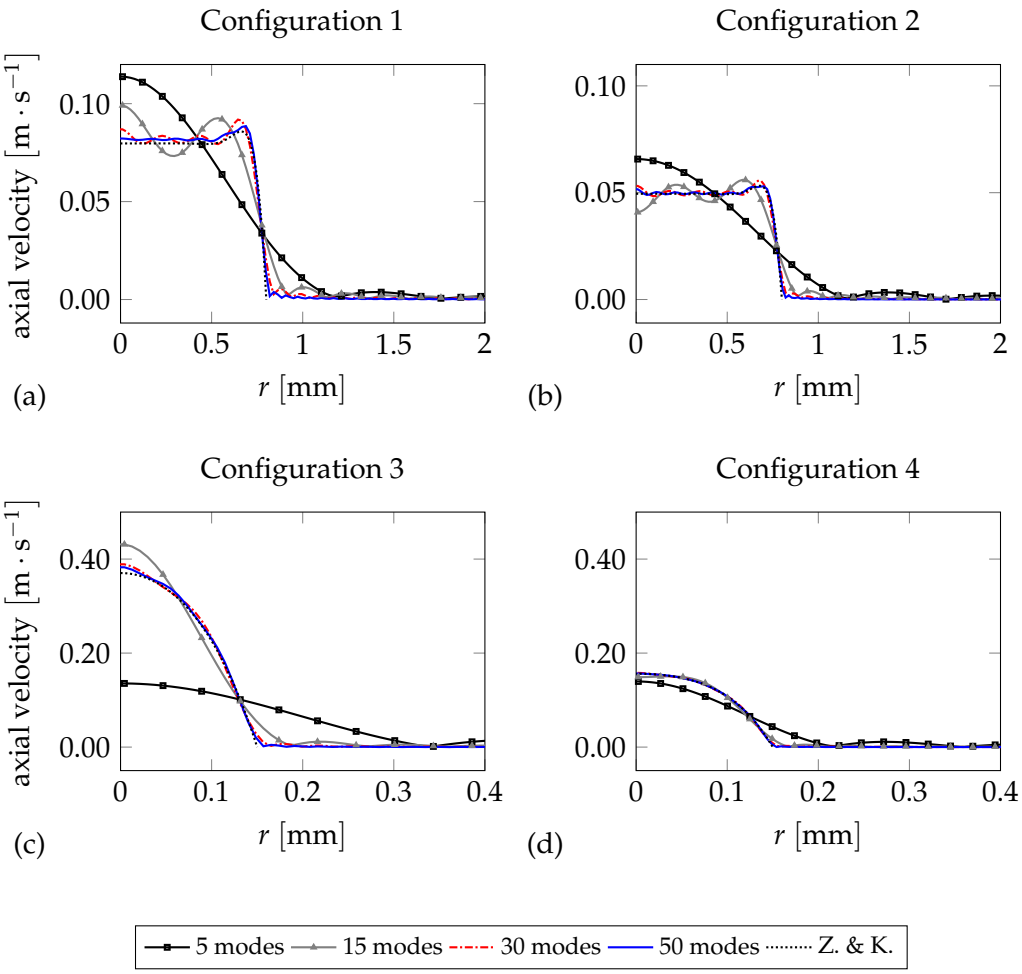

FIGURE 1.7: Modules of the velocity along the radial coordinate for (a) configuration 1 at 1344 Hz, (b) configuration 2 at 1680 Hz, (c) configuration 3 at 1088 Hz and for (d) configuration 4 at 1808 Hz.

As expected, increasing the number of modes improves the approximation. When switching from 5 to 15 modes, the velocity profile approximation is substantially improved and is even better for 30 and 50 modes. However, for the macro-perforated configurations in figures 1.7 (a) and (b) we notice Gibbs oscillations of which the amplitudes gets smaller when the number of modes increases. These oscillations are also visible for the micro-perforated configurations but to a lesser extent, as the velocity profile that we seek to approximate is smoother.

In figure 1.8, we plot the impedance computed for different number of modes from 2 to 50.

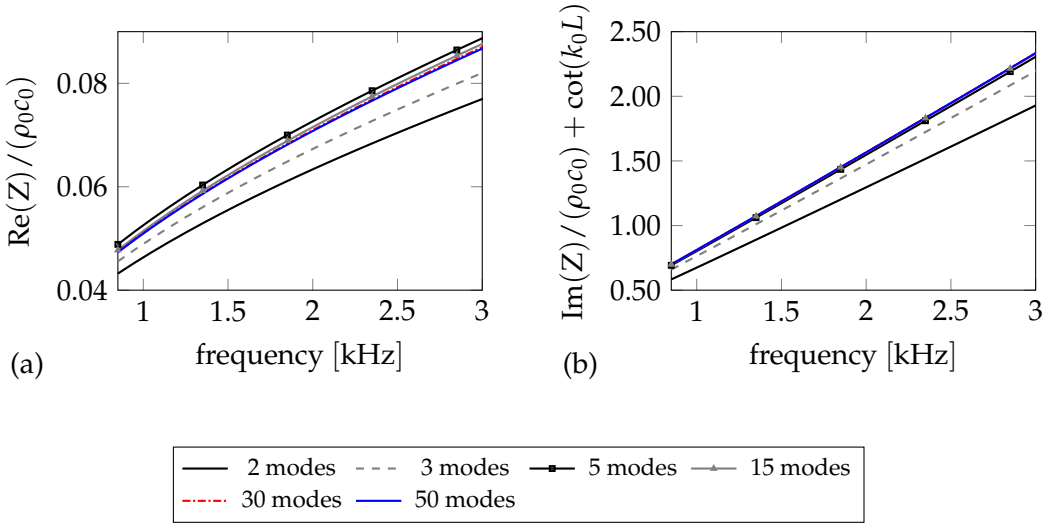

FIGURE 1.8: Impedance for different number of modes for configuration 1. (a) Normalized resistance, (b) normalized plate reactance.

The number of modes has a significant impact on the velocity profile approximation. However, according to figure 1.8, its impact on the impedance real and imaginary part is marginal when more than 5 modes are used. The mode-matching converges very quickly, as far as the impedance is concerned. We can hardly see a difference between the impedance obtained for 15, 30 and 50 modes, hence the choice is of 15 modes for the computation presented in the previous section 1.4.

1.6 Conclusion

The impedance modeling of the physical effects occurring in the linear regime has been reviewed, followed by the description of the standard semi-empirical model from Guess (1975). A model removing the short-tube approximation and accounting for the radiation and interaction effects through higher order modes has been introduced.

From the comparisons of both models with impedance tube measurements, the modeling importance of the viscous edges effects is highlighted. In order to complete the mode-matching model, this important dissipative effects could be added by using higher order viscous modes (Kirchhoff, 1868), allowing to consider evanescent modes in the neck and to account for viscous losses in the exterior domain and in the cavity. This would take into account at the same time losses occurring in the plate, in the vicinity of the jet, and due to strong gradients close to the corners. Analytic expressions of these modes exist for slits (Stinson, 1991), but not for cylindrical perforations. The development of an analytic formulation for higher order viscous modes in cylindrical wave-guides constitutes a promising perspective as they could describe the viscous edges effects.

Despite this lack of completeness, the mode-matching model is shown to correctly capture the radiation and interaction effects in the linear regime. Furthermore, a limited number of modes is necessary to reach the impedance convergence. Therefore, when the complete velocity or pressure fields need to be determined, its efficiency is good compared to those of other model based on numerical methods such as finite elements.

In the following chapter, we wish to investigate more precisely the dissipation mechanisms occurring in a perforation in the linear regime and to further study the edges effects in order to give guidelines for semi-empirical and MM modeling strategies. For this purpose, the finite element method is used to model the impedance of perforated plate liners.

Chapter 2

Numerical models in the linear regime

After the review of impedance models for perforated plates in chapter 1, we now move to computational modeling. In the linear regime and in the absence of mean flow, the impedance of perforated liners is driven by visco-thermal effects. In this chapter, two numerical models are employed for predicting these visco-thermal losses. The first model is the linearized compressible Navier–Stokes equations (LNSE) solved in the frequency domain. The second model is the Helmholtz equation with a visco-thermal boundary condition accounting for the influence of the acoustic boundary layers. These models are compared and validated against measurements. The quantitative analysis of the dissipation rate due to viscosity, computed from the LNSE solutions of 4 perforated plates, highlights significant differences between the edge effects of a macro- and a micro-perforated plate. In the latter case, a jet is present at the entrances of the perforation. The proposed numerical method to calculate the impedance of perforated liners, based on the Helmholtz equation and a visco-thermal boundary condition, is found to be computationally cheaper and to provide reliable predictions.

2.1 Introduction

In the linear regime without mean flow, the main dissipation mechanisms responsible for the acoustic dissipation are the visco-thermal losses. They can be described using the theory from Stinson (1991) for the visco-thermal losses inside the neck (discussed in the previous chapter) and the experimental works from Ingard (1953) for the viscous dissipation close to the entrances of the perforations. In addition, mathematical background are proposed by Laurens *et al.* (2013) for the Rayleigh conductivity of cylindrical perforation and unconventional apertures. In a similar modeling effort, Honzík *et al.* (2013) propose a transfer function derived from Zwikker *et al.* (1949) theory to model the viscous and thermal boundary layers in small horns.

Numerical methods such as the Boundary Element Method (BEM) (Cutanda-Henríquez *et al.*, 2013) or the Finite Element Method (FEM) are also used to model visco-thermal acoustics. In this chapter we focus on the FEM. In Joly *et al.* (2006) and Joly (2010) the FEM is used to solve a coupled linear formulation based on the particle velocity and the temperature variation. This approach is shown to be computationaly efficient. In the same vein, in Kampinga *et al.* (2011) and Kampinga *et al.* (2010) the Linearized Navier-Stokes Equations (LNSE) are implemented in COMSOL (Pryor, 2009).

More numerical studies have been performed to highlight physical mechanisms in perforated liners. This is the case in Roche *et al.* (2009) in which Direct Numerical Simulations are carried out to solve the non-linear compressible Navier-Stokes equations in a 2-dimensional (2D) and a 3-dimensional (3D) geometry. Solving the latter equations has an important computational cost but it includes an exhaustive list of physical mechanisms. In Temiz *et al.* (2015) the linearized incompressible Navier-Stokes equations are solved in a 2D geometry to study the impact of perforation edge geometry on the impedance of a liner.

In the present chapter, two different numerical models are presented and validated, with a view to investigate the acoustic losses occurring at a perforation. The first model solves the Helmholtz equation with a boundary condition accounting for the viscous and thermal acoustics boundary layers Berggren *et al.* (2018). This boundary condition is obtained by assuming that the rigid wall is smooth and that its curvature radius is much greater than the viscous and thermal boundary layers thicknesses. This so-called "Helmholtz with losses" model is compared against a more detailed, but more costly, alternative model based on the linearized compressible Navier–Stokes equations. A study using this set of equations can be found in Malinen *et al.* (2004). Both models are solved in the frequency domain using finite elements. Their results are compared with impedance tube measurements. This allows to assess the validity of the Helmholtz with losses model. Additionally, the LNSE model allows for a detailed investigation of the losses phenomenon of the micro-perforated and the standard macro-perforated liners ($R_{\text{neck}} > 0.5\,\text{mm}$, defined in section 2.2). The dissipation rate per mass unit due to viscous effects is computed and the differences between micro- and macro-perforate liners are investigated. The latter investigation gives more insights into the modeling effort needed to provide accurate impedance predictions and an explanation on the lack of accuracy of the mode-matching model developed in the previous chapter.

The rest of this chapter is as follows. We first present the theoretical models in section 2.2. In section 2.3, a brief description of the numerical methods is given. A comparison between the numerical models and measurements follows in section 2.4 and the dissipation rate is analyzed in section 2.5. In section 2.6, the convergence of the numerical models is assessed. Finally, we conclude on the relevance of the Helmholtz with losses model in section 2.7. Note that the journal paper Billard *et al.* (2021) forms the basis for this chapter.

2.2 Numerical models

In this section, two numerical models are described to predict the acoustic impedance of a perforated plate.

The geometry of the perforated plate, which is composed of a periodic arrangement of cylindrical holes is simplified to a single hole. The computational domain is composed of three cylindrical ducts corresponding to the exterior, the neck and the cavity of the liner. The geometry is further simplified to the 2D axi-symmetrical domain Ω showed in Figure 2.1.

To ensure that this non-pavable single-hole model is representative of a periodic arrangement of perforations, the Percentage of Open Area (POA), also known as porosity σ, must correspond to the one of the actual perforated plate. The cavity radius R_{cav}, which is equal to the exterior radius, is chosen to achieve the target plate porosity σ such that

$$\sigma = \left(\frac{R_{\text{neck}}}{R_{\text{cav}}} \right)^2, \tag{2.1}$$

where R_{neck} is the radius of the neck.

In Figure 2.1, the Γ_{s} boundary corresponds to a sliding surface whereas Γ_{bc} and Γ_{neck} are walls with a no-slip condition. Γ_{axis} is the symmetry axis of the domain Ω. An implicit time dependence $\mathrm{e}^{+\mathrm{j}\omega t}$ is used, where ω is the angular frequency. An incoming plane wave is imposed as a boundary condition on Γ_{in}. The LNSE and the Helmholtz equation are solved in the domain Ω to calculate the reflected waves and, hence, the reflection coefficient and the effective impedance of the liner.

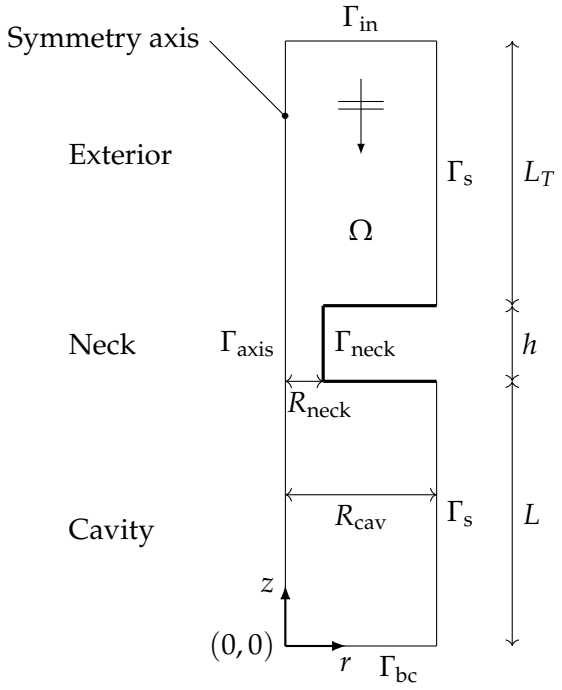

FIGURE 2.1: Axi-symmetric representation of the model.

2.2.1 Linearized Navier–Stokes equations

The problem is made non-dimensional by using the following quantities: the sound speed c_0^*, the fluid density ρ_0^* and the reference length $L_{\text{ref}}^* = R_{\text{neck}}$ (recall that $R_{\text{cav}} = R_{\text{neck}}/\sqrt{\sigma}$). The symbol * denotes dimensional quantities. It follows that variables are made non-dimensional as follows

$$x = \frac{x^*}{L_{\text{ref}}^*}\,, \quad \mathbf{u} = \frac{\mathbf{u}^*}{c_0^*}\,, \quad \rho = \frac{\rho^*}{\rho_0^*}\,, \quad p = \frac{p^*}{\rho_0^* c_0^{*2}}\,, \quad T = \frac{T^* c_p^*}{c_0^{*2}}\,, \quad e = \frac{e^*}{c_0^{*2}}\,.$$

$\mathbf{u} = (u_r, u_z)^{\mathrm{T}}$ is the fluid velocity, ρ is the density, p is the pressure, T is the temperature, c_p^* is the specific heat capacity at constant pressure and e the specific internal energy.

The acoustic Reynolds number based on the sound speed, and the Prandlt number are defined as follows

$$Re_a = \frac{\rho_0^* c_0^* L_{\text{ref}}^*}{\mu^*} \text{ and } Pr = \frac{c_p^* \mu^*}{\kappa^*} \tag{2.2}$$

where μ^* is the dynamic viscosity and κ^* is the thermal conductivity. Both are assumed independent of temperature.

A perfect gas is assumed, which leads to the following relations between thermodynamic quantities:

$$c^2 = \gamma r T,\ e = \frac{T}{\gamma} \text{ and } p = \rho r T \text{ with } r = \frac{\gamma - 1}{\gamma}.$$

Here, c is the dimensionless sound speed, $\gamma = c_p^*/c_v^*$ is the heat capacity ratio and c_v^* is the specific heat capacity at constant volume.

The equations stating the conservation of mass, momentum and energy are as follows:

$$\frac{\partial \rho}{\partial t} + \nabla \cdot (\rho \mathbf{u}) = 0, \tag{2.3}$$

$$\rho \frac{\partial \mathbf{u}}{\partial t} + \rho \left(\mathbf{u} \cdot \nabla\right) \mathbf{u} = -\nabla p + \nabla \cdot \underline{\tau}, \tag{2.4}$$

$$\frac{\rho}{\gamma} \left(\frac{\partial T}{\partial t} + \mathbf{u} \cdot \nabla T \right) = -p \nabla \cdot \mathbf{u} + \underline{\tau} : \nabla \mathbf{u} + \frac{1}{Re_a Pr} \nabla^2 T. \tag{2.5}$$

The viscous stress tensor $\underline{\tau}$ is given by

$$\underline{\tau} = \frac{1}{Re_a} \left[\nabla \mathbf{u} + (\nabla \mathbf{u})^{\mathrm{T}} + \left(\mu_B - \tfrac{2}{3}\right) (\nabla \cdot \mathbf{u}) \mathcal{I} \right], \tag{2.6}$$

where $\mathcal{I}$ is the 2-by-2 identity matrix and $\mu_B = \mu_B^* / \mu^*$ is the normalized bulk viscosity. We follow the Stokes hypothesis by setting $\mu_B = 2/3$. This choice, which implies that the effect of dilatation on the viscous stress tensor is ignored, is discussed in more details by Schlichting (1979).

The mass conservation equation (2.3), the momentum conservation equation (2.4) and the energy conservation equation (2.5) are linearized around a steady state defined by ρ_0, $\mathbf{u}_0$, p_0 and T_0:

$$\rho = \rho_0 + \rho' \,, \quad \mathbf{u} = \mathbf{u}_0 + \mathbf{u}' \,, \quad p = p_0 + p' \,, \quad T = T_0 + T' \,,$$

in which ρ' is the perturbed density, $\mathbf{u}'$ is the perturbed velocity, p' is the perturbed pressure and T' is the perturbed temperature. We consider a uniform quiescent medium, hence $\mathbf{u}_0 = \mathbf{0}$, $\rho_0 = 1$, $c_0 = 1$, $p_0 = 1/\gamma$ and $T_0 = 1/(\gamma - 1)$. In addition we solve these equations in the frequency domain assuming a $\mathrm{e}^{+\mathrm{j}\omega t}$ time dependence. To discuss the results, we introduce the thickness δ_V^* of the acoustic viscous boundary layer as well as the shear number Sh:

$$\delta_V^* = \sqrt{\frac{2\mu^*}{\rho_0^* \omega}}, \; Sh = \frac{R_{\mathrm{neck}}}{\delta_V^*}. \tag{2.7}$$

Sh relates the viscous boundary layer thickness to the radius of the perforation. It is useful to distinguish between the macro- and micro-perforated regimes and to assess the range of validity of the Helmholtz equation with losses. When Sh is high, the viscous boundary layer thickness is small compared to the perforation radius.

Therefore, the linearized Navier–Stokes equations reduce to

$$\mathrm{j}\omega \rho' + \nabla \cdot \mathbf{u}' = 0, \tag{2.8}$$

$$\mathrm{j}\omega \mathbf{u}' = -\nabla p' + \frac{\omega}{2Sh^2} \nabla \cdot \left[\nabla \mathbf{u}' + \left(\nabla \mathbf{u}'\right)^{\mathrm{T}} \right], \tag{2.9}$$

$$\mathrm{j}\omega T' = -\nabla \cdot \mathbf{u}' + \frac{\omega \gamma}{2Sh^2 Pr} \nabla^2 T'. \tag{2.10}$$

This set of equation is for instance implemented in Malinen *et al.* (2004) in the FEM software Elmer to model the thermo-viscous effects in acoustics. In the present study we rely on the GetFEM library (Renard *et al.*, 2020). An incident plane wave is defined on the upper boundary of the domain Ω:

$$\nabla p' \cdot \mathbf{n} + \mathrm{j}k p' = 2\mathrm{j}kW \mathrm{e}^{+\mathrm{j}kL_Z} \text{ on } \Gamma_{\mathrm{in}}, \tag{2.11}$$

where $\mathbf{n}$ is the outgoing normal vector, $L_Z = L + h + L_T$, and W is the amplitude of the incoming plane wave. k is the acoustic wave number accounting for the viscosity of the fluid and neglecting

thermal effects we obtain:

$$k = \omega \left(1 + \mathrm{j}\omega^2 \frac{\mu_B + \frac{4}{3}}{2Sh^2} \right)^{-\frac{1}{2}} . \tag{2.12}$$

Further details are provided in Appendix B.1.

Equations (2.8), (2.9) and (2.10) are solved together with the following boundary conditions. On the perforated plate and the back cover, a no-slip condition is implemented together with an isothermal condition:

$$\mathbf{u}' = \mathbf{0} , \quad T' = 0 \text{ on } \Gamma_{\text{neck}} \text{ and } \Gamma_{\text{bc}} . \tag{2.13}$$

Alternatively, we will also consider the case where an adiabatic condition is imposed by setting $\nabla T' \cdot \mathbf{n} = 0$ on these surfaces. In section 2.4, we will compare numerical results obtained with the isothermal and the adiabatic boundary conditions. We will observe that the results are very similar and that the choice of this boundary condition is non-significant. In practical applications, an isothermal boundary condition is considered as a good approximation, given the thermal conductivities of the wall materials.

On the sides and the axis of the domain, a free-slip boundary condition is enforced with an adiabatic condition:

$$\mathbf{u}' \cdot \mathbf{n} = 0 , \quad \nabla T' \cdot \mathbf{n} = 0 \text{ on } \Gamma_{\text{axis}} \text{ and } \Gamma_{\text{s}} . \tag{2.14}$$

This free-slip condition is indeed representative of the interaction between perforations for a normal plane wave, due to the symmetry of the configuration.

The reflection coefficient R on the surface of the perforated plate is defined by

$$R = \left(\frac{\overline{p}}{W} - \mathrm{e}^{\mathrm{i}kL_T} \right) \mathrm{e}^{\mathrm{i}kL_T}, \tag{2.15}$$

where $W = 1$ and $\overline{p}$ is the averaged pressure over the boundary Γ_{in}.

Thus, the normalized impedance at the surface of the perforated plate is determined using the following expression:

$$\mathrm{z} = \frac{Z}{\rho_0 c_0} = \frac{R+1}{R-1}. \tag{2.16}$$

2.2.2 Helmholtz with losses model

Inside the computational domain we solve the Helmholtz equation written for pressure:

$$\nabla^2 p + \omega^2 p = 0 \text{ in } \Omega. \tag{2.17}$$

Like for the LNSE, an incident plane wave is defined on the upper boundary of the domain by writing

$$\nabla p \cdot \mathbf{n} + \mathrm{j}\omega p = 2W\mathrm{j}\mathrm{e}^{+\mathrm{j}\omega L_Z} \text{ on } \Gamma_{\text{in}}. \tag{2.18}$$

On the axis and the sides of the domain we impose a free-slip boundary condition:

$$\nabla p \cdot \mathbf{n} = 0 \text{ on } \Gamma_{\text{axis}} \text{ and } \Gamma_{\text{s}}. \tag{2.19}$$

Even though a lossless Helmholtz equation is used in the computational domain, it is still possible to account for some visco-thermal losses through the use of a boundary condition that accounts for these effects within the acoustic boundary layers over the solid surfaces. This approach was first proposed and developed by Morse *et al.* (1968) and was recently further refined by Berggren *et al.* (2018). These equivalent boundary conditions are derived by performing an asymptotic expansion around the viscous boundary layer thickness. The boundary condition derived by

Berggren *et al.* (2018) reads

$$\nabla p \cdot \mathbf{n} = \delta_V \frac{\mathrm{j}-1}{2} \nabla_T^2 p + \delta_T \omega^2 \frac{(\gamma-1)(\mathrm{j}-1)}{2} p \text{ on } \Gamma_{\text{neck}} \text{ and } \Gamma_{\text{bc}}, \tag{2.20}$$

in which ∇_T^2 is the tangential Laplacian defined as

$$\nabla^2 p \equiv \nabla_T^2 p + \frac{\partial^2 p}{\partial n^2} + (\nabla_T \cdot \mathbf{n}) \frac{\partial p}{\partial n}. \tag{2.21}$$

Here, $\partial/\partial n = \mathbf{n} \cdot \nabla$. The dimensionless viscous and thermal boundary layer thicknesses are defined as follows

$$\delta_V = \frac{1}{Sh} \text{ and } \delta_T = \frac{1}{Sh\sqrt{Pr}}.$$

One objective of the present chapter is to assess the applicability of this equivalent boundary condition to predict the acoustic impedance of perforated plate liners. Equation (2.20) is derived from the linearized compressible Navier–Stokes equations. A no-slip condition and an isothermal condition are applied on the rigid walls. The radius of curvature of the surface should also be large compared to the viscous boundary layer thickness. Therefore, in the case of a perforate plate, this boundary condition is valid when the radius of the neck is much larger than δ_V and δ_T. This limitation is stated by Mbailassem *et al.* (2019) in a similar approach. Since the wall model (2.20) is not suitable for strongly curved surfaces, this model is not expected to be valid at the corners of the hole. The corners of the perforation and their sharpness can play an important role in the acoustic dissipation, as discussed by Morse *et al.* (1968). Another limitation is that the viscous boundary layer should not interact. For a perforate plate, this occurs when $\delta_V \geq R_{\text{neck}}$. Berggren *et al.* (2018) compared their solutions to those of Keefe (1984) for cylindrical wave guides of radius 0.1 mm and obtained good correspondence for $Sh > 2$. In order to perform consistent comparisons between the numerical models and measurements, we will not consider $Sh < 2$.

Equation (2.20) is derived using an isothermal boundary condition. If an adiabatic boundary condition is used instead, the term $\delta_T \omega^2 (\gamma-1)(\mathrm{j}-1)p/2$ in (2.20) is removed because it represents the heat flux through the thermal boundary layer.

This model based on the classical Helmholtz equation and the equivalent boundary condition (2.20) allows to perform rapid predictions of the acoustic impedance of a perforated plate. This is because it involves only a single variable, compared to the LNSE which involves density, velocity and temperature. In addition, the LNSE model requires a very fine mesh to resolve the thermal and viscous boundary layers while here the net effect of the acoustic boundary layers are directly modeled by the equivalent boundary condition (2.20). This is especially true for high frequencies, when the boundary layers are very thin compared to the wavelength.

2.3 Numerical method

The LNSE model and the Helmholtz model are both solved using the finite element method. The variational formulations are detailed in B.2 and B.3. These formulations are implemented using the GetFEM++ package (Renard *et al.*, 2020) and the meshes are generated using Gmsh (Geuzaine *et al.*, 2009). Unstructured, triangular meshes are used. In the LNSE model, first order polynomials are used to approximate the density and the temperature while second-order polynomials are used for the velocity. In the Helmholtz model, the pressure field is approximated with second-order polynomials.

Figure 2.2 shows an example of finite element mesh used for the LNSE model. This mesh corresponds to configuration 3, detailed in Table 2.1 further below. The mesh is refined near the neck to properly resolve the boundary layers. In addition, the corners of the neck are rounded

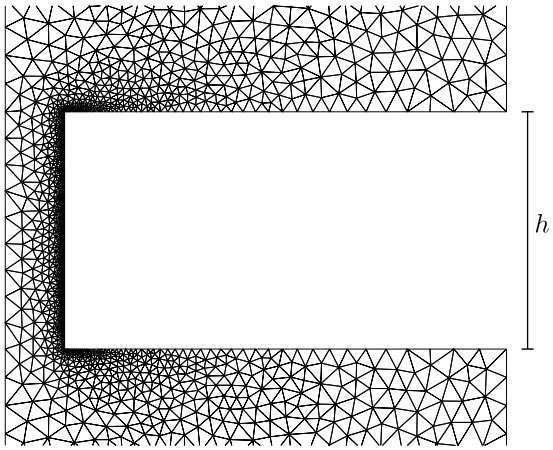

FIGURE 2.2: Example of finite element mesh for the LNSE model. This a zoom on the perforation of configuration 3.

Configuration	σ (%)	R_{neck} (mm)	R_{cav} (mm)	h (mm)
1 (macro)	6	0.8	3.27	1.5
2 (macro)	10	0.8	2.53	1.5
3 (micro)	1.4	0.15	1.27	0.6
4 (micro)	4.2	0.15	0.73	0.6

TABLE 2.1: Perforated plate configurations.

with a radius $R_c = R_{\text{neck}}/100$ to avoid geometrical singularities. No measurable difference is observed on the predicted impedance when the computations are performed using sharp corners, but rounded corners lead to a faster mesh convergence of the numerical model. This method is also used by Temiz *et al.* (2015) to perform numerical simulations based on the linearized incompressible Navier-Stokes equations.

2.4 Comparison with measurements

The results obtained from the numerical models are now compared with impedance tube measurements. The measurements used here are the same as in the Chapter 1. We recall the chosen parameters for each configuration in Table 2.1.

Figures 2.3 shows the impedances obtained for the macro-perforated plates, for which $10.6 < Sh < 18.5$ approximately. The LNS model appears to underestimate the resistance of the macro-perforated liners. It is also the case for the Helmholtz model but to a lesser extent. However, the significance of these differences is limited since we are looking at low resistance values. As a result, the corresponding absolute error is low. The computed plate reactances present a good correspondence with the measurements.

Figure 2.4 shows the impedances for the micro-perforated configurations, for which $2 < Sh < 3.5$, which correspond to the validity limit of the Helmholtz model. In the micro-perforated case, according to Figures 2.4(a) and 2.4(b), the resistance is accurately predicted by the linearized Navier–Stokes model. The Helmholtz model also provides correct predictions of the resistance despite the fact that it is less accurate close to its validity limit (Figure 2.4(a)), *i.e.* when $Sh \simeq 2$. Good correspondence between the measured and the modelled plate reactances is visible in Figures 2.4(c) and 2.4(d).

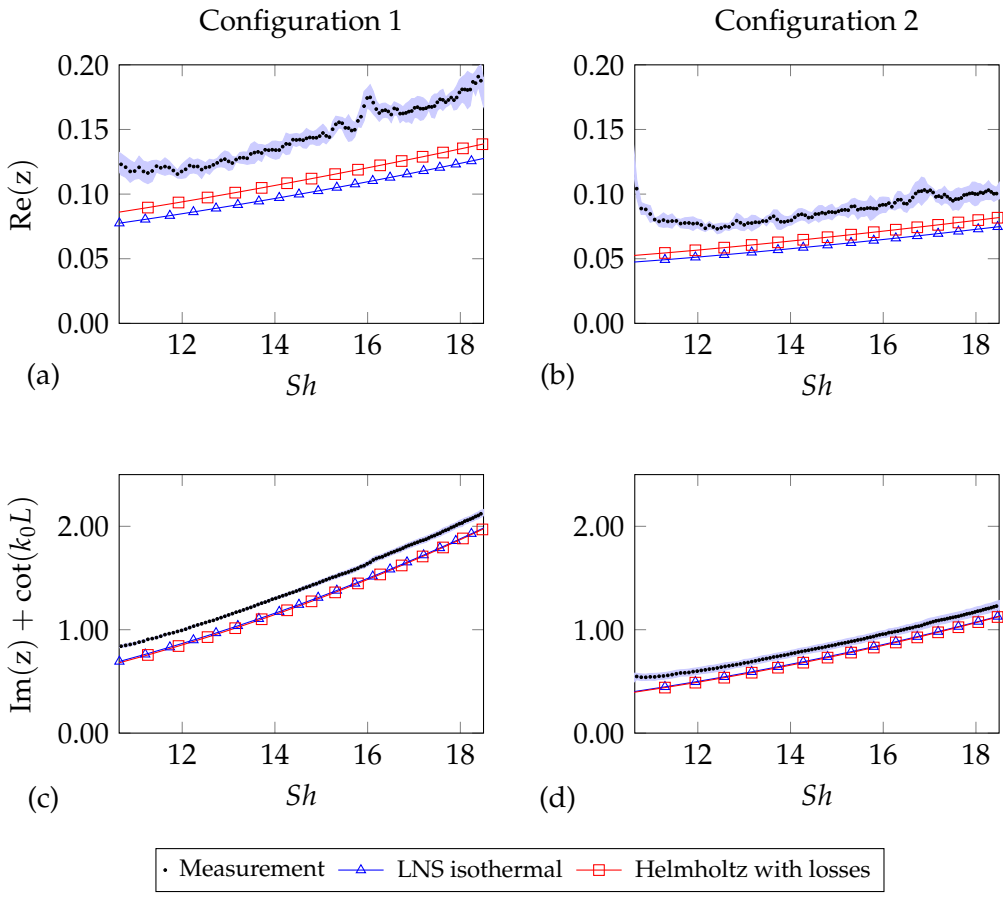

FIGURE 2.3: (a), (c) Normalized resistance and normalized plate reactance for configuration 1: a macro-perforated case with a low porosity ($Re_a = 18201$, $Pr = 0.707$). (b), (d) Normalized resistance and normalized plate reactance for configuration 2: a macro-perforated case with a high porosity ($Re_a = 18201$, $Pr = 0.707$).

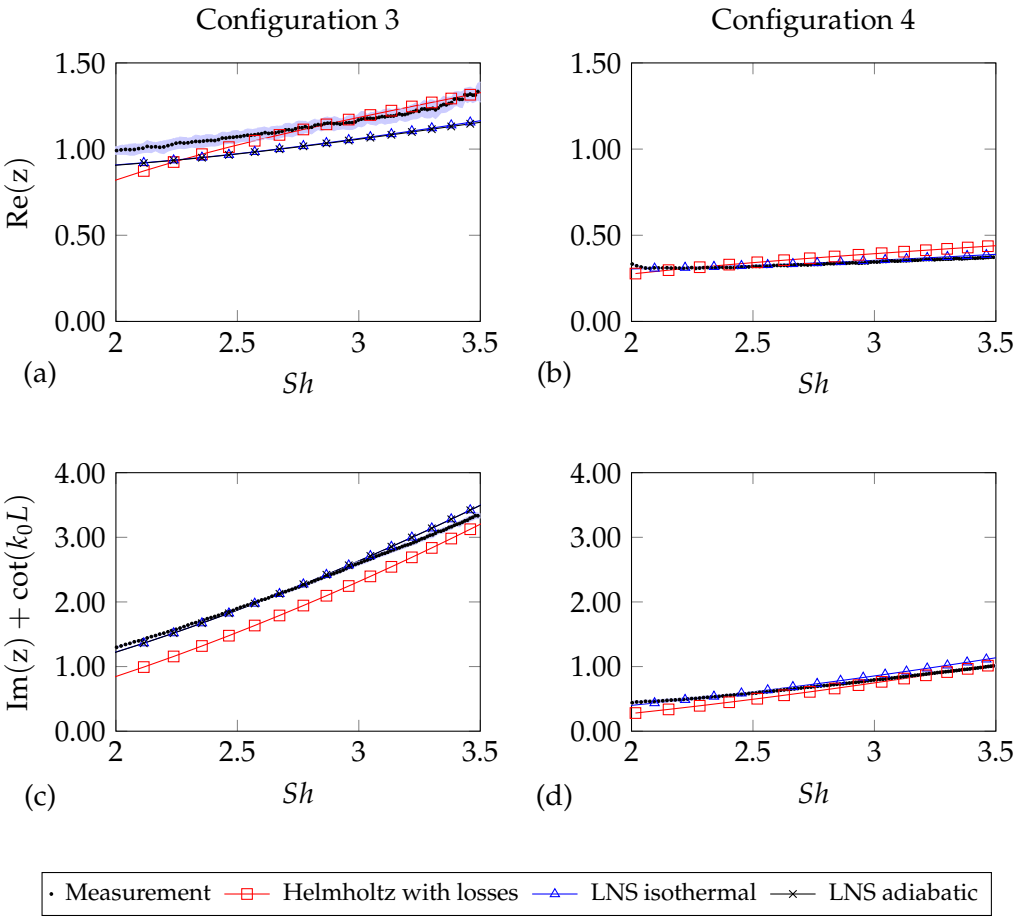

FIGURE 2.4: (a), (c) Normalized resistance and normalized plate reactance for configuration 3: a micro-perforated case with a low porosity ($Re_a = 3413$, $Pr = 0.707$). (b), (d) Normalized resistance and normalized plate reactance for configuration 4: a micro-perforated case with a high porosity ($Re_a = 3413$, $Pr = 0.707$).

As mentioned in the previous section, the LNSE predictions are based on the isothermal condition on the plate and the backing plate. It is interesting to assess whether the use of an adiabatic condition would significantly change these predictions. This is shown in Figure 2.4(a) where the results with an adiabatic and isothermal conditions are presented side-by-side for configuration 3. Changing the nature of the thermal boundary condition only has a very limited influence on the predicted impedance. This observation was expected since the dissipation is dominated by shear effects rather than thermal effects in this particular case.

2.5 Analysis of the rate of dissipation

In order to gain more insight into the dissipation mechanisms influencing the impedance of a perforated plate, we calculate the viscous dissipation rate Lighthill (1978). From equation (2.6), we derive its expression, separating the dissipation due to shear and bulk effects. In the time domain, the dissipation rate per unit mass resulting from shear stresses is

$$\Phi_{\text{shear}} = \frac{1}{Re_a}\left\{\frac{1}{2}\left[\nabla\mathbf{u} + (\nabla\mathbf{u})^{\mathrm{T}}\right] : \left[\nabla\mathbf{u} + (\nabla\mathbf{u})^{\mathrm{T}}\right] - \frac{2}{3}(\nabla\cdot\mathbf{u})^2\right\}, \tag{2.22}$$

and the dissipation rate per unit mass due to the bulk viscosity is:

$$\Phi_{\text{bulk}} = \frac{1}{Re_a}\mu_B(\nabla\cdot\mathbf{u})^2 \ . \tag{2.23}$$

The expression of Φ_{shear} and Φ_{bulk} are consistent with Batchelor (1967). In the results presented below, the integral over the whole FEM domain of the mean value of the dissipation due to bulk effect $\overline{\Phi}_{\text{bulk}}$ was found to be negligible compared to the overall value of $\overline{\Phi}_{\text{shear}}$ for all four configurations. Indeed, the dissipation due to dilatation is expected to be negligible in our range of shear number, *i.e.* $2 < Sh < 20$. For this reason, $\overline{\Phi}_{\text{bulk}}$ is not discussed further.

The dissipation rates $\overline{\Phi}_{\text{shear}}$ for the macro-perforated configurations 1 & 2 and the micro-perforated configurations 3 & 4 are shown in Figure 2.5 at their respective resonance frequencies for $rL^*_{\text{ref}} \in [0; R_{\text{cav}}]$ and $zL^*_{\text{ref}} \in [L - 2R_{\text{neck}}; L + h + 2R_{\text{neck}}]$. In both cases, an important part of the dissipation is localized in the neck. This well-known dissipation mechanism is modelled by the theory from Zwikker *et al.* (1949). In the case of a micro-perforated plate, the viscous boundary layer thickness is large compared to the neck radius, thus the dissipation is spread across the neck. In the macro-perforated configuration, for which the ratio Sh is high, the dissipation is concentrated close to the wall of the neck.

In addition to the viscous losses in the neck, significant losses can also be seen just outside of the neck and at its corners. However the relative magnitude of these losses varies markedly between the macro- and micro-perforated cases. In the first case, the losses are localized mainly at the corners of the neck, while in the second case they are found outside the neck, at its entrances. The net effects on the acoustic impedance of the viscous losses occurring outside the neck and at the corners edges are generally modeled using end correction terms. For instance, Guess (1975) introduces a correction length $h' = h + 2R_{\text{neck}}$, determined empirically. This correction originates from Ingard (1953) and is defined as the viscous edges effects in Chapter 1. From figure 2.5, it is clear that the viscous edges effects are not only localized on the wall of the plate and the corners edges as suggested by Ingard (1953), but also extend outside the perforations. More recently, it has been possible to use numerical simulations to calculate these end correction terms more systematically. For instance, Temiz *et al.* (2015) solved the linearized incompressible Navier-Stokes equations to determine the end correction for a wide range of perforates ($1 < Sh < 35$) covering both micro- and macro-perforates. While the determination of an end correction is useful to build

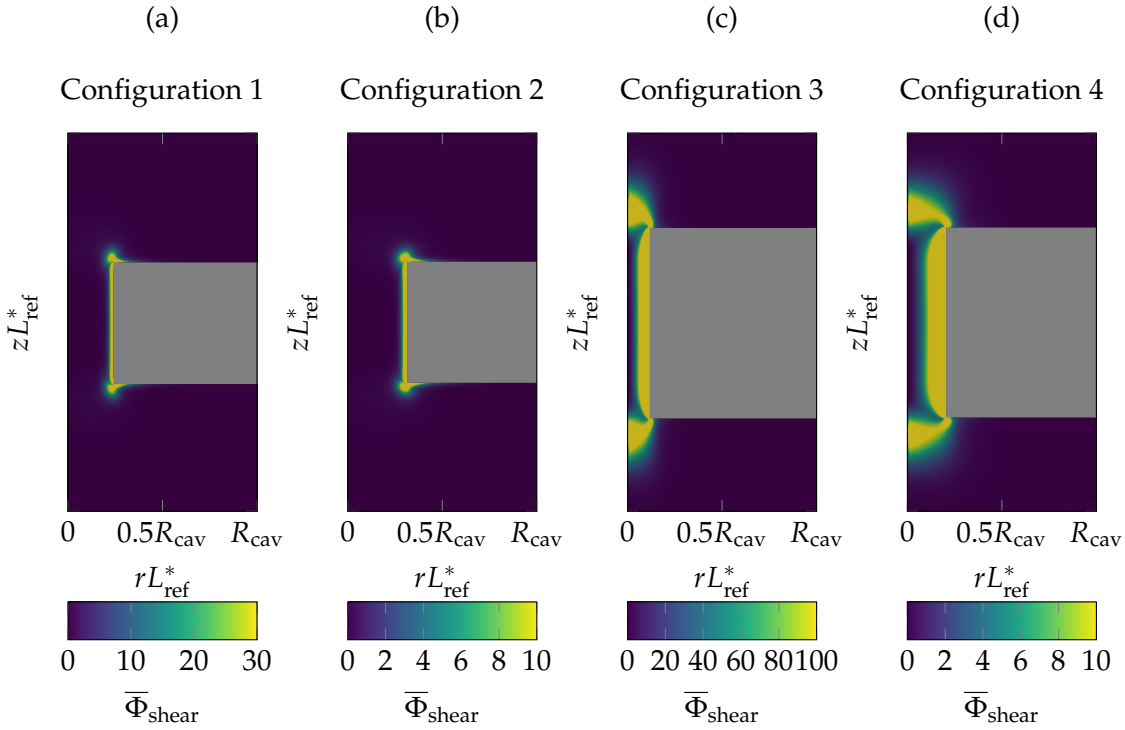

FIGURE 2.5: Mean value of the dissipation rate per unit mass due to shear effects at the resonance frequency of configuration 1 at $Sh = 13.4$ (a), configuration 2 at $Sh = 15$ (b), configuration 3 at $Sh = 2.2$ (c) and configuration 4 at $Sh = 2.9$ (d).

Configuration	Sh	Exterior (%)	Neck corners (%)	Neck (%)	Wall (%)
1 (macro)	13.4	12.7	37.8	2.1	46.9
2 (macro)	15	11.1	39.4	1.6	47.5
3 (micro)	2.2	25.1	7.1	31.3	36.1
4 (micro)	2.9	25.3	7.1	31.3	36.9

TABLE 2.2: Comparison of the contributions for each configuration.

a simple formula for the acoustic impedance, the detailed analysis of the dissipation rate presented here helps to understand where the viscous losses are located.

In order to quantitatively assess the differences in the distribution of dissipation rate between the micro- and macro-perforated cases, the dissipation rate due to shear effects is integrated over four domains shown in Figure 2.6. The domains correspond to: the exterior close to the hole entrances, the neck, the wall of the neck and the corners of the neck. The contributions from these zones are computed for the four previous configurations and compared to each others.

Table 2.2 summarizes the contributions from each zone to the overall dissipation rate for each configuration at their respective resonance frequencies. The remaining losses in the domain do not exceed 0.6% for each configuration.

The relative distribution of losses is significantly different between the macro-perforated cases 1 & 2 and the micro-perforated cases 3 & 4. In the first cases, the viscous boundary layer thickness is small compared to the neck radius and the dissipation is localized mainly near the corners and along the neck wall. The important contribution from the corners is partly due to the fact that the ratio $h/(2R_{\mathrm{neck}})$ is close to 1 in the macro-perforated case, meaning that the corner integration zone extends far in the wall of the neck. Therefore, most of the losses occur close to the wall.

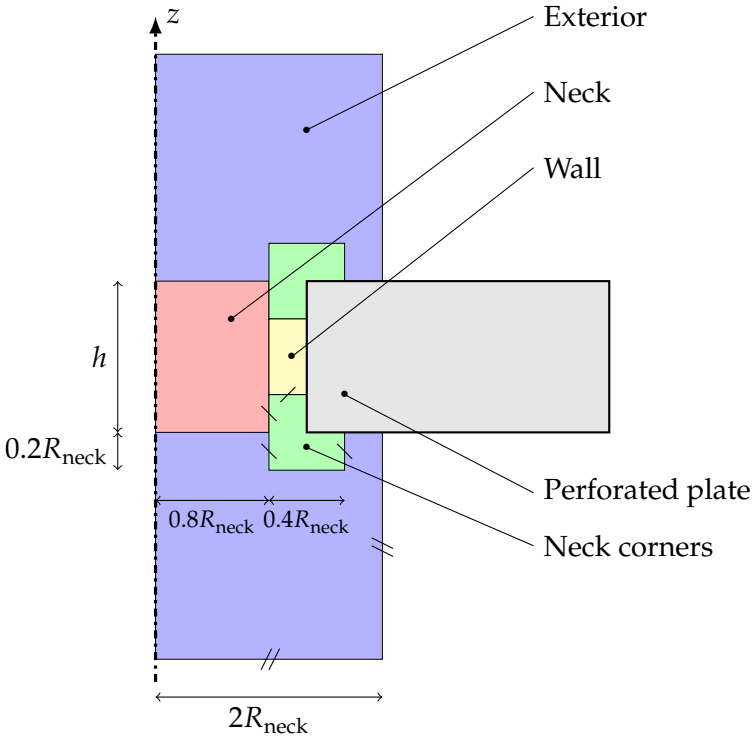

FIGURE 2.6: Schematic of the integrated surfaces.

This explains why, for macro-perforated configurations, the Helmholtz model with the equivalent boundary condition (2.20) is able to provide results similar to the LNSE model. In the micro-perforated cases, the shear number Sh is low and a significant contribution from the neck and the wall regions is visible. In addition, about a quarter of the losses occurs in the exterior domain, near the entrance of the holes. This highlights the presence of a jet in the linear regime when considering micro-perforation. Despite the fact that the Helmholtz approach is not modeling this effect, it so happens that, for this configuration, it provides correct predictions of the impedance.

2.6 Convergence of the numerical models

The convergence of the numerical models is investigated in this section. In a first stage, we compare the results obtained from impedance tube measurements to computations performed with different numbers of degrees of freedom (DOF) using the macro-perforated configuration 1.

Good convergence of the LNSE model is obtained with 36.8 kDOF (Figure 2.7(b)). This corresponds to elements of size $3.34\delta_V$ on the axis and $0.43\delta_V$ on the surface of the neck. The size of the elements on the edges of the perforation is the same as the size of the elements on the surface of the neck. In fact, the normalized plate reactance in Figure 2.7(d) has already converged for a very coarse model with just 11.4 kDOF. Figures 2.7(a) and (c) show that the Helmholtz model converges for a number of DOF near 6.4 kDOF. This corresponds to elements of size $8.16\delta_V$ on the axis and $1.07\delta_V$ on the surface of the neck. This much smaller model size is explained by the facts that (i) the Helmholtz equation is a scalar model while the LNSE involves 4 variables, (ii) there is no need to resolve the boundary layers with the Helmholtz model, and (iii) there is no need to have polynomials with different orders for each variables.

Indeed, according to Kellogg *et al.* (1996), when solving the LNSE, it is necessary to respect the inf-sup condition for numerical stability. In fact, this is why P1 elements are used to solve the density and the temperature, and P2 elements are used to solve the velocity. Therefore, P1 elements might slow down the convergence rate of the numerical model. When solving the Helmholtz with

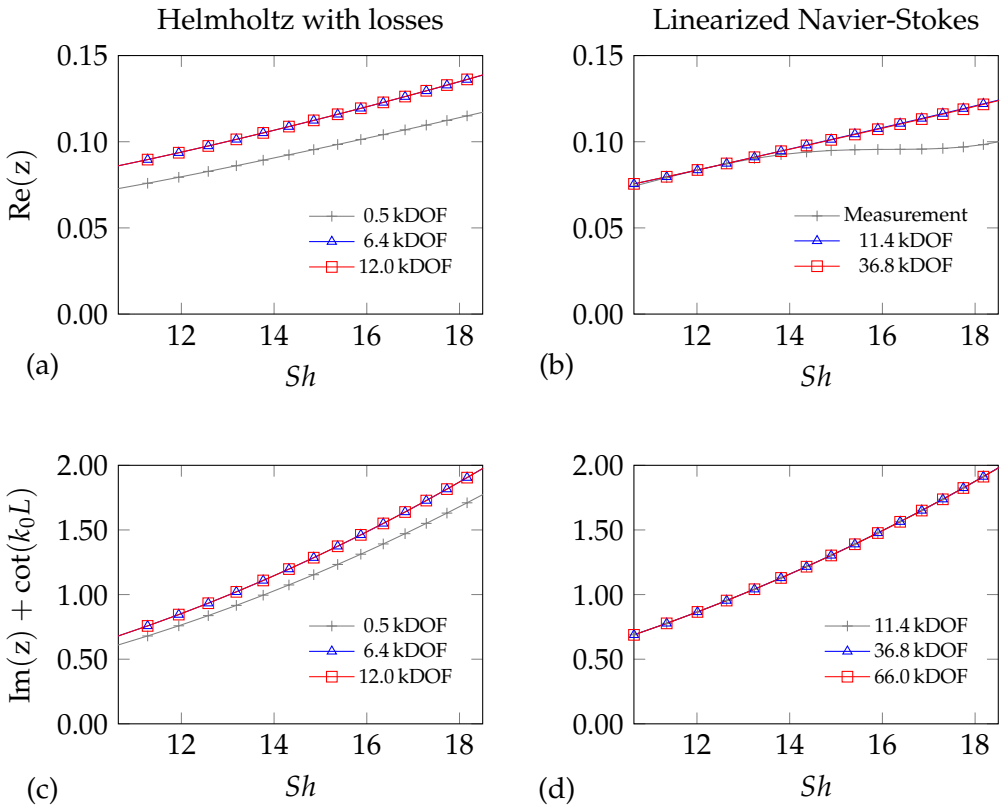

FIGURE 2.7: (a), (c) Resistance and normalized plate reactance computed with the Helmholtz with losses model for different numbers of DOF. (b), (d) Resistance and normalized plate reactance computed with the LNSE model for different numbers of DOF.

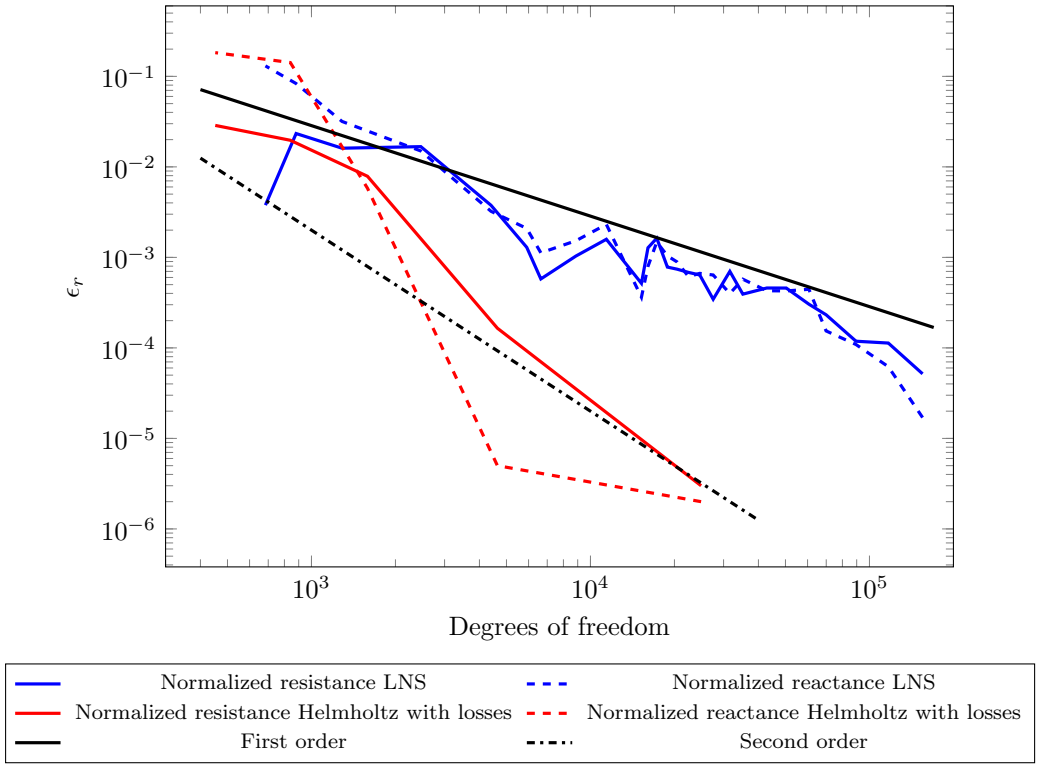

FIGURE 2.8: Resistance (a), (b) and plate reactance (c), (d) predicted for configuration 1 as a function of the number of degrees of freedom ($Re_a = 18201$, $Pr = 0.707$) for both numerical models. The point for which the convergence is attained is indicated.

losses equations, the inf-sup condition is unnecessary as only the pressure is solved. Hence, P2 elements are used and the convergence rate might be increased.

In a second stage, the accuracy of the models is investigated by computing the impedance at the resonance frequency of configuration 1. A series of computations is performed with increasingly fine meshes. To assess the accuracy of each of these computations, the error on the predicted impedance is calculated as follows

$$\epsilon_r = \frac{|Z - Z_f|}{\rho_0 c_0}, \tag{2.24}$$

where Z_f is the reference value of impedance calculated for each model using an extremely fine mesh. This error on the impedance is shown in Figure 2.7 for configuration 1 at the resonance frequency. It is clear that the Helmholtz model with the boundary condition (2.20) converges more rapidly than the LNSE model. As a consequence, a converged prediction of the impedance ($\epsilon_r \simeq 10^{-4}$) is obtained with a much smaller problem size with the Helmholtz model (around 5000 degrees of freedom, compared to around 10^5 degrees of freedom for the LNSE model). Additionnaly, the rate of convergence of the models are consistent with our choices of elements. The LNS model is close to a first order convergence while the Helmholtz with losses model is close to a second order convergence. This provides quantitative evidence of the computational benefits of this Helmholtz model.

2.7 Conclusion

In this chapter, two computational models were considered to predict the acoustic impedance of perforated plates in the linear regime. Both macro- and micro-perforated configurations were

considered and detailed comparisons with measured data from an impedance tube were used for validation.

The model based on the linearized Navier–Stokes equations is particularly expensive to solve, but it provides a more detailed and complete picture of the absorption mechanisms. It was used to calculate the viscous dissipation rate for a single hole. It was observed that the overall distribution of dissipation is very different between the macro- and micro-perforated cases. For the macro-perforated case, there is a significant amount of dissipation taking place at the corners of the perforation. In the micro-perforated case, an important contribution to the viscous dissipation comes from the regions just above and below the neck. These contributions to the acoustic absorption are generally accounted for by introducing end correction terms that have been determined empirically (Guess, 1975) or numerically (Temiz *et al.*, 2015). The quantitative analysis of the dissipation rate presented here provides more detailed insight into the location and significance of these dissipation mechanisms.

The second model considered is based on the classical Helmholtz equation combined with an equivalent boundary condition developed by Berggren *et al.* (2018) that accounts for the visco-thermal losses in the acoustic thermal and viscous boundary layers. This model is much cheaper to solve compared to the LNSE since it is a scalar model and does not require to resolve the thermal and viscous boundary layers in the finite element mesh.

Based on comparisons with experimental data, both models are able to predict accurately the impedance. Despite its inherent simplifications (compared to the LNSE model), the approach based on the Helmholtz equation and the equivalent boundary condition appears to provide reliable predictions both for macro- and micro-perforated plates. While this can be expected for macro-perforates since most of the losses occurs along the walls of the perforation, this is more unexpected for micro-perforates since the underlying assumption of the equivalent boundary condition are not strictly satisfied. This is however consistent with the recent results on the use of this model to predict losses occurring in porous materials (Cops *et al.*, 2020).

In chapter 1, we came to the conclusion that the mode-matching model is incomplete as it does not account for viscous edges effects. This conclusion is confirmed through the visualization of the viscous dissipation rate in this chapter. In chapters 1 and 2, the physical mechanisms in the linear regime were studied and different modeling approaches proposed. In chapter 3, we extend our analysis to the non-linear regime, by studying and validating several semi-empirical models.

Chapter 3

Impedance model in the non-linear regime

In the previous chapters, the linear regime without flow was analyzed. In this chapter, our framework extends to the non-linear regime without flow. The Guess (1975) model proposes a non-linear impedance correction depending on the velocity in the perforations. However, this velocity depends on the unknown impedance. In Beck *et al.* (2015) and in Laly *et al.* (2018b) an iterative procedure is used. It allows to predict the impedance and the velocity in the perforations under high sound pressure level. The model from Guess is modifed by implementing this procedure. The latter model is compared to impedance tube measurements performed with either a white noise source or a sine-swept source. The iterative procedure is adapted to the type of source and reasonable to excellent agreement is found between both the models from Guess (1975) and Laly *et al.* (2018b) and the measurements. We also compute the impedance without iteration using the Guess model to show that using the iterative process is essential to get good predictions. Furthermore, our measurements were performed on various macro- and micro-perforated. Hence the models can be compared to an important data set and their validity limit can be explored.

3.1 Introduction

Non-linear effects can occur for perforated liners at high sound pressure levels, which correspond to important acoustic velocities in the hole. Extensive research has been conducted on this topic since the early experimental work of Ingard *et al.* (1950), Ingard (1953) and Ingard *et al.* (1967). Afterwards, more theoretical work followed with Zinn (1970) and Cummings *et al.* (1983). The main result from their work is the fact that the jet formation and vortex shedding due to high velocity amplitudes increases the resistance and decreases the reactance.

More recently, numerical methods allowed to simulate the acoustic response of perforates to high sound amplitudes. To cite but a few, numerical simulations were performed in Roche *et al.* (2009), Zhang *et al.* (2012), and in Scarpato (2014), which highlights the physical mechanisms in the non-linear regime. In the latter works, the vortex shedding and the jet formation are clearly visible. An interesting observation in Roche *et al.* (2009) is that the absorption coefficient increases with the sound pressure level and decreases once a certain sound pressure is reached, depending on the frequency and the geometrical parameters of the perforated plate.

In this chapter, we focus on the impedance modeling of the perforates in the non-linear regime and how to improve the predictions of an existing model: the Guess (1975) semi-empirical model. This model proposes an impedance prediction that depends on the acoustic velocity in the perforations. However, this velocity depends on the unknown impedance. To solve this non-linear problem, the impedance and the velocity can be determined iteratively until convergence of both quantities. This iterative method is used in Beck *et al.* (2015) and in Laly *et al.* (2018b) and shows good agreement with measurements performed with a sine-swept source. Hence, we modify the Guess model by implementing this procedure. Afterwards, the modified model is compared to

measurements carried out for sound pressure levels up to $L_p = 150\,\text{dB}$. Either a white noise or a sine-swept source is used. The iterative procedure is adapted to account for the effective velocity in the perforations, depending on the source type.

The remainder of this chapter is as follows. First, we describe the well-known model from Guess (1975) in the non-linear regime. Second, a more recent model including an iterative procedure, based on the fluid equivalent approach from Laly *et al.* (2018b) is introduced. Third, the iteration procedure, which is used for both models, is detailed. Finally, the models are compared to impedance tube measurements at high sound pressure levels for macro- and micro-perforated plates. This allows to assess the validity range of both models for micro- and macro-perforated plates on a wide dataset. Additionally, we compute the impedance without iteration using the Guess model to highlight the important prediction improvement brought by the iteration procedure. Measurements with a grazing incidence to the plate are also considered to extend the predicting possibilities of the iterative approach.

3.2 The Guess model in the non-linear regime

In chapter 1, the model from Guess (1975) in the linear regime was compared to the mode-matching model and impedance tube measurements. In this section, we introduce the model from Guess including the non-linear effects depending on the acoustic velocity in the perforations. The non-linearities are known to produce a coupling between frequencies (Ingard *et al.*, 1967). Defining an impedance correction accounting for non-linear effects at a given frequency is not straightforward. In Guess (1975), the impact of the non-linearities on the impedance is predicted for a specific frequency. In the following we briefly review how the corrections on the resistance and the reactance in the Guess model are derived and how they can be interpreted.

Ingard *et al.* (1967) proposed a non-linear resistance correction based on an experimental investigation. Their experimental method is described and their modeling approach is reviewed.

A tube with a circular cross section is used. At one end of this tube, an acoustic driver is placed, at the other end a single orifice plate is attached. The driver generates an acoustic pressure p_{cav} in the cavity formed by the tube, the driver and the orifice plate. This pressure is measured by a microphone placed in the cavity wall. Ingard and Ising are able to measure the acoustic velocity in the aperture using a hot-wire probe located at the center of the orifice. The sound pressure level in the cavity varies from 120 dB to 157 dB in the cavity, which in this particular experimental setup, corresponds to an acoustic peak velocity u_0 in the neck varying from $2.7\,\text{m}\cdot\text{s}^{-1}$ to $41\,\text{m}\cdot\text{s}^{-1}$. The graph showing u_0 as a function of the pressure in the cavity present in Ingard *et al.* (1967) is reproduced here in figure 3.1. It is clear that the relation between the pressure in the cavity and the velocity depends on the pressure amplitude. For low amplitudes, this relation is linear ($p_{\text{cav}} \propto u_0$: dot-dashed line), and for high amplitudes it is quadratic ($p_{\text{cav}} \propto u_0^2$: dashed line). The transition between these two regimes occurs for $u_0 = 8.5\,\text{m}\cdot\text{s}^{-1}$, approximately.

Ingard *et al.* (1967) showed that for high sound pressure level, the impedance of a Helmholtz resonator is dominated by the resistance which can be approximated by $R \approx \rho_0 u_0$. In doing so, Ingard an Ising assumed that the resistance is frequency independent. This assumption was validated by measuring the frequency dependence of the velocity u_0, which confirmed that the non-linear resistance is independent of the frequency when the orifice resistance at least equals the orifice reactance.

For $u_0 > 8.5\,\text{m}\cdot\text{s}^{-1}$ and in order to propose a non-linear resistance correction, Ingard *et al.* (1967) provided an interpretation of this behavior based on Bernoulli's law in the time domain. The latter law is applied at the peak value of the velocity and the pressure, which are in phase for high sound pressure levels. Assuming that the pressure in a perforation is close to the average on both sides of this aperture, Ingard *et al.* (1967) derived the following expression of the

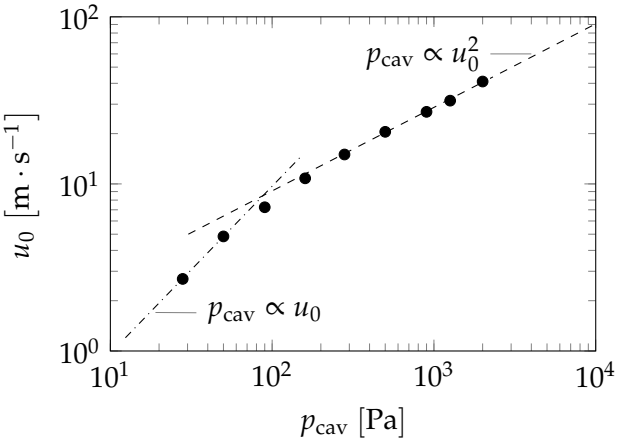

FIGURE 3.1: Peak velocity in the orifice as a function of pressure amplitude in a cavity at 150 Hz. This graph is reproduced from the data from Ingard *et al.* (1967). The dashdotted and dashed line are least mean square fit to the experimental data.

non-linear resistance

$$R_{nl} = \frac{p_{\text{cav}}}{u_0} = \rho_0 u_0 (1 - \sigma^2). \tag{3.1}$$

The non-linear resistance correction R_{nl} proposed by Ingard *et al.* (1967) is included in the model from Guess such that

$$\mathrm{z}_{\text{Guess}} = \mathrm{z}_\nu + \frac{2\pi^2}{\sigma}\left(\frac{R_{\text{neck}}}{\lambda}\right)^2 + \mathrm{j}\left(\frac{\omega\delta}{\sigma c_0} - \cot(k_0 L)\right) + \frac{1-\sigma^2}{\sigma}\frac{|u_{rms}|}{c_0}, \tag{3.2}$$

where u_{rms} is the Root Mean Square (RMS) acoustic particle velocity in the neck at a given frequency. The end-correction δ is further modified such that

$$\delta = \frac{16 R_{\text{neck}}}{3\pi}\left(1 - 0.7\sqrt{\sigma}\right)\frac{1 + 5\cdot 10^3 M_0^2}{1 + 10^4 M_0^2}. \tag{3.3}$$

Here, $M_0 = |u_{rms}|/c_0$ is the orifice Mach number. The term $(1 + 5\cdot 10^3 M_0^2)/(1 + 10^4 M_0^2)$ results from a fit proposed by Guess (1975) based on the analysis of Groeneweg (1969). It accounts for the non-linear effects on the reactance. Groeneweg (1969) studied the experimental results from Ingard (1953) and Ingard *et al.* (1967) to highlight the effect of pressure amplitude on δ for M_0 up to 0.1. Two perforated plates configurations were treated with radius of 3.5 mm and 2.5 mm at respectively 150 Hz and 229 Hz. Groeneweg (1969) highlighted the fact that the reactance end correction decreases with growing orifice Mach number and that it reaches half the value of the end correction for very low pressure amplitudes. A possible physical explanation to this by Ingard *et al.* (1967), is that the inertia contribution at the exit of the perforation is removed when a turbulent jet is present.

In Ingard *et al.* (1967), the measurements are performed on a single orifice with a radius of 3.5 mm. This radius is much higher than the perforation radius used in our measurements on realistic perforated plates. Therefore, we wish to verify whether the expression of the non-linear resistance in Guess (1975) if one knows the velocity at the surface of a perforated plate. Various configurations with different porosities and perforation radii are considered, allowing to validate the non-linear term in the Guess model for micro- and macro-perforated plates.

A way of proceeding to this validation consists in computing the porosity of a perforated plate from impedance tube measurements performed with a white noise source. This porosity will be referred to as the *acoustic porosity* σ_{ac}. We recall that with a white noise source, the effective velocity

at the surface of the plate corresponds to the RMS value of the velocities at each frequency. In the following, the velocity that we consider at the surface of the plate when using a white noise source is

$$u_{rms} = \sqrt{\sum_i u_{e,i}^2}, \tag{3.4}$$

where $u_{e,i}$ is the velocity at the frequency f_i. u_{rms} is determined for a frequency varying from 400 Hz to 6400 Hz with 16 Hz steps. It is noteworthy that, in the following, the range on which we look at the impedance is reduced, but the frequency range that defines u_{rms} is bounded between 400 and 6400 Hz. The relation between the acoustic pressure p_{mic} at the farthest microphone from the plate, and the acoustic pressure p_e and the acoustic velocity $u_{e,i}$ at the surface of the plate is

$$p_{\text{mic}} = p_e \cos(k_0 l) + u_{e,i} \mathrm{j} \rho_0 c_0 \sin(k_0 l), \tag{3.5}$$

where l is the distance between the microphone and the plate. Knowing the measured normalized impedance at the surface of the plate z and using equation (3.5), the velocity at the surface of the plate reads

$$u_{e,i} = \frac{p_{\text{mic}}}{\rho_0 c_0 \left[\mathrm{z} \cos(k_0 l) + \mathrm{j} \sin(k_0 l)\right]}, \tag{3.6}$$

where $\mathrm{z} = p_e / u_{e,i}$.

The acoustic porosity can be determined by using the resistance from Guess in the non-linear regime such that

$$\Theta_{\text{Guess}} = \Theta_l + \frac{1 - \sigma_{\text{ac}}^2}{\sigma_{\text{ac}}^2} \frac{|u_{rms}|}{c_0}. \tag{3.7}$$

Here $\Theta_l = \mathrm{Re}(\mathrm{z}_v) + 2\pi^2 R_{\text{neck}}^2 / (\sigma \lambda^2)$ is the linear resistance. Equation (3.7) shows that the resistance increases linearly with the velocity with a slope $a_{\text{Guess}} = (1 - \sigma_{\text{ac}}^2)/\sigma_{\text{ac}}^2$. Hence, if we are able to compute a_{Guess}, σ_{ac} can be determined. Impedance tube measurements are performed to determine the averaged normalized resistance between 1504 Hz and 2992 Hz. The resistance is observed to be constant on this frequency range. As the measurements are performed for a frequency range between 400 Hz and 6400 Hz, the effective velocity at the surface of the liner u_{rms} must be determined by the contribution of each frequency included in this range and not the reduced range used to compute the average resistance.

The measurements are operated for five different pressure levels, namely at 120 dB, 130 dB, 140 dB, 145 dB and 150 dB. Therefore, a sufficient number of data points is obtained to compute a_{Guess}. The best fit to the straight line defined by equation (3.7) is calculated using the least mean square method. We finally get

$$\sigma_{\text{ac}} = \sqrt{\frac{1}{1 + a_{\text{Guess}}}}. \tag{3.8}$$

The acoustic porosity is compared to the porosity characterized by optical measurements for micro-perforated plates, or with a set of calibration standards for macro-perforated plates. This comparison is repeated for 34 perforated plates with a porosity going from 1.4 % to 20 %, a radius between 0.15 mm and 1.00 mm and a thickness going from 0.60 mm to 4.00 mm. The geometrical parameters of each plate is detailed in Appendix C. Figure 3.2 shows a very good agreement between the acoustic porosity and the characterized porosity especially for low porosity values. However, we observe small discrepancies with increasing porosity. A possible explanation is that for a high porosity, the velocity in the perforations decreases, therefore, for low sound pressure level, the corresponding configurations might be in the linear regime and equation (3.7) might not be valid.

The non-linear term from Ingard *et al.* (1967) is therefore validated for a wide range of perforated plates including micro-perforated liners, in the following detailed impedance comparisons

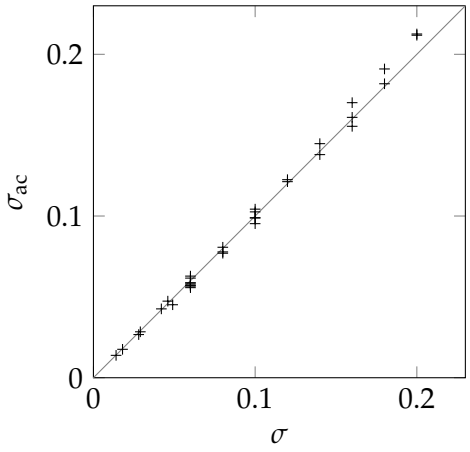

FIGURE 3.2: Acoustic porosity as a function of the measured porosity for 34 configurations.

are performed between the predictions and the measurements.

3.3 Equivalent fluid model in the non-linear regime

In this section, we introduce a recent model accounting for the effect of high sound pressure levels by Laly *et al.* (2018b). It uses the iterative procedure presented in section 3.4 on the velocity. In Laly *et al.* (2018b), this model is compared to measurements with either a low radius ($< 0.5\,\text{mm}$) or a low porosity ($< 5\,\%$) but not both at the same time. In section 3.5, it is compared to measurements completed on micro-perforated liners with low radius and low porosity, allowing to explore its validity range further.

The equivalent fluid approach (Allard *et al.*, 2009) is a method which allows to characterize a material as an equivalent fluid by defining a complex density $\rho_{en}(\omega)$ and a complex compressibility $C(\omega)$. A similar approach is used by Stinson (1991) for cylindrical perforations. The degree of complexity of the equivalent fluid method was progressively improved from the Johnson-Champoux-Allard (JCA) approach which accounts for viscous and inertial effects. Thereafter the thermal effects where added in the model from Johnson-Champoux-Allard-Lafarge (JCAL). For all three methods, the main assumptions are that the wavelength is much greater than the characteristic length of the material, *i.e.* the pore size, that the separation of spatial scale is important and that the skeleton is rigid. These assumptions must be verified to apply the homogenization theory to the considered material and to define several physical parameters such as the resistivity and the tortuosity, defined further below. Note that this methods are mostly used for porous materials but to other geometries if the previous assumptions are verified (Zieliński *et al.*, 2020).

In the linear regime, the JCA approach is used in Atalla *et al.* (2007) to characterize a plate with sub-millimeter perforations. The fact that the perforation radius is small compared to the plate thickness appears to verify the spatial scales separation and to validate the use of such model in this context. Using this method, Atalla *et al.* (2007) are able to retrieve the impedance predicted by existing models for perforated liners.

More recently, an extension of the model was developped in Atalla *et al.* (2007) to account for non-linear effects. The non-linear resistance term from Zinn (1970) and the non-linear reactance term from Maa (1994) are used for that purpose. This model will be compared to measurements on both micro- and macro-perforated plates to assess its validity range. We recall that for macro-perforated plates, the spatial scales separation is not guaranteed to be verified.

In this section, we describe this model and highlight its main characteristics. The resistivity of the fluid represents the resistance encountered by a particle in the fluid and is defined as a

function of u_{rms} such that

$$R_t = \frac{8\mu}{\sigma\Lambda^2} + \beta\frac{\rho_0(1-\sigma^2)}{\pi h\sigma C_D^2}\sqrt{2}u_{rms}, \tag{3.9}$$

where $\Lambda = R_{\text{neck}}$, $\beta = 1.6$ is a constant value and C_D is the discharge coefficient varying between 0.6 and 0.8. In the following we use $C_D = 0.76$ (Laly *et al.*, 2018a). The term $8\mu/(\sigma\Lambda^2)$ can be found in Guess (1975) and represents a low-frequency approximation of the visco-inertial impedance of a circular aperture from Zwikker *et al.* (1949) in the linear regime. The right term with a u_{rms} dependence is derived using the non-linear resistance from Zinn (1970) of a Helmholtz resonator defined as

$$\Theta_{\text{Zinn}} = \frac{4}{3\pi}\frac{1-\sigma^2}{\sigma c_0 C_D^2}\sqrt{2}u_{rms}. \tag{3.10}$$

The main difference between the non-linear resistance defined by Ingard *et al.* (1967) (equation (3.2)) and that defined by Zinn (1970) (equation (3.10)) is the fact that Zinn accounts explicitly for the *vena contracta* effect, which results in the appearance of the discharge coefficient C_D. The *vena contracta* effect corresponds to the reduction of the effective cross section area of the orifice for high velocity amplitudes.

The tortuosity represents the length of the path followed by a particle compared to the shortest possible path. The non-linear tortuosity $\alpha_{\infty nl}$ is defined with

$$\alpha_{\infty nl} = 1 + \frac{2\epsilon_{enl}}{h}, \tag{3.11}$$

where ϵ_{enl} is a correction length accounting for the non-linear effects and interaction between perforations

$$\epsilon_{enl} = \frac{\Psi}{1 + \dfrac{\sqrt{2}u_{rms}}{\sigma c_0}} 0.48\sqrt{\pi\Lambda^2}\left[\sum_{n=0}^{8} a_n\left(\sqrt{\sigma}\right)^n\right]. \tag{3.12}$$

Here, Ψ is set to $4/3$ and the coefficients a_n are defined by $a_0 = 1.0$, $a_1 = -1.4092$, $a_2 = 0.0$, $a_3 = 0.33818$, $a_4 = 0.0$, $a_5 = 0.06793$, $a_6 = -0.02287$, $a_7 = 0.003015$, $a_8 = -0.01614$. These coefficients correspond to the Fok's function (Fok, 1941) accounting for hole interaction effects. The term $1/\left[1 + u_0/(\sigma c_0)\right]$ accounts for the non-linear effects (Maa, 1994). The latter term appears to be consistent with the fact that the length correction decreases with an increasing acoustic velocity in the perforations (Groeneweg, 1969).

Finally, the effective density (Laly *et al.*, 2018a) is defined from the resistivity and tortuosity expressions

$$\rho_{en}(\omega) = \rho_0\alpha_{\infty nl}\left(1 + \frac{R_t\sigma}{\mathrm{j}\omega\rho_0\alpha_{\infty nl}}\sqrt{1 + \frac{4\mathrm{j}\rho_0\omega\mu\alpha_{\infty nl}^2}{\sigma^2 R_t^2\Lambda^2}}\right). \tag{3.13}$$

This equivalent density accounts for visco-inertial effects in the linear regime and non-linear effects. The normalized impedance of a micro-perforated plate z_{MPP} is retrieved using the following expression:

$$\mathrm{z}_{\text{MPP}} = \mathrm{j}\frac{\omega h}{\sigma\rho_0 c_0}\rho_{en}(\omega). \tag{3.14}$$

Finally the normalized impedance of the liner including the cavity reactance is given by

$$\mathrm{z}_{\text{Laly}} = \mathrm{z}_{\text{MPP}} - \mathrm{j}\cot\left(k_0 L\right). \tag{3.15}$$

In the linear regime, the model from Laly *et al.* (2018a) accounts for the same physical mechanisms as in Guess (1975). Hence, in this regime, both models should provide the same impedance

predictions when considering micro-perforated plates. In the non-linear regime, these models account differently for the impact of the acoustic velocity on both the resistance and the reactance. In Laly *et al.* (2018a), the *vena contracta* effect is taken into account. Therefore, different predictions are expected. It is noteworthy that, in the linear regime, the model from Laly *et al.* is expected to be more accurate for micro-perforated liners than for macro-perforated liners. However, as the non-linear resistance contribution is much greater than the linear resistance, this lack of accuracy should be mitigated.

3.4 Computation of the acoustic velocity

In the non-linear regime, the impedance z of the liner is strongly dependent on the velocity in the perforations and conversely. In the case of a plane wave with a normal incidence to the plate, the velocity u_{rms} can be expressed as

$$u_{rms} = \frac{p_{\text{ref}} 10^{L_p/20}}{\rho_0 c_0 |\mathrm{z}| \sigma}, \tag{3.16}$$

in which $p_{\text{ref}} = 2 \cdot 10^{-5}$ Pa is the reference pressure and L_p is the sound pressure level in dB.

As the impedance is unknown, a first approach consists in using the air normalized impedance $\mathrm{z} = 1$ to approximate the value of u_{rms}. In section 3.5, this method is used with the Guess model to highlight the relevance of the iteration procedure in the non-linear regime.

Indeed, another way to determine the impedance and the acoustic velocity in the perforation is to use an iteration procedure (Beck *et al.* (2015) and Laly *et al.* (2018b)). This method consists in first finding a solution to equation (3.16) by a first definition of u_{rms} in equation (3.2) (Guess) or equation (3.15), to compute the impedance. This will give a new value of u_{rms} to be used again in equation (3.2) or (3.15). This procedure is repeated until the acoustic velocity converges, *i.e.* when the difference between two successive iterated velocities is below a prescribed tolerance (here we use $10^{-7}\,\mathrm{m} \cdot \mathrm{s}^{-1}$). The number of iteration is below 30 for the configurations used here, it results in a very low computation time.

This iteration procedure can be adapted when either a sine-swept or a white noise source is used in impedance tube measurements. In the case of a sine-swept source, the sound pressure level at the surface of the sample remains the same for all frequencies. Furthermore, the effective velocity at the surface of the liner depends on the frequency. Hence the iteration procedure must be done for each frequency.

In the case of white noise source, the effective velocity at the surface of the plate corresponds to u_{rms}, which is formed by the velocity contribution from each frequency (Rice, 1971), consistently with equation (3.4). This method allows to issue a single velocity to represent the whole frequency spectrum. As the non-linear resistance strongly depends on the acoustic velocity, it is expected to be uniform with frequency when using a white noise source. Thus, the iteration procedure is performed on u_{rms} and the impedance of the whole frequency spectrum.

In the linear regime, small differences are observed on the measured impedance when either a white noise or a sine-swept source is used. However, in the non-linear regime, the measured resistance is substantially different. This aspect is further discussed in the following comparisons with measurements.

3.5 Comparisons with impedance tube measurements

In order to validate the modified model from Guess (1975) with iterations, impedance tube measurements in the non-linear regime are performed. The model from Laly *et al.* (2018b) with iterations on the velocity is also compared to the measurements to explore its validity range on the

sample presented below. 3 perforated plates are tested at $L_p = 130$ dB and 150 dB at the surface of the sample. The geometrical parameters for each configuration are detailed in table 3.1.

Configuration	σ (%)	R_{neck} (mm)	h (mm)	L (mm)
1 (macro)	10	0.8	1.50	16 (sine-swept), 19 (white noise)
2 (micro)	4.2	0.15	0.6	19
3 (micro)	1.4	0.15	0.6	19

TABLE 3.1: Perforated plate configurations.

Configuration 1 is a macro-perforated plate with a high porosity. Configuration 2 and configuration 3 are micro-perforated plates with a high and a low porosity, respectively. In Laly *et al.* (2018a), the equivalent fluid model was compared to impedance measurements in the non-linear regime for configurations having either a small porosity or a small perforation radius, but not both at the same time. Therefore, by measuring the impedance of configuration 3, we will be able to extend the assessment of the validity domain of the model from Laly *et al.* and the Guess modified model.

In the following, the normalized resistance $\mathrm{Re}(z)$, the normalized plate reactance $\mathrm{Im}(z) + \cot(k_0 L)$, the velocity and the absorption coefficient are plotted against frequency. The absorption coefficient reads

$$\alpha = 1 - \left| \frac{z-1}{z+1} \right|^2 . \tag{3.17}$$

Both the case of the sine-swept source and a white noise source are treated for a frequency range between 500 Hz and 5000 Hz.

3.5.1 Sine-swept source

Figure 3.3 corresponds to macro-perforated configuration 1 at a sound pressure level of 130 dB and 150 dB, respectively. Both iterative models correctly predict the impedance between 1800 Hz and 5000 Hz. Below 1800 Hz, important discrepancies are observed between the predictions and the measurements. However, the resistance predictions from the Guess model appear to be more accurate than those of the model from Laly *et al.* This limited lack of accuracy from the equivalent fluid model may be explained by the fact that, when considering a macro-perforated liner, the spatial scales separation may not be sufficient for the model to be valid. This would result in poor predictions of the linear resistance at high frequency.

It is worth noting that velocity predictions of both models are very close and accurate and that the main differences between the models are observed on the normalized resistance. This is consistent with the fact that the same formula (equation (3.16)) is used to compute the velocity for both models and that the non-linear resistance term is different. Accounting for the *vena contracta* effect in the model from Laly *et al.* (2018a) appears to have a limited impact on the overall resistance when compared to the resistance prediction from Guess (1975).

The plate reactance predictions from both models are very close and are very accurate close to the resonance frequency. The resistance also appears to be more accurately predicted close to the resonance frequency. This is consistent with the fact that at the resonance frequency, the impedance is purely resistive and the underlying assumption of the non-linear resistance term is more accurate (Ingard *et al.*, 1967).

The absorption coefficient appears to be very well predicted by both models although it is not the case of the impedance on the whole frequency range. Therefore, one might be careful not to assess the accuracy of the models looking at the absorption coefficient only.

The resistance predicted without iteration is of the same order of magnitude as the measured resistance but its shape is totally different. The resistance bump close to resonance frequency cannot be captured without iteration. A bump is also visible on the plate reactance and is well described by the iteration procedure.

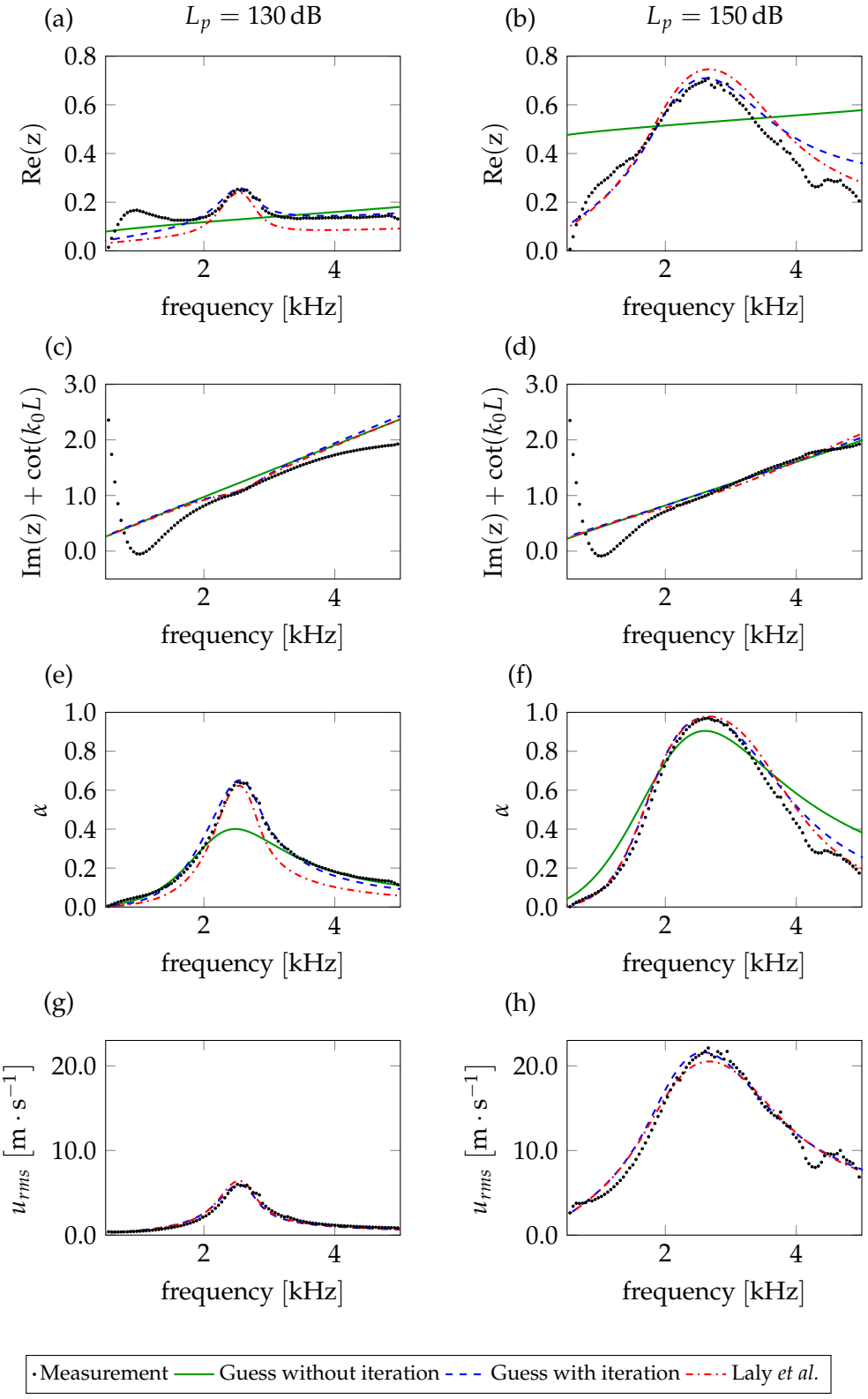

FIGURE 3.3: (a) Normalized resistance, (c) normalized plate reactance, (e) absorption coefficient and (g) velocity in a perforation of a macro-perforated configuration 1 using a sine-swept source at 130 dB. (b), (d), (f) and (h): same graphs at 150 dB.

We now look at the micro-perforated configuration 2 (figure 3.4). Without iterations, the resistance is overestimated by 100% at $L_p = 150\,\mathrm{dB}$. At $L_p = 130\,\mathrm{dB}$ it is of the correct order of

magnitude but not of the correct shape. In this case, we can see that the iterations have a limited impact on the reactance prediction when considering the Guess model.

Globally, the predictions from the modified Guess model are also in good agreement with measurements. The most important discrepancies are observed on the velocity at 150 dB which is underestimated, and the resistance which is overestimated by both iterative models. Again, the absorption coefficient is very well predicted. In the following, we will see that the predicted α shows good correspondence with all the measurements performed in this chapter.

At 130 dB the model from Laly *et al.* is more accurate than the Guess modified model and is able to capture the plate reactance bump close to the resonance frequency. At 150 dB, the model from Guess is slightly more accurate than the equivalent fluid model. As expected (Groeneweg, 1969), the measured plate reactance decreases when the sound pressure level increases. This is also the case of the computed reactances. We can observe that the reactance discrepancy between the two models increases at 150 dB. At the latter sound pressure level, the reactance predicted by the Laly *et al.*model is more accurate.

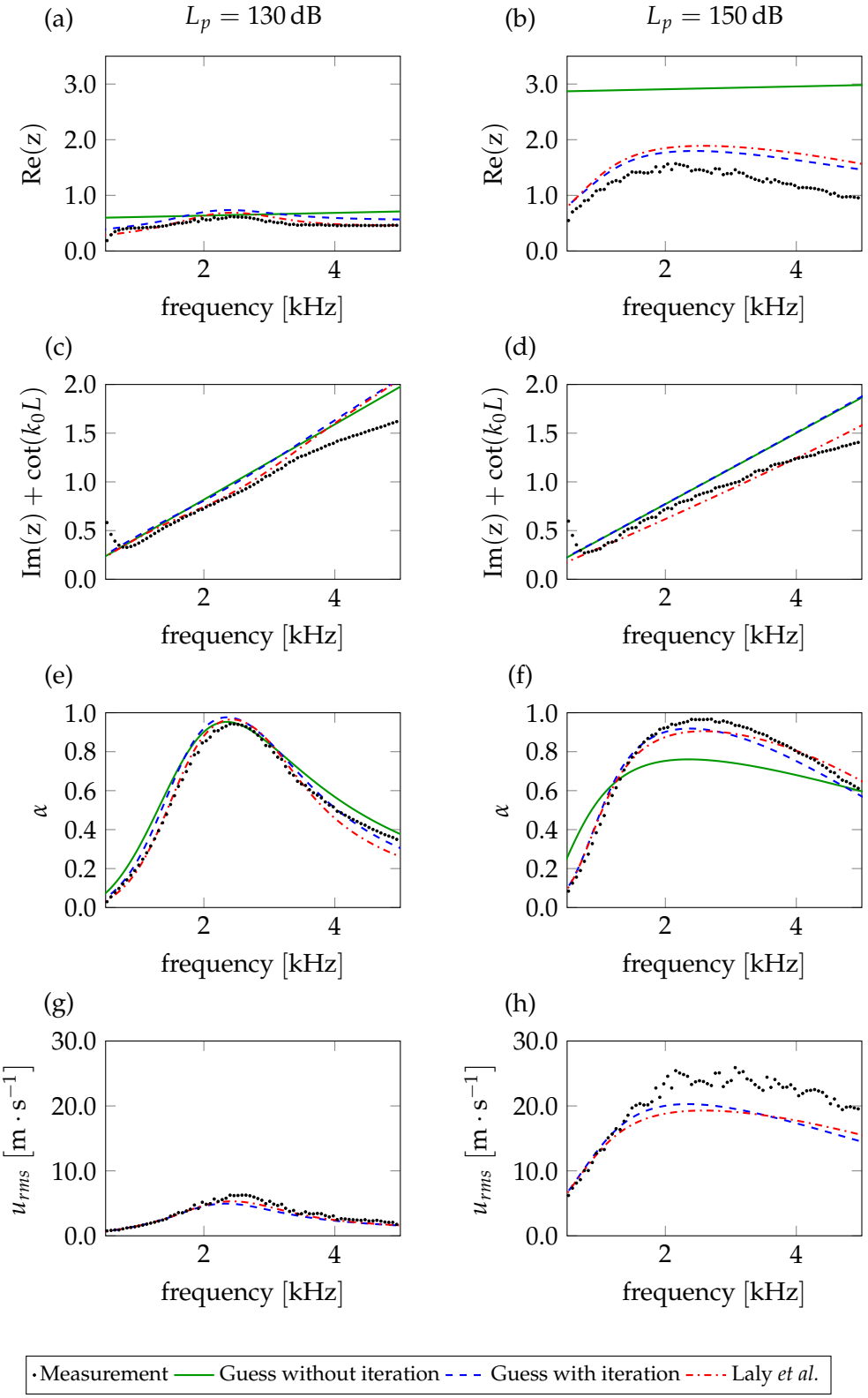

FIGURE 3.4: (a) Normalized resistance, (c) normalized plate reactance, (e) absorption coefficient and (g) velocity in a perforation of a micro-perforated configuration 2 using a sine-swept source at 130 dB. (b), (d), (f) and (h): same graphs at 150 dB.

The results of micro-perforated configuration 3 (figure 3.5) shows similar tendencies than configuration 2 in terms of the accuracy of the iterative impedance models. At both sound pressure levels, the reactance predicted by Guess appears to be more accurate than the reactance modeled by Laly *et al.*

Without iterations the resistance is overestimated at $L_p = 130\,\mathrm{dB}$ and highly overestimated at $L_p = 150\,\mathrm{dB}$. The plate reactance remains in good agreement with the measurements.

At $L_p = 150\,\mathrm{dB}$, the velocity oscillates around a constant value of $20\,\mathrm{m}\cdot\mathrm{s}^{-1}$. However the resistance decreases drastically. This behavior differs from configuration 1 and 2, for which the resistance follows the same trend as the acoustic velocity. Also, the absorption coefficient decreases significantly when passing from $L_p = 130\,\mathrm{dB}$ to $L_p = 150\,\mathrm{dB}$. Such phenomenon is observed in Roche *et al.* (2009) with axi-symetrical Direct Numerical Simulations (DNS) of perforated liners. According to Roche *et al.* (2009), a possible explanation is that the efficiency of a perforated liner is reduced by the non-linear dissipation mechanisms involving vortices at the entrances of the apertures.

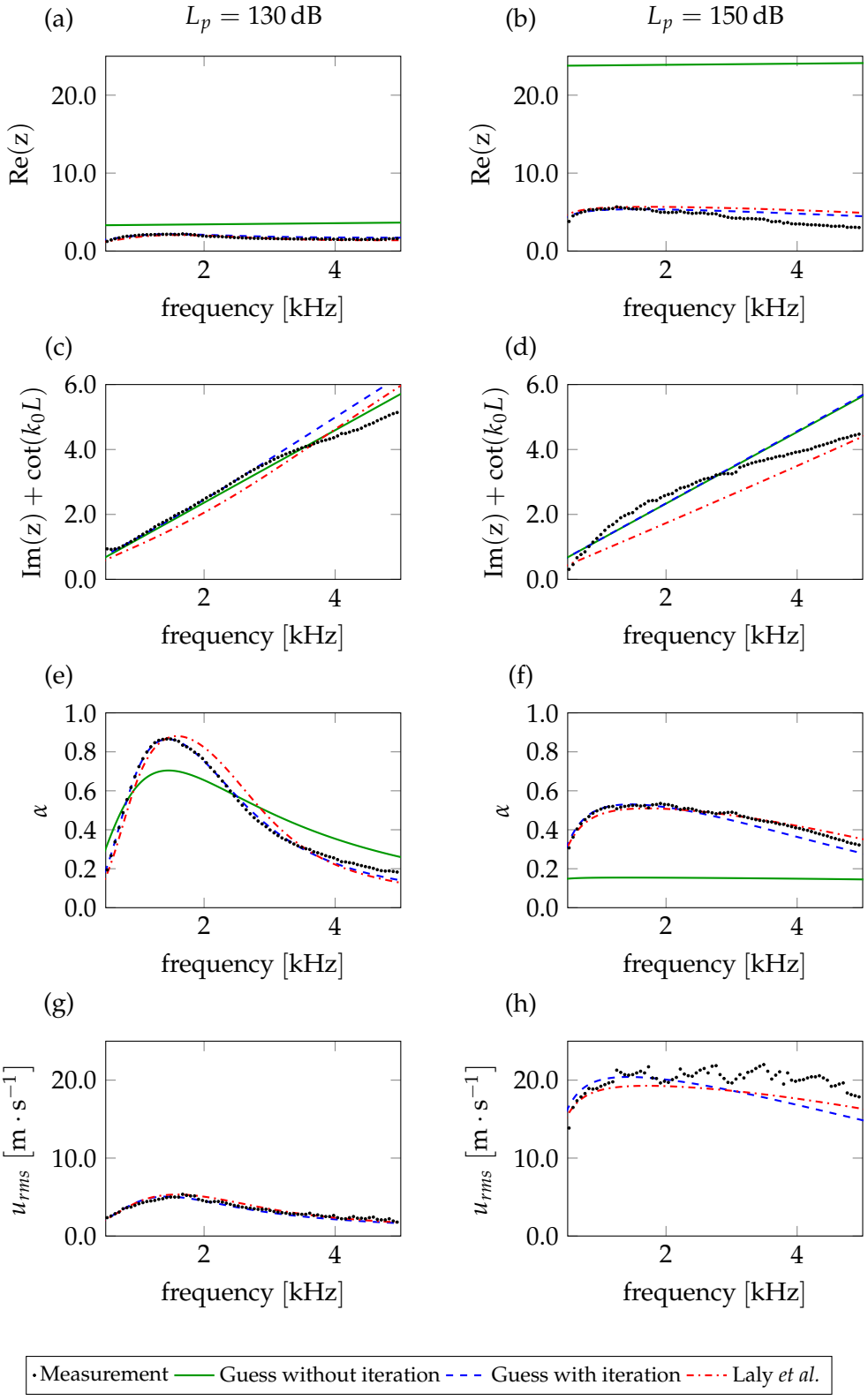

FIGURE 3.5: (a) Normalized resistance, (c) normalized plate reactance, (e) absorption coefficient and (g) velocity in a perforation of a micro-perforated configuration 3 using a sine-swept source at 130 dB. (b), (d), (f) and (h): same graphs at 150 dB.

3.5.2 White noise source

In the case of a white noise source, we recall that the effective acoustic velocity at the surface of the plate corresponds to u_{rms}, which is determined on the frequency range going from 400 Hz to 6400 Hz. However, the following model and measurement comparisons are made for a frequency between 500 Hz and 5000 Hz.

Figure 3.6 shows the results obtained with the macro-perforated configuration 1. The measured normalized resistance is uniform with frequency on a majority of the frequency range. This is consistent with the fact that the effective velocity at the surface of the liner remains constant for every frequency. We note that the measured resistance is very high at 500 Hz and rapidly stabilizes. This is also the case of the plate reactance. This phenomenon is also observed on the sine-swept source measurements and is not captured by the models.

From figure 3.6 to 3.8, the impedance computed without iterations is the same as in the previous section. The resistance is still overestimated for configuration 2 and 3, especially at $L_p = 150$ dB but its shape is correct as the resistance remains flat when using a white noise source. For configuration 1, we can see that the resistance computed with the air impedance is rather accurate at both sound pressure levels. The plate reactance is correctly predicted without iterations.

The resistance predicted by the model from Laly *et al.* is constant with frequency at both 130 dB and 150 dB. On the other hand, the modified Guess model predicts an increase of the resistance with increasing frequency and appears to be more accurate than the equivalent fluid model in that sense.

With iterations, the predicted reactances are very similar and in good agreement with measurements at both sound pressure levels. The measured reactance remains almost the same for both values of L_p although an inflection can be observed after 4 kHz. The latter phenomenon is also observed when considering configuration 2 and 3, both on the resistance and the reactance, especially at a sound pressure levels of 150 dB. Unfortunately, we have no clear physical explanation for this observation.

The computed and measured velocity values are indicated in table 3.2 for $L_p = 130$ dB and in table 3.3 for $L_p = 150$ dB. The computed velocities ($u_{rms,\text{Laly}}$ and $u_{rms,\text{Guess}}$), and the measured velocities ($u_{rms,\text{m}}$) are of the same order of magnitude. However, we note that the measured velocity is systemically overestimated by both models. Less than 30 iterations are needed to reach convergence for every configuration. Just as for the sine-swept source case, a few seconds are needed to compute the impedance and the velocity. The worst velocity prediction is observed for configuration 1 at $L_p = 130$ dB. This might indicate that both non-linear models are valid at a minimum velocity value, which is consistent with Ingard *et al.* (1967) where the linear to non-linear transition is around a peak velocity of $8.5\,\text{m}\cdot\text{s}^{-1}$. In Temiz *et al.* (2016) a criteria on the Strouhal number in the perforations $St = 2\omega R_{\text{neck}} / \left|\sqrt{2}u_{rms}\right|$ is proposed to characterize the behavior of the liner. If $St > 1$, the behavior is linear, if $St = \mathcal{O}(1)$ we are in the transition regime and if $St \ll 1$ the regime is strongly non-linear. For configuration 1 at 500 Hz, the measured value of St is 2.31. Hence, we are close to the transition regime at low frequency for this configuration, and the non-linear model might not be applicable in this situation.

Configuration	$u_{rms,\text{m}}$	$u_{rms,\text{Guess}}$	$u_{rms,\text{Laly}}$
1 (macro)	1.54	2.61	2.98
2 (micro)	2.22	3.07	3.38
3 (micro)	2.55	3.32	2.70

TABLE 3.2: Measured and computed u_{rms} in $\text{m}\cdot\text{s}^{-1}$ at 130 dB.

Configuration	$u_{rms,\mathrm{m}}$	$u_{rms,\mathrm{Guess}}$	$u_{rms,\mathrm{Laly}}$
1 (macro)	11.90	14.47	14.13
2 (micro)	15.03	17.08	16.89
3 (micro)	16.60	17.86	17.80

TABLE 3.3: Measured and computed u_{rms} in $\mathrm{m} \cdot \mathrm{s}^{-1}$ at 150 dB.

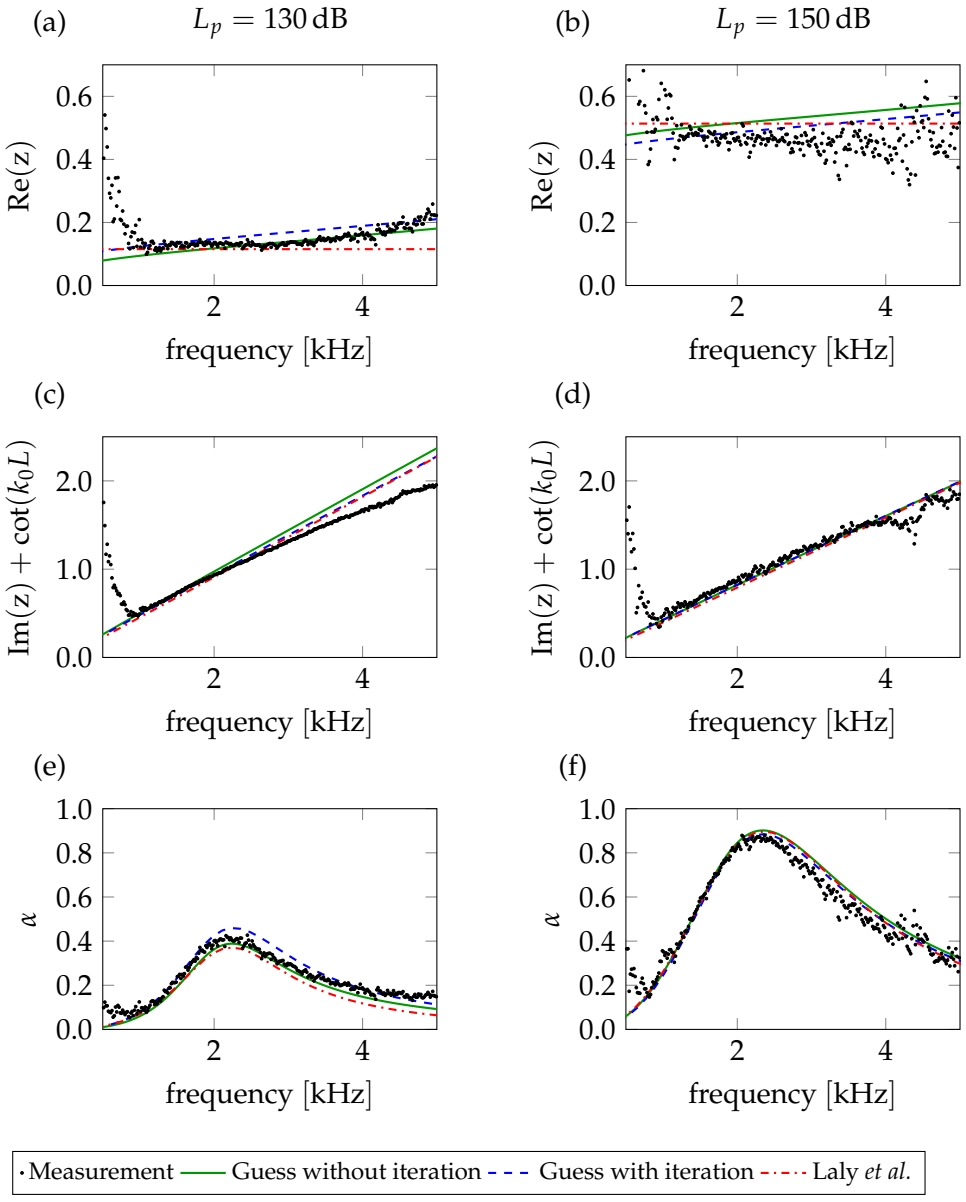

FIGURE 3.6: (a) Normalized resistance, (c) normalized plate reactance and (e) absorption coefficient of a macro-perforated configuration 1 using a white noise source at 130 dB. (b), (d), (f): same results at 150 dB.

In figure 3.7, the normalized resistance is overestimated at 150 dB, this was already the case when a sine-swept source was used. At both L_p, the plate reactance and the resistance appear to be predicted more accurately by the model from Laly *et al.* (2018b). The measured plate reactance decreases with the sound pressure level, as expected. The absorption is misleading in the case as well.

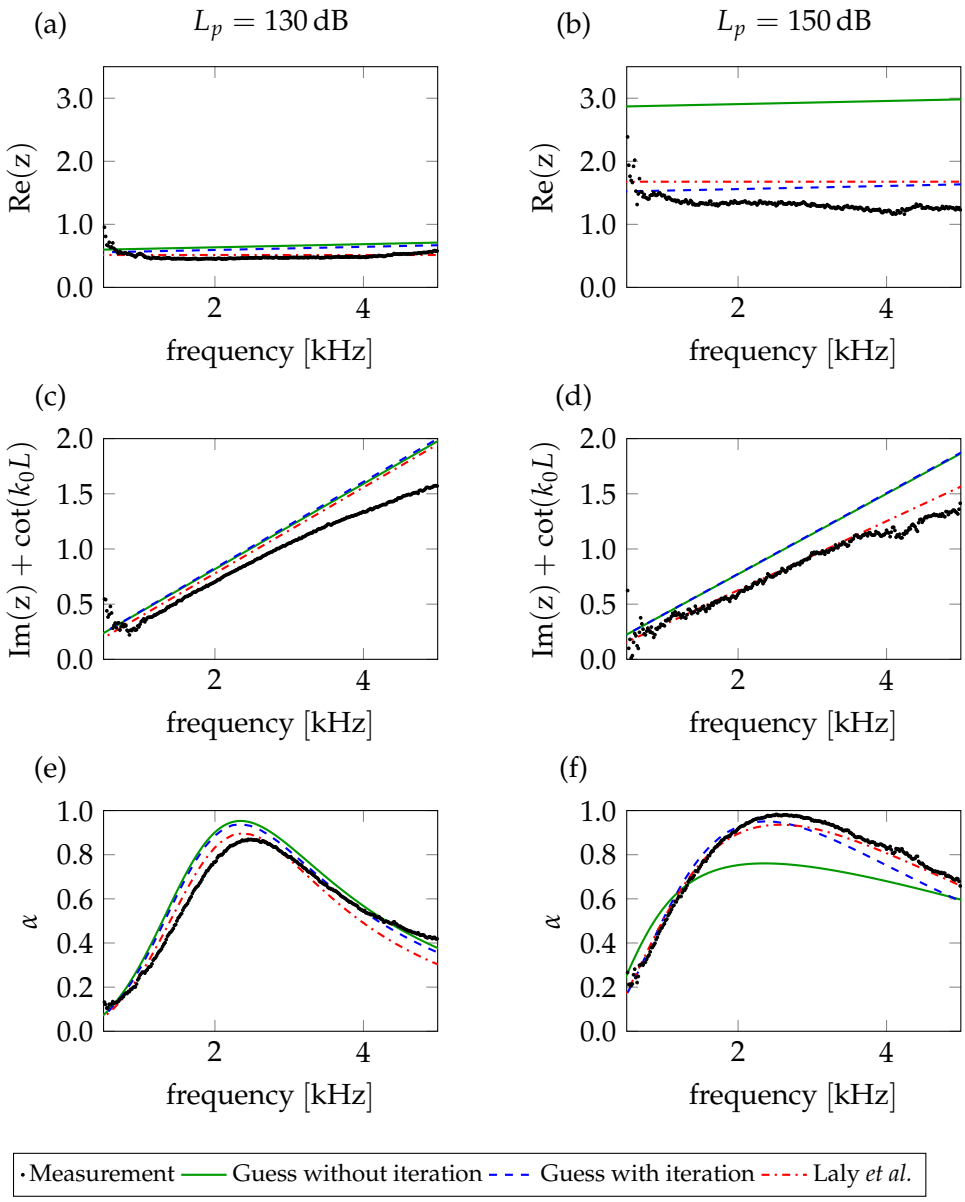

FIGURE 3.7: (a) Normalized resistance, (c) normalized plate reactance and (e) absorption coefficient of a macro-perforated configuration 2 using a white noise source at 130 dB. (b), (d), (f): same results at 150 dB.

For configuration 3 (figure 3.8) the resistance is again overestimated at 150 dB when using iterations but is relatively much more accurate than the resistance computed without iterations. For this sound pressure level, we can see that the resistance decreases from 500 Hz to 4000 Hz and then stabilizes. On the measurements, the inflection observable at 4000 Hz is particularly visible. This phenomenon is more pronounced with higher velocities. It can be noted that, among the three configurations treated here, the porosity of configuration 3 is the smallest and the measured velocity is the highest.

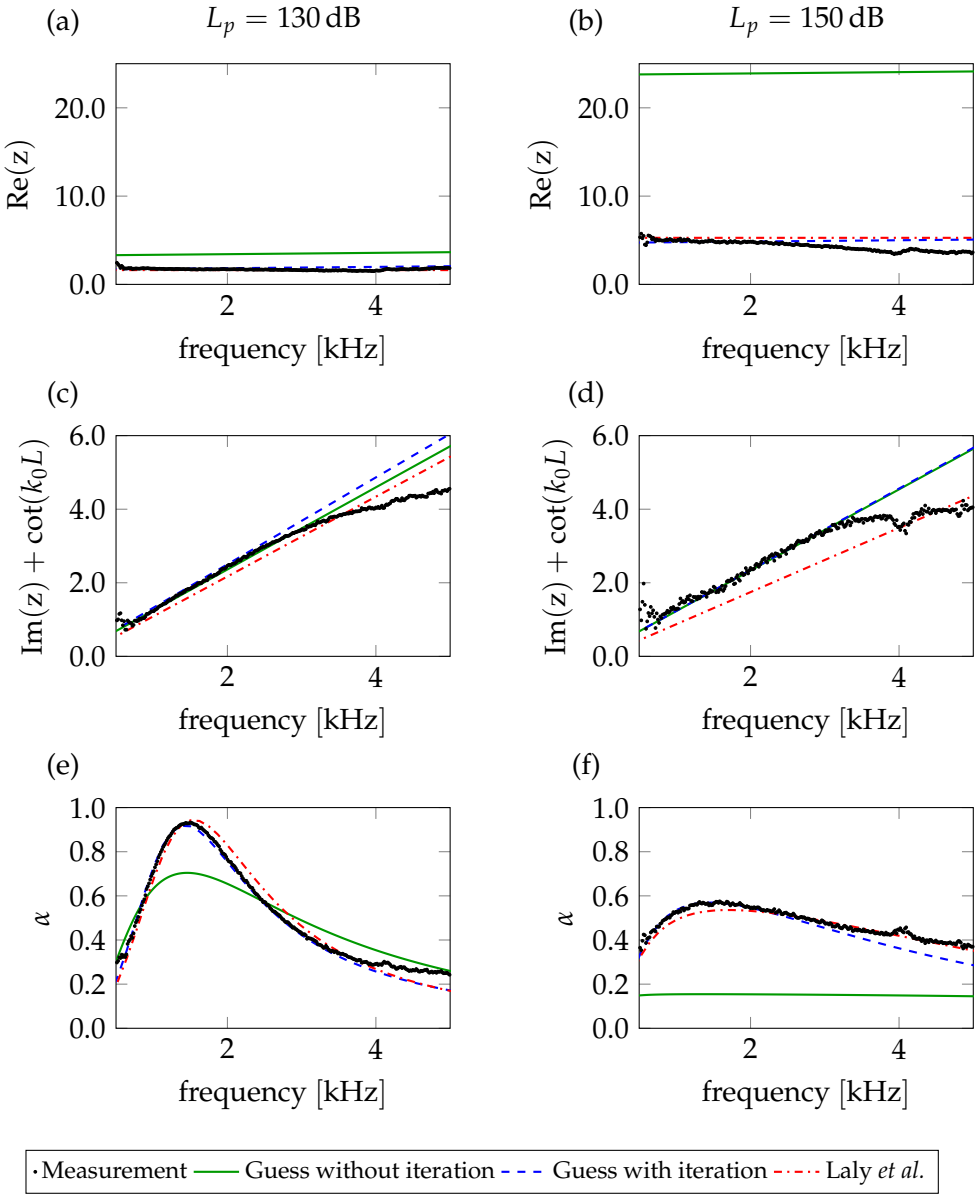

FIGURE 3.8: (a) Normalized resistance, (c) normalized plate reactance and (e) absorption coefficient of a macro-perforated configuration 2 using a white noise source at 130 dB. (b), (d), (f): same results at 150 dB.

Globally, when passing from a sine-swept source to a white noise source, the resistance is impacted drastically as the effective velocity changes. The plate reactance has a similar behavior with both sources. The predictions from Guess (1975) with iterations and Laly *et al.* (2018a) are accurate when considering the macro-perforated configuration 1. The impedance models are less accurate when studying the micro-perforated configuration 2 and 3 but still provide a very reasonable agreement with the measurements. Accounting for the *vena contracta* seems to have a limited impact on the impedance and velocity predictions. In terms of the acoustic velocity in the perforation, the validity limits of both models appear to be close to $15\,\mathrm{m}\cdot\mathrm{s}^{-1}$ for the micro-perforated plate presented here. When using a sine-swept source it was closer to $20\,\mathrm{m}\cdot\mathrm{s}^{-1}$. A dedicated investigation is needed to refine and understand these validity limits.

Using the iteration procedure is essential to obtain a good agreement between the Guess model and the measurements. This is particularly true when the effective velocity in the perforation is important, *i.e.* when the radius and the porosity are reduced and the sound pressure level is

increased. Additionally, the iterations allows to obtain the correct shape for the resistance when using a sine-swept source.

3.6 Comparisons with impedance measurements with a grazing incidence

So far, the modified model from Guess (1975) and the model from Laly *et al.* (2018a) have been compared to measurements performed with a plane wave with a normal incidence. In view of comparisons with flow in chapter 4, we compare the model to measurements carried out with a grazing incidence to the plate on the MACIA test bench. In figure 3.9, a schematic of the rig is presented. Note that this rig is designed to measure the impedance of perforated plates under grazing flow. However, in the following description we focus on the source and test section sections.

The source section is composed of 33 compression chambers. The test section is mounted next to the source section and is of dimensions 52.2 mm $\times$ 80 mm $\times$ 1.7 m. A cylindrical cavity of diameter 25 mm and height 21.1 mm is mounted on the test section. The cut-on frequency of the first non-plane mode is 3983 Hz approximately. The tests samples are of diameter 50 mm. They are perforated on a 25 mm radius and the remaining non perforated crown is used to place the plate on the sample holder on the cavity.

The method from Dean (1974) is used, which means that the pressure is measured at the surface of the sample and the bottom of the cavity in order to get the surface impedance of the perforate. To that purpose, the sample are perforated in their center to place a $1/8''$ microphone. Two $1/8''$ microphones are mounted at the bottom of the cavity and the effective pressure is taken as the average pressure of both microphones.

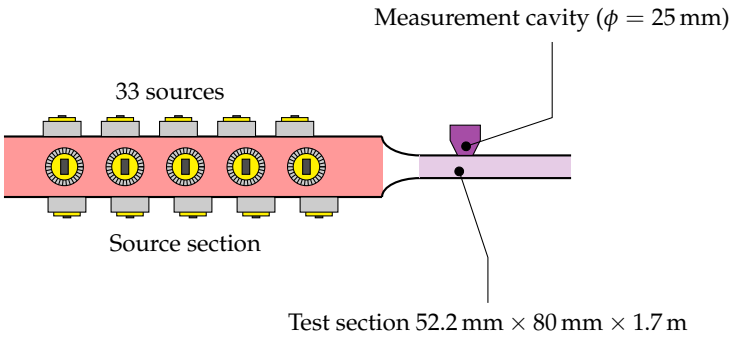

FIGURE 3.9: MACIA test bench designed to perform measurements with a grazing flow.

The measurements are performed between 600 Hz and 3300 Hz at $L_p = 130$ dB and between 600 Hz and 2200 Hz at $L_p = 150$ dB using the two microphones method (Dean, 1974). A sine-swept source is used.

Two micro-perforated configurations. Table 3.4 shows the geometrical parameters of both plates verified by optical measurements. Configuration 4 has a high porosity and configuration 5 has a low porosity.

Configuration	$2R_{\text{neck}}/h$	σ (%)
4	0.62	6.30
5	0.23	1.87

TABLE 3.4: Perforated plate configurations for the grazing incidence measurements. The values of R_{neck} and h are not given for confidentiality reasons.

Despite the fact that the incidence is not normal to the plate, the velocity is computed in the same manner as for the previous measurements, performed with a normal incidence. Hence we make the assumption that the velocity in the perforation does not depend on the angle of incidence of the plane wave. One could argue this hypothesis is correct as only the plane wave propagates in the perforations but it as not been verified thus far.

Figures 3.10 and 3.11 compare the normalized resistance, the normalized plate reactance, the absorption coefficient and the velocity in the perforations for the two configurations at $L_p = 130\,\text{dB}$ and $L_p = 150\,\text{dB}$.

Regarding configuration 4, the resistance is accurately predicted by both iterative models at both sound pressure levels. The plate reactance is slightly overestimated by the modified Guess model. The acoustic velocity in the perforations is surprisingly very accurately predicted considering the grazing incidence of the plane wave.

The resistance predictions underestimate the measured resistance of configuration 5 after the resonance bump at $L_p = 130\,\text{dB}$. At $L_p = 150\,\text{dB}$, small discrepancies can be observed between the iterative models and the measurement. At both sound pressure levels, the plate reactance is slightly overestimated by the modified Guess model. Here again the velocity is very well predicted.

From the previous comparisons, it appears that both iterative non-linear models are applicable to micro-perforated liners under high sound pressure levels with a propagation of the plane wave tangent to the perforate. In this section, the measured frequency range was quite restrained. A possible perspective would be to perform similar measurements with a wider frequency range. However, this can not be done on the current experimental set-up as we need to ensure the plane wave propagation only.

3.7 Conclusion

The model from Guess (1975) includes a non-linear term depending on the acoustic velocity in the perforation. As this velocity is unknown, a common practice is to evaluate the non-linear impedance using the air impedance to estimate the velocity. This assumption provides reasonable results on our macro-perforated configuration at $L_p = 130\,\text{dB}$ and $L_p = 150\,\text{dB}$. It was inaccurate for the micro-perforated configurations as it significantly overestimate the resistance. This is especially true for lower values of R_{neck} and σ and greater values of L_p, *i.e.* when the acoustic velocity in the perforations is significant. When a sine-swept source is used, the model without iterations is completely inaccurate as it cannot predict the correct shape for the resistance.

We modified the model from Guess (1975) with an iteration procedure used in Laly *et al.* (2018b) and Beck *et al.* (2015). This method is adapted to a sine-swept source and to white noise source. When comparing the modified Guess model to the measurements, the resistance predictions are drastically improved for macro- and micro-perforated plates. The iteration procedure has a minor impact on the plate reactance. The iterations are demonstrated to be essential and to be applicable to a standard model such as the Guess model, which may bring perspectives to improve any existing semi-empirical models in the non-linear regime.

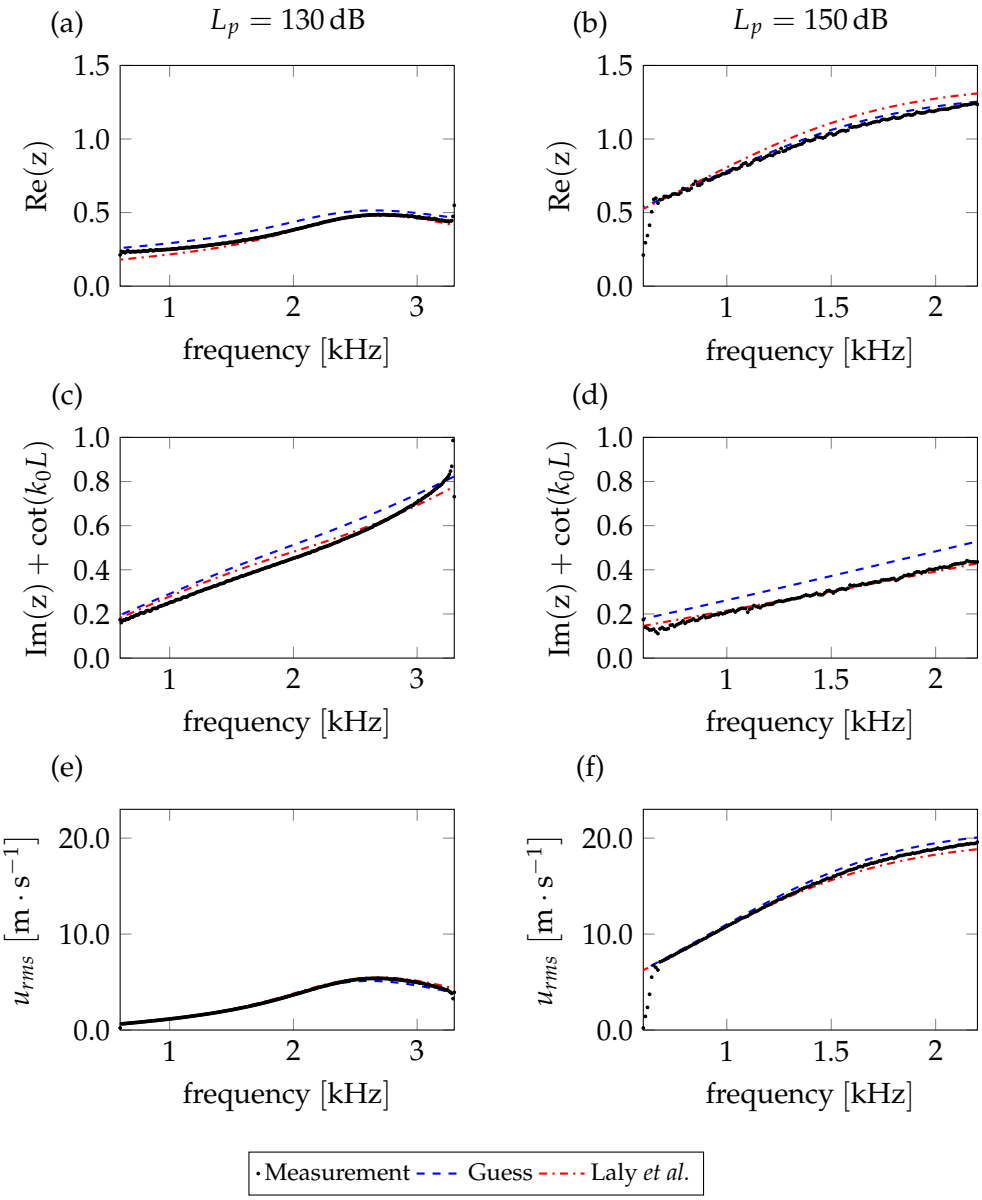

FIGURE 3.10: (a) Normalized resistance, (c) normalized plate reactance, (e) absorption coefficient and (g) velocity in a perforation of a macro-perforated configuration 4 using a sine-swept source at 130 dB. (b), (d), (f) and (h): same graphs for 150 dB.

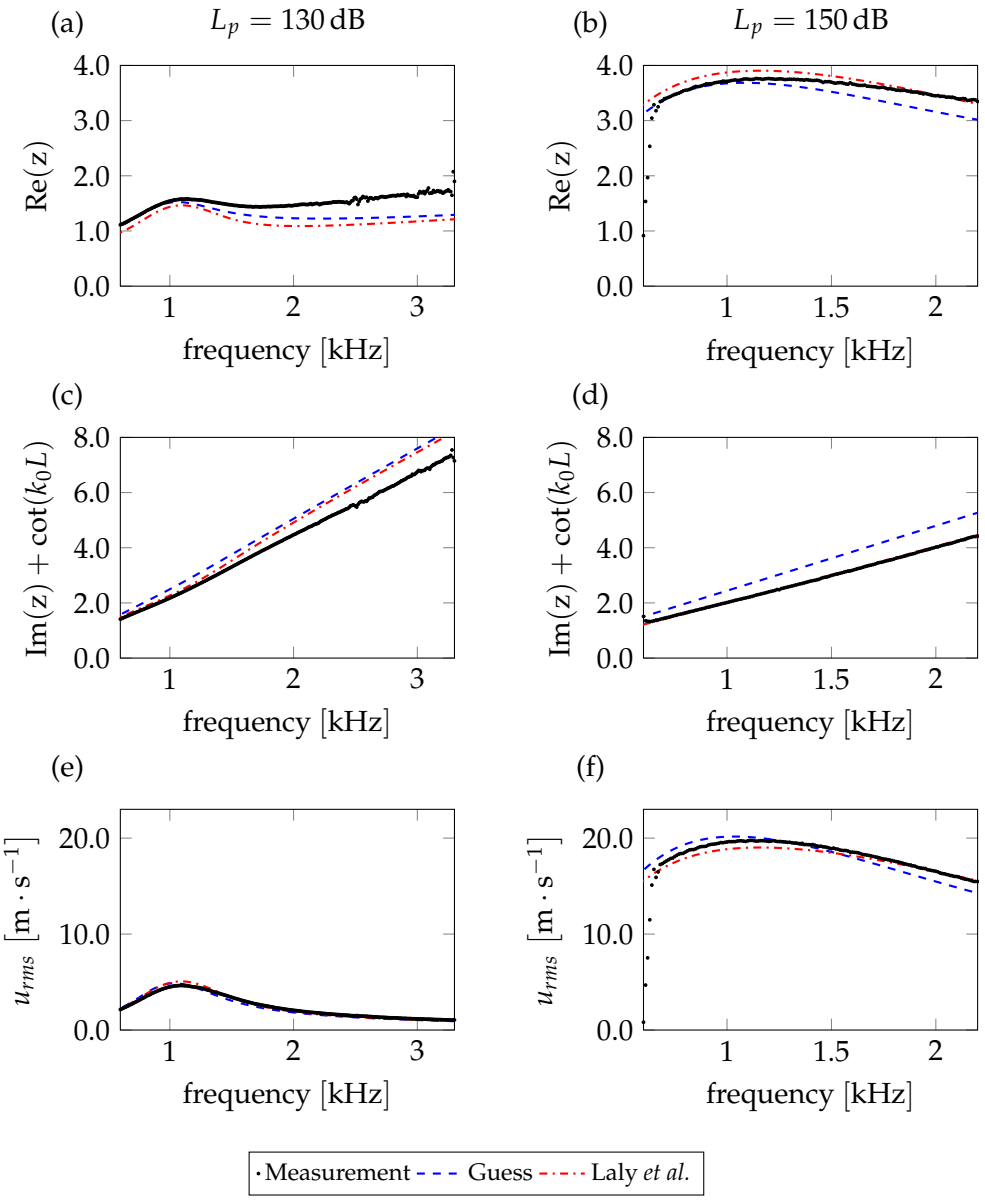

FIGURE 3.11: (a) Normalized resistance, (c) normalized plate reactance, (e) absorption coefficient and (g) velocity in a perforation of a macro-perforated configuration 5 using a sine-swept source at 130 dB. (b), (d), (f) and (h): same graphs for 150 dB.

The model from Laly *et al.* is also shown to be in good agreement with our measurements on micro-perforated liners. Its validity range may therefore be extended to perforates having both a low perforation radius and a low porosity.

Globally, the equivalent fluid model from Laly *et al.* and the modified Guess model provide similar predictions, although the model from Laly *et al.* (2018a) appears to be slightly less accurate than the Guess (1975) model. This is expected as the equivalent fluid approach is more accurate when the spatial scales separation is important. Moreover, accounting for the *vena contracta* effect through a discharge coefficient (Laly *et al.*, 2018a) has a limited impact on the predictions.

Additionally, good correspondence is observed between the grazing incidence measurements and the iterative models. As the same expression is used to compute the velocity for the normal and grazing incidence measurements, this suggests that the angle of incidence has a very limited impact on the velocity in the perforations. A possible explanation is that only the plane wave propagates in the perforations. In all cases, these results are encouraging for impedance predictions when a grazing flow to the perforated plate is present. In the next chapter, measurements are performed with a grazing flow and compared to semi-empirical models.

Chapter 4

Impact of the grazing flow on the impedance

In the non-linear regime with grazing flow, the model from Guess (1975) modified with the iteration procedure as discussed in the previous chapter is used. Now, the grazing flow effect on the impedance is investigated. The previous model is further modified by accounting for the grazing flow effect using the correction proposed by Meng *et al.* (2019). In both models, an empirical factor is identified based on the measured data for Mach numbers between 0.3 and 0.45, typical regimes encountered in jet engines. The sound pressure level goes up to $L_p = 150\,\text{dB}$. The dependence of this empirical parameter with several factors is discussed.

4.1 Introduction

In the previous chapters of this thesis, the linear and non-linear phenomenon occurring in perforated plate liners were investigated and modeled. The last, but not the least, effect to account for is the impact of a grazing flow on the liner impedance. In Cummings (1986), impedance measurements of an orifice submitted to a tangential flow were performed. In Howe *et al.* (1996), the effect of grazing flow on the Rayleigh conductivity and the impedance of an aperture was investigated analytically considering the continuity of normal displacement across the shear layer. In Jing *et al.* (2001), the theory from Howe *et al.* (1996) was adapted to enforce the continuity of normal velocity instead of the continuity of displacement. In Jing *et al.* (2001), the two approaches were referred to as the Particle Displacement Match (PDM) and the Particle Velocity Match (PVM). Good correspondence with measurements was observed when using the PVM for Mach numbers up to $M = 0.15$. Peat *et al.* (2003) compared the PDM and the PVM to measurements and obtained good agreement when considering the resistance.

More recently, Marx *et al.* (2010) used the Particle Image Velocimetry (PIV) to demonstrate the presence of hydrodynamic instability over a liner. This effect is also highlighted using numerical methods in Fabre *et al.* (2020). From an impedance modeling point of view, the main trend is that when a flow tangential to a liner is present, the resistance increases, and the reactance decreases. The semi-empirical model from Guess (1975) includes a resistance term and an end-correction on the reactance accounting for the grazing flow effect. This model is based on the experimental work conducted in Ingard (1968). Recently, Meng *et al.* (2019) introduced a model based on the PVM which was compared to measurements for a maximum Mach number of 0.15. In both models, a semi-empirical factor is introduced. In Guess (1975), it is proportional to the velocity fluctuation in the perforations caused by a turbulent boundary layer. In Meng *et al.* (2019), it corresponds to the convection speed of vorticity above the apertures.

In this chapter, both models are revisited. The model from Guess (1975) is further modified to account for the grazing flow effect using the modelling proposed by Meng *et al.* (2019) instead of Ingard (1968). Then, the models are compared to impedance measurements with flow using

the two microphones method (Dean, 1974) on a data set of 21 perforated plate samples for Mach numbers up to 0.45.

The empirical parameters are educed from the measured resistance. This allows to extract the trends of the velocity fluctuation and the convection speed of vorticity depending on the characteristics of the plate and of the grazing flow.

The quality of the fit is discussed as well as the physical meaning of the empirical parameters. The trend of these parameters observed in Meng *et al.* (2019) is confirmed and appears to remain the same at higher Mach numbers. The same trend is obtained in Yu *et al.* (2008). An empirical function is proposed to refine the resistance prediction under a grazing flow with the model from Guess (1975).

Finally, we conclude on the predictive possibilities offered by these models. We namely discuss if a recommendation of the values of the empirical parameters, based on the geometry and the physical characteristics of the shear flow, is possible.

4.2 Semi-empirical impedance models with grazing flow

4.2.1 Guess model with flow

The model from Guess (1975) including non-linear effects and grazing flow effects is recalled. The expression of the impedance becomes

$$\mathrm{z}_{\mathrm{Guess}} = \mathrm{z}_{\nu} + \frac{2\pi^2}{\sigma}\left(\frac{R_{\mathrm{neck}}}{\lambda}\right)^2 + \mathrm{j}\left[\frac{\omega\delta}{\sigma c_0} - \cot\left(k_0 L\right)\right] + \frac{1-\sigma^2}{\sigma}\left(\frac{|u_{rms}|}{c_0} + \frac{|v|}{c_0}\right), \tag{4.1}$$

where where $|v|$ is an estimate of the magnitude of the turbulent velocity fluctuation in the perforations due to a turbulent boundary layer at the frequency of interest. The term $|v|/c_0$ is derived experimentally in Ingard *et al.* (1967) and in Ingard (1968) by considering a superimposed steady flow through the perforation. Ingard and Ising bring the following physical explanation. The turbulent boundary layer located at the surface of the perforated plate produces a fluctuating flow through the perforation which is superimposed on the acoustic fluctuations. They assume that the turbulent velocity fluctuations occur at a frequency much lower than the acoustic velocity fluctuations and therefore act as a quasi-steady flow through the perforations. Hence, the impact of a grazing flow on the impedance is considered to be the same as the effect of the acoustic velocity. This leads to the fact the acoustic velocity and the turbulent velocity are simply added in equation (4.1).

An approximation of $|v|/c_0$ is used by Guess, based on the experimental data from Feder *et al.* (1969) such that

$$\frac{|v|}{c_0} \sim k_{\mathrm{Guess}} M, \tag{4.2}$$

where $k_{\mathrm{Guess}} = 0.3$ is an empirical coefficient determined experimentally which is supposed to increase with growing boundary layer thickness. In Allam *et al.* (2011), a value of 0.15 is used for perforated liners with a hole diameter of 1 mm, a thickness of 1 mm and for a porosity of either 0.5 %, 1 % or 2 % with a Mach number up to 0.15. It is noteworthy that this model does implicitly account for the boundary layer thickness effect on the resistance through the choice of the empirical parameter k_{Guess}. In the following this parameter is educed from resistance measurements.

The reactance end correction δ is modified to account for the grazing flow effects. It becomes

$$\delta = \frac{16 R_{\mathrm{neck}}}{3\pi}\left(1 - 0.7\sqrt{\sigma}\right)\frac{1 + 5\cdot 10^3 M_0^2}{1 + 10^4 M_0^2}\frac{1}{1 + 305 M^3} \tag{4.3}$$

where M is the Mach number in the nominal flow. Here, $1/(1+305M^3)$ is a multiplying correction factor determined experimentally which can be found in Groeneweg (1969) and Rice (1971). According to the latter end correction, the reactance is supposed to decrease with increasing Mach numbers.

4.2.2 Impedance correction proposed by Meng *et al.* (2019)

Meng *et al.* (2019) developed a semi-empirical impedance model for a circular perforation submitted to a grazing flow using the Particle Velocity Match (PVM). The effect of the boundary layer is taken into account through the convection speed ς_{Meng} of vorticity in the shear layer above the aperture. ς_{Meng} is homogeneous to a Mach number, and is considered to be function of the dimensionless boundary layer displacement thickness δ^*/R_{neck}.

The main assumptions of this model are that the Mach number is small enough such that $M < 0.3$, and that the aperture is acoustically compact such that $k_0 R_{\text{neck}} \ll 1$. Meng *et al.* (2019) considered that the impedance at low Mach number is the same as the impedance without grazing flow, hence the impedance of a single aperture under a grazing flow ζ_{E} is defined by its real part

$$\Theta_{\text{E}} = \max\left(\Theta_{\text{A}}, \Theta_0\right) \tag{4.4}$$

and its imaginary part

$$\chi_{\text{E}} = \min\left(\chi_{\text{A}}, \chi_0\right). \tag{4.5}$$

The impedance without grazing flow, denoted by a $\cdot_0$ subscript reads

$$\zeta_0 = \Theta_0 - \mathrm{j}\chi_0 = -\mathrm{j}k_0\left(\frac{16}{3\pi}R_{\text{neck}} + h\right). \tag{4.6}$$

In equation (4.6), the reactance without flow χ_0 accounts for the mass inertance of the orifice and the radiation through the well-known length correction $16R_{\text{neck}}/(3\pi)$. When a grazing flow over the orifice is considered, the asymptotic impedance is defined as

$$\zeta_{\text{A}} = \Theta_{\text{A}} - \mathrm{j}\chi_{\text{A}}, \tag{4.7}$$

where its real part reads

$$\Theta_{\text{A}} = C_1\varsigma M - \frac{\left(k_0 R_{\text{neck}}\right)^2}{\varsigma M}\left(C_2 + C_3 t + C_4 t^2\right), \tag{4.8}$$

with $t = h/R_{\text{neck}}$. The imaginary part of ζ_{A} is

$$\chi_{\text{A}} = k_0\left(C_5 R_{\text{neck}} + C_6 h\right) + \frac{\left(k_0 R_{\text{neck}}\right)^3}{\varsigma^2 M^2}\left(C_7 + C_8 t + C_9 t^2 + C_{10} t^3\right). \tag{4.9}$$

The coefficients in equations (4.8) and (4.9) are determined by evaluating the solution of the particle velocity match, which is written assuming a small plate thickness. In this case, the PVM is an integral equation which as no analytic solution. Hence, in Meng *et al.* (2019), it is solved numerically for a circular aperture. The values of these parameters are

$$C_1 = 0.94,\ C_2 = 0.14,\ C_3 = 0.29,\ C_4 = 0.13,\ C_5 = 1.26,$$
$$C_6 = 0.48,\ C_7 = 0.030,\ C_8 = 0.060,\ C_9 = 0.090,\ C_{10} = 0.029.$$

In equation (4.9), the term accounting for the orifice reactance and radiation is modified. The end correction accounting for radiation is decreased, and the length of the orifice is multiplied by

$C_6 = 0.48$. This is consistent with the fact that the reactance is expected to decrease in the presence of a grazing flow.

In Meng *et al.* (2019), the resistance and the reactance obtained with respectively equation (4.4) and (4.5) are compared with the measurements from Jing *et al.* (2001) for the parameters listed in table 4.1.

R_{neck} (mm)	h (mm)	$2R_{\text{neck}}/h$	$k_0 R_{\text{neck}}$	ς_{Meng}	δ^*/R_{neck}
1.5	2.0	1.5	$5.54 \cdot 10^{-3}$	0.43	1.64
2.25	2.0	2.25	$8.31 \cdot 10^{-3}$	0.45	1.08
3.5	0.5	14	$3.23 \cdot 10^{-2}$	0.53	0.7
3.5	2.0	3.5	$3.23 \cdot 10^{-2}$	0.53	0.7

TABLE 4.1: Parameters of the measured configurations in Jing *et al.* (2001).

The Mach number varies from 0 to 0.15. Meng *et al.* fit the convection speed ς_{Meng} to the measured resistance over this Mach number range of the 4 configurations of which the parameters are listed in table 4.1. A good correspondence is obtained between the computed and measured resistance. However, the reactance is underestimated. A possible cause proposed by Meng *et al.* is that the viscosity and the interaction effect between the perforations is neglected. Interestingly, in Meng *et al.* (2019), the convection speed is found to decrease with growing dimensionless displacement thickness δ^*/R_{neck}, though only 3 data points are available.

In this section, we intend to modify the model from Guess (1975) by removing the terms accounting for the grazing flow both on the resistance and the reactance. Then, we wish to account for the flow effect using the semi-empirical model from Meng *et al.* (2019). The resulting model will be referred to as the "hybrid Guess–Meng model". By doing so, we account for the linear and non-linear effects using the model from Guess and we account for the impact of the grazing flow using the correction from Meng *et al.* The experimental parameter is also identified from a more complete dataset.

The normalized impedance from the hybrid model is

$$\mathrm{z}_{\text{Guess}-\text{Meng}} = \mathrm{z}_\nu + \frac{2\pi^2}{\sigma}\left(\frac{R_{\text{neck}}}{\lambda}\right)^2 + \mathrm{j}\left(\frac{\omega\delta}{\sigma c_0} - \cot\left(k_0 L\right)\right) + \frac{1-\sigma^2}{\sigma}\frac{|u_0|}{c_0} + \Theta_{\text{Meng}} + \mathrm{j}\chi_{\text{Meng}}, \quad (4.10)$$

where δ is now defined by

$$\delta = \frac{16 R_{\text{neck}}}{3\pi}\left(1 - 0.7\sqrt{\sigma}\right)\frac{1 + 5\cdot 10^3 M_0^2}{1 + 10^4 M_0^2}. \quad (4.11)$$

In order to account only for the grazing flow contribution when using the model from Meng *et al.* (2019), the resistance correction is defined as

$$\Theta_{\text{Meng}} = \frac{\Theta_{\text{E}} - \Theta_0}{\sigma}, \quad (4.12)$$

and the reactance correction is

$$\chi_{\text{Meng}} = \frac{\chi_{\text{E}} - \chi_0}{\sigma}. \quad (4.13)$$

Equations (4.1) and (4.10) define two impedance models with flow from the work from Guess (1975) and Meng *et al.* (2019). In the following, both models are compared with measurements performed with a sine-swept source. In order to account for non-linear effects, the iteration procedure on the acoustic velocity remains the same, except that the grazing flow effect is now

(A) Complete test bench.

(B) Source, convergent and test sections.

FIGURE 4.1: Photographs of the MACIA test bench.

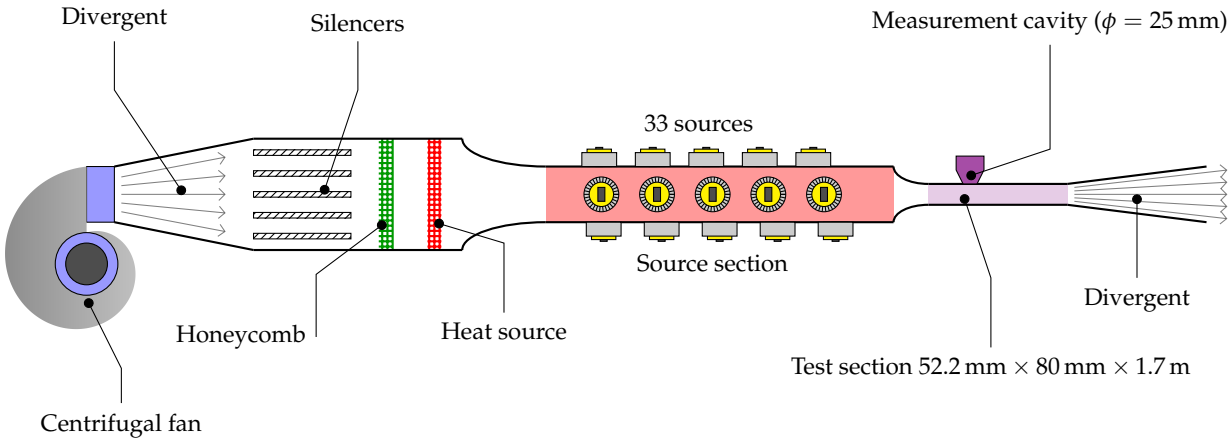

FIGURE 4.2: Schematic of the MACIA test bench.

accounted for. More importantly, the empirical parameters of both models, k_{Guess} and ς_{Meng}, are educed from the measured resistance before the iterations. Hence, the acoustic velocity and the impedance predictions are impacted by the choice of k_{Guess} and ς_{Meng}. A least-squares fitting is used.

4.3 Experimental set-up

In this section, we describe the experimental set-up used to measure the impedance at the surface of the liner in the presence of a grazing flow. The measurements were performed on the MACIA test bench by the *Centre de Transfert de Technologie du Mans* (CTTM). Photographs of the rig are shown on figure 4.1.

On figure 4.2, the rig is described with a schematic. It is composed of centrifugal fan followed by a divergent. Next, a section includes silencers, honeycomb, and heat source. A convergent allows to reduce the cross-section, followed by the source section. A total of 33 compression chambers are installed. Following the source section, the test section is integrated, upon which the cavity and the sample holder can be mounted. Finally, a divergent is placed at the end of the rig.

The 2 microphones method from Dean (1974) is used to measure the impedance at the surface of the perforated plate. Three 1/8" microphones are located in the cavity backing the perforate

plate. One microphone is mounted flush to the surface of the plate, and the two other microphones are mounted at the bottom of the cavity. The effective pressure at the bottom of the cavity is taken as the average pressure of the two microphones. The diameter of the cavity is 25 mm, which corresponds to a cut-on frequency of the first non plane mode of 3983 Hz approximately.

The cavity can be mounted in 3 different positions along the X axis of the duct defined on the simplified schematic in figure 4.3. The origin of the X axis is placed at the end of the convergent, which is the beginning of the test section. By changing the position of the cavity, different boundary layer thicknesses are obtained above the perforated plate without changing any other parameters in the measurement. Hence the effect of the boundary layer thickness on the impedance can be isolated. The position 1, 2 and 3 are located at, respectively, $X = 50\,\text{mm}$, $X = 550\,\text{mm}$ and $X = 1050\,\text{mm}$.

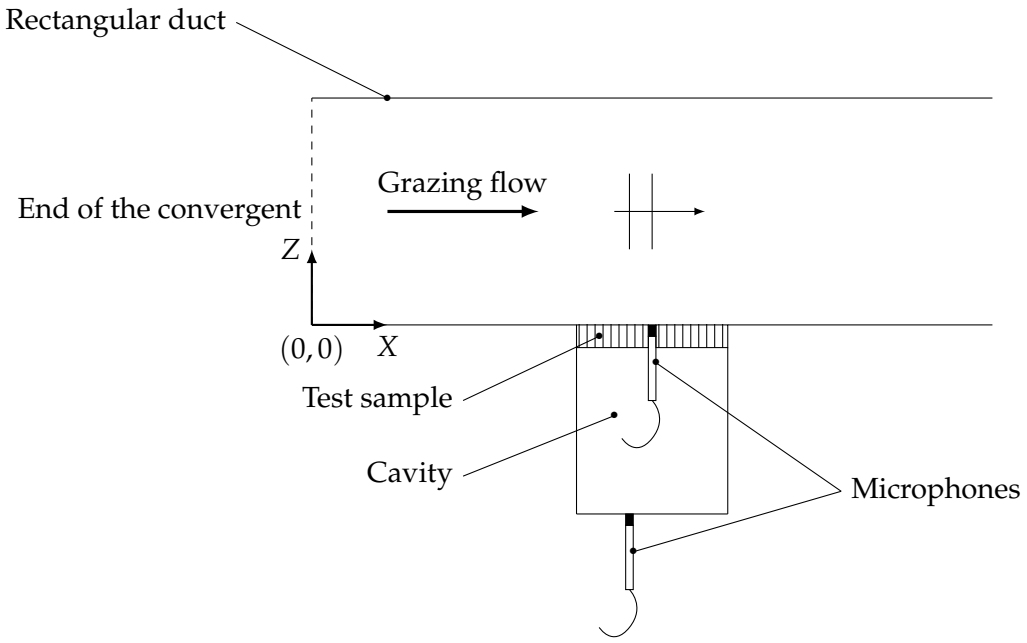

FIGURE 4.3: Simplified schematic to illustrate the measurement method from Dean (1974).

The boundary layer displacement thickness δ^* was measured through a Pitot probe at the 3 positions for several Mach numbers. The displacement values at the center of the sample are available in table 4.2. We note that δ^* remains almost constant with increasing Mach numbers, except for $M = 0.2$ at position 1. During the aerodynamic characterization, the velocity profiles as function of the Mach number were measured at the 3 positions in test section. It was reported that the velocity profile at position 1 and $M = 0.2$ was fundamentally different from the other. By investigating the shape factor, it was found that the flow is in the transition regime at position 1. At $M = 0.2$ it is closer to be laminar, and at $M = 0.6$ it is closer to be turbulent. At position 2 and 3, the flow was reported to be turbulent at any Mach number. As expected, δ^* is varying with the position. Note that the Mach indicated in table 4.2 is the Mach number at the center.

Position	X (mm)	δ^* (mm) at $M = 0.2; 0.3; 0.45; 0.6$
1	50	0.3
2	550	2
3	1050	3

TABLE 4.2: Approximate values of the boundary layer displacement thickness at different Mach numbers.

In the following, we look into the measurements performed at $M = 0.3$ and $M = 0.45$ in order to remain in the same flow regime. Note that $M = 0.45$ is close to the Mach numbers found in the industrial application such as turbofan *nacelles*.

4.4 Perforated plates

In total, the impedances of 21 perforated plates were measured in the rig presented above. Their parameters are shown in table 4.3 in which the plates are classified in descending order of $2R_{\text{neck}}/h$. In the next sections, the latter ratio appears to have an important impact on the impedance with flow. A sine-swept source is used with a frequency varying from 600 Hz to 2200 Hz. The sound pressure level at the surface of the plate is set to $L_p = 150$ dB and $L_p = 130$ dB, which are realistic sound pressures in a jet engine.

Sample	σ (%)	$2R_{\text{neck}}/h$
1	2.17	4.21
2	6.89	4.19
3	16.70	4.12
4	5.97	1.21
5	1.96	1.02
6	1.98	1.00
7	14.23	1.00
8	2.02	0.99
9	5.70	0.98
10	6.44	0.97
11	14.65	0.95
12	10.56	0.94
13	6.14	0.88
14	6.30	0.62
15	2.00	0.59
16	5.83	0.58
17	6.18	0.47
18	14.45	0.38
19	6.20	0.35
20	6.65	0.34
21	1.87	0.23

TABLE 4.3: Perforated plates geometrical parameters. The values of R_{neck} and h are not given for confidentiality reasons.

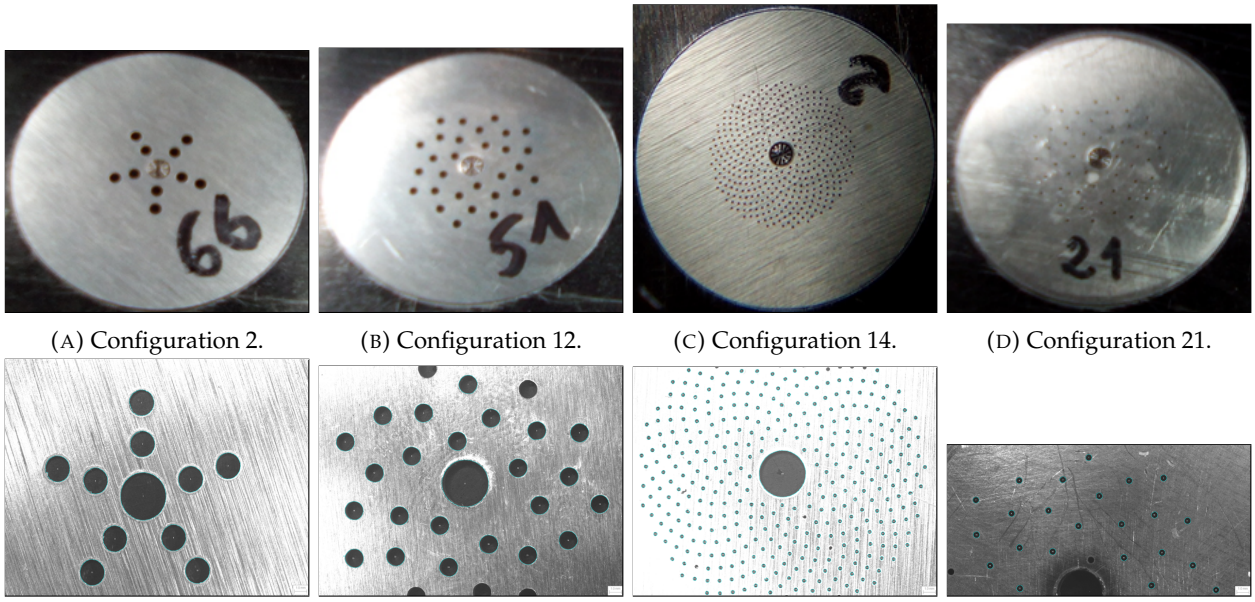

(A) Configuration 2. (B) Configuration 12. (C) Configuration 14. (D) Configuration 21.

(E) Configuration 2. (F) Configuration 12. (G) Configuration 14. (H) Configuration 21.

FIGURE 4.4: (A), (B), (C), (D) Photography of the perforated plates with the microphone flush with the surface of the plate. Figures (E), (F), (G), (H) are a zoom on the perforations without the microphone.

Among the 21 configurations, we operate detailed comparisons between the model previously described and the measurements for 4 configurations. The chosen configurations correspond to samples 2, 12, 14 and 21. The photographs in figure 4.4 shows the samples, which are discs of diameter 5 cm of varying thicknesses. The perforation at the center of the discs allows to mount the microphone flush to the surface of the plate. The perforations are circular. Note that the perforations are distributed on a disc of diameter of 25 mm and that the outer non-perforated rim is used to mount the perforated plate on the sample holder.

Configurations 2 and 12 are macro-perforated plates with, respectively, a low porosity and a high porosity. Configuration 14 and 21 are micro-perforated plates with a high and a low porosity, respectively.

4.5 Eduction of the empirical parameters from measurements

We now educe the empirical parameters k_{Guess} and ς_{Meng} from the measurements performed for the 21 configurations. The calculated resistance is fitted on the measured resistance using the least mean square method. In this section, we focus on the 4 configurations chosen in the previous section to assess the quality of this fit for both impedance corrections.

This procedure is performed for the 3 positions in the vein, for 2 Mach numbers ($M = 0.3$ and $M = 0.45$) and two sound pressure levels (130 dB and 150 dB). However, as the impedance measurements from positions 2 and 3 are similar, we do not plot the impedance from position 3 on the following graphs. Also, we only plot the results at $L_p = 150$ dB as their trends are similar to the results at $L_p = 130$ dB. The values of the empirical parameters are provided in table 4.4 (k_{Guess}) and in table 4.5 (ς_{Meng}).

	Conf. 2	Conf. 12	Conf. 14	Conf. 21
$M = 0.3$, $L_p = 130\,\text{dB}$, Position 1	0.47	0.34	0.21	0.14
$M = 0.3$, $L_p = 130\,\text{dB}$, Position 2	0.31	0.26	0.16	0.11
$M = 0.45$, $L_p = 130\,\text{dB}$, Position 1	0.48	0.30	0.23	0.14
$M = 0.45$, $L_p = 130\,\text{dB}$, Position 2	0.33	0.25	0.17	0.12
$M = 0.3$, $L_p = 150\,\text{dB}$, Position 1	0.44	0.35	0.20	0.08
$M = 0.3$, $L_p = 150\,\text{dB}$, Position 2	0.29	0.25	0.14	0.05
$M = 0.45$, $L_p = 150\,\text{dB}$, Position 1	0.48	0.35	0.26	0.11
$M = 0.45$, $L_p = 150\,\text{dB}$, Position 2	0.32	0.26	0.16	0.08

TABLE 4.4: Educed values of k_{Guess} for the 4 configurations at different Mach number, sound pressure level and position in the vein.

	Conf. 2	Conf. 12	Conf. 14	Conf. 21
$M = 0.3$, $L_p = 130\,\text{dB}$, Position 1	0.50	0.37	0.23	0.18
$M = 0.3$, $L_p = 130\,\text{dB}$, Position 2	0.34	0.30	0.17	0.16
$M = 0.45$, $L_p = 130\,\text{dB}$, Position 1	0.52	0.32	0.24	0.17
$M = 0.45$, $L_p = 130\,\text{dB}$, Position 2	0.35	0.27	0.18	0.15
$M = 0.3$, $L_p = 150\,\text{dB}$, Position 1	0.47	0.38	0.22	0.13
$M = 0.3$, $L_p = 150\,\text{dB}$, Position 2	0.31	0.29	0.15	0.10
$M = 0.45$, $L_p = 150\,\text{dB}$, Position 1	0.51	0.34	0.24	0.13
$M = 0.45$, $L_p = 150\,\text{dB}$, Position 2	0.34	0.29	0.18	0.12

TABLE 4.5: Educed values of ς_{Meng} for the 4 configurations at different Mach number, sound pressure level and position in the vein.

In Guess (1975), the choice of k_{Guess} does not impact the reactance, hence it is plotted once under the label Guess pos. 1. In the impedance correction from Meng *et al.* (2019), the choice of ς_{Meng} does impact the reactance, therefore it is plotted for both positions in the following graphs with labels Meng *et al.* pos. 1 and Meng *et al.* pos. 2.

For each configuration, the normalized resistance $\text{Re}(\text{z})$ and the normalized plate reactance $\text{Im}(\text{z}) + \cot(k_0 L)$ are plotted for $M = 0.3$ and $M = 0.45$. We consider that the resistance is fitted and the reactance is predicted.

For all 4 configurations, the normalized resistance without flow is accurately fitted by the Guess model for each plate. On the other hand, the normalized plate reactance appears to be slightly overestimated. The impact of the boundary layer thickness is clearly visible on the resistance. The resistance is higher at position 1, *i.e.* when the boundary layer is in the transition regime. For position 2 and 3, *i.e.* when the boundary layer is turbulent, the resistance is lower and remains almost the same even though the displacement boundary layer thickness is different. Therefore, in the following comparisons, only the impedance for position 1 and 2 are plotted. For position 1 to 3 the measurements provide similar plate reactance values.

It can be noted that, as the empirical parameters are accounted for during the iteration procedure, it impacts the velocity in the perforations and changes the slope of the resistance and slightly the slope of the reactance. This is important to fit correctly the resistance. Indeed, if the grazing flow correction was added after the iteration procedure, it would simply shift the resistance without flow without impacting its slope and the fit wouldn't be as accurate.

With flow, the fitted resistance of sample 2 (figure 4.5) is in very good agreement with the measurements for the 2 positions and at both Mach numbers. The measured plate reactance decreases with growing Mach number as previously observed in previous experimental studies, for instance in Jing *et al.* (2001). Although the measured plate reactance appears to be noisy, it is correctly predicted by both models.

When considering configuration 12, the fitted resistance is in correct agreement with the measurements. Small discrepancies are visible between the two models. The full Guess model provides a reasonable plate reactance predictions. The Guess–Meng model underestimates the measured reactance.

Figure 4.7 corresponds to sample number 14. Here, both models accurately fit the measured resistance on both positions. Again, the plate reactance is underestimated by the hybrid model.

The fitted resistance from configuration 21 (figure 4.8) is in good correspondence with the full Guess model. However, the Guess-Meng model is less accurate. A possible explanation to this is the fact that when the porosity is low, the impact of the grazing flow on the resistance is limited. Hence, only a small resistance correction is needed and small values of ς_{Meng} and k_{Guess} are obtained. In the case of the sample number 21, $\varsigma_{\text{Meng}} \approx 0.15$. For small values of the convection speed, the grazing flow resistance (equation (4.8)) in the Guess–Meng model may become small because of the important contribution of the term

$$-\frac{(k_0 R_{\text{neck}})^2}{\varsigma_{\text{Meng}} M}(C_2 t + C_3 t + C_4 t^2). \tag{4.14}$$

This would be consistent with the fact that the fit obtained with the Guess–Meng model is slightly better for a Mach number of $M = 0.45$ than for $M = 0.3$. This situation is not encountered in Meng *et al.* (2019) in which the convection speed is close to 0.5. The measured plate reactance, which appears not to be impacted by the grazing flow is acceptably predicted by the full Guess model. Here again, it is underestimated by Meng *et al.* (2019).

In a global manner, the resistance fits appear to be better when using the full Guess model rather than the hybrid Guess–Meng model. The reactance is also better predicted by the full Guess model. The previous fits show that both models may be modified in order to be predictive in presence of grazing flow. For that purpose, it is necessary to recommend a value of the empirical parameters depending on the configuration. In the next section, this perspective is explored.

4.6 Discussion on the empirical parameters k_{Guess} and ς_{Meng}

In the previous section, the empirical parameters k_{Guess} and ς_{Meng} were educed from the measured resistance. Globally, the resistance obtained with both models is in good agreement with measurements although the grazing flow correction proposed in the model from Guess (1975) is more accurate than the correction from Meng *et al.* (2019) when considering the previous 4 configurations. Based on the previous resistance comparisons, the empirical parameters appear to be relevant and deserve more interest.

It can be noted that the two parameters are of the same order of magnitude, this can be explained on the basis of equations (4.1) and (4.10). When using the grazing flow correction from Guess, we educe k_{Guess} with $(1-\sigma^2)k_{\text{Guess}}M/\sigma$. When using the hybrid model, the term with the C_1 multiplying factor is dominating in the grazing flow correction, hence it can be approximated by $1/\sigma C_1 \varsigma_{\text{Meng}} M$. Thus, we get the approximation

$$\frac{1-\sigma^2}{\sigma} k_{\text{Guess}} M \approx \frac{1}{\sigma} C_1 \varsigma_{\text{Meng}} M, \tag{4.15}$$

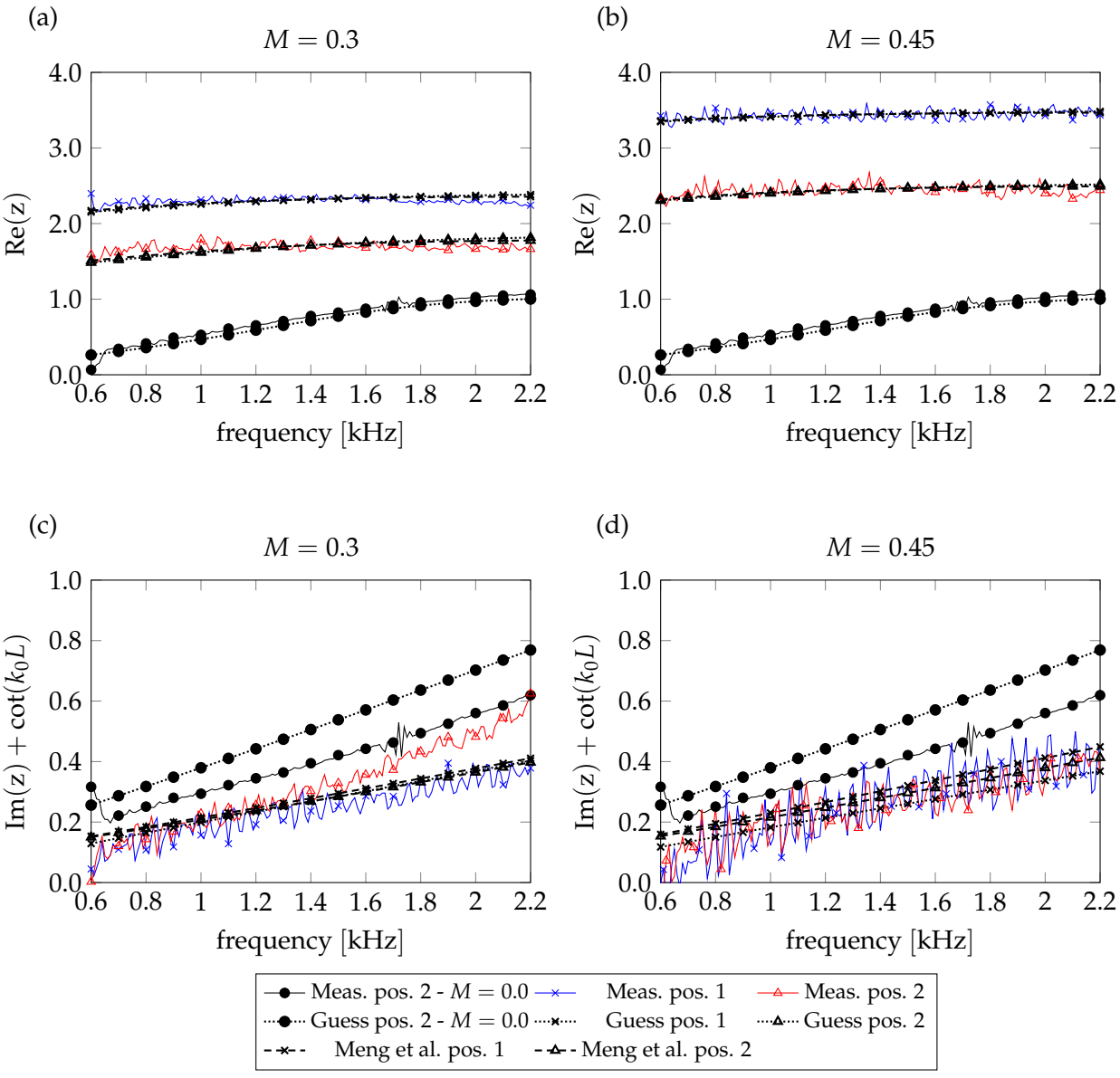

FIGURE 4.5: Configuration 2: a macro-perforated configuration with a low porosity - Normalized resistance (top) and normalized plate reactance (down).

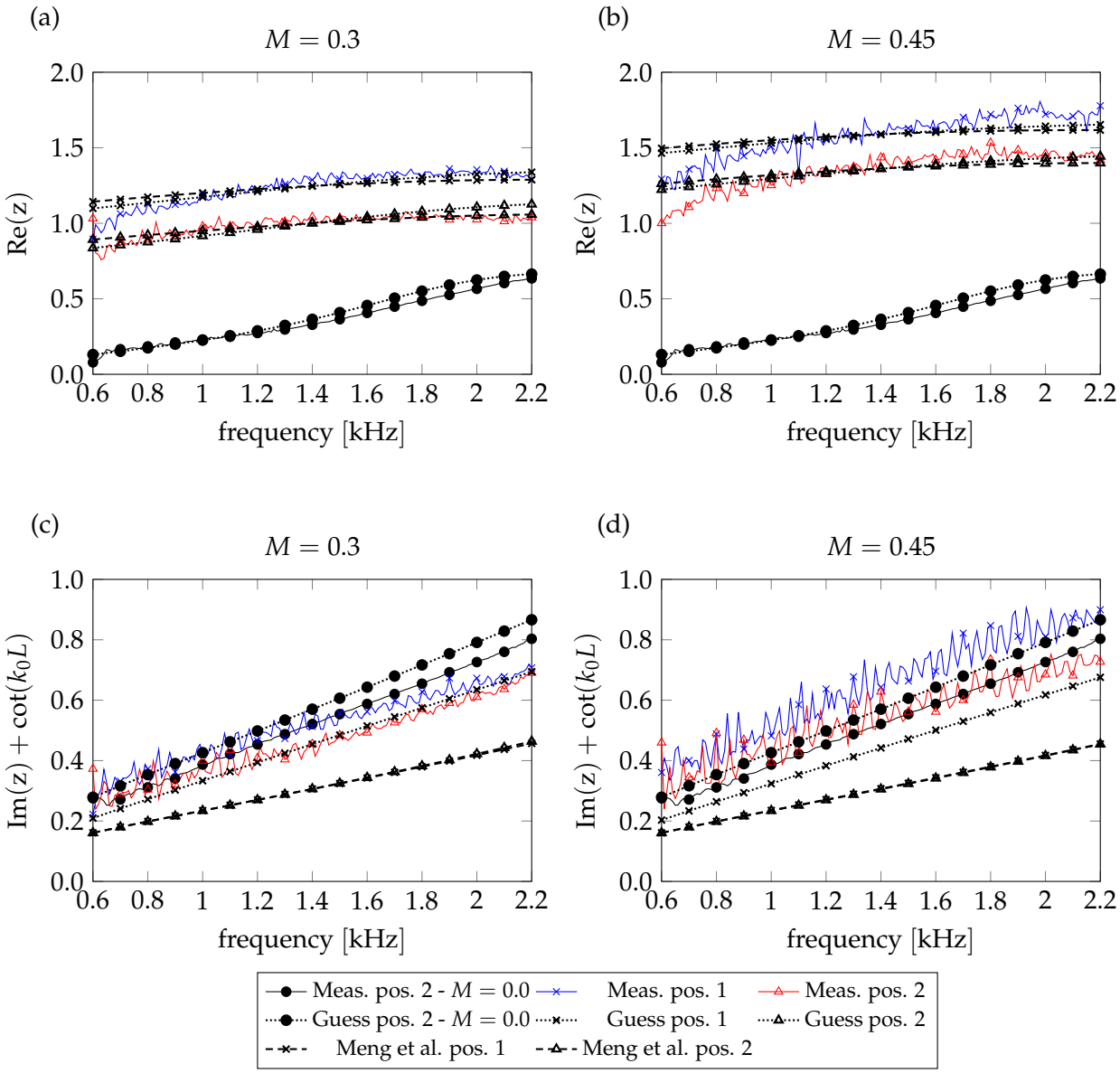

FIGURE 4.6: Configuration 12: a macro-perforated configuration with a high porosity - Normalized resistance (top) and normalized plate reactance (down).

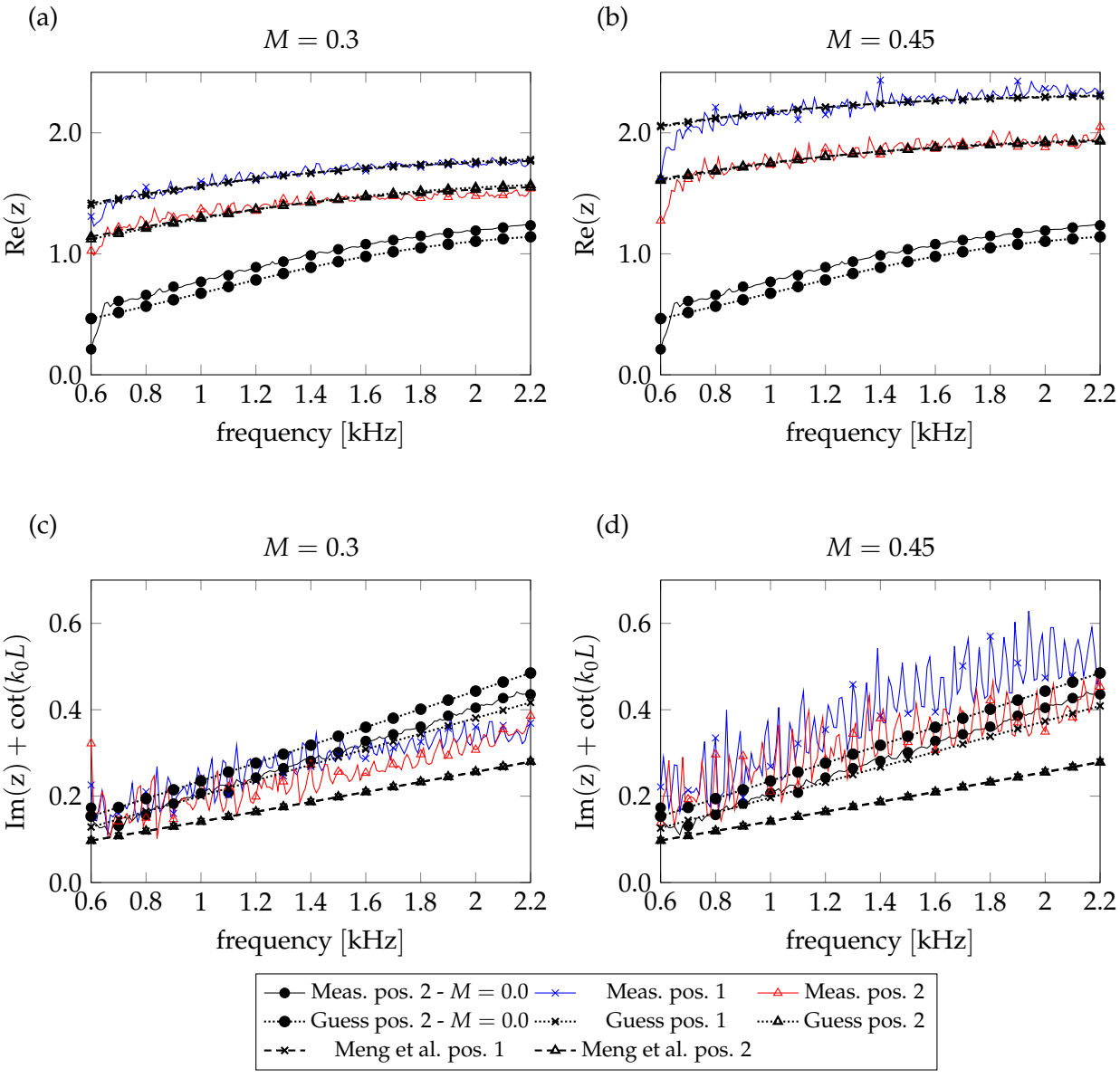

FIGURE 4.7: Configuration 14: a micro-perforated configuration with a high porosity - Normalized resistance (top) and normalized plate reactance (down).

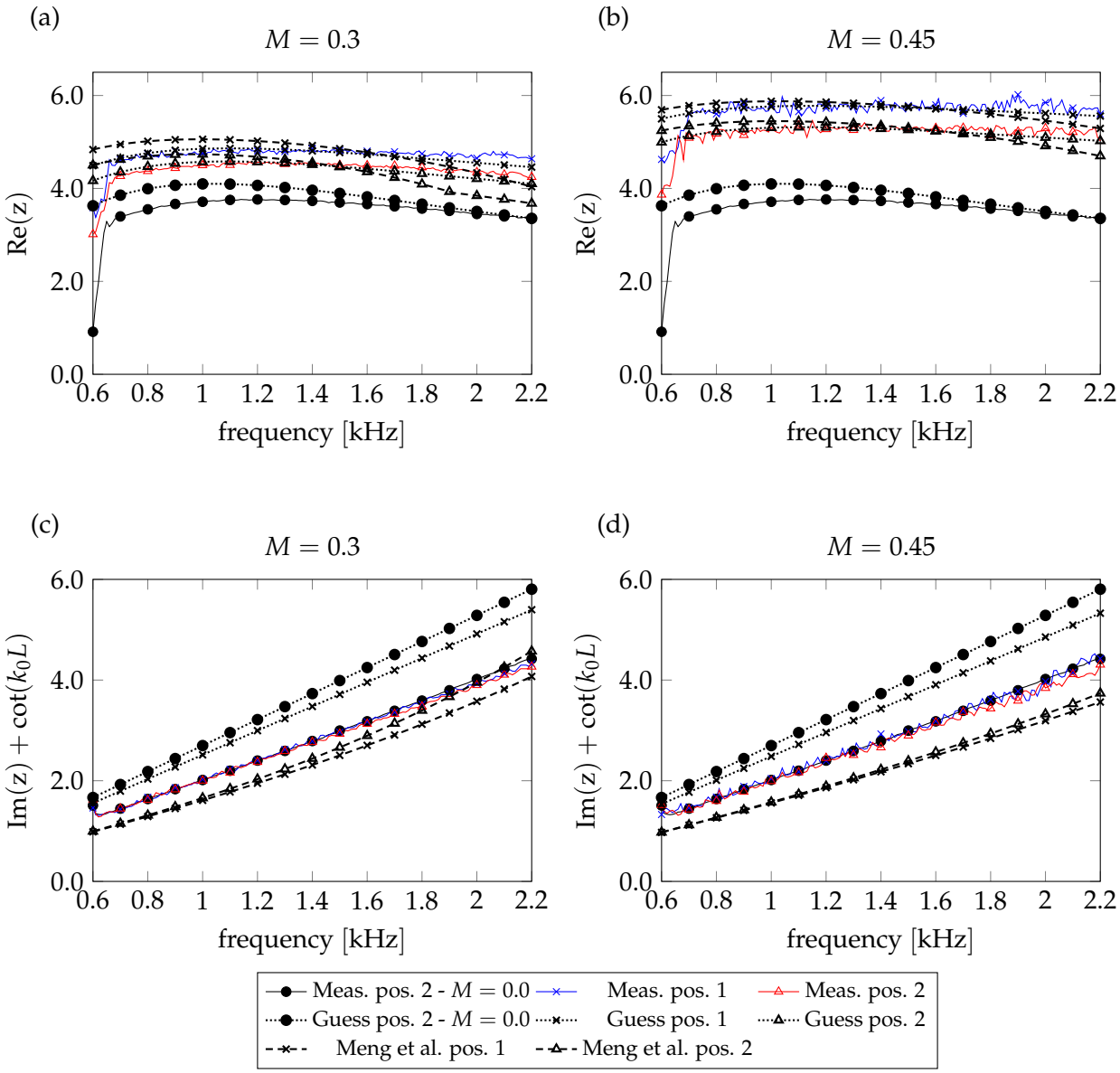

FIGURE 4.8: Configuration 21: a micro-perforated configuration with a low porosity - Normalized resistance (top) and normalized plate reactance (down).

which is expected to be more accurate for low values of R_{neck} and t. The previous equation leads to

$$\varsigma_{\text{Meng}} \approx \frac{1-\sigma^2}{C_1} k_{\text{Guess}}. \tag{4.16}$$

In order to predict the impedance of a perforate plate under grazing flow, it is of interest to understand how the fitted parameters k_{Guess} and ς_{Meng} vary. In Meng *et al.* (2019), the convection speed is plotted as a function of the dimensionless displacement boundary layer thickness δ^*/R_{neck}. Here, the same approach is used for a sound pressure level of $L_p = 130\,\text{dB}$ and $L_p = 150\,\text{dB}$, and a Mach number of $M = 0.3$ and $M = 0.45$ on figures 4.9 for k_{Guess} and 4.10 for ς_{Meng}. The results for $L_p = 130\,\text{dB}$ are in Appendix D as we did not observe major differences with the results at $L_p = 150\,\text{dB}$. For each configuration, 3 data points are available as their are 3 positions in the vein. On these figures, the colors of the plot depends on the ratio $2R_{\text{neck}}/h$. According to figure 4.9, the educed data for k_{Guess} are consistent with the recommendation from the Goodrich model in Yu *et al.* (2008)

$$k_{\text{Guess}} = \frac{2}{4 + 1.256\dfrac{\delta^*}{R_{\text{neck}}}}. \tag{4.17}$$

Equation (4.17) is derived from empirical data and was validated with measurements performed on macro-perforated liners with $2R_{\text{neck}}/h \approx 1$, porosity of 7.7 % to 11.8 % and Mach numbers between 0.2 and 0.45. The trend and order of magnitude of equation (4.17) are similar to our measurements, however, important discrepancies are observed. This suggests that if k_{Guess} is chosen based on this recommendation, the impedance prediction would not be accurate. The effect of the $2R_{\text{neck}}/h$ ratio seems to have a significant impact on the empirical parameter, as opposed to the porosity, which appears to be secondary. A possible explanation is that the perforations becomes more receptive to the boundary layer turbulent fluctuations with increasing radius. From a physical point of view, the variation of k_{Guess} is supposed to indicate the variation of the fluctuating velocity in the perforations. For a boundary layer thick compared to the radius, v increases and conversely. This is also the case for ς_{Meng}.

Interestingly, the boundary layer thickness impacts significantly the resistance. We recall that in position 1 (low displacement thickness), the boundary layer is in the transition regime and in position 2 and 3 (high displacement thickness) it is turbulent. Moreover, the impedance is not significantly impacted when passing from position 2 to 3, increasing the boundary layer displacement thickness. This suggests that the impedance might be more impacted by the nature of the boundary layer rather than its displacement thickness.

From there, two options are available to predict the value of k_{Guess}. The first option is to add more physics to the current model from Guess (1975) and to understand the interaction between the shear flow and the impedance. This the case of the model from Meng *et al.* (2019), but it also relies on an empirical parameter. The second option is to attempt to derive a law from our empirical data as in Yu *et al.* (2008). In this section we choose the second option. This law can be refined by fitting the following function to our data

$$k_{\text{Guess}} = \frac{1}{a + b\dfrac{\delta^*}{R_{\text{neck}}}}, \tag{4.18}$$

where a and b are fitted parameters. Equation (4.18) can be used for each configuration and then the trends of a and b can be extracted. It is found that a has an inverse law dependence as function

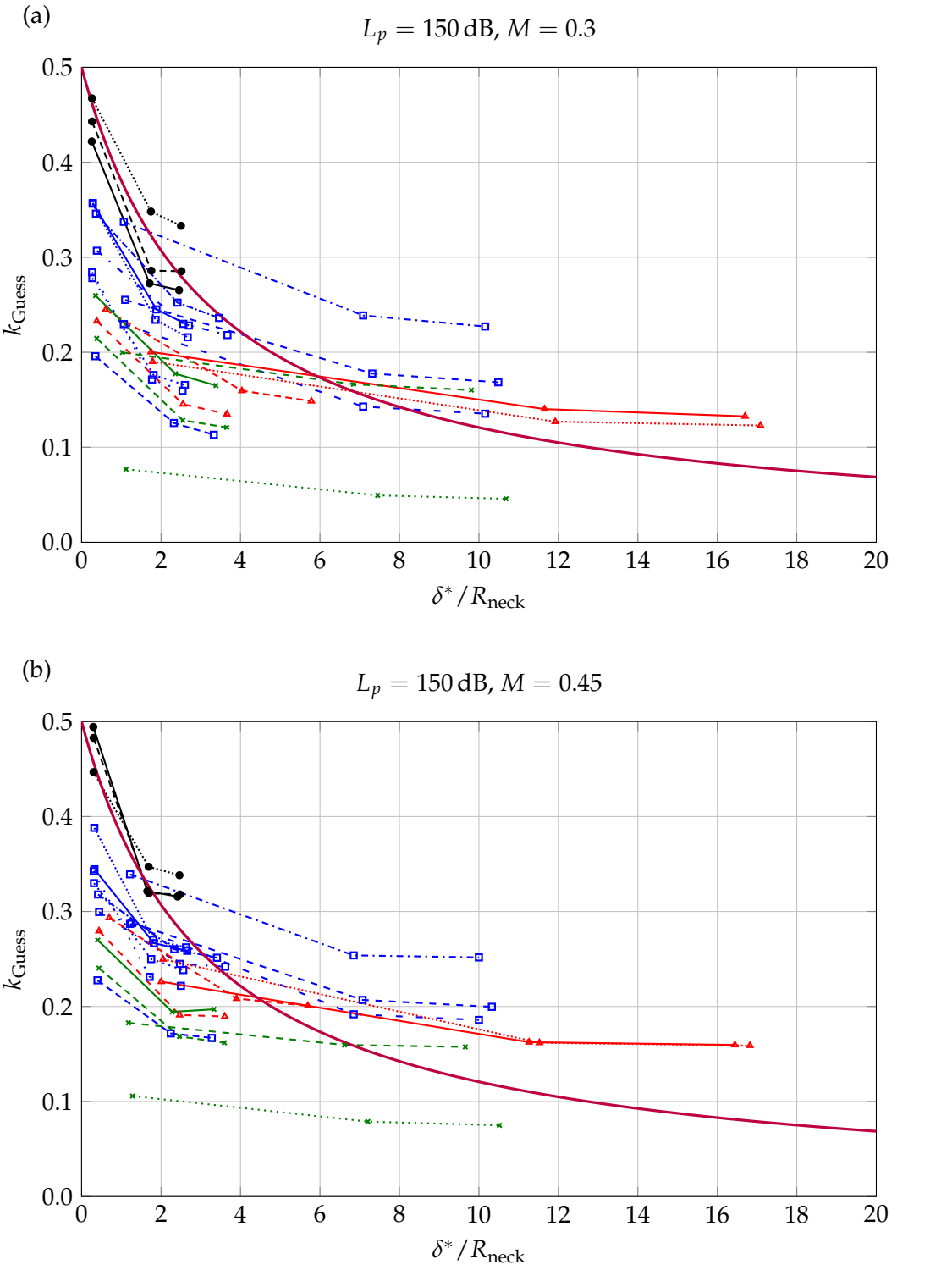

FIGURE 4.9: Empirical parameter k_{Guess} as a function of $\delta^* / R_{\mathrm{neck}}$ for configuration 1 to 21. For sample 1 to 3, we have $4.12 \leq 2R_{\mathrm{neck}}/h \leq 4.21$ which corresponds to the black plots; For sample 4 to 13, we have $1.21 \leq 2R_{\mathrm{neck}}/h \leq 0.88$ which corresponds to the blue plots; For sample 14 to 17, we have $0.62 \leq 2R_{\mathrm{neck}}/h \leq 0.47$ which corresponds to the red plots; For sample 18 to 21, we have $0.38 \leq 2R_{\mathrm{neck}}/h \leq 0.23$ which corresponds to the green plots.

R_{neck}/h, hence, we now use

$$a(R_{\text{neck}}/h) = \frac{1}{a_0 + a_1 \dfrac{R_{\text{neck}}}{h}}, \tag{4.19}$$

where a_0 and a_1 are parameters to be fitted. Regarding b, a linear dependence as a function of R_{neck} is observed, we therefore use

$$b(R_{\text{neck}}) = b_0 + b_1 R_{\text{neck}}, \tag{4.20}$$

where b_0 and b_1 are parameters to be fitted. The function defined by equation (4.18) is fitted on the data obtained with the 21 configurations mixing two Mach numbers (0.3 and 0.45) and two sound pressure levels (130 dB and 150 dB). Additionally, ς_{Meng} (4.10) has the same trend as k_{Guess}, hence we propose the same function to fit the convection speed of vorticity. The values of a_0, a_1, b_0 and b_1 are given in table 4.6 for the two empirical parameters with their respective standard deviation in brackets.

Empirical parameter	a_0	a_1	b_0	b_1
k_{Guess}	0.231(0.007)	0.071(0.004)	0.128 (0.028)	409(56.3)
ς_{Meng}	0.288(0.007)	0.057(0.004)	0.174 (0.024)	228(45.5)

TABLE 4.6: Values of the fitted parameters with their respective standard deviation in brackets. These data can be used to obtain a value of k_{Guess} or ς_{Meng} for δ^*/R_{neck} between 0 and 20.

The standard deviations of a_0 and a_1 are relatively low, which means that the R_{neck}/h dependence is captured correctly. This is not the case for b_0 and b_1, which suggests that the radius dependence is not dominant. A benefit of this method is that the value of k_{Guess} for $\delta^*/R_{\text{neck}} = 0$ changes as a function of the R_{neck}/h ratio. Also, the rate of decline is a function of the radius R_{neck}. This is illustrated by figure 4.11 in which equation (4.18) is compared to the law from Yu *et al.* (2008).

The final step of this study is to assess how predictive is the law proposed in equation (4.18). For the 4 configurations, we compute the resistance with the model from Guess (1975) using the k_{Guess} recommendation defined by equation (4.18). We also compute the resistance using $k_{\text{Guess}} = 0.3$ as prescribed by Guess (1975). The results are shown on figures 4.12 and 4.13. The value of k_{Guess} determined using equation (4.18) for position 1 is noted k_1, for position 2 it is noted k_2.

We only perform this validation for the model from Guess (1975) as it provides better resistance fit and reactance predictions than the correction from Meng *et al.* (2019). When considering configuration 2, we can observe that the values 0.3 and 0.28 provide accurate resistance predictions for position 2. The resistance corresponding to $k_1 = 0.36$ provides an improvement of the prediction for position 1, but is still below the measurements. Regarding configuration 12, the resistance corresponding to $k_{\text{Guess}} = 0.3$ appears to be in good agreement with the measurements at both positions. On the other hand, the resistance is underestimated when using the law in equation (4.18).

In the case of configuration 14, the fit in equation (4.18) clearly improves the resistance prediction compared to $k_{\text{Guess}} = 0.3$ at both Mach numbers. When using $k_{\text{Guess}} = 0.3$ the resistance is overestimated. This observation is also true for configuration 21. For this configuration, using k_1 and k_2 improves the predictions but the resistance is still overestimated.

From the previous comparisons, it appears that equation (4.18) clearly improves the resistance prediction for the micro-perforated configurations 14 and 21. For the macro-perforated configurations 2 and 12 with high perforation radius, it provides reasonable predictions for the measured

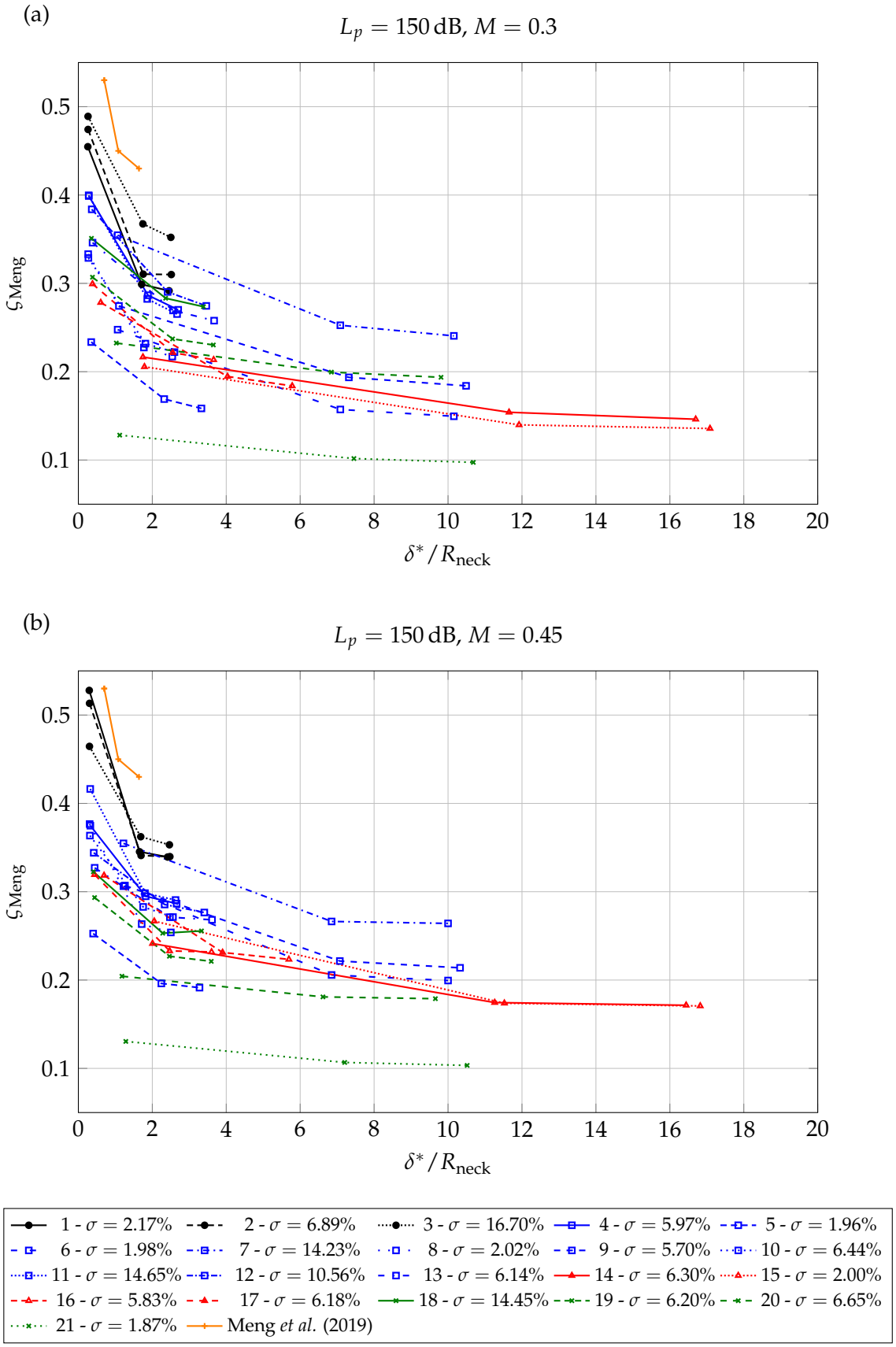

FIGURE 4.10: Empirical parameter ζ_{Meng} as a function of $\delta^* / R_{\mathrm{neck}}$ for configuration 1 to 20. For sample 1 to 3, we have $4.12 \leq 2R_{\mathrm{neck}}/h \leq 4.21$ which corresponds to the black plots; For sample 4 to 13, we have $1.21 \leq 2R_{\mathrm{neck}}/h \leq 0.88$ which corresponds to the blue plots; For sample 14 to 17, we have $0.62 \leq 2R_{\mathrm{neck}}/h \leq 0.47$ which corresponds to the red plots; For sample 18 to 21, we have $0.38 \leq 2R_{\mathrm{neck}}/h \leq 0.23$ which corresponds to the green plots.

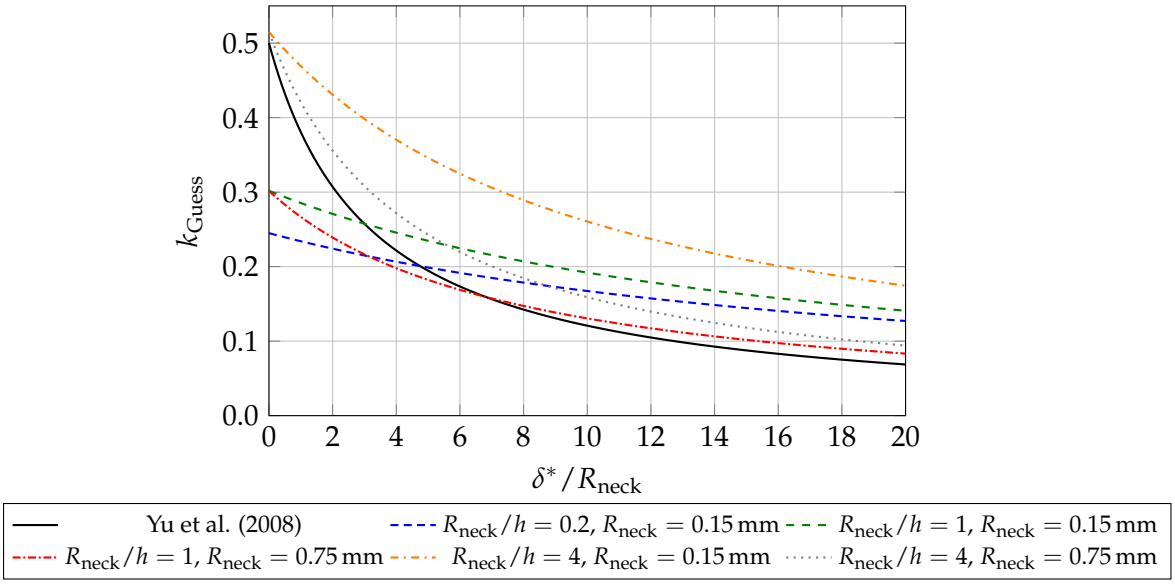

FIGURE 4.11: Values of k_{Guess} from Yu et al. (2008) and with equation (4.18) for different R_{neck}/h ratio and radius.

resistance at position 2.

An important remark is that during the iteration procedure, the velocity in the apertures is computed with the same formula than without flow, which relies on a plane wave assumption. This approach was validated without flow with a plane wave propagation normal and grazing to the perforated plate (in chapter 4), but there are no guarantee of its validity it the presence of shear flow. At this time, it is rather unclear how to derive the velocity in the perforations from our measurements with a grazing flow. Without flow, we consider an homogeneous velocity in the apertures as the effective velocity. With flow, the effective velocity impacting the impedance is unknown.

Finally, as the empirical parameters are impacted by the method used to compute the velocity in the holes, their physical meaning should be considered with care.

4.7 Conclusion

Two semi-empirical models were compared to measurements with a grazing flow with varying boundary layer displacement thicknesses. The first model is the model from Guess (1975) with a grazing flow resistance correction derived from Ingard (1968) and a reactance correction based on the experimental data from Groeneweg (1969). The second, hybrid model, is still based on the work from Guess (1975) except the impedance correction is derived from Meng *et al.* (2019).

Both approaches include an empirical parameter, in the first model it is proportional to the velocity fluctuation in the perforations v, and in the second model, the empirical parameter corresponds to convection speed of vorticity above the apertures ς_{Meng}. These parameters are educed from the resistance measurements for 21 configurations. From the close impedance comparisons performed for 4 configurations, it appears that the resistance fit performed with the model from Guess is globally more accurate than the hybrid model, although the latter model provides very reasonable agreement with the experiments. The validity domain for the use of the correction from Meng *et al.* (2019) is extended and appears to be applicable for Mach numbers above 0.3. An important remark is that including the grazing flow correction allows to obtain the correct resistance slope as a function of the frequency, while simply shifting the resistance without flow by adding the flow correction after the iteration would result in lower quality fit of the resistance.

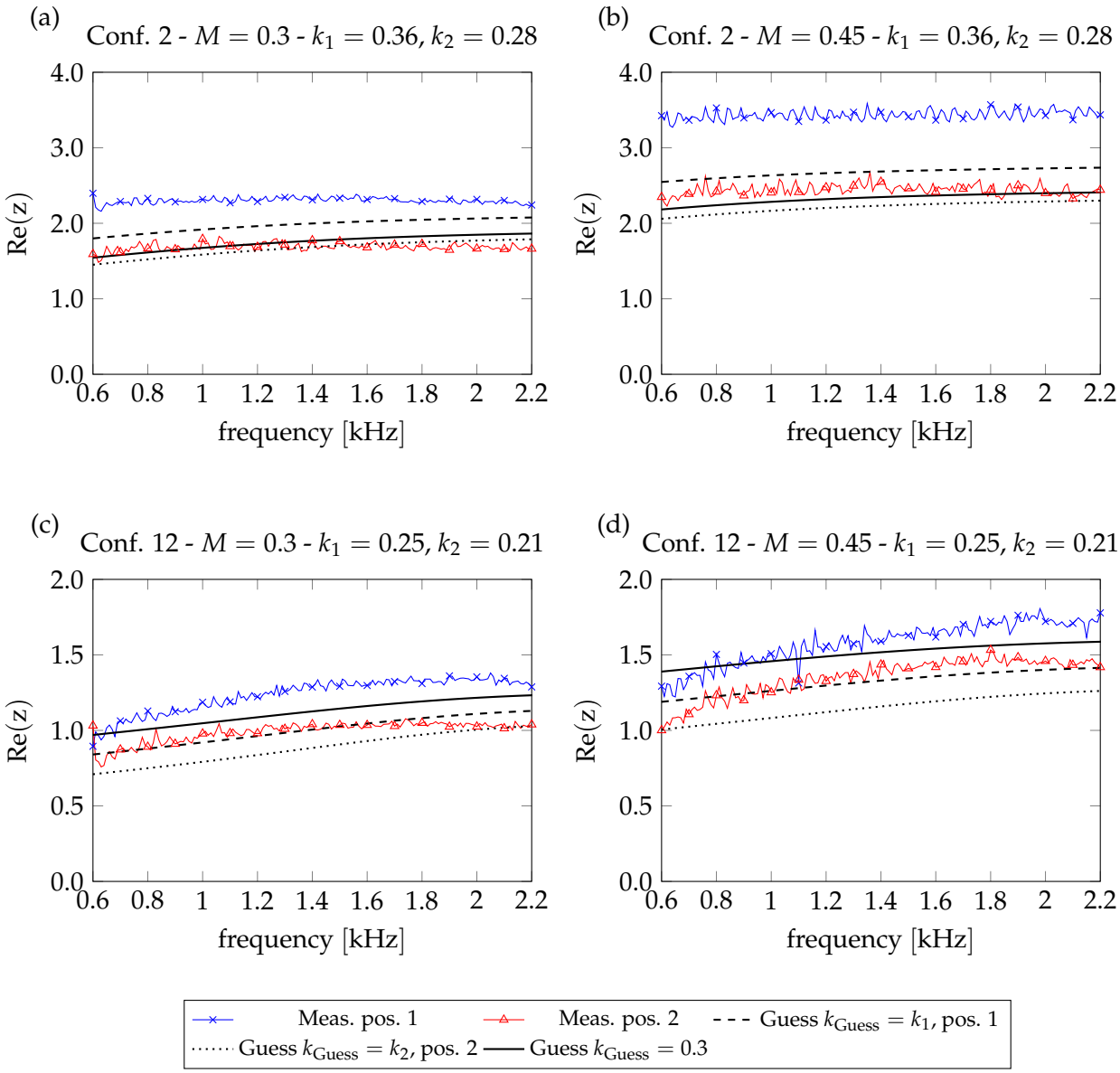

FIGURE 4.12: Predicted resistance using the law in equation (4.18) and $k_{\text{Guess}} = 0.3$ for configurations 2 and 12 compared to the measurements at position 1 and 2.

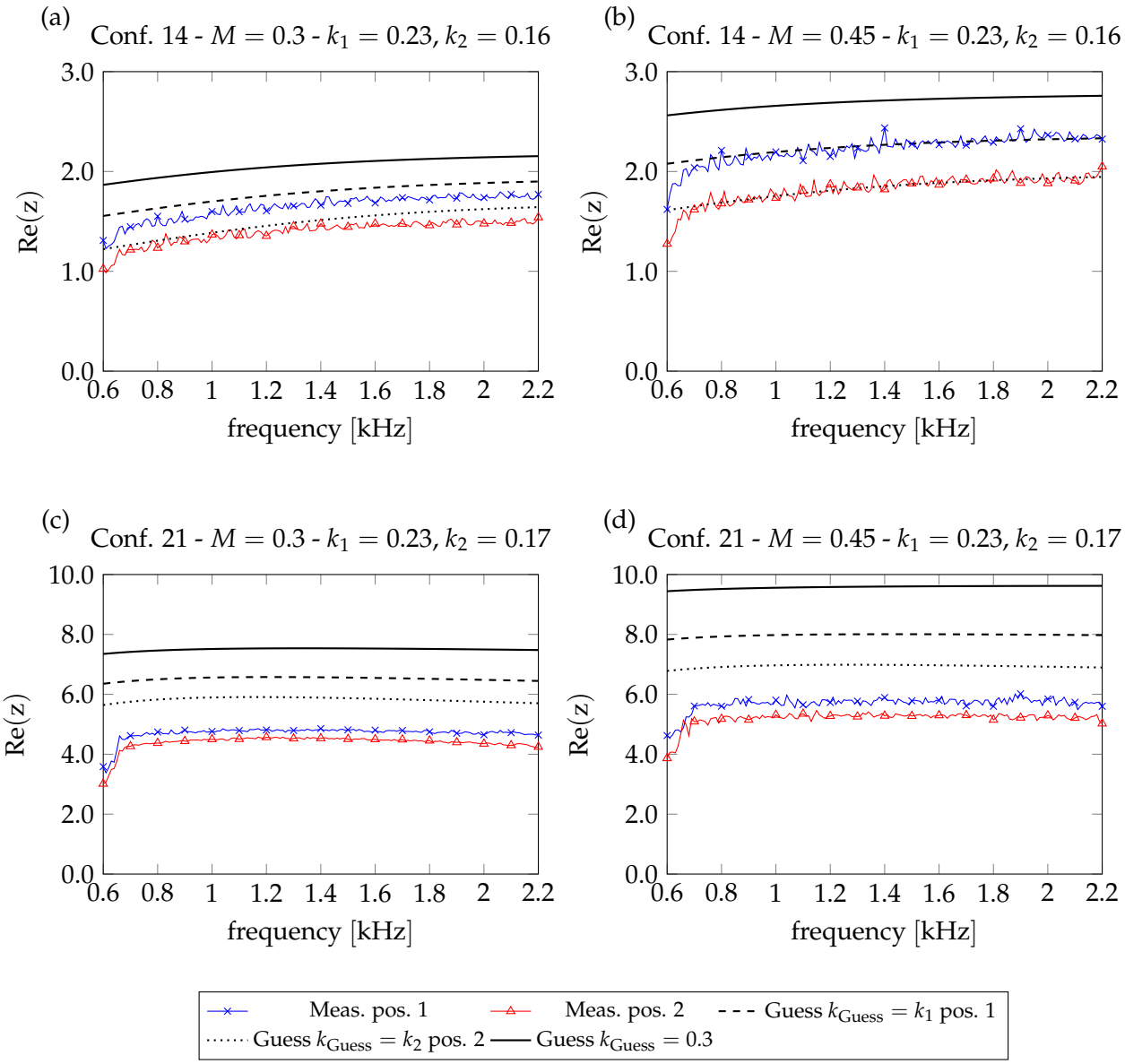

FIGURE 4.13: Predicted resistance using the law in equation (4.18) and $k_{\text{Guess}} = 0.3$ for configurations 14 and 21 compared to the measurements at position 1 and 2.

The trends of k_{Guess} and ς_{Meng} are similar. The empirical parameters decrease with increasing values of δ^*/R_{neck} following a hyperbolic law. This hyperbole is shifted for each configuration. The latter parameters decrease with increasing values of δ^*/R_{neck} consistently with Yu *et al.* (2008) and the data from Meng *et al.* (2019). As to now, we have no strong physical explanation to these observations. An empirical function is proposed based on the measurements performed on the 21 configurations to predict the value of k_{Guess}. This function is different from the function in Yu *et al.* (2008) as its value for $\delta^*/R_{\text{neck}} = 0$ depends on the ratio R_{neck}/h and its rate of decline depends on the radius. When using this function to predict the resistance with the model from Guess (1975), it is shown to be more accurate for micro-perforated and to provide reasonable predictions for the macro-perforated plates.

Based on the method used to compute the velocity and educe the empirical parameters, the relevance of ς_{Meng} and k_{Guess} is discussed. For the moment, we have no clear insights on the effective velocity in the perforations impacting the impedance in the presence of flow and the empirical parameters shall be viewed more as corrections rather than physically based parameters. In the following chapter, an impedance sensitivity analysis is performed to provide more insights on the effective physical quantity impacting the impedance of a perforation under grazing flow backed by a cavity.

Chapter 5

Sensitivity analysis in the presence of non-linear effects and grazing flow

To analyze the effects of non-linearities on the impedance of a perforation backed by a cavity in presence of a grazing flow, a sensitivity analysis is described in this chapter. For this purpose, a finite element model solving the linearized Navier-Stokes equations is used. COMSOL Multiphysics is used for the numerical implementation.

5.1 Introduction

Extended work has been performed on non-linear effects in acoustic treatments in recent years. In the abscence of a grazing flow, early experimental work has been carried out by Ingard *et al.* (1950), showing non-linear physical mechanisms having an impact on the impedance of a resonator with a single perforation. The nature of these mechanisms changes as a function of the acoustic particle velocity in the orifice and the frequency. More recently, numerical methods such as FEM allowed to visualize more precisely these mechanisms for different sound pressure levels and frequencies. Such studies are performed by Tam *et al.* (2001), Zhang *et al.* (2012) or Roche (2011) for a single perforation backed by a cavity and show vortex shedding from the corners of the perforation, obtained by solving the full Navier-Stokes equations. In the presence of a grazing flow, and still for a single perforation backed by a cavity, Zhang *et al.* (2016) and Roche *et al.* (2010) performed detailed numerical investigations of the velocity fields showing a huge amount of details in the boundary layer in the presence of high sound pressure levels. For multiple orifices, Avallone *et al.* (2019) conducted numerical simulations showing eddies in a large numerical domain at a Mach number of 0.3.

However, the impact on the impedance of the non-linear effects induced by vortex shedding and hydro-acoustic coupling needs further investigations to be fully understood and modeled. In the previous chapter, the semi-empirical models from Guess (1975) and Meng *et al.* (2019) were compared to measurements with grazing flow. Both models rely on empirical parameters to account for the grazing flow impact on the impedance. In chapter 4, these parameters were educed from measurements and are found to depend on the grazing flow boundary layer thickness, the geometrical characteristics of the perforated plates, and the Mach number. Some trends were highlighted, but the physical mechanisms responsible for the latter are not yet fully understood.

In this chapter we propose a method to identify qualitatively the physical mechanisms having a significant impact on the impedance, with and without flow. The proposed method is a particular case of the resolvent analysis introduced in Schmid *et al.* (2001) and used extensively in the fluid mechanics community (see Álamo *et al.* (2006), McKeon *et al.* (2010), Dergham *et al.* (2013), Towne *et al.* (2018), Martini *et al.* (2020a), Abreu *et al.* (2020)). A brief definition of the resolvent analysis can be found in Herrmann *et al.* (2020): "Resolvent analysis identifies the most responsive forcings and most receptive states of a dynamical system, in an input–output sense, based on its governing equations".

In this chapter, it is used to investigate the non-linear effects in a perforation under a grazing flow, considered as a source to the compressible linearized Navier-Stokes equations. The response of a single perforation to this non-linear forcing is investigated subsequently. As the initial model forcing term corresponds to a plane wave, the comparison between a response to a plane-wave forcing and a response to an arbitrary forcing interpreted as a missing non-linear term is possible.

The remainder of this chapter is as follow: first, we introduce the sensitivity analysis for a simple mechanical system. Second, we apply this method to a perforation backed by a cavity to study its impedance without and with flow. The finite element method is used. We compute the frequency response to a linear term, *i.e.*, a plane wave with a normal incidence with and without a grazing flow. Thereafter, we describe the method used to obtain the impedance sensitivity of this response to a non-linear term. We will extract the non-linear source and the associated response. Afterward, we focus on the finite element domain corresponding to the neck region to discuss the sensitivity fields as well as the response to a non-linear term fields. A case study without and with a grazing flow are considered. Finally, the impedance definition is discussed and we present our perspectives for the present method and formulate conclusive remarks.

5.2 Resolvent analysis for a simple mechanical system

The resolvent analysis corresponds to the identification of the optimal harmonic forcing of a system.

In order to give an insight on how to interpret results from the resolvent analysis, we first illustrate its approach for a simple mechanical system composed of two springs and two masses under the external forces shown in figure 5.1. The left spring is clamped at its left end.

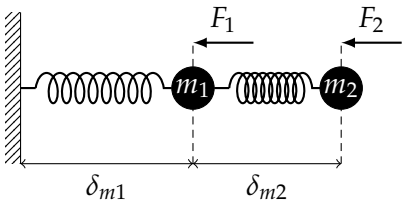

FIGURE 5.1: Simple mechanical system illustrating the resolvent analysis.

The degrees of freedom are the displacement and the velocity of each mass. Therefore, only 4 variables are obtained. The governing equations of the system can be formally written in matrix form as follows (with an $e^{+j\omega t}$ notation)

$$j\omega \mathbf{x} = \mathcal{A}\mathbf{x} + \mathbf{f}. \tag{5.1}$$

where $\mathcal{A}$ is a matrix and $\mathbf{x} = (\delta_{m1}, v_1, \delta_{m2}, v_2)^{\mathrm{T}}$. Here, δ_{m1} and δ_{m2} are the displacements of the masses, v_1 and v_2 are their velocities. The forcing is defined by $\mathbf{f} = \mathcal{B}\mathbf{q}$, where $\mathcal{B}$ is a rectangular matrix and $\mathbf{q} = (F_1, F_2)^T$. F_1 and F_2 are the forces applied on the first and second masses, respectively.

In this case, the resolvent operator of the governing equations corresponds to

$$\mathcal{R} = (j\omega\mathcal{I} - \mathcal{A})^{-1} \text{ so that } \mathbf{x} = \mathcal{R}\mathbf{f}. \tag{5.2}$$

From an acoustic stand point, the resolvent operator corresponds to the convolution operator with the Green function that relates the input $\mathbf{f}$ to the output $\mathbf{x}$.

For instance, if one wants to study the total length $\delta_m = \delta_{m1} + \delta_{m2}$ of the system, a line vector $\mathcal{H}$ such that $\delta_m = \mathcal{H}\mathbf{x}$ can be defined. In this particular case, the resolvent analysis can be applied

to the transfer function operator $\mathcal{HRB}$ to find the forcing for which δ_m is maximum, such that the following gain is maximum

$$G(\omega) = \max_{\mathbf{q}\neq 0} \left|\left| \frac{\mathcal{HRB}\mathbf{q}}{\mathbf{q}} \right|\right|. \tag{5.3}$$

It is important to note that the resolvent operator is intrinsic to the system and its governing equations. On the other hand, the transfer function operator is defined according to the outputs and the inputs of the system.

In the next step, $G(\omega)$ can be determined by computing the Singular Value Decomposition (SVD) of $\mathcal{HRB}$ to obtain

$$\mathcal{H}\mathbf{x} = \mathcal{U}\Sigma\mathcal{V}^{\mathrm{T}}\mathbf{q}, \tag{5.4}$$

where $\mathcal{U}$ is an orthonormal matrix containing in columns a basis of responses of the system and $\mathcal{V}$ is an orthonormal matrix containing the corresponding forcing. Σ is a diagonal matrix composed of the singular values representing the amplification gains. The first singular value is equal to $G(\omega)$. $\mathcal{V}$ contains the optimal phase/amplitude relationship between F_1 and F_2 to produce the largest displacement amplitude of the mass m_2.

In a general case, $\mathcal{H}$ and $\mathcal{B}$ can be of large dimensions, producing optimal forcing/response modes. In this particular example, since $\mathcal{H}$ is a line vector, $\mathcal{U} = 1$, $\mathcal{V}$ is a column vector, and Σ is scalar. In this simplified case, the computation of a SVD is not necessary and by defining the sensitivity field $\mathbf{s} = \mathcal{V}\Sigma$, $\mathbf{s}$ can be determined by solving

$$\mathcal{R}^{\mathrm{H}}\mathbf{s} = \mathcal{H}^{\mathrm{H}}, \tag{5.5}$$

that is numerically tractable, even for large-scale systems. Here, $\cdot^{\mathrm{H}}$ denotes the Hermitian transpose. After normalization, $\mathcal{V}$ and Σ can be recovered.

In the following sections, this method is applied to a more complex problem involving the solving of the linearized Navier-Stokes equations solved with the finite element method.

5.3 Definition of the problem and frequency response

5.3.1 Linearized Navier-Stokes equations and impedance definition

In this section, the equations being solved and the finite element domain are defined. The FEM domain is 2-dimensional with Cartesian coordinates and its geometry is a single perforation backed by a cavity. Above the perforation, a half disc bounded by a Perfectly Matched Layer (PML) is implemented to avoid spurious reflection. In Vandemaele *et al.* (2019), the linearized Navier-Stokes equations are solved in the time domain for a similar numerical problem. In the latter study, a non-reflecting boundary condition implemented with a half disc as well. It appears to be an efficient method to simulate an infinite exterior domain above the perforation. In figure 5.2, $L = 19\,\mathrm{mm}$ is the cavity height, $h = 1.5\,\mathrm{mm}$ is the plate thickness, $\delta_{\mathrm{bl}} = 2.5\,\mathrm{mm}$ is the boundary layer thickness, $d_{\mathrm{cav}} = 2.53\,\mathrm{mm}$ is the cavity width, and $d_{\mathrm{neck}} = 0.8\,\mathrm{mm}$ is the perforation width. We obtain the ratio $\delta_{bl}/R_{\mathrm{neck}} = 6.25$, which is a realistic value located in the operating regime of the measurements presented in the previous chapter.

The grazing flow profile is defined by $\mathbf{u}_0 = (U_0(y), 0)^{\mathrm{T}}$ such that a uniform flow is obtained for $y > L + h + \delta_{\mathrm{bl}}$ with

$$U_0(y) = Mc_0, \tag{5.6}$$

where M is the Mach number and c_0 is the sound speed. A mean boundary layer is defined for $y \in [L + h; L + h + \delta_{\mathrm{bl}}]$ with the following profile

$$U_0(y) = Mc_0 - Mc_0 \left(1 - \frac{y - L - h}{\delta_{\mathrm{bl}}}\right)^n, \tag{5.7}$$

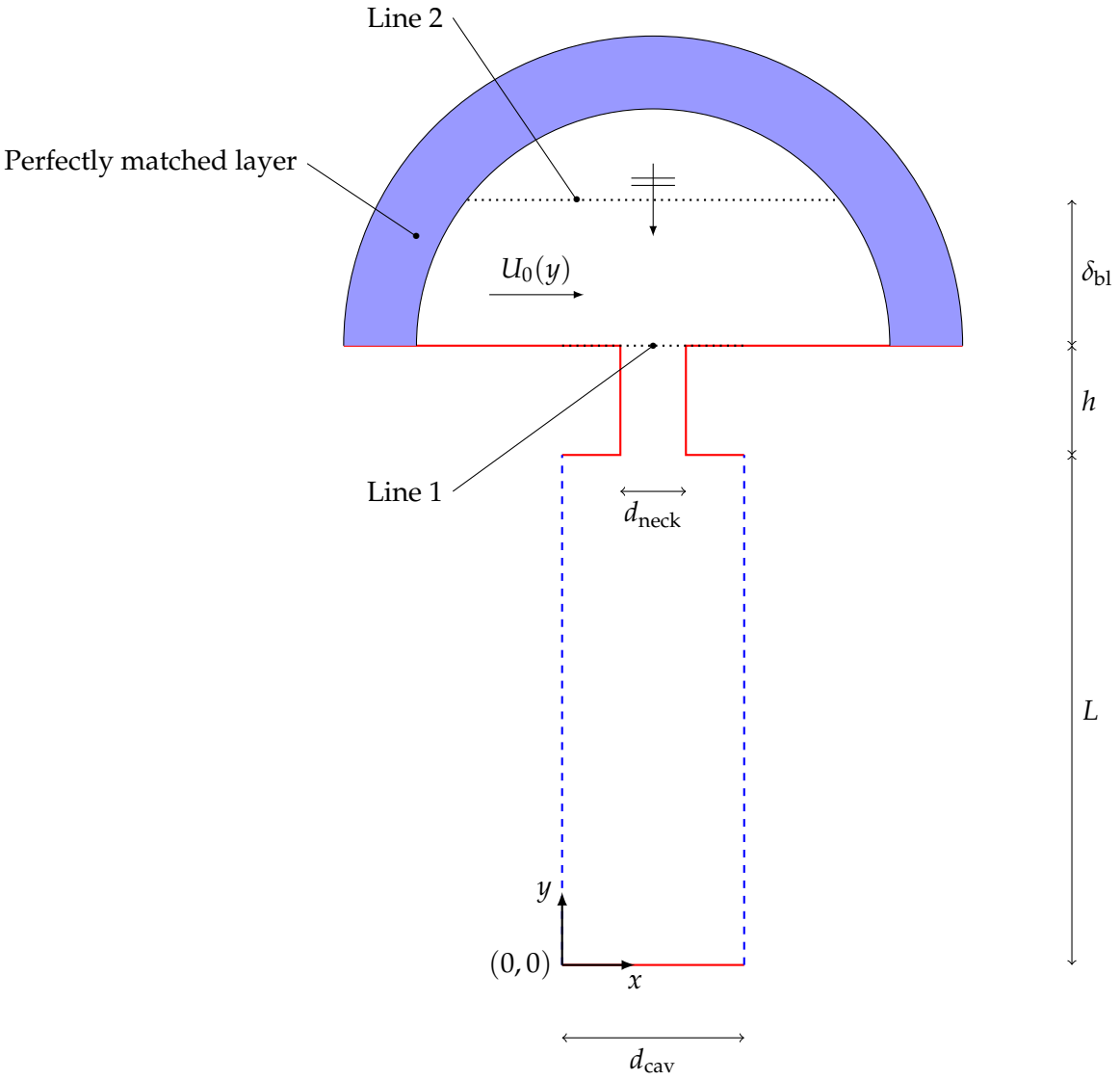

FIGURE 5.2: Numerical domain for the linearized Navier-Stokes equations.

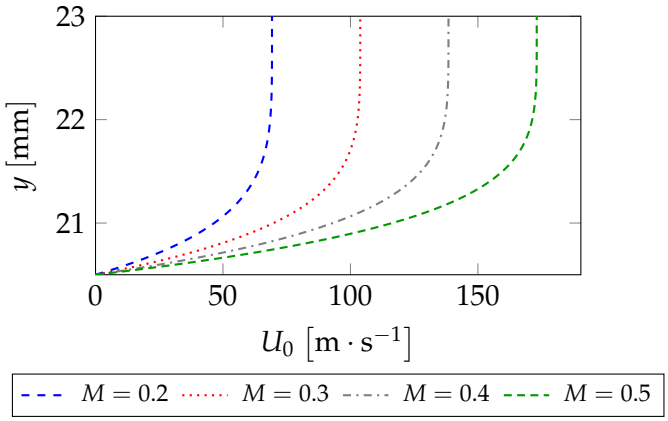

FIGURE 5.3: Imposed velocity profile for different Mach numbers with $n = 5$, $L = 20.5\,\text{mm}$, $h = 1.5\,\text{mm}$ and $\delta_{\text{bl}} = 2.5\,\text{mm}$.

where n is the polynomial power of the velocity profile in the shear region. In Gabard (2013), equation (5.7) is used with $n = 2$. In this chapter we choose $n = 5$ in an attempt to obtain a turbulent boundary layer profile. In figure 5.3, we plot U_0 as a function of the y coordinate for different Mach numbers.

We work in the frequency domain with an $\mathrm{e}^{+\mathrm{j}\omega t}$ convention. An incoming plane wave is imposed in COMSOL (Pryor, 2009) as a *background acoustics field* by implementing the following background pressure, normal velocity, and temperature

$$p_b = A\mathrm{e}^{\mathrm{j}k_0 y},\ v_b = -\frac{1}{\mathrm{j}\omega\rho_0}\frac{\partial p_b}{\partial y},\ T_b = \frac{\alpha_p T_0 p_b}{\rho_0 C_p}, \tag{5.8}$$

with $A = 1\,\text{Pa}$ the amplitude of the wave going towards the negative y. Here, α_p is the coefficient of thermal expansion (unit: K^{-1}) and C_p is the thermal capacity per unit mass at a constant pressure. $k_0 = \omega/c_0$ is the wave number. This plane wave with a normal incidence to the plate, is imposed in the entire finite element domain except in the perfectly matched layer. This is not expected to have an impact on the finite element solution.

The total pressure $\boldsymbol{p}_t$, velocity $\mathbf{u}_t = (\boldsymbol{u}_t, \boldsymbol{v}_t)^{\mathrm{T}}$, and temperature $\boldsymbol{T}_t$, fluctuations around the base state (T_0, p_0, U_0, v_0), are introduced such that

$$p_t = p + p_b, \quad u_t = u, \quad v_t = v + v_b, \quad T_t = T + T_b, \tag{5.9}$$

where p, u, v, and T are the scattered fields. The density ρ_t is also introduced with

$$\rho_t = \rho_0\left(\beta_T p_t - \alpha_p T_t\right), \tag{5.10}$$

where β_T is the iso-thermal compressibility (unit: Pa^{-1}). The boundaries in red in figure 5.2 correspond to a no-slip boundary condition

$$\mathbf{u}_t = \mathbf{0}. \tag{5.11}$$

The dashed blue lines correspond to a free slip boundary condition defined as

$$\mathbf{u}_t \cdot \mathbf{n} = 0. \tag{5.12}$$

Finally, an iso-thermal boundary condition is implemented on the dashed blue lines and the solid red line with

$$T_t = 0. \tag{5.13}$$

The Navier-Stokes equations with flow are linearized around ρ_0, $\mathbf{u}_0$, and T_0. The linearized mass conservation equation is

$$\mathrm{j}\omega\rho_t + \nabla\cdot\left(\rho_t\mathbf{u}_0 + \rho_0\mathbf{u}_t\right) = 0. \tag{5.14}$$

The linearized momentum conservation is

$$\rho_0\left[\mathrm{j}\omega\mathbf{u}_t + \left(\mathbf{u}_t\cdot\nabla\right)\mathbf{u}_0 + \left(\mathbf{u}_0\cdot\nabla\right)\mathbf{u}_t\right] + \rho_t\left(\mathbf{u}_0\cdot\nabla\right)\mathbf{u}_0 = \nabla\cdot\underline{\sigma}. \tag{5.15}$$

with $\underline{\sigma}$ the stress tensor defined as

$$\underline{\sigma} = -p_t\mathcal{I} + \mu\left[\nabla\mathbf{u}_t + \left(\nabla\mathbf{u}_t\right)^T\right] + \left(\mu_B - \frac{2}{3}\mu\right)\left(\nabla\cdot\mathbf{u}_t\right)\mathcal{I}, \tag{5.16}$$

where μ is the dynamic viscosity and μ_B is the bulk viscosity.

The linearized energy conservation equation reads

$$\begin{aligned}&\rho_0 C_p\left(\mathrm{j}\omega\boldsymbol{T}_t + \mathbf{u}_t\cdot\nabla T_0 + \mathbf{u}_0\cdot\nabla\boldsymbol{T}_t\right) + \rho_t C_p\left(\mathbf{u}_0\cdot\nabla T_0\right)\\ &-\alpha_p T_0\left(\mathrm{j}\omega\boldsymbol{p}_t + \mathbf{u}_t\cdot\nabla p_0 + \mathbf{u}_0\cdot\nabla\boldsymbol{p}_t\right) - \alpha_p\boldsymbol{T}_t\left(\mathbf{u}_0\cdot\nabla p_0\right) = \nabla\cdot\left(k\nabla\boldsymbol{T}_t\right) + \Phi.\end{aligned} \tag{5.17}$$

In equation (5.17), Φ is the viscous dissipation function expressed as

$$\Phi = \nabla\mathbf{u} : \underline{\tau}\left(\mathbf{u}_0\right) + \nabla\mathbf{u}_0 : \underline{\tau}\left(\mathbf{u}\right), \tag{5.18}$$

where $\underline{\tau}\left(\mathbf{u}\right)$ and $\underline{\tau}\left(\mathbf{u}_0\right)$ are the dissipation rate tensors corresponding to the fluctuating velocity and to the base flow velocity

$$\underline{\tau}\left(\mathbf{u}\right) = \mu\left[\nabla\mathbf{u} + \left(\nabla\mathbf{u}\right)^{\mathrm{T}}\right] + \left(\mu_B - \frac{2}{3}\mu\right)\left(\nabla\cdot\mathbf{u}\right)\mathcal{I}, \tag{5.19}$$

and

$$\underline{\tau}\left(\mathbf{u}_0\right) = \mu\left[\nabla\mathbf{u}_0 + \left(\nabla\mathbf{u}_0\right)^{\mathrm{T}}\right] + \left(\mu_B - \frac{2}{3}\mu\right)\left(\nabla\cdot\mathbf{u}_0\right)\mathcal{I}. \tag{5.20}$$

The finite element discretisation leads to the following linear system

$$-\left(\mathcal{A} - \mathrm{j}\omega\mathcal{I}\right)\mathbf{x}_l = \mathbf{f}_l, \tag{5.21}$$

with $\mathbf{x} = \left(\boldsymbol{T}_t, \boldsymbol{p}_t, \boldsymbol{u}_t, \boldsymbol{v}_t\right)^{\mathrm{T}}$ containing the unknown variables. $\boldsymbol{T}_t$, $\boldsymbol{p}_t$, $\boldsymbol{u}_t$, and $\boldsymbol{v}_t$ are vectors containing the values of the fields T_t, p_t, u_t, and v_t at their corresponding degrees of freedom in the FEM mesh. P1 elements are used for the temperature and the pressure, and P2 elements are used for the y velocity v_t and the x velocity u_t. An unstructured triangular mesh is utilized. $\mathcal{A}$ is the finite element matrix and $\mathbf{f}_l$ is a vector corresponding to the forcing at each degree of freedom of the FEM mesh. In this case, $\mathbf{f}_l$ corresponds to the plane wave imposed in the *background acoustics field.*

From the solution $\mathbf{x}_l$, we calculate the effective impedance on horizontal line 1 above the perforation (shown in figure 5.2), such that

$$\mathrm{Z} = -\frac{\int_{l_1} p_t(x)dx}{\int_{l_1} v_t(x)dx}, \tag{5.22}$$

where p_t is the pressure and v_t is the y velocity on this line. l_1 is the length of line 1. The integrals are calculated from the finite element solution

$$Z = -\frac{\mathcal{H}_p \mathbf{x}_l}{\mathcal{H}_v \mathbf{x}_l} \text{ with } \mathcal{H}_p \mathbf{x}_l = \int_{l_1} p_t(x)dx \text{ and } \mathcal{H}_v \mathbf{x}_l = \int_{l_1} v_t(x)dx, \tag{5.23}$$

where $\mathcal{H}_p$ and $\mathcal{H}_v$ are matrices containing the integrals of the shape functions of P1 and P2 elements respectively, over line 1.

5.3.2 Frequency response to a plane wave with and without flow

The frequency response is computed between 200 Hz and 5000 Hz. The resistance and the reactance obtained with and without flow are shown in figure 5.4.

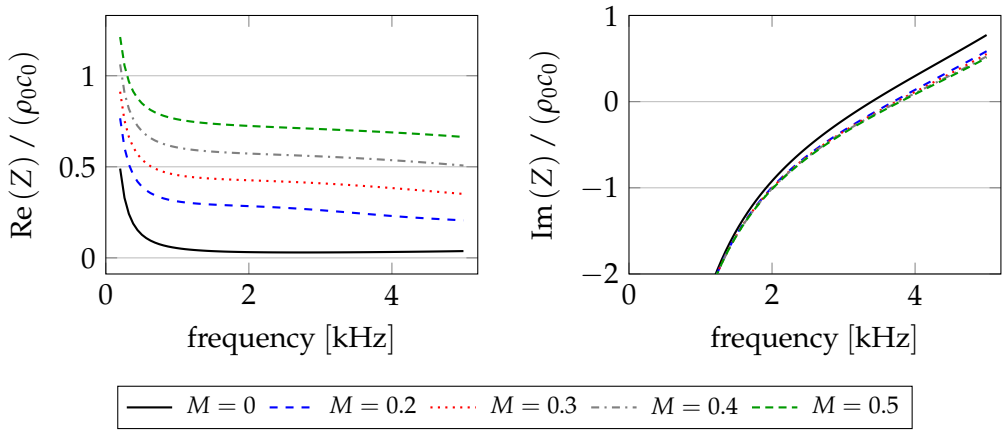

FIGURE 5.4: Normalized resistance (left) and normalized reactance (right) between 200 Hz and 5000 Hz.

As expected, the resistance increases with growing Mach number while the reactance decreases. On table 5.1, we give the frequency close to the resonance for which $\text{Im}(Z)/(\rho_0 c_0) \simeq 0$ for the different Mach numbers. We observe that the resonance frequency moves towards high frequencies when the Mach number increases. This trend is consistent with the end correction proposed in Groeneweg (1969).

Mach number	Approximate resonance frequency (Hz)
0	3393
0.2	3697
0.3	3739
0.4	3769
0.5	3794

TABLE 5.1: Approximate resonance frequency for each Mach number.

We also observe that the resistance is strong in the low frequency regime and stabilizes slowly above 1500 Hz. Its value, especially without flow, is very low due to the 2-dimensional nature of our problem. We now introduce the method used to compute the so-called "sensitivity" and the linear response to an optimal forcing.

5.4 Sensitivity and response computation with and without flow

5.4.1 Sensitivity

In the previous section, we have computed the acoustic response to a linear term (the incident plane wave) by solving the FEM linear system below

$$-\left(\mathcal{A}-\mathrm{j}\omega\mathcal{I}\right)\mathbf{x}_l=\mathbf{f}_l. \tag{5.24}$$

We now study the sensitivity of the impedance to changes in the solutions $\mathbf{x}_l$ or changes to the forcing $\mathbf{f}_l$. For this purpose, we follow the resolvent method outlined in section 5.2.

More specifically, the objective is to investigate the impact of a non-linear term $\mathbf{f}_{nl}$ on the impedance. During the linearization of the Navier-Stokes equations, the non-linear terms are removed. As this term is unknown and is not straightforward to compute, we choose to interpret this missing non-linear term as a forcing on the linearized equations. Hence, we focus on the response of the system to this non-linear forcing. Alternatively, perspectives are provided in section 5.8 to compute this non-linear term using an iterative procedure.

We want to identify the change in external forcing $\delta\mathbf{f}_{nl}$ that has the strongest influence on the impedance. We perform the following substitutions

$$\mathbf{f}_l\rightarrow\mathbf{f}_l+\delta\mathbf{f}_{nl},\ \mathbf{x}_l\rightarrow\mathbf{x}_l+\delta\mathbf{x}_{nl},\ \mathrm{Z}\rightarrow\mathrm{Z}+\delta\mathrm{Z}.$$

Although in standard resolvent analysis the non-linear forcing and response are not supposed to be small, here, the output operator extracting impedance is a non-linear operator. This is a non-standard situation. The associated tangent-linear operator is considered at $\mathbf{x}_l$, *i.e.* linearized over the linear response. We are thus looking at a sensitivity of the linear response to a small non-linearity. This assumption can be relaxed by an iterative procedure, as proposed in section 5.8, that requires to update the linearization point to $\mathbf{x}_l+\mathbf{x}_{nl}$.

From equation (5.24), it is easy to see that

$$\delta\mathbf{x}_{nl}=\mathcal{R}(\omega)\delta\mathbf{f}_{nl}\text{ with }\mathcal{R}\left(\omega\right)=-\left(\mathcal{A}-\mathrm{j}\omega\mathcal{I}\right)^{-1}, \tag{5.25}$$

where $\mathcal{R}\left(\omega\right)$ is the resolvent operator. For small changes $\delta\mathbf{x}_{nl}$, we can use a Taylor expansion in equation (5.23) to write

$$\delta\mathrm{Z}=\mathcal{H}_Z\delta\mathbf{x}_{nl}\text{ with }\mathcal{H}_Z=\frac{\mathcal{H}_p\mathbf{x_l}}{\left(\mathcal{H}_v\mathbf{x}_l\right)^2}\mathcal{H}_v-\frac{\mathcal{H}_p}{\mathcal{H}_v\mathbf{x}_l}, \tag{5.26}$$

where $\mathcal{H}_Z$ is a row vector relating changes in the impedance and the solution.

Combining the last two results from equations (5.25) and (5.26), we get

$$\delta Z=\mathbf{s}^{\mathrm{H}}\delta\mathbf{f}_{nl}\text{ with }\mathbf{s}=\mathcal{R}(\omega)^{\mathrm{H}}\mathcal{H}_Z. \tag{5.27}$$

In other words, $\mathbf{s}$ can be calculated by solving the following linear system

$$-\left(\mathcal{A}-\mathrm{j}\omega\mathcal{I}\right)^{\mathrm{H}}\mathbf{s}=\mathcal{H}_{\mathrm{Z}}^{\mathrm{H}}. \tag{5.28}$$

The vector $\mathbf{s}$ is the sensitivity of the impedance to a perturbation $\delta\mathbf{f}_{nl}$ of the forcing vector $\mathbf{f}_l$. Obviously, the non-linearity $\delta\mathbf{f}_{nl}$ is not "external" and depends on the solution, and more precisely is a result of a convolution integral over all frequencies. This is further detailed in Appendix E in which a triadic interaction is introduced. Due to the complexity, for the moment, $\delta\mathbf{f}_{nl}$ is unknown, and we study how the linearised system responds to non-linearities. Although we cannot define a "realistic" non-linear source, an optimal non-linear forcing, *i.e.* a source which impacts the most

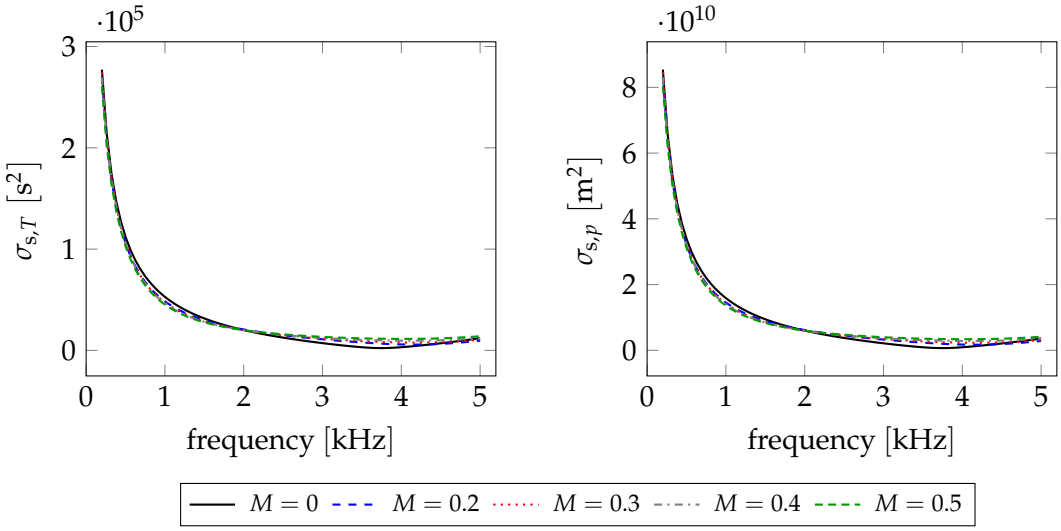

FIGURE 5.5: Temperature (left) and pressure (right) sensitivity gains.

the impedance, can be determined through the analysis of the sensitivity. This is performed in section 5.4.2.

From $\mathbf{s}$, we extract the sensitivity fields corresponding to the temperature $\mathbf{s}_T$, the pressure $\mathbf{s}_p$, the tangential velocity $\mathbf{s}_u$, and the normal velocity $\mathbf{s}_v$ with

$$\mathbf{s}_T = \mathcal{B}_T \mathbf{s}, \quad \mathbf{s}_p = \mathcal{B}_p \mathbf{s}, \quad \mathbf{s}_u = \mathcal{B}_u \mathbf{s}, \quad \mathbf{s}_v = \mathcal{B}_v \mathbf{s},$$

where $\mathcal{B}_T$, $\mathcal{B}_p$, $\mathcal{B}_u$, and $\mathcal{B}_v$ are rectangular matrices selecting the degrees of freedom associated to respectively, the temperature, the pressure, the tangential (to the plate) velocity, and the normal (to the plate) velocity. It can be noted that, since the output space is scalar, the restrictions of the sensitivity to a given component is still optimal regarding the transfer function defined by equation (5.26). This is not true when multiple outputs and a SVD computation are considered.

The sensitivity field can be seen as an operator relating a source variation and an impedance variation. The unit of this field is different for each variable. The unit of the source terms is determined according to the energy conservation equation (5.17) for the heat source (unit: $\mathrm{kg} \cdot \mathrm{m}^{-1} \cdot \mathrm{s}^{-3}$), acting on the temperature. The mass conservation equation (5.14) for the mass source (unit: $\mathrm{kg} \cdot \mathrm{m}^{-3} \cdot \mathrm{s}^{-1}$), acting on the pressure. The moment conservation equation (5.15) for the force source (unit: $\mathrm{kg} \cdot \mathrm{m}^{-2} \cdot \mathrm{s}^{-2}$), acting on the tangential and normal velocity. The impedance is expressed in $\mathrm{kg} \cdot \mathrm{m}^{-2} \cdot \mathrm{s}^{-1}$, hence, the unit of the temperature sensitivity is $\mathrm{m}^{-1} \cdot \mathrm{s}^2$, the pressure sensitivity is in m, and the tangential and normal velocity sensitivities are in s.

The individual sensitivity fields are normalized by their L2-norms, which can be seen as amplification gains, defined as

$$\sigma_{\mathrm{s},T} = \sqrt{\mathbf{s}_T^{\mathrm{H}} \mathcal{M}_{\mathrm{P1}} \mathbf{s}_T} \text{ in } \mathrm{s}^2, \quad \sigma_{\mathrm{s},p} = \sqrt{\mathbf{s}_p^{\mathrm{H}} \mathcal{M}_{\mathrm{P1}} \mathbf{s}_p} \text{ in } \mathrm{m}^2, \quad \sigma_{\mathrm{s},u} = \sqrt{\mathbf{s}_u^{\mathrm{H}} \mathcal{M}_{\mathrm{P2}} \mathbf{s}_u} \text{ in } \mathrm{m} \cdot \mathrm{s},$$
$$\text{and } \sigma_{\mathrm{s},v} = \sqrt{\mathbf{s}_v^{\mathrm{H}} \mathcal{M}_{\mathrm{P2}} \mathbf{s}_v} \text{ in } \mathrm{m} \cdot \mathrm{s},$$

where $\mathcal{M}_{\mathrm{P1}}$ and $\mathcal{M}_{\mathrm{P2}}$ are the mass matrices associated to P1 and P2 elements on the computational domain.

In figures 5.5 and 5.6, we plot the sensitivity amplification gain for each variable for different Mach numbers.

The temperature and pressure sensitivity gains appear to be stronger in the low frequency and to rapidly decrease when the frequency increases. The impact of the Mach number on both these

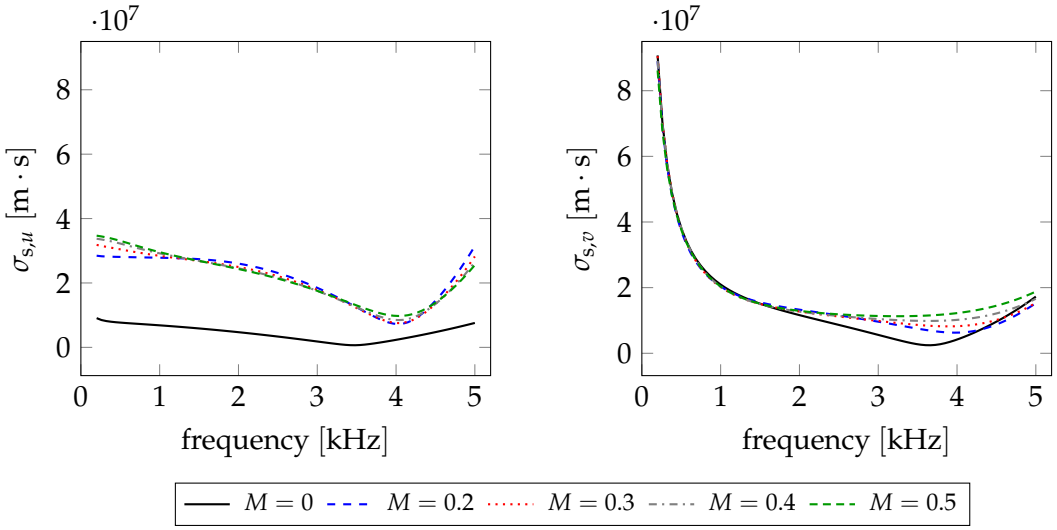

FIGURE 5.6: Tangential (left) and normal velocity (right) sensitivity gains.

quantities is small. However, between 2000 Hz and 5000 Hz the sensitivity is slightly increased by increasing the Mach number.

Without flow, the tangential velocity gain is lower than the normal velocity sensitivity gain. When flow is added, the amplitude of $\sigma_{s,u}$ is clearly intensified, suggesting a drastic change of physical mechanism.

The amplitude of $\sigma_{s,v}$ and $\sigma_{s,u}$ are of the same order of magnitude close to 4 kHz, that is close to the resonance frequency. Furthermore, the tangential velocity sensitivity gain appears to be minimal close to the resonance frequency with and without flow. Without flow, this minimum is reached at 3481 Hz. With flow it is 4028 Hz and it does not change with the Mach number. This is consitent with the resonance frequency shift observed when computing the frequency response to a plane wave in section 5.3.2.

5.4.2 Response to a non-linear optimal forcing

The impedance variation δZ is the largest when $\mathbf{s}$ and $\delta \mathbf{f}_{nl}$ are colinear, based on equation (5.27). Therefore the optimal forcing to change the impedance is given by $\mathbf{s}$. In the following, TF $[\cdot]$ denotes the Fourier transform.

This optimal forcing can be interpreted as the contribution of the non-linear terms that were initially ignored in the governing equations. The non-linear terms dropped when writing the LNSE are

- TF $[\nabla \cdot (\rho_t \mathbf{u}_t)]$ in the mass conservation equation,
- TF $[\mathbf{u}_t \cdot \nabla \mathbf{u}_t]$ in the momentum equation,
- TF $[\mathbf{u}_t \cdot \nabla \boldsymbol{p}_t]$ and TF $[\mathbf{u}_t \cdot \nabla \boldsymbol{T}_t]$ in the energy conservation equation.

Here we focus on the term TF $[\mathbf{u}_t \cdot \nabla \mathbf{u}_t]$ in the momentum equation which is responsible for coupling the acoustic and vorticity fields. This term acts as a force on the acoustic field. For this reason we retain only the force terms from the optimal forcing (*i.e.* the source for the momentum equation in $\mathbf{s}$). We thus define the so-called optimal non-linear forcing

$$\mathbf{f}_{nl}^{\text{opt}} = \mathcal{B}_{\mathbf{u}} \mathbf{s}, \tag{5.29}$$

where $\mathcal{B}_{\mathbf{u}}$ is a rectangular matrix selecting the degrees of freedom corresponding to the tangential and normal velocity associated to the momentum conservation equation (5.15). In doing so, we

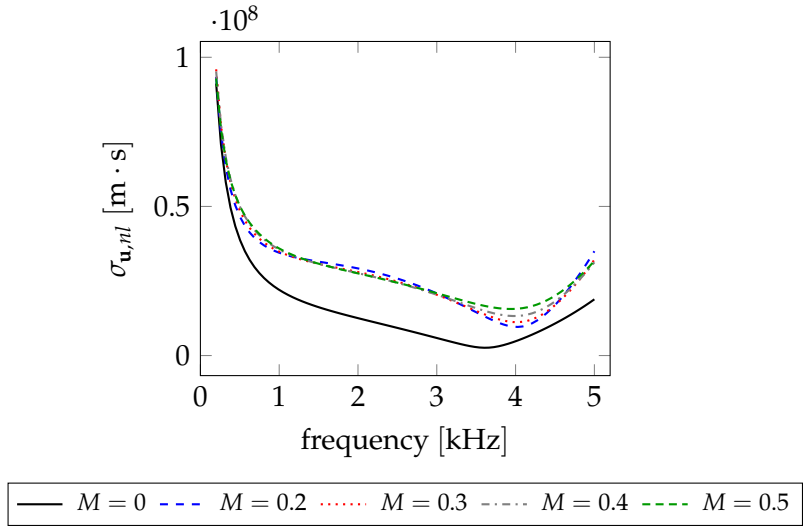

FIGURE 5.7: Amplification rates corresponding to the non-linear optimal forcing, the tangential and normal velocities sensitivities.

have identified the most effective non-linearity, without having to explicitly compute the interactions over frequencies. This of course does not give insight if this non-linearity is present in the flow. To become predictive, the projection of TF $[\mathbf{u}_t \cdot \nabla \mathbf{u}_t]$ onto the optimal forcing would lead to the amplitude of the non-linear response.

In order to better characterize the forcing, post-processing of a numerical temporal database would be helpful to define $\mathcal{B}_\mathbf{u}$, for instance by defining its columns based on Proper Orthogonal Decomposition (POD) or spectral POD modes (Towne *et al.*, 2018). In any case, the amplitude is not determined since only the response gains are available. For a proper scaling, iterative strategies as in Symon *et al.* (2019) for instance, could be considered.

The amplification gain $\sigma_{\mathbf{u},nl}$ of the non linear optimal forcing reads

$$\sigma_{\mathbf{u},nl} = \sqrt{\left(\mathbf{f}_{nl}^{\text{opt}}\right)^{\text{H}} \mathcal{W}_{\text{P2}} \mathbf{f}_{nl}^{\text{opt}}} \text{ in m} \cdot \text{s}, \tag{5.30}$$

where

$$\mathcal{W}_{\text{P2}} = \begin{pmatrix} \mathcal{M}_{\text{P2}} & 0 \\ 0 & \mathcal{M}_{\text{P2}} \end{pmatrix}. \tag{5.31}$$

Note that the amplification gain of the non-linear forcing can be calculated with $\sigma_{\mathbf{u},nl} = \sqrt{\sigma_{\text{s},u}^2 + \sigma_{\text{s},v}^2}$. In figure 5.7, we plot the gain of the non-linear forcing as a function of the frequency.

The gain of the non-linear forcing is stronger with flow than without flow. This is due to the contribution of the tangential velocity, which becomes significant when a flow is added.

Now, we normalize the non-linear forcing by its L2-norm such that

$$\tilde{\mathbf{f}}_{nl}^{\text{opt}} = \frac{\mathbf{f}_{nl}^{\text{opt}}}{\sigma_{\mathbf{u},nl}} \text{ in m}^{-1}. \tag{5.32}$$

The linear response $\mathbf{x}_{nl} = (\boldsymbol{T}_\text{r}, \boldsymbol{p}_\text{r}, \boldsymbol{u}_\text{r}, \boldsymbol{v}_\text{r})^\text{T}$ to the normalized optimal non-linear forcing is computed by solving

$$-\left(\mathcal{A} - \text{j}\omega\mathcal{I}\right)\mathbf{x}_{nl} = \tilde{\mathbf{f}}_{nl}^{\text{opt}}. \tag{5.33}$$

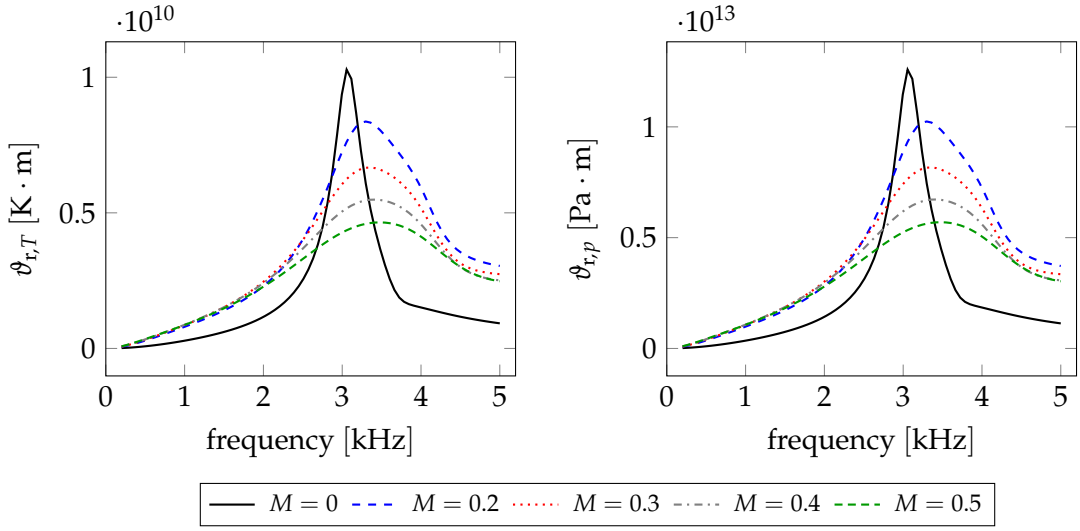

FIGURE 5.8: Temperature (left) and pressure (right) response gains.

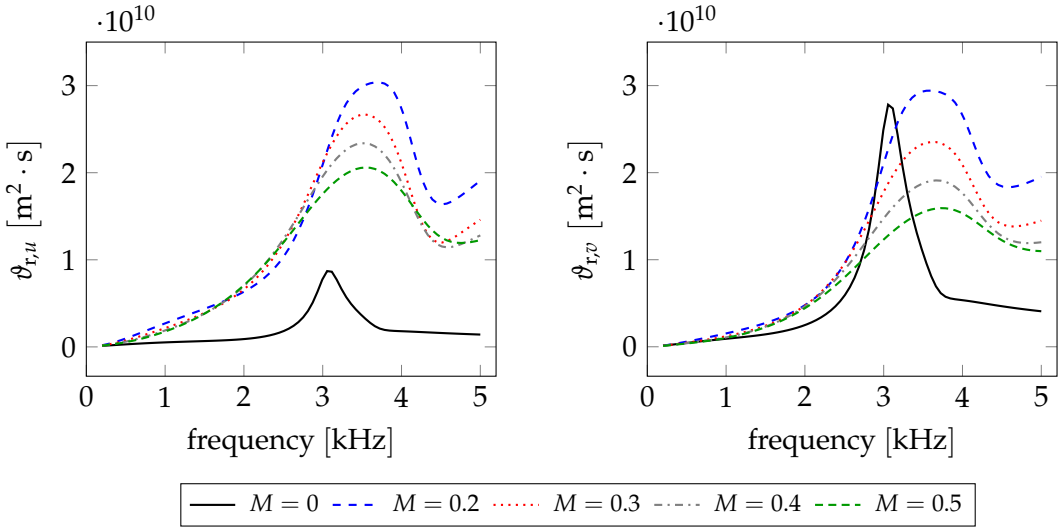

FIGURE 5.9: Tangential (left) and normal velocity (right) to the plate response gains.

From $\mathbf{x}_{nl}$ we extract the response fields corresponding to the temperature $\boldsymbol{T}_\mathrm{r}$, the pressure $\boldsymbol{p}_\mathrm{r}$, the tangential velocity $\boldsymbol{u}_\mathrm{r}$, and the normal velocity $\boldsymbol{v}_\mathrm{r}$ with

$$\boldsymbol{T}_\mathrm{r} = \mathcal{B}_T \mathbf{x}_{nl}, \quad \boldsymbol{p}_\mathrm{r} = \mathcal{B}_p \mathbf{x}_{nl}, \quad \boldsymbol{u}_\mathrm{r} = \mathcal{B}_u \mathbf{x}_{nl}, \quad \boldsymbol{v}_\mathrm{r} = \mathcal{B}_v \mathbf{x}_{nl}.$$

The latter fields are normalized by their respective L2-norm defined as

$$\vartheta_{\mathrm{r},T} = \sqrt{\boldsymbol{T}_\mathrm{r}^\mathrm{H} \mathcal{M}_{\mathrm{P1}} \boldsymbol{T}_\mathrm{r}} \text{ in } \mathrm{K \cdot m}, \quad \vartheta_{\mathrm{r},p} = \sqrt{\boldsymbol{p}_\mathrm{r}^\mathrm{H} \mathcal{M}_{\mathrm{P1}} \boldsymbol{p}_\mathrm{r}} \text{ in } \mathrm{Pa \cdot m},$$
$$\vartheta_{\mathrm{r},u} = \sqrt{\boldsymbol{u}_\mathrm{r}^\mathrm{H} \mathcal{M}_{\mathrm{P2}} \boldsymbol{u}_\mathrm{r}} \text{ in } \mathrm{m^2 \cdot s}, \quad \text{and } \vartheta_{\mathrm{r},v} = \sqrt{\boldsymbol{v}_\mathrm{r}^\mathrm{H} \mathcal{M}_{\mathrm{P2}} \boldsymbol{v}_\mathrm{r}} \text{ in } \mathrm{m^2 \cdot s}.$$

In figure 5.8 the amplification gains of the response are plotted for the temperature and the pressure. In figure 5.9, the response gains are plotted for the tangential and the normal velocities.

Temperature and pressure responses appear to have a similar behavior. Without flow, a peak can be observed at 3000 Hz. When adding flow, the peak is smoothed and decreases with increasing Mach number.

The tangential velocity response gain increases significantly when a flow is present. On the other hand, the normal velocity response gain remains of the same order of magnitude when $M = 0.2$. For the 4 variables, the response gain decreases when the Mach number increases, suggesting that the impedance is less responsive to a non-linear perturbation when the grazing flow is strong. For the moment, the ambiguity is not raised if this stabilizing effect is due to a stronger velocity or compressibility effects.

5.5 Case study without flow

In this section, we focus on the neck region of the finite element domain. This region is where most of the physical phenomenon impacting the impedance occurs. The fields corresponding to the response to a plane wave are discussed, as well as the sensitivity and the response to a non-linear optimal forcing. A frequency of 3500 Hz is kept throughout this study. According to the response gains presented in section 5.4.2, we expect to have important non-linear effects at this frequency in the presence of a grazing flow. In order to remain consistent in our analysis, we also choose 3500 Hz for the case without flow.

The sensitivity fields are normalized by their L2-norms as follows

$$\tilde{\mathbf{s}}_T = \frac{\mathbf{s}_T}{\sigma_{\mathrm{s},T}}, \quad \tilde{\mathbf{s}}_p = \frac{\mathbf{s}_p}{\sigma_{\mathrm{s},p}}, \quad \tilde{\mathbf{s}}_u = \frac{\mathbf{s}_u}{\sigma_{\mathrm{s},u}}, \quad \tilde{\mathbf{s}}_v = \frac{\mathbf{s}_v}{\sigma_{\mathrm{s},v}},$$

and are now expressed in m^{-1}.

The response fields, that are shown after the sensitivity fields, are normalized by their L2-norms as well, such that

$$\tilde{\boldsymbol{T}}_{\mathrm{r}} = \frac{\boldsymbol{T}_{\mathrm{r}}}{\vartheta_{\mathrm{r},T}}, \quad \tilde{\boldsymbol{p}}_{\mathrm{r}} = \frac{\boldsymbol{p}_{\mathrm{r}}}{\vartheta_{\mathrm{r},p}}, \quad \tilde{\boldsymbol{u}}_{\mathrm{r}} = \frac{\boldsymbol{u}_{\mathrm{r}}}{\vartheta_{\mathrm{r},u}}, \quad \tilde{\boldsymbol{v}}_{\mathrm{r}} = \frac{\boldsymbol{v}_{\mathrm{r}}}{\vartheta_{\mathrm{r},v}},$$

and expressed in m^{-1}.

Iso-contour plotted with solid lines correspond to the positive values and iso-contour with dashed lines are plotted for negative values.

In figure 5.10, the real part, the imaginary part, and the absolute value of the three types of temperature fields are shown. To illustrate how to interpret these results, we start with the real part of sensitivity field $\mathrm{Re}(\tilde{\mathbf{s}}_T)$. In figure 5.10(b), the resistance would be significantly impacted by a heat source positioned inside the cavity. When looking at the imaginary part of the sensitivity $\mathrm{Im}(\tilde{\mathbf{s}}_T)$, it appears that the reactance is sensitive to a heat source located in the thermal boundary layer inside the cavity. It can be noted that for both the real and the imaginary parts, the sensitivity is zero on the boundary of the finite element domain at the edge of the thermal boundary layer, which is consistent with the implemented iso-thermal boundary condition.

On the sensitivity imaginary part, we can observe a clear contrast between the neck and the exterior domain. Indeed, above the plate, a heat source would increase the reactance. On the opposite, a heat source in the cavity or the neck would decrease the reactance. We also note that the amplitudes of the real and imaginary parts of $\tilde{\mathbf{s}}_T$ and $\tilde{\boldsymbol{T}}_{\mathrm{r}}$ are very close one to another.

We now compare the response to a non-linear forcing $\tilde{\boldsymbol{T}}_{\mathrm{r}}$ to the response to a plane wave $\boldsymbol{T}_t$. The phase between the two responses is different and appears to be inverted when looking at the imaginary parts. Globally, the absolute value of $\tilde{\boldsymbol{T}}_{\mathrm{r}}$ translates a similar response to the plane wave response. The main difference is that the response in the neck is more homogeneous when considering a non-linear forcing rather than the plane wave forcing.

The pressure fields are presented in figure 5.11. It appears that the pressure fields are very similar to the temperature fields. Furthermore, the amplitudes of $|\tilde{\mathbf{s}}_T|$, $|\tilde{\mathbf{s}}_p|$, $|\tilde{\boldsymbol{T}}_{\mathrm{r}}|$ and $|\tilde{\boldsymbol{p}}_{\mathrm{r}}|$ are close.

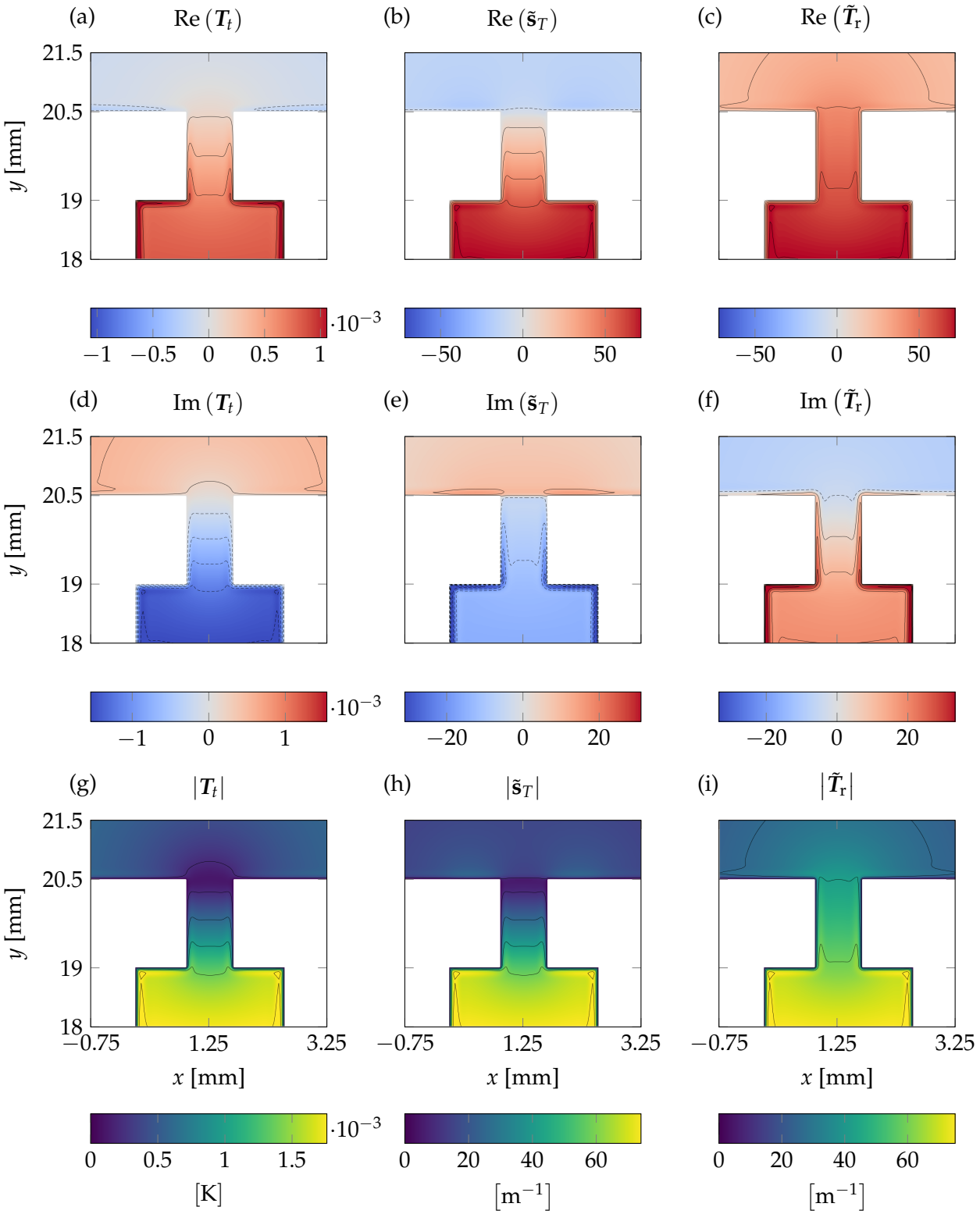

FIGURE 5.10: (a), (b), (c) are respectively, the real parts of the temperature response to a plane wave, the sensitivity to a heat source, and the temperature response to an optimal non-linear forcing. (d), (e), (f): Imaginary parts. (g), (h), (i): Absolute values.

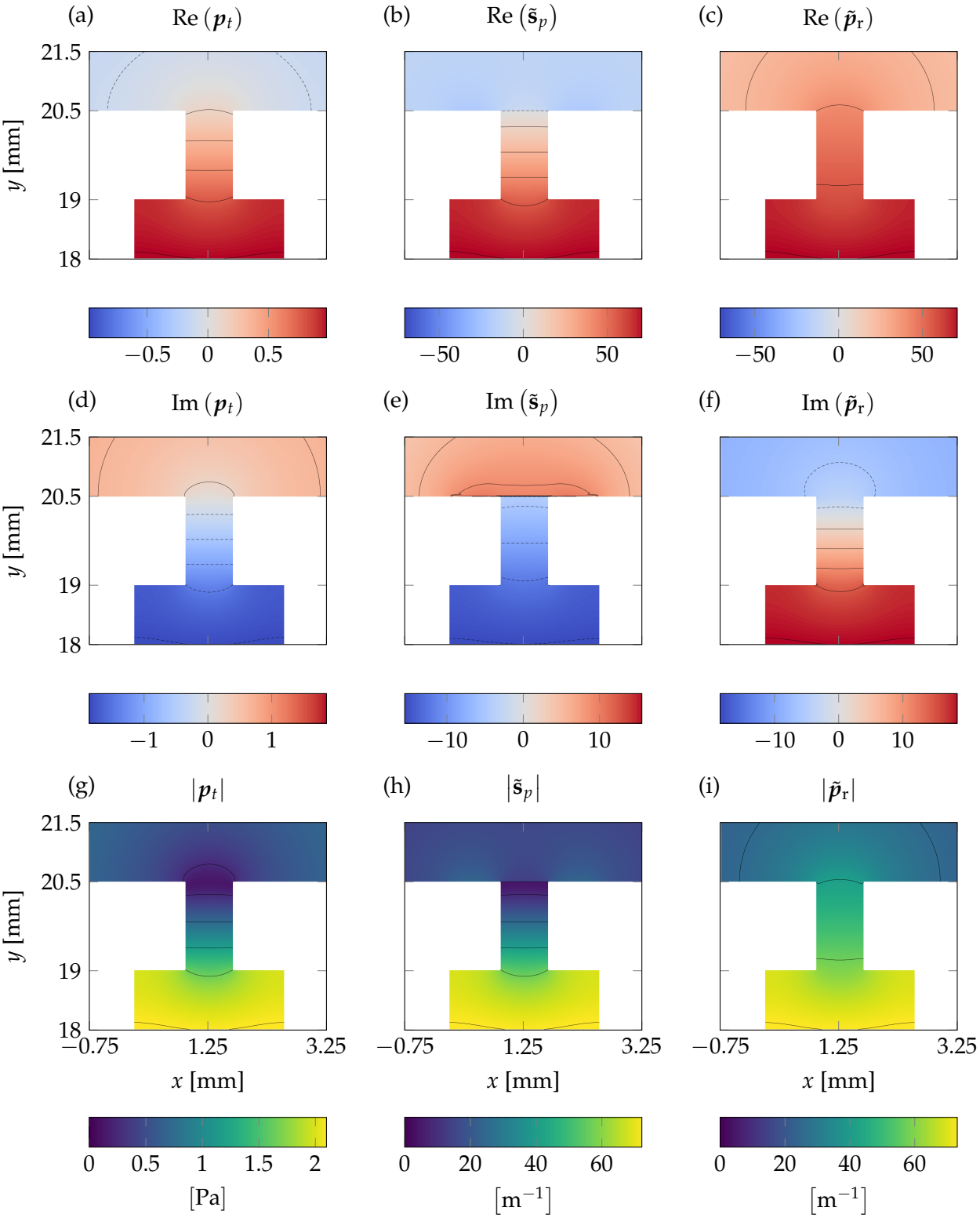

FIGURE 5.11: (a), (b), (c) are respectively, the real parts of the pressure response to a plane wave, the sensitivity to a mass source, and the pressure response to an optimal non-linear forcing. (d), (e), (f): Imaginary parts. (g), (h), (i): Absolute values.

The tangential velocity sensitivity fields shown in figure 5.12 highlight that the impedance is very sensitive to a force applied at the corners of the perforation. Another sensitive location is the edges of line 1. Consistently with the rigid wall boundary condition, the sensitivity is zero on the wall of the neck and the wall of the plate.

The main difference between $\boldsymbol{u}_t$ and $\tilde{\boldsymbol{u}}_\mathrm{r}$ is noticed on the phase of the fields. The imaginary parts seem to have the same sign, and the real parts signs seem to be opposed, which suggests a phase quadrature between the response to plane wave and the response to a non-linear forcing. This may be explained on the basis of the momentum conservation equation (2.4). In the frequency domain, the unsteady term $\mathrm{j}\omega\hat{\mathbf{u}}$ where $\mathbf{u} = \hat{\mathbf{u}}\mathrm{e}^{\mathrm{j}\omega t}$, can be compared with $\mathrm{TF}\left[(\mathbf{u}\cdot\nabla)\mathbf{u}\right]$. In the linear regime, the term $\mathrm{j}\omega\hat{\mathbf{u}}$ is dominating, as opposed to the non-linear regime where $\mathrm{TF}\left[(\mathbf{u}\cdot\nabla)\mathbf{u}\right]$ is dominating. This would be consistent with the work from Ingard (1953) in the non-linear regime. More importantly, the $\mathrm{j}\omega$ term could explain the appearance of a phase quadrature between the responses to a linear and non-linear sources.

More details on the non-linear term $\mathrm{TF}\left[(\mathbf{u}\cdot\nabla)\mathbf{u}\right]$ can be found in appendix E, in which the role of triadic interactions is developed for the momentum conservation equation.

Both responses are similar when looking at their absolute values, besides the fact that the two responses do not have the same phase when looking at their real and imaginary parts. This means that the first resolvent mode may be sufficient to describe the physical mechanisms in the non-linear regime. Indeed, if the shapes had been different, several resolvent modes would have been necessary to represent the response to a plane wave, thus rejecting the hypothesis of dominance of the first mode in terms of singular values. However, this can not be directly verified with the current sensitivity analysis as it accounts for the first resolvent mode only.

Regarding the normal velocity sensitivity in figure 5.13, it appears that the resistance would decrease if a force was located in the viscous boundary layer inside the neck and especially on the corners of the aperture. On the opposite, it would increase if a force was applied at the surface of the plate on line 1. The reactance is sensitive to a force located in the whole neck and on line 1 as well.

Similarly, as for the tangential velocity, the imaginary parts of $\boldsymbol{v}_t$ and $\tilde{\boldsymbol{v}}_\mathrm{r}$ are similar and have the same sign. On the other hand, their real parts seem to be of opposite signs. Here again, this may be the consequence of a phase quadrature and the same explanation as previously may be given.

It is worth noting that, according to figures 5.13 (h) and (i), the sensitivity and the response to a non linear term are homogeneous and strong in the neck, which is consistent with the non-linear correction proposed in Ingard *et al.* (1967). Indeed, Ingard et al. consider that the effective velocity impacting the impedance is the normal velocity in the neck.

We further highlight the difference between the velocity fields obtain with a non-linear forcing and a plane wave forcing by computing the vorticity in each case. The vorticity computed from the normalized tangential and normal velocity obtained with a non-linear source is

$$\tilde{\omega}_r = \nabla \times \begin{pmatrix} \tilde{\boldsymbol{u}}_r \\ \tilde{\boldsymbol{v}}_r \end{pmatrix} \text{ in } \mathrm{m}^{-2}. \tag{5.34}$$

The voriticity computed from the tangential and normal velocity computed with a plane wave source is

$$\omega_t = \nabla \times \begin{pmatrix} \boldsymbol{u}_t \\ \boldsymbol{v}_t \end{pmatrix} \text{ in } \mathrm{s}^{-1}. \tag{5.35}$$

The real and imaginary parts of the corresponding fields are plotted below, in figure 5.14. The vorticity obtained with the optimal forcing seems to show vortex emerging at the corners of the perforation, which would be consistent with the response of perforated liner submitted to a high

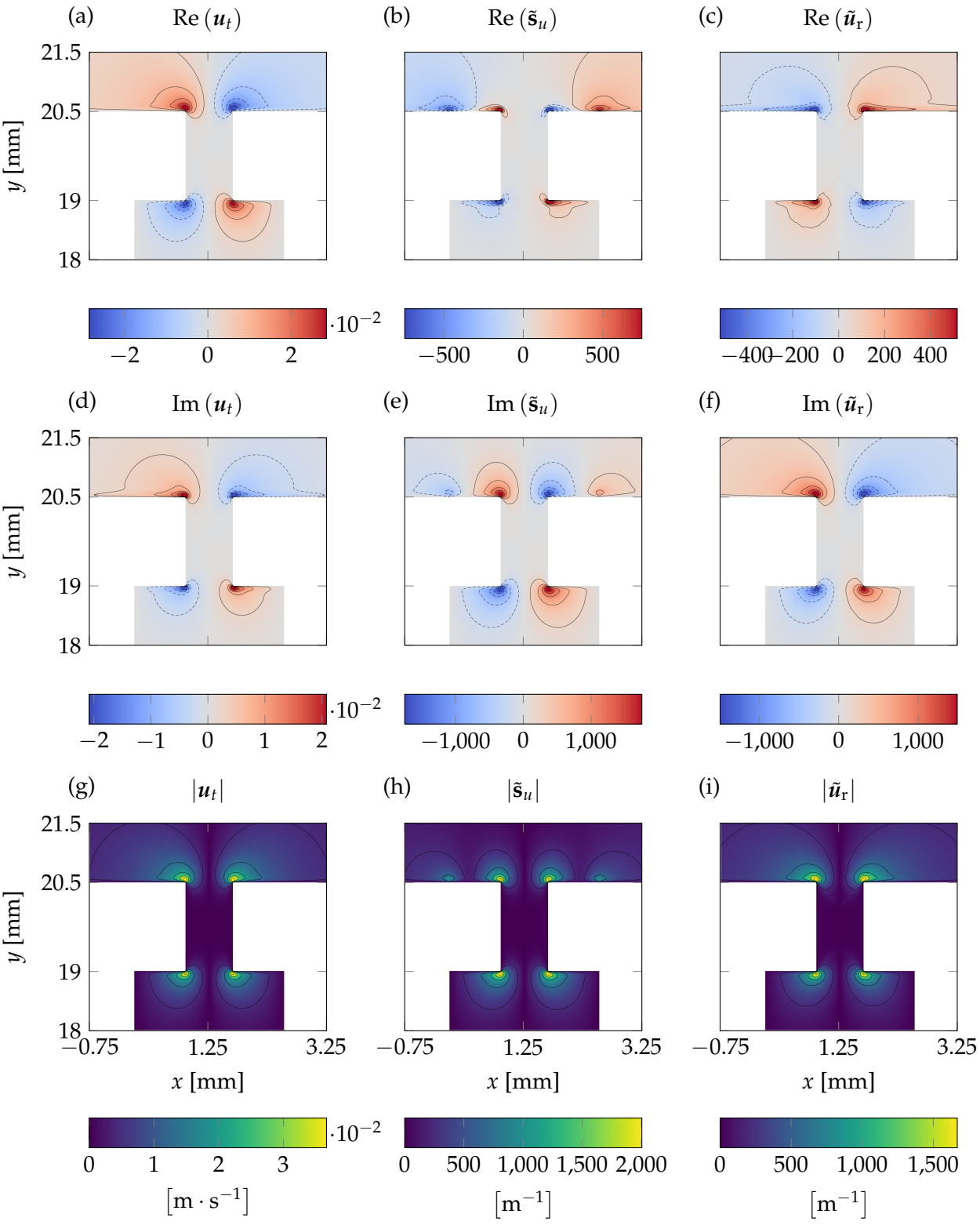

FIGURE 5.12: (a), (b), (c) are respectively, the real parts of the tangential velocity response to a plane wave, the sensitivity to a force and the tangential velocity response to an optimal non-linear forcing. (d), (e), (f): Imaginary parts. (g), (h), (i): Absolute values.

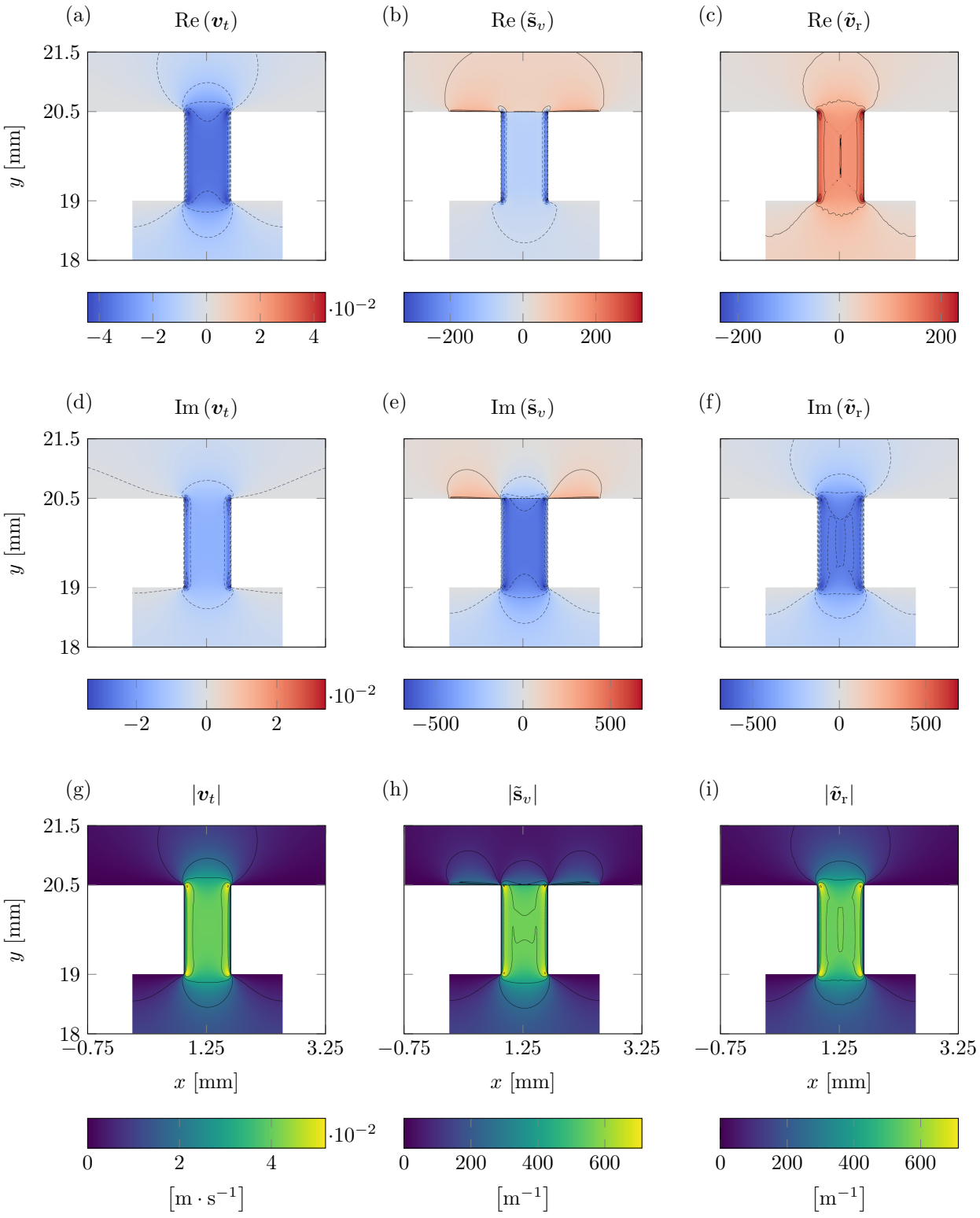

FIGURE 5.13: (a), (b), (c) are respectively, the real parts of the normal velocity response to a plane wave, the sensitivity to a force, and the normal velocity response to an optimal non-linear forcing. (d), (e), (f): Imaginary parts. (g), (h), (i): Absolute values.

sound pressure level. Such effects are highlighted numerically with direct numerical simulations (DNS) by Roche (2011) for various sound pressure levels. Tam *et al.* (2001) also computed the density field from the compressible Navier-Stokes equations and showed the shedding of vortices near the mouth of a slit resonator. In a similar manner, Zhang *et al.* (2012) solved numerically the same set of equations for a cavity backed with a circular orifice under various sound pressure levels and displayed the vorticity emerging at the corners of the orifice.

In order to gain more insights on the viscous dissipation difference between the response to a plane wave and the response to a non-linear term, we now focus our interest on the rate of viscous dissipation per unit mass due to shear effects. When considering the plane wave response, in the time domain, it is defined as (Batchelor, 1967)

$$\Phi_{\text{shear}} = \mu \left[\nabla \mathbf{u}_t + (\nabla \mathbf{u}_t)^{\mathrm{T}} - \frac{2}{3} \nabla \cdot \mathbf{u}_t \mathcal{I} \right] : \frac{1}{2} \left[\nabla \mathbf{u}_t + (\nabla \mathbf{u}_t)^{\mathrm{T}} \right] \text{ in Pa} \cdot \text{s}. \tag{5.36}$$

When considering the response to a non-linear source, the normalized velocity $\tilde{\mathbf{u}}_{\text{r}}$ is used and we get

$$\tilde{\Phi}_{\text{shear}} = \mu \left[\nabla \tilde{\mathbf{u}}_{\text{r}} + (\nabla \tilde{\mathbf{u}}_{\text{r}})^{\mathrm{T}} - \frac{2}{3} \nabla \cdot \tilde{\mathbf{u}}_{\text{r}} \mathcal{I} \right] : \frac{1}{2} \left[\nabla \tilde{\mathbf{u}}_{\text{r}} + (\nabla \tilde{\mathbf{u}}_{\text{r}})^{\mathrm{T}} \right] \text{ in Pa} \cdot \text{s}^{-5} \cdot \text{m}^{-4}. \tag{5.37}$$

The rate of dissipation due to bulk effects was found to be negligible in comparison to the dissipation due to shear effects. Hence, it is not discussed further in the following. In figure 5.15, the mean values $\tilde{\Phi}_{\text{shear}}$ and Φ_{shear} are shown in the frequency domain. Regarding the plane wave response, the dissipation is located in the viscous boundary layers inside the neck and at the corners of the perforations, a detailed analysis of this distribution is available in chapter 2. When considering the response to a non-linear forcing, the dissipation distribution is significantly different. It is mainly located at the corners and extends along the plate. The viscous boundary layer in the neck is now a secondary zone.

Without flow, figures 5.10 to 5.13 show results consistent with the behavior of a Helmholtz resonator. For instance, the impedance is very sensitive to a heat source located in the cavity. If the latter source is situated above the perforation, it has only a small impact on the impedance. The corners of the aperture and the viscous boundary layers in the neck can also be considered has sensitive zones when looking at the velocity sensitivity fields. The vorticity (figure 5.14) appears to highlight vortex shedding when a non-linear source is used. There again, this physical mechanism is well-known for Helmholtz resonators (Roche, 2011). Regarding the viscous dissipation (figure 5.15), an important fact highlighted by figure 5.15 is that the dissipation due to shear effects is mainly localized at the corners of the perforation when considering a non-linear source. We recall that, when using a plane wave as a source, the dissipation is distributed mostly in the viscous boundary layer inside the neck and the corners of the aperture. The resemblance of the two response fields indicates that the first resolvent mode is likely to be dominating. This is encouraging in terms of model reduction perspectives. Nevertheless, this assumption needs to validated by computing a full resolvent analysis for instance, requiring efficient numerical algorithms (Moarref *et al.* (2013); Brynjell-Rahkola *et al.* (2017); Martini *et al.* (2020b); Ribeiro *et al.* (2020)).

5.6 Case study with flow

In this section, the same graphs as in section 5.5 are shown with the presence of a grazing flow with a Mach number of 0.3 in the homogeneous part of the flow. As in section 5.5, we focus on

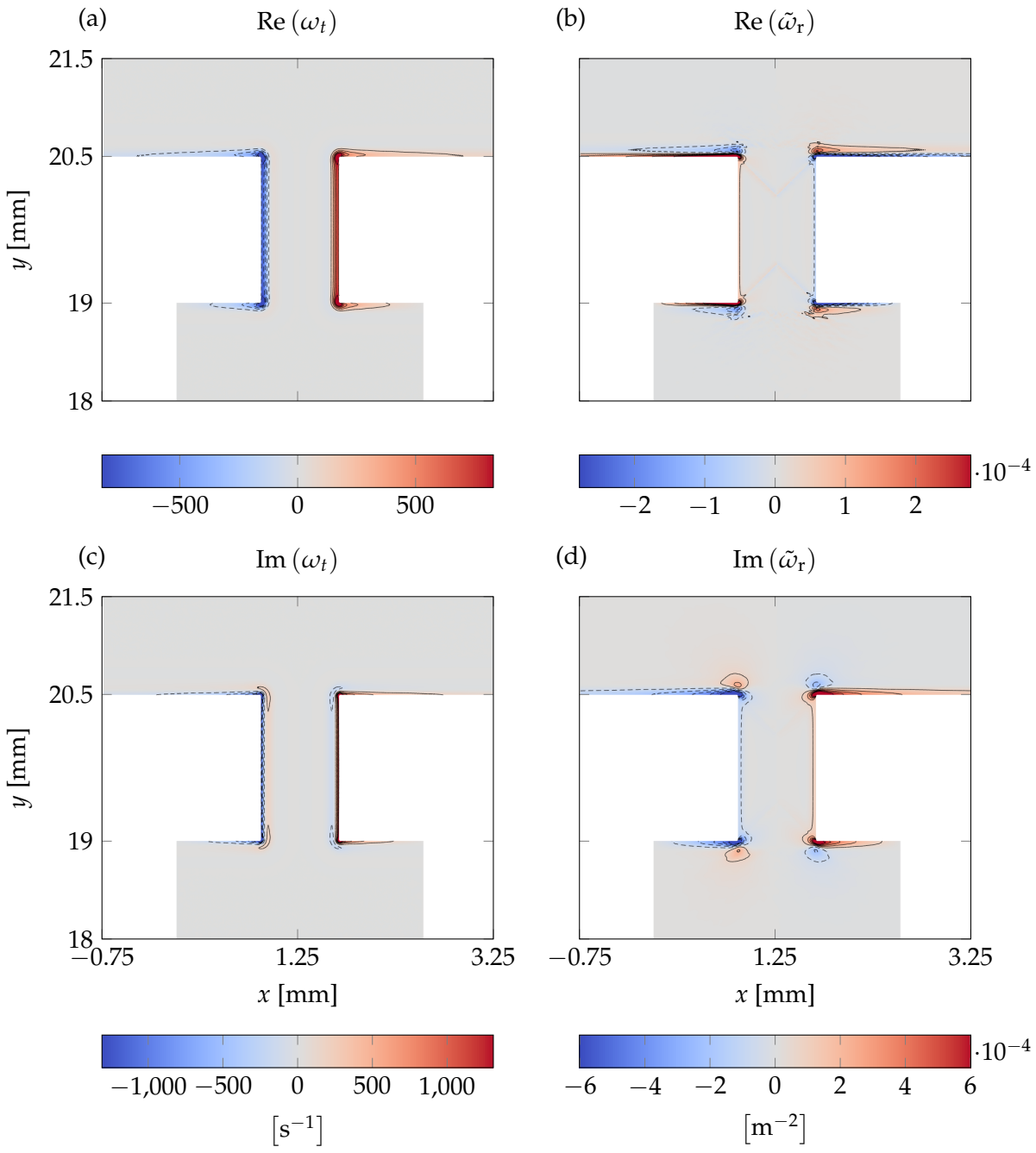

FIGURE 5.14: (a), (b): Real parts of the vorticity field for respectively the response to the plane wave, and the response to the non-linear forcing. (c), (d): Imaginary parts.

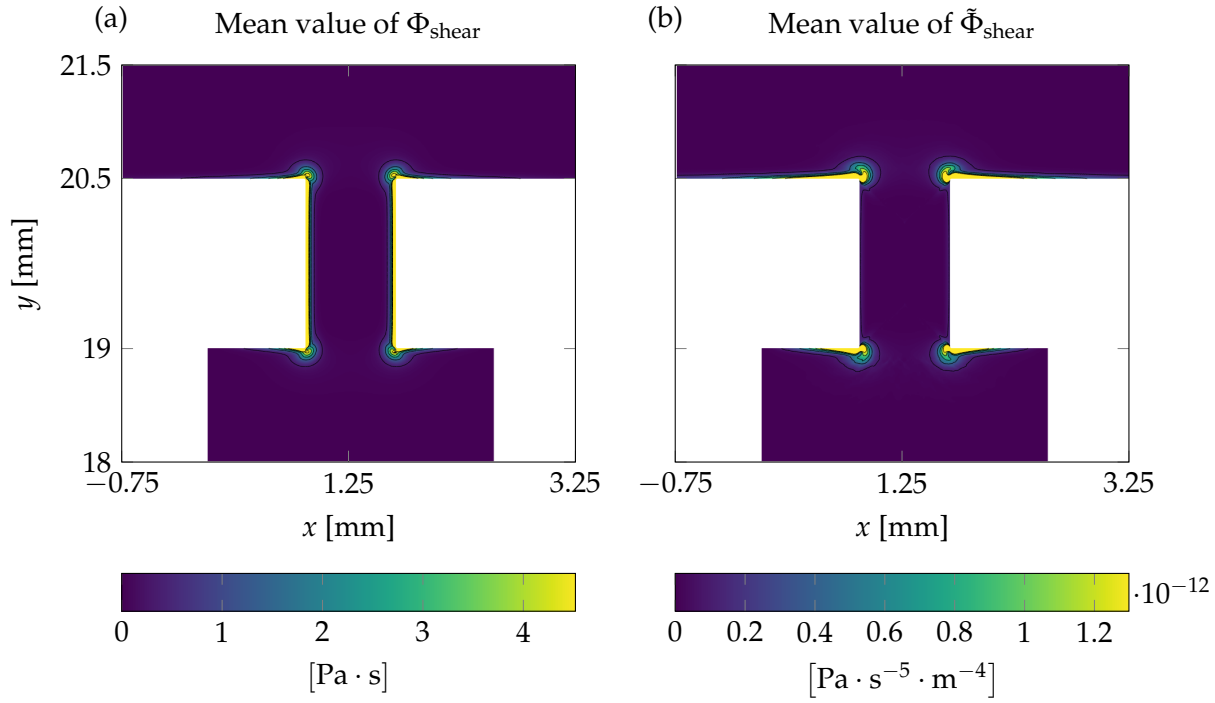

FIGURE 5.15: (a), (b): Mean values of the shear dissipation for respectively the response to the plane wave and the response to the non-linear forcing.

the frequency 3500 Hz, for which we expect to have non-linear effects with important amplitudes according to the response gains in section 5.4.2.

In figure 5.16, the real part, the imaginary part, and the absolute values of the fields corresponding to the plane wave response $\boldsymbol{T}_t$, the sensitivity $\tilde{\mathbf{s}}_T$, and the response to a non-linear forcing $\tilde{\boldsymbol{T}}_\text{r}$ are shown. According to $\text{Re}(\tilde{\mathbf{s}}_T)$, the resistance is sensitive to a heat source located above and upstream of the aperture. We can also see that $\text{Re}(\tilde{\mathbf{s}}_T)$ is not negligible in the thermal boundary layer inside the cavity.

$\text{Im}(\tilde{\mathbf{s}}_T)$ shows that the reactance is sensitive to a temperature variation upstream from the perforation. It is also the case inside the cavity. We remind that the cavity is a sensitive region without flow as well. The temperature response to a plane wave and to a non-linear forcing are alike, a strong pressure gradient can be observed in the downstream corner region both on the real and the imaginary parts.

It can be noted that the temperature sensitivity is zero on the boundary of the finite element domain, accordingly with the iso-thermal boundary condition $T_t = 0$.

According to figure 5.17, the pressure has a behavior similar to the temperature. This is already the case without flow. The impedance is sensitive to a perturbation in the upstream region of the aperture and inside the cavity. An important difference with temperature fields is the presence of a clear contrast on sensitivity field on line 1.

Here again, a high pressure gradient is present in the region of the downstream corner.

An important remark regarding the analysis with flow is that the sensitivity and the response to a non-linear term are not alike anymore. As opposed to the case study without flow, these fields are not symmetrical. It is physically consistent with the convective non-normality induced by the flow in this case (Sipp *et al.*, 2010). A forcing is present upstream, and a response is present downstream.

According to the resemblance of $|\tilde{\boldsymbol{p}}_\text{r}|$ and $|\tilde{\boldsymbol{p}}_t|$, the first resolvent mode is still dominating. This remark can be generalized to the fields of the 4 model variables presented in this section.

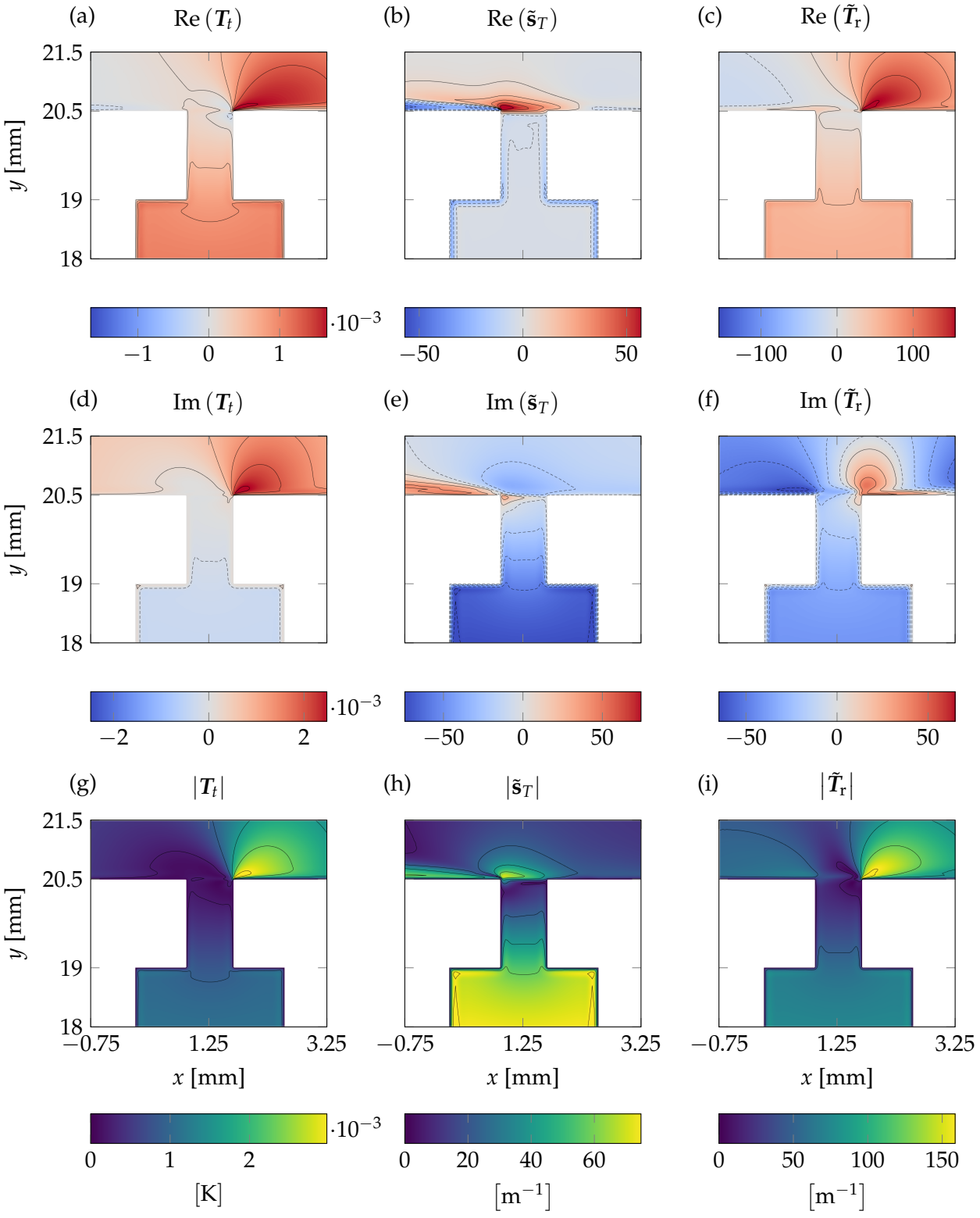

FIGURE 5.16: (a), (b), (c) are respectively, the real parts of the temperature response to a plane wave, the sensitivity to a heat source, and the temperature response to an optimal non-linear forcing with $M = 0.3$. (d), (e), (f): Imaginary parts. (g), (h), (i): Absolute values.

The fields corresponding to the tangential velocity are shown in figure 5.23. The sensitivity indicates that the impedance would be significantly impacted by a force applied upstream from the aperture. The corners play a secondary role on the impedance, as opposed to the case without flow. The response to a plane wave and to the non-linear forcing are similar, especially their real parts. The imaginary part $\mathrm{Im}(\tilde{\boldsymbol{u}}_\mathrm{r})$ shows a strong response all over the entrance of the aperture, in contrast with $\mathrm{Im}(\boldsymbol{u}_t)$ which shows a response more localized on the downstream corner region.

The normal velocity responses and sensitivity are presented in figure 5.19. $\mathrm{Re}(\tilde{\mathbf{s}}_v)$ shows that the resistance is sensitive to perturbations in the region of the upstream corner and, with a lower intensity, in the neck. The imaginary part of $\tilde{\mathbf{s}}_v$ indicates that the reactance is receptive to a force applied at the upstream corner and in the viscous boundary layer inside the neck. Line 1 appears to be a sensitive region as well, which is consistent with how the impedance is defined in this study.

The real parts of $\boldsymbol{v}_t$ and $\tilde{\boldsymbol{v}}_\mathrm{r}$ are very similar with a strong gradient in the downstream corner region. A second order difference is that the upstream corner region of $\mathrm{Re}(\tilde{\boldsymbol{v}}_\mathrm{r})$ is higher in amplitude than for $\mathrm{Re}(\tilde{\boldsymbol{v}}_t)$. The imaginary part of $\tilde{\boldsymbol{v}}_\mathrm{r}$ presents a rather homogeneous response from the neck, although a strong velocity gradient is present at the downstream corner. Globally, when looking at the absolute values of $\boldsymbol{v}_t$ and $\tilde{\boldsymbol{v}}_\mathrm{r}$, the main difference between the two fields is situated at the upstream corner of the aperture where $|\tilde{\boldsymbol{v}}_\mathrm{r}|$ is non negligible as opposed to $|\boldsymbol{v}_t|$.

Figure 5.19(h) shows that the effective velocity impacting the impedance is no longer evenly distributed in the neck and that the upstream corner is of importance.

In order to gain more insight on the comparison between the plane wave response and the non-linear source response, the vorticity is computed in both cases and shown in figure 5.20. We can see that $\mathrm{Re}(\omega_t)$ and $\mathrm{Re}(\tilde{\omega}_\mathrm{r})$ are very similar. On the other hand, $\mathrm{Im}(\omega_t)$ and $\mathrm{Im}(\tilde{\omega}_\mathrm{r})$ have a similar structure in the neck but the region above the aperture is rather different. Indeed, in the case of $\mathrm{Im}(\tilde{\omega}_\mathrm{r})$, the vorticity extends slightly higher above the aperture than $\mathrm{Im}(\omega_t)$.

The vorticity downstream sweep observed for $\tilde{\omega}_\mathrm{r}$ is also observed by Zhang *et al.* (2016) in a numerical study performed with a grazing flow and high sound pressure levels.

The mean value of the dissipation for both responses is computed according to equations (5.36) and (5.37) and shown in figure 5.21. It can be observed that for Φ_shear and $\tilde{\Phi}_\mathrm{shear}$, the dissipation is very strong at the downstream corner. The mean value of $\tilde{\Phi}_\mathrm{shear}$ highlights that the dissipation is lower at the upstream corner but not negligible.

We now formulate global remarks in figures 5.16 to 5.21. When a grazing flow is added, the upstream-downstream symmetry is broken, this is consistent with the observations from Zhang *et al.* (2016). The sensitivity fields for all 4 model variables show that the impedance is strongly impacted by a perturbation located upstream from the aperture. As such a perturbation is advected above the aperture, this phenomenon appears to be physically plausible. The upstream corner and the region above the aperture are also receptive zones. An important remark is that the response to a plane wave and the response to an optimal non-linear forcing are similar. Although small differences can be observed between the two responses, the main structure with a strong gradient at the downstream corner are comparable for each model variable. This is also translated by the vorticity and the dissipation due to shear effects. The latter remark indicates that, in the presence of a grazing flow, the first resolvent mode might be dominating the structure of the flow. Indeed, we recall that our output space is scalar, which means that only the first resolvent mode is analyzed throughout this study. Therefore, the resemblance between the two responses might indicate that the first mode is sufficient to accurately model the behavior of a single aperture under

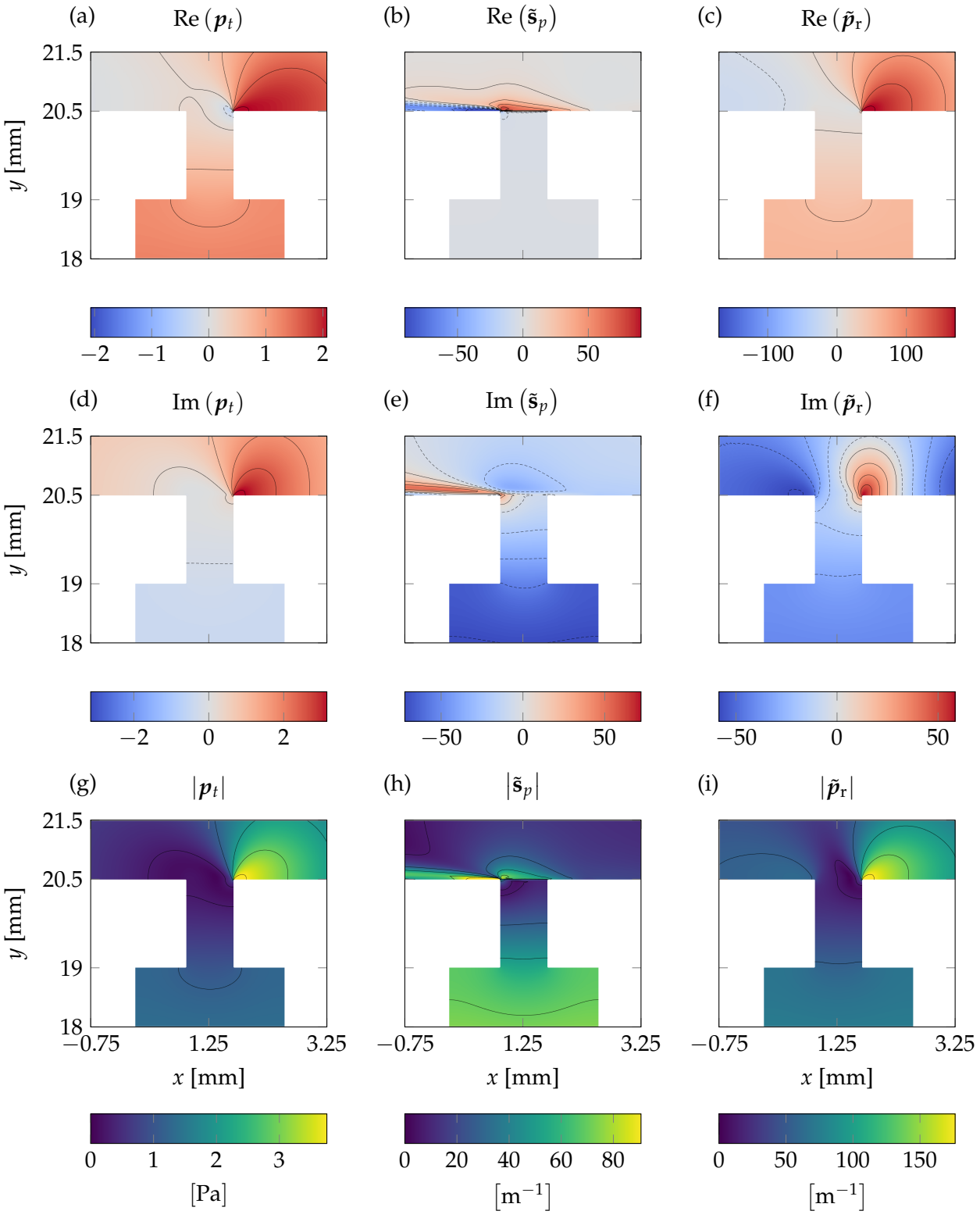

FIGURE 5.17: (a), (b), (c) are respectively, the real parts of the pressure response to a plane wave, the sensitivity to a mass source and the pressure response to an optimal non-linear forcing with $M = 0.3$. (d), (e), (f): Imaginary parts. (g), (h), (i): Absolute values.

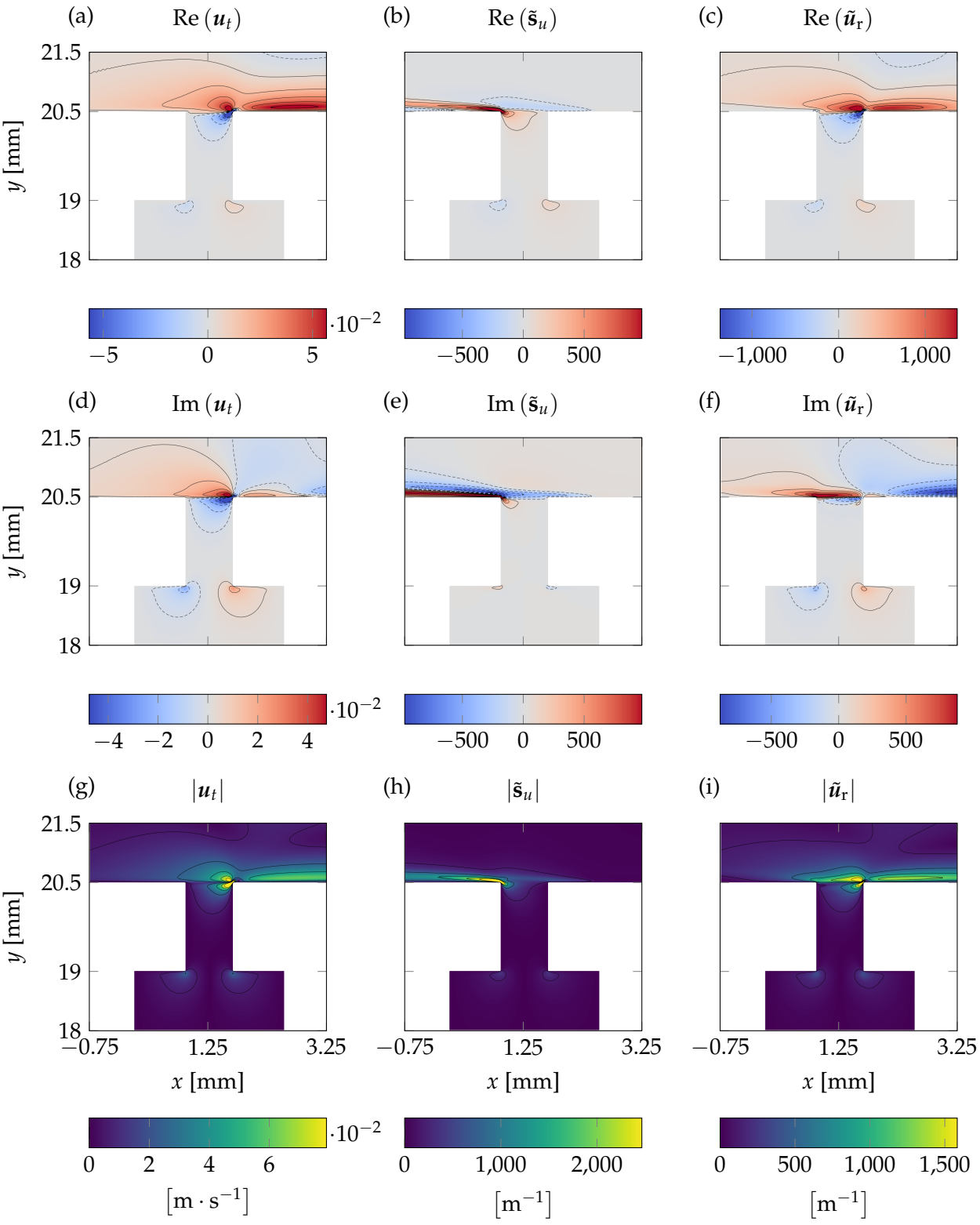

FIGURE 5.18: (a), (b), (c) are respectively, the real parts of the tangential velocity response to a plane wave, the sensitivity to a force, and the tangential velocity response to an optimal non-linear forcing with $M = 0.3$. (d), (e), (f): Imaginary parts. (g), (h), (i): Absolute values.

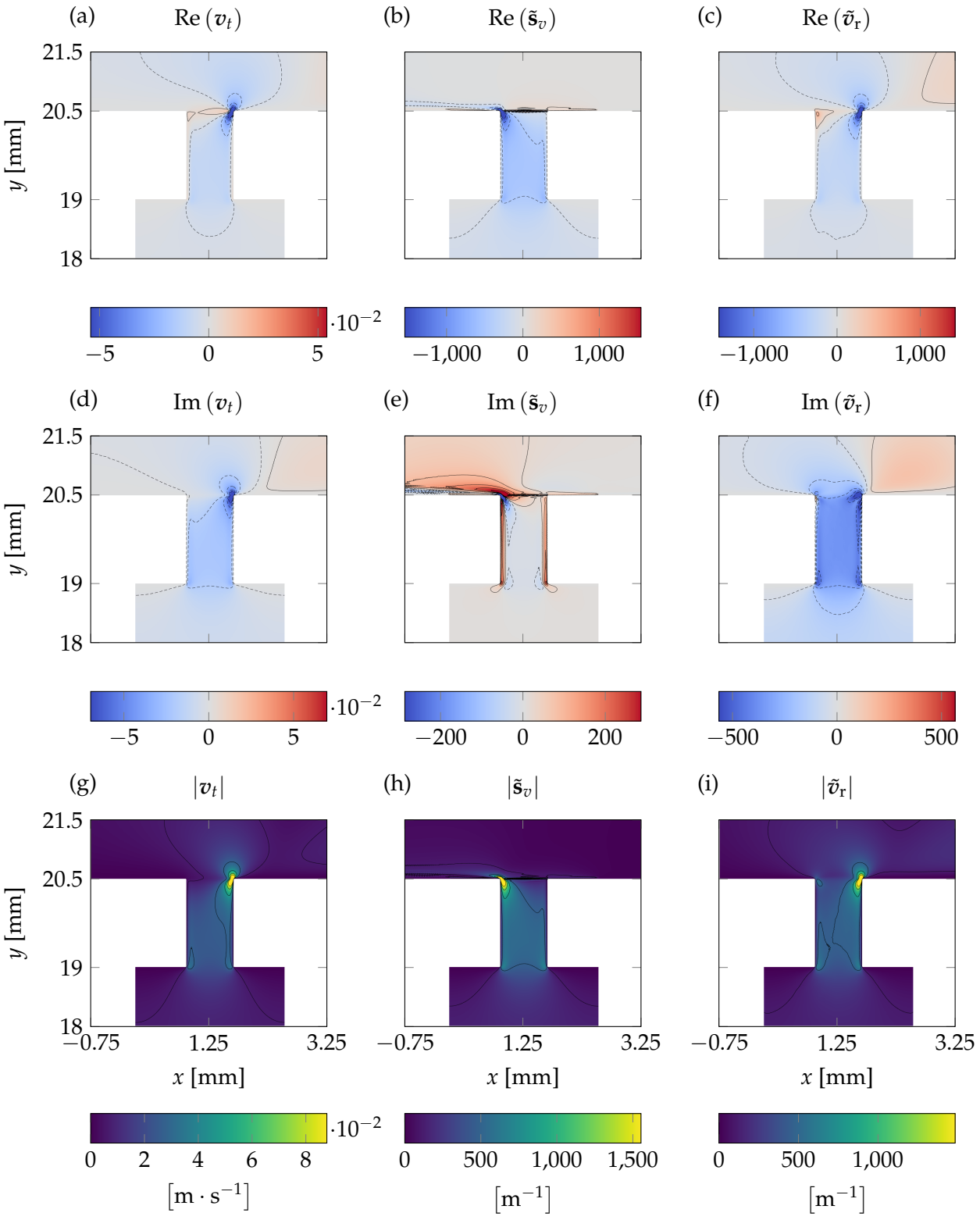

FIGURE 5.19: (a), (b), (c) are respectively, the real parts of the normal velocity response to a plane wave, the sensitivity to a force, and the normal velocity response to an optimal non-linear forcing with $M = 0.3$. (d), (e), (f): Imaginary parts. (g), (h), (i): Absolute values.

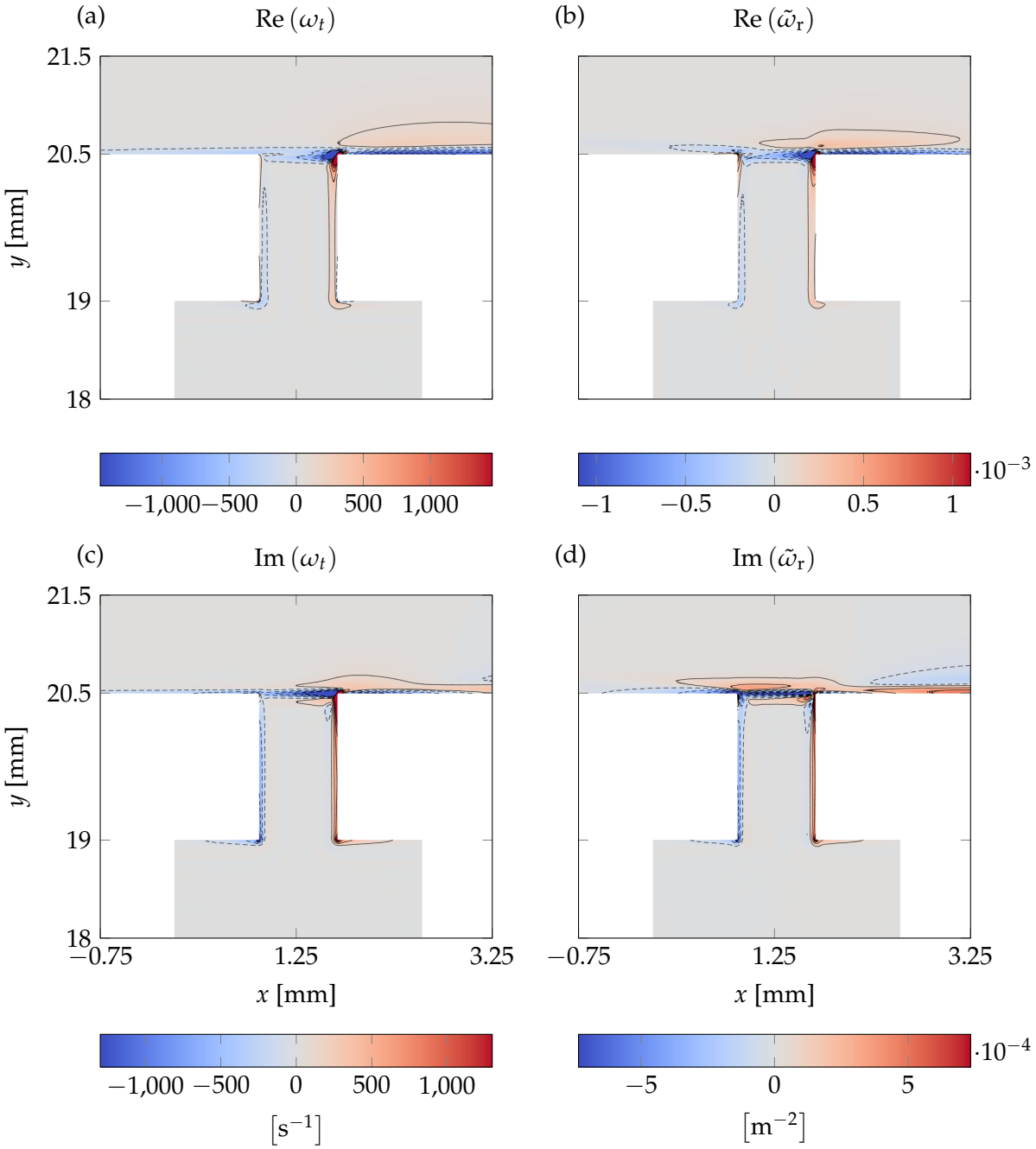

FIGURE 5.20: (a), (b): Real parts of the vorticity field for respectively the response to the plane wave, and the response to the non-linear forcing for $M = 0.3$. (c), (d): Imaginary parts.

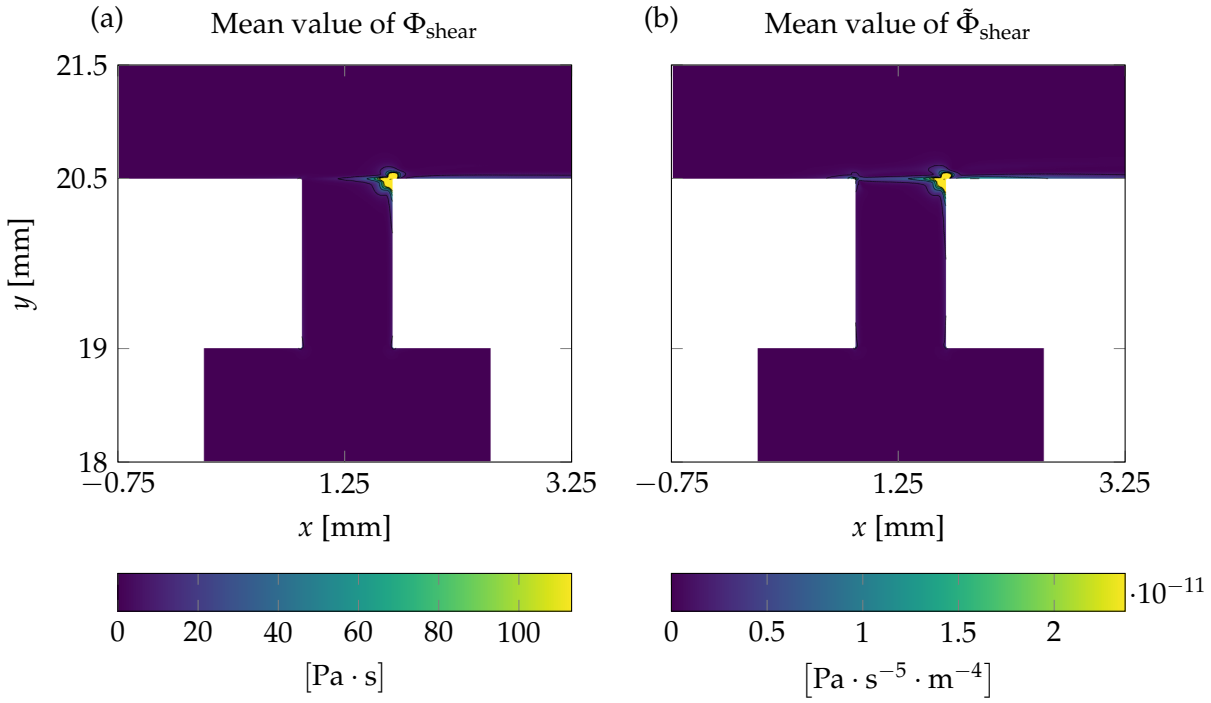

FIGURE 5.21: (a), (b): Mean values of the shear dissipation for respectively the response to the plane wave, and the response to the non-linear term for $M = 0.3$.

grazing flow. This is consistent with the fact that we are focusing on a frequency close to resonance. However, it would be necessary to account for higher order resolvent modes to validate this hypothesis. Thus, this validation can not be performed with the sensitivity analysis used so far.

5.7 Choice of another line to define the impedance with flow

The impedance is a quantity representative of the acoustic properties of a material. The definition of the impedance on line 1 is known to be relevant in the linear regime. However, when non-linear effects and a grazing flow are added, this definition might not be applicable due to the complexity of the physical phenomenon occurring. Defining an impedance above the flow boundary layer would round this fact, but it would represent the acoustic characteristics of the system composed of the liner and the boundary layer, and not only of the liner.

Alternatively, the impedance can be defined on line 1 using a "measure" of the acoustic pressure and normal velocity above the boundary layer on line 2 indicated in figure 5.2. Using, this new definition, we perform the sensitivity analysis and compute the response to the non-linear optimal forcing.

To this end, we evaluate the pressure on line 1 at the surface of the plate using the plane wave hypothesis in the boundary layer. We get

$$\int_{l_1} p_t(x)\, dx = \left[\frac{p_2}{l_2} e^{jk_0\delta_{bl}} + A\left(e^{jk_0 L} - e^{jk_0(L+\delta_{bl})} e^{jk_0\delta_{bl}} \right) \right] l_1, \tag{5.38}$$

where $p_2 = \int_{l_2} p_t(x)\, dx$, and l_2 denotes the length of line 2. We recall that $A = 1\,\text{Pa}$ is the amplitude of the plane wave imposed in the finite element domain.

Likewise, the normal velocity integral on line 1 is expressed as a function of the normal velocity integral over line 2 with

$$\int_{l_1} v_t(x)\, dx = \left[\frac{v_2}{l_2}\mathrm{e}^{\mathrm{j}k_0\delta_{bl}} - \frac{A}{\rho_0 c_0}\left(\mathrm{e}^{\mathrm{j}k_0 L} - \mathrm{e}^{\mathrm{j}k_0(L+\delta_{bl})}\mathrm{e}^{\mathrm{j}k_0\delta_{bl}}\right)\right] l_1, \tag{5.39}$$

with $v_2 = \int_{l_2} v_t(x)\, dx$.

In a similar manner to the previous sensitivity analysis, a first-order Taylor series is used to express the impedance perturbation δZ as a function of the non-linear perturbation $\delta \mathbf{x}_{nl}$:

$$\delta Z = \mathcal{H}_{Z,2}\delta \mathbf{x}_{nl}. \tag{5.40}$$

where

$$\begin{aligned}\mathcal{H}_{Z,2} =& \frac{\mathrm{e}^{\mathrm{j}k_0\delta_{bl}}}{l_2}\frac{\dfrac{\mathrm{e}^{\mathrm{j}k_0\delta_{bl}}}{l_2}\mathcal{H}_{p,2}\mathbf{x}_{nl} + A\left(\mathrm{e}^{\mathrm{j}k_0 L} - \mathrm{e}^{\mathrm{j}k_0(L+\delta_{bl})}\mathrm{e}^{\mathrm{j}k_0\delta_{bl}}\right)}{\left[\dfrac{\mathrm{e}^{\mathrm{j}k_0\delta_{bl}}}{l_2}\mathcal{H}_{v,2}\mathbf{x}_{nl} - \dfrac{A}{\rho_0 c_0}\left(\mathrm{e}^{\mathrm{j}k_0 L} - \mathrm{e}^{\mathrm{j}k_0(L+\delta_{bl})}\mathrm{e}^{\mathrm{j}k_0\delta_{bl}}\right)\right]^2}\mathcal{H}_{v,2} \\ &- \frac{\mathrm{e}^{\mathrm{j}k_0\delta_{bl}}}{l_2}\frac{\mathcal{H}_{p,2}}{\dfrac{\mathrm{e}^{\mathrm{j}k_0\delta_{bl}}}{l_2}\mathcal{H}_{v,2}\mathbf{x}_{nl} - \dfrac{A}{\rho_0 c_0}\left(\mathrm{e}^{\mathrm{j}k_0 L} - \mathrm{e}^{ik_0(L+\delta_{bl})}\mathrm{j}k_0\delta_{bl}\right)}.\end{aligned} \tag{5.41}$$

Here, $\int_{l_2} p_t(x)dx = \mathcal{H}_{p,2}\mathbf{x}_l$ and $\int_{l_2} v_t(x)dx = \mathcal{H}_{v,2}\mathbf{x}_l$.

In order to assess the impact of the impedance definition line, we compare the sensitivity results obtained with line 1 and line 2 at 3500 Hz and $M = 0.3$ in figure 5.22 and the response results in figure 5.23. The same colorbar scale is used when comparing the fields.

It can be observed that the sensitivity fields computed with line 1 and 2 are slightly different although they have the same structure. The region upstream from the aperture remains a sensitive zone for impedance.

The responses to a non-linear optimal forcing have a very similar structure when moving from line 1 to line 2. The response is important immediately above the aperture and in the downstream region.

It appears that the choice of a different line for the impedance definition has a limited impact on the sensitivity and response fields. The structures of the latter remain the same. This brings more confidence in the use of the sensitivity analysis on the impedance of a perforated plate. It can be noted that the robustness of this method may be due to the fact that the first resolvent mode is dominating.

5.8 Perspectives with an iterative procedure

In this section we explain how an iterative procedure could improve the present approach to become predictive. The diagram in figure 5.24 illustrates the method. A similar approach can be found in Symon *et al.* (2019).

From the linearized Navier-Stokes equations, we first compute a response to a plane wave which gives an initial value of $\mathbf{u}_t(\omega)$ for a determined frequency range. The sensitivity analysis is performed to focus our interest on the mode of the non-linear response impacting the most the impedance. Keeping only the most amplified modes (in singular value and/or among frequencies) allows to reduce the order of our model and to highlight the relevant physics.

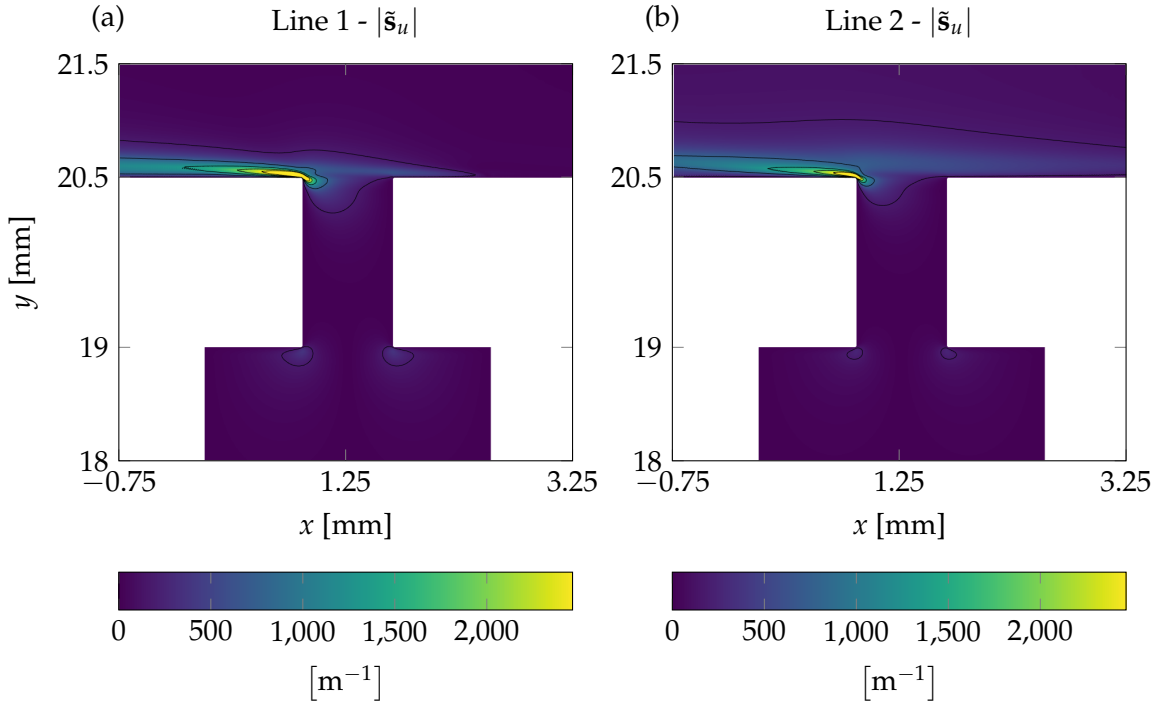

FIGURE 5.22: Tangential velocity sensitivity computed using line 1 (left) and line 2 (right).

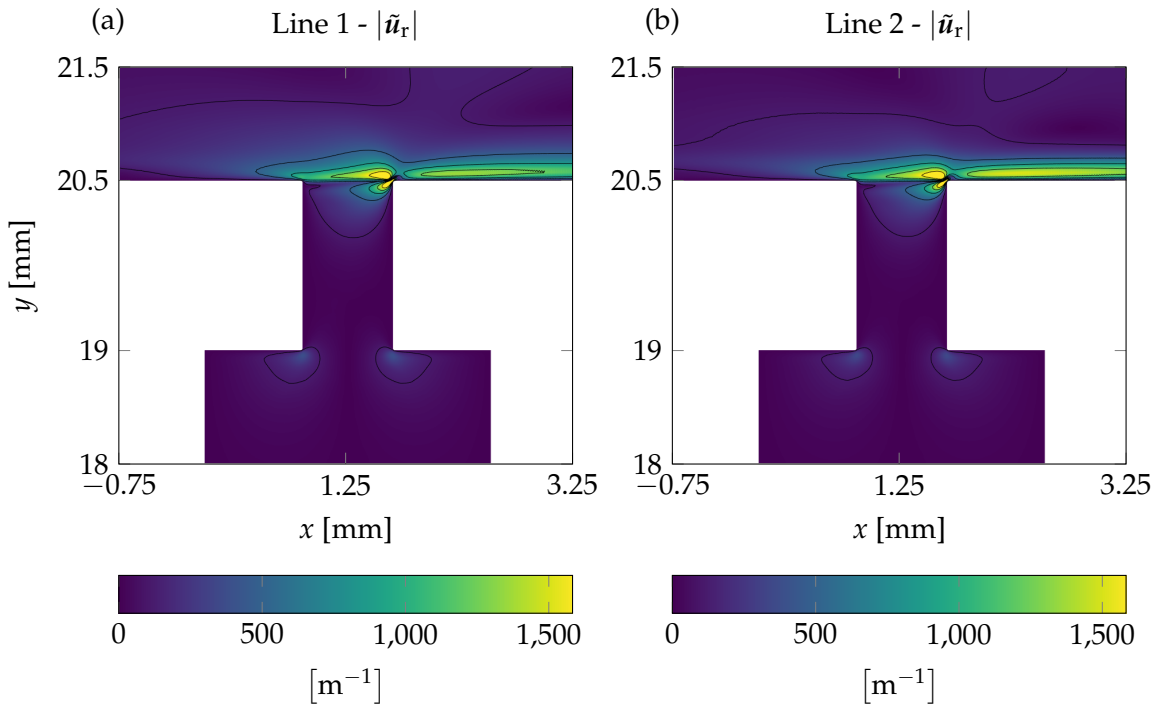

FIGURE 5.23: Tangential velocity response to a non-linear optimal forcing computed using line 1 (left) and line 2 (right).

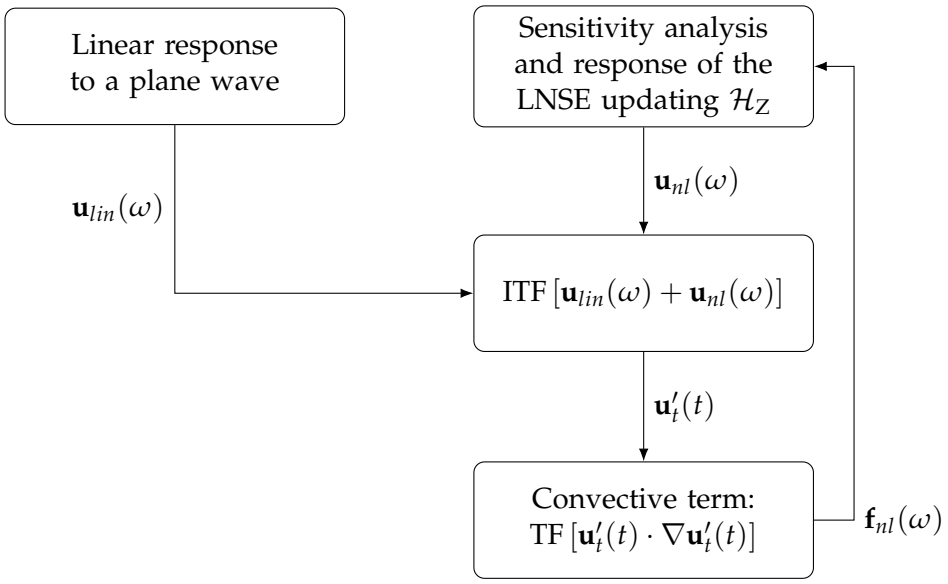

FIGURE 5.24: Diagram of the iteration procedure. Here, ITF$[\cdot]$ stands for the inverse Fourier transform and TF$[\cdot]$ for the forward Fourier transform.

Then, we perform an inverse Fourier transform using the values of $\mathbf{u}_t(\omega) = \mathbf{u}_{lin}(\omega) + \mathbf{u}_{nl}(\omega)$ in order to mix the frequency contribution and to obtain the velocity $\mathbf{u}'_t(t)$ in the time domain. Thereafter, the convective term $\mathbf{f}_{nl} = \text{TF}\left[\mathbf{u}'_t(t) \cdot \nabla \mathbf{u}'_t(t)\right]$ is determined in the frequency domain. Finally, the response of the LNSE to this non-linear term is computed on the considered frequency range. This procedure is repeated until convergence of the velocity amplitude.

A major benefit of this procedure is that it gives access to a realistic non-linear term, including the contribution of multiple frequencies, impacting the most the impedance. This is illustrated in appendix E, in which an example of triadic interaction on the momentum conservation equation involving the convective non-linear term is presented. Thereafter, quantitative information regarding the model variables are available and could help the understanding of the non-linear physical mechanisms in the presence of a grazing flow. For instance, this could lead to a definition of an effective quantity to define the non-linear impedance with flow, as in the model from Ingard (1968) where this effective quantity is the velocity in the neck.

5.9 Conclusion

A sensitivity analysis, which is a specific case of the more general resolvent analysis, was introduced to investigate the behavior of a single perforation backed by a cavity to non-linearities.

The response gains to an optimal non-linear source are computed for each model variables. An interesting fact is that these gains decrease with growing Mach number. This indicates that the non-linearities have a lower impact on the impedance when the velocity of the grazing flow increases.

Cases without flow and with flow at a Mach number of 0.3 are presented in detail.

Without flow, the main characteristics of a Helmholtz resonator are retrieved. The resistance appears to be sensitive to a heat source located inside the cavity and the reactance is sensitive to a heat source situated in the thermal boundary layer inside the cavity. The impedance is also shown to be sensitive to a pressure perturbation inside the cavity. The tangential velocity sensitivity shows that the corners of the aperture form a very sensitive zone. The normal velocity

sensitivity highlights the importance of the viscous boundary layers inside the neck on the resistance (Zwikker *et al.*, 1949). The important impact of the neck region on the reactance is also shown.

When comparing the response to a plane wave and the response to a non-linear source, a phase quadrature seems to be present between the two responses. The vorticity fields seems to highlight vortex shedding from the corner of the aperture when using a non-linear source. Furthermore, the dissipation fields clearly show that the main shear dissipation region is located at the corners of the perforation when using a non-linear source. We recall that when using a plane wave source, *i.e.* a linear source, the dissipation is located mostly in the viscous boundary layer of the neck and the corners of the aperture.

With flow at $M = 0.3$, the sensitive zones highlighted without flow become secondary. The most sensitive regions are now located upstream of the aperture, at the upstream corner and immediately above the neck. The shear dissipation fields show that most of the losses occur at the downstream corner of the aperture when either a plane wave or a non-linear source is used. The effective velocity impacting the impedance is dominated by the upstream corner. Hence, computing the velocity in the perforations using the same approach as without flow is questionable. The impact of the line upon which the impedance is defined on the sensitivity and response computations is investigated. Regarding the tangential velocity fields, it appears to have mostly an impact on the amplitude rather than on the structure of fields. Therefore, our method remains valid as it focuses on highlighting physical mechanisms.

The sensitivity analysis could be applied to more complex models. For instance, a model with a periodic arrangement of perforations, which is more realistic when compared to an actual perforated liners. Alternatively, the grazing flow could also be solved using a RANS (Reynolds-averaged Navier-Stokes) model. The geometrical characteristics of the perforations, namely their radius and their length are known to have an impact on the impedance. This is also the case of the boundary layer thickness. Hence, a parametric study could be envisaged and the physical mechanisms underlying the impact of non-conventional or complex geometries on the impedance could be explored and quantified.

In the present study, we have computed an optimal non-linear forcing which is not physically realistic. However, the forcing and the solution to the system could be predicted by using an iterative procedure. Indeed, one could use the sensitivity analysis the reduce the order of the model and to focus on the impedance. Thereafter, a forcing and its associated response could be computed iteratively until convergence, as explained in section 5.8. A similar approach is used in Symon *et al.* (2019). For a sine-swept source, this would need to be performed for each frequency, while for a white noise source it would be for all the frequencies. One of the main benefits of such method is to gain access to the whole perturbed fields of the model variables as opposed to only an effective quantity as used in Ingard *et al.* (1967).

Conclusion

In this manuscript, different models and methods are developed to study the acoustic impedance of perforated plate liners with various geometrical parameters. The starting point is that the micro-perforated liners are of interest to reduce the flow drag of jet engines. However, the current models are not accurate when considering micro-perforated liners under grazing flow. Therefore, we investigate the impact on the impedance of having sub-millimeter perforation and a low porosity. This thesis begins with a simple model in the linear regime without flow and unfold with increasing physical complexity. Chapters 1 and 2 are dedicated to the linear regime without flow. Chapter 3 focuses on the non-linear regime. Chapters 4 and 5 deal with the non-linear regime in presence of a grazing flow. In this general conclusion, we recall the main results of each chapter and provide possible perspectives.

In the first chapter, the physical mechanisms occurring in the linear regime without flow are reviewed. The semi-empirical model from Guess (1975), which accounts for viscous losses inside and outside the perforations, the radiation and hole interaction is introduced. Subsequently a model based on the mode-matching (MM) method is presented. Due to its construction, the latter approach allows to release the short tube approximation and to describe the complete velocity profile based on the theory from Stinson (1991). It accounts for the radiation and hole interaction effects through evanescent modes at the entrances of the perforation. Having compared both models to impedance measurements, the mode-matching model resistance predictions underestimate the measured resistance significantly. This is due to the fact that the mode-matching does not account for the viscous edges effects which are included with an empirical correction in the model from Guess (1975) following the work from Ingard (1953). However, the MM method allows to capture correctly the radiation and hole interaction effects without relying on an end correction, as opposed to Guess (1975). Another result is that releasing the short tube approximation and modeling the velocity profile has a minor impact on the impedance prediction. In order to obtain an exhaustive model, an interesting perspective would be to use higher order viscous modes (Kirchhoff, 1868) outside the perforation to account for viscous edges effects. Moreover, the MM model could be adapted for conical shape apertures and small horns based on the visco-thermal transfer function in Honzík *et al.* (2013).

Remaining in the linear regime, finite element models are used in chapter 2. The linearized compressible Navier-Stokes equations are solved as well as the Helmholtz equation with a boundary condition including the effect of the viscous and thermal acoustic boundary layers (Berggren *et al.*, 2018). Both models are found to be accurate when compared to impedance tube measurements for macro- and micro-perforated plates. The dissipation rate due to shear effects is computed from LNSE solution. Accordingly with the shear number values, it is shown that the viscous dissipation is distributed in a different manner when considering a macro- or a micro-perforate. Interestingly, a quarter of the overall dissipation occurs outside the perforation in the micro-perforated case and the corner region is secondary. In the macro-perforated case, the dissipation is concentrated close to the walls as the boundary layer is small compared to the perforation radius. Consequently, the dissipation is strong near the corners. Based on the results from chapter 1 and 2, it is interesting to note that the empirical end correction from Ingard (1953) remains accurate both for macro- and micro-plates although the viscous edges effects are differently distributed from one case to another. We recall that Ingard performed measurements for perforation in the macro-perforated

regime. From a more numerical point of view, the "Helmholtz with losses" model is found to converge much faster than the LNSE model. This is explained by several facts, the Helmholtz model uses only 1 variable instead of 4 for the LNSE, the acoustic boundary layers do not need to be accurately discretised and there is no need for representing the velocity in a smoother space than the state variables (Kellogg *et al.*, 1996). Surprisingly, this model is able to accurately predict the impedance. Due to its underlying assumptions, it is not supposed to be accurate at the corners of the perforations and to account for viscous edges effects as it carries a wall model. Nevertheless, this is consistent with recent results from Cops *et al.* (2020) in which the same model is used in porous materials.

In chapter 3, the model from Guess (1975) is modified with an iterative procedure to predict the non-linear impedance and the acoustic velocity in the perforations for high sound pressure levels. This procedure is used in Beck *et al.* (2015) and in the model from Laly *et al.* (2018a) for a sine-swept source. The non-linear resistance from Guess is based on the early experimental work from Ingard *et al.* (1967), and the model from Laly *et al.* is based on the equivalent fluid approach with the non-linear resistance from Zinn (1970) which accounts for the *vena contracta* effect. The non-linear term from Ingard *et al.* (1967) is validated for a wide range of perforated plates under a white noise source. Both Guess and Laly *et al.* models are compared to impedance tube measurements using either a sine-swept or a white noise source for macro- and micro-perforated plates. The iterative procedure is adapted to both sources. The impedance and velocity predictions from the two approaches are found to be in reasonable to good agreement with the measurements. We observe discrepancies between the two models, which could be explained by the *vena contracta* modeling in Laly *et al.* (2018b). Globally the modified Guess model is slightly more accurate than the recent model from Laly *et al.* This might be explained by the fact that the spatial scales separation assumption inherent to an equivalent fluid approach is not respected for macro-perforated plate. Additionally, the predictions are in good agreement with measurements performed with a plane wave having a grazing incidence to the perforated plate.

In the fourth chapter, the impact of the grazing flow on the impedance is studied. The model from Guess is used and the grazing flow resistance correction from Ingard (1968) is accounted for during the iteration procedure introduced in chapter 4. Alternatively, the impedance correction from Meng *et al.* (2019) is used. We recall that both corrections depend on an empirical parameters. Educed here from the measurement performed at the LAUM for a number of perforated plate and three different boundary layer thicknesses. The measurements are at $L_p = 130\,\mathrm{dB}$ or $L_p = 150\,\mathrm{dB}$ and $M = 0.3$ or $M = 0.45$. The boundary layer displacement thickness is found to have an important impact on the resistance, however, it appears that once the boundary layer is fully developed, the displacement thickness has only a limited impact on the impedance. The Mach number also has a significant impact on the impedance. The resistance increases and the reactance decreases with increasing Mach number, consistently with the litterature. The fluctuating velocity due to a turbulent boundary layer and the convection speed of vorticity are found to decrease with growing boundary layer displacement thickness following an inverse law, consistently with Yu *et al.* (2008) and Meng *et al.* (2019). The relevance of this velocity is discussed in terms of an effective quantity impacting the impedance. Furthermore, we propose an empirical function for k_{Guess} different from the one of Yu *et al.* (2008) as its value at $\delta^*/R_{\mathrm{neck}} = 0$ depends on the ratio R_{neck}/h and its rate of decline depends on the radius. When computing the resistance with the modified model from Guess, this function clearly improves the prediction for plates with low perforation radius and porosity, compared to the initial value of $k_{\mathrm{Guess}} = 0.3$ in Guess (1975). Moreover, in the macro-perforated case, it does not deteriorate the predictions.

The last chapter introduces a method based on the resolvent analysis. This sensitivity analysis is performed on the linearized Navier-Stokes equations with and without mean flow on a perforation submitted to a plane wave and backed by a cavity. Without flow, the main characteristics of a Helmholtz resonator are retrieved. Additionally, it is found that the dissipation is mostly concentrated at the corners of the aperture when submitted to a non-linear forcing. Vortex

shedding from the corners is also highlighted. With flow, the sensitive zone identified without flow becomes secondary. The region upstream from the perforation and the upstream corners are the most sensitive region to a non-linear source. The response to a non-linear forcing is strong downstream of the perforation and at the downstream corner. The viscous dissipation is mainly localized in the downstream corner region when considering both the responses to a plane wave and to the non-linear forcing. Both with and without flow, the response to a plane wave and the response to a non-linear forcing are similar. This suggests that the first resolvent mode is dominating and is an encouraging observation in terms of reduced-order modeling. Following this study, the impact of the line upon which the impedance is defined is discussed and redefined above the boundary layer. The sensitivity and response fields obtained with both lines appear to be similar. This provides more confidence in the use of the sensitivity analysis to study the impedance. This method can lead to a number of perspectives. It could be used for various geometrical parameters of perforated plates and shear flow boundary layers. Also, a periodic boundary condition could be implemented to obtain a more realistic layout. The angle of incidence of the plane wave could be varied. An iterative procedure could be introduced to compute the non-linear convective term. In doing so, the current sensitivity analysis could be improved to become predictive.

Global perspectives In this thesis, several methods were developed to model the impedance of perforated liners from the linear regime to the non-linear regime with flow. In the linear and non-linear regimes, the prediction provided by the presented models are correct both for macro- and micro-perforated liners. In chapter 4, it is shown that, in the non-linear regime with grazing flow, the impedance predictions are perfectible, especially for micro-perforates. The underlying physics impacting the impedance in the presence of a grazing flow needs further investigations to obtain accurate predictions. The sensitivity analysis introduced in chapter 5 is a suitable method to reach this objective. Perspectives allowing to make this approach predictive were presented and would be a consistent continuation of this thesis. Furthermore, the presented studies can be adapted for perforations with a conical or tilted shape.

Appendix A

Details of the mode-matching formulation

A.1 Pressure continuity

A.1.1 Interface between the neck and the exterior

The pressure continuity derivations is detailed for the boundary between the exterior domain and the neck. In the exterior domain, the pressure field reads

$$p_{\text{ext}}(r,z) = \sum_{m=0}^{\infty} \left(A_{\text{ext}}^{m} \mathrm{e}^{-\mathrm{j}k_{\text{ext}}^{z,m} z} + B_{\text{ext}}^{m} \mathrm{e}^{\mathrm{j}k_{\text{ext}}^{z,m} z} \right) \Psi_{\text{ext}}^{m}, \tag{A.1}$$

with

$$\Psi_{\text{ext}}^{m} = \mathrm{J}_0 \left(k_{\text{ext}}^{r,m} r \right). \tag{A.2}$$

m is the mode index and J_0 is the Bessel function of order zero of the first kind. The radial wave number $k_{\text{ext}}^{r,m}$ and the axial wave number $k_{\text{ext}}^{z,m}$ are related by the dispersion relation

$$\left(k_{\text{ext}}^{z,m}\right)^2 = k_0^2 - \left(k_{\text{ext}}^{r,m}\right)^2, \tag{A.3}$$

where $k_0 = \omega / c_0$ and $k_{\text{ext}}^{r,m} = \gamma^{0,m} / R_{\text{ext}}$ in which $\gamma^{0,m}$ are the solutions of $\mathrm{J}_0' \left(\gamma^{0,m}\right) = 0$. Only the axi-symmetrical modes are accounted for. In the neck, the pressure field is

$$p_{\text{neck}}(z) = A_{\text{neck}} \mathrm{e}^{-\mathrm{j}k_{\text{neck}}(z+h)} + B_{\text{neck}} \mathrm{e}^{\mathrm{j}k_{\text{neck}} z}. \tag{A.4}$$

The axial wave number accounting for viscous and thermal effects k_{neck}, derived in Stinson (1991), is

$$k_{\text{neck}} = \omega \sqrt{\rho\left(\omega\right) C\left(\omega\right)}. \tag{A.5}$$

Here $\rho(\omega)$ is the equivalent complex density and $C(\omega)$ is the equivalent complex compressibility defined respectively as

$$\rho\left(\omega\right) = \rho_0 \left[1 - \frac{2}{K R_{\text{neck}}} \frac{\mathrm{J}_1\left(K R_{\text{neck}}\right)}{\mathrm{J}_0\left(K R_{\text{neck}}\right)} \right]^{-1}, \tag{A.6}$$

and

$$C\left(\omega\right) = \frac{1}{\gamma P_0} \left[1 + \frac{2\left(\gamma - 1\right)}{R_{\text{neck}}} \sqrt{\frac{\nu'}{-\mathrm{j}\omega\gamma}} \frac{\mathrm{J}_1\left(\sqrt{\frac{-\mathrm{j}\omega\gamma}{\nu'}} R_{\text{neck}} \right)}{\mathrm{J}_0\left(\sqrt{\frac{-\mathrm{j}\omega\gamma}{\nu'}} R_{\text{neck}} \right)} \right], \tag{A.7}$$

where P_0 is the atmospheric pressure, γ is the adiabatic coefficient and $\nu' = \kappa / \left(\rho_0 c_p\right)$.

At the interface between the neck and the exterior for $z = 0$, we wish to approximate the relation $p_{\text{neck}} = p_{\text{ext}}$ on the cross section of the neck such that

$$\int_0^{R_{\text{neck}}} p_{\text{neck}} \Phi_{\text{neck}} r dr = \int_0^{R_{\text{neck}}} p_{\text{ext}} \Phi_{\text{neck}} r dr. \tag{A.8}$$

Here, we choose the test function $\Phi_{\text{neck}} = 2/R_{\text{neck}}^2$. The modes from the exterior domain are projected onto the neck plane wave. As the modes from the neck are orthogonal, equation (A.8) can be written as

$$A_{\text{neck}} \mathrm{e}^{-\mathrm{j}k_{\text{neck}}h} + B_{\text{neck}} = \sum_{m=0}^{N} E^m \left(A_{\text{ext}}^m + B_{\text{ext}}^m \right), \tag{A.9}$$

where

$$E^m = \frac{2\mathrm{J}_1 \left(R_{\text{neck}} k_{\text{ext}}^{r,m} \right)}{R_{\text{neck}} k_{\text{ext}}^{r,m}}, \tag{A.10}$$

and N is the index of the highest order mode accounted for.

A.1.2 Interface between the neck and the cavity

The same derivations are performed for the interface between the neck and the cavity for $z = -h$. The pressure field in the cavity is

$$p_{\text{cav}}(r,z) = \sum_{m=0}^{\infty} \left(A_{\text{cav}}^m \mathrm{e}^{-\mathrm{j}k_{\text{cav}}^{z,m}(z+h+L)} + B_{\text{cav}}^m \mathrm{e}^{\mathrm{j}k_{\text{cav}}^{z,m}(z+h)} \right) \Psi_{\text{cav}}^m, \tag{A.11}$$

with $\Psi_{\text{cav}}^m = \mathrm{J}_0 \left(k_{\text{cav}}^{r,m} \right)$ and $\left(k_{\text{cav}}^{z,m} \right)^2 = k_0^2 - \left(k_{\text{cav}}^{r,m} \right)^2$. Here, $k_{\text{cav}}^{r,m} = \gamma^{0,m} / R_{\text{cav}}$. The pressure continuity between the neck and the cavity is

$$A_{\text{neck}} + B_{\text{neck}} \mathrm{e}^{-\mathrm{j}k_{\text{neck}}h} = \sum_{i=0}^{N} G^m \left(A_{\text{cav}}^m \mathrm{e}^{-\mathrm{j}k_{\text{cav}}^{z,m}L} + B_{\text{cav}}^m \right), \tag{A.12}$$

where

$$G^m = \frac{2\mathrm{J}_1 \left(R_{\text{neck}} k_{\text{cav}}^{r,m} \right)}{R_{\text{neck}} k_{\text{cav}}^{r,m}}. \tag{A.13}$$

A.2 Axial velocity continuity

A.2.1 Interface between the neck and the exterior

The axial velocity continuity is detailed for the boundary between the exterior domain and the neck. The axial velocity field in the exterior domain is described by

$$v_{\text{ext}} = \frac{1}{\rho_0 \omega} \sum_{m=0}^{\infty} k_{\text{ext}}^{z,m} \left(A_{\text{ext}}^m \mathrm{e}^{-\mathrm{j}k_{\text{ext}}^{z,m} z} - B_{\text{ext}}^m \mathrm{e}^{\mathrm{j}k_{\text{ext}}^{z,m} z} \right) \Psi_{\text{ext}}^m. \tag{A.14}$$

In the neck, the velocity profile accounting for viscosity reads

$$v_{\text{neck}} = \frac{\partial p_{\text{neck}}}{\partial z} \frac{1}{\mathrm{j}\omega\rho_0} \Psi_{\text{neck}} \tag{A.15}$$

with

$$\Psi_{\text{neck}} = \frac{\mathrm{J}_0(Kr)}{\mathrm{J}_0(KR_{\text{neck}})} - 1, \tag{A.16}$$

and $K = \sqrt{-\mathrm{j}\omega/\nu}$ is the Stokes wave number. Hence,

$$v_{\text{neck}} = \frac{k_{\text{neck}}}{\rho_0 \omega} \left(A_{\text{neck}} \mathrm{e}^{-\mathrm{j}k_{\text{neck}}(z+h)} - B_{\text{neck}} \mathrm{e}^{\mathrm{j}k_{\text{neck}} z} \right) \Psi_{\text{neck}}. \tag{A.17}$$

We enforce the axial velocity continuity $v_{\text{ext}} = v_{\text{neck}}$ on the surface S_{ext} for $z = 0$ with the weak formulation

$$\forall m \in \mathbb{N} \int_0^{R_{\text{ext}}} v_{\text{ext}} \Phi_{\text{ext}}^m r dr = \int_0^{R_{\text{neck}}} v_{\text{neck}} \Phi_{\text{ext}}^m r dr, \tag{A.18}$$

in which we choose the test function

$$\Phi_{\text{ext}}^m = \frac{\mathrm{J}_0 \left(k_{\text{ext}}^{r,m} r \right)}{\displaystyle\int_0^{R_{\text{ext}}} \mathrm{J}_0^2 \left(k_{\text{ext}}^{r,m} r \right) r dr}. \tag{A.19}$$

Equation (A.18) implies that $v_{\text{ext}}(z = 0) = 0$ on $S_{\text{ext}} \backslash S_{\text{neck}}$, imposing naturally a free-slip boundary condition on the surface of the plate. The modes from the exterior duct are orthogonal, hence the axial velocity continuity is

$$\forall m \in \mathbb{N} \quad k_{\text{ext}}^{z,m} \left(A_{\text{ext}}^m - B_{\text{ext}}^m \right) = k_{\text{neck}} \left(A_{\text{neck}} \mathrm{e}^{-\mathrm{j}k_{\text{neck}} h} - B_{\text{neck}} \right) F^m, \tag{A.20}$$

in which

$$F^m = 2 \frac{\displaystyle\int_0^{R_{\text{neck}}} \left[1 - \frac{\mathrm{J}_0(Kr)}{\mathrm{J}_0 \left(K R_{\text{neck}} \right)} \right] \mathrm{J}_0 \left(k_{\text{ext}}^{r,m} r \right) r dr}{R_{\text{ext}}^2 \left[\mathrm{J}_0^2 \left(k_{\text{ext}}^{r,m} R_{\text{ext}} \right) + \mathrm{J}_1 \left(k_{\text{ext}}^{r,m} R_{\text{ext}} \right) \right]}. \tag{A.21}$$

A.2.2 Interface between the neck and the cavity

The same derivations are performed in the cavity. The velocity in the cavity field reads

$$v_{\text{cav}} = \frac{1}{\rho_0 \omega} \sum_{m=0}^{\infty} k_{\text{cav}}^{z,m} \left(A_{\text{cav}}^m \mathrm{e}^{-\mathrm{j}k_{\text{cav}}^{z,m}(z+h+L)} - B_{\text{cav}}^m \mathrm{e}^{\mathrm{j}k_{z,m}^{\text{cav}}(z+h)} \right) \Psi_{\text{cav}}^m. \tag{A.22}$$

By following the same steps as for the continuity between the exterior and the neck, the axial velocity continuity between the cavity and the neck is

$$\forall m \in \mathbb{N} \quad k_{\text{cav}}^{r,m} \left(A_{\text{cav}}^m \mathrm{e}^{-\mathrm{j}k_{z,m}^{\text{cav}} L} - B_{\text{cav}}^m \right) = k^{\text{neck}} \left(A_{\text{neck}} - B_{\text{neck}} \mathrm{e}^{-\mathrm{j}k_{\text{neck}} h} \right) H^m, \tag{A.23}$$

in which

$$H^m = 2 \frac{\displaystyle\int_0^{R_{\text{neck}}} \left[1 - \frac{\mathrm{J}_0(Kr)}{\mathrm{J}_0 \left(K R_{\text{neck}} \right)} \right] \mathrm{J}_0 \left(k_{\text{cav}}^{r,m} r \right) r dr}{R_{\text{cav}}^2 \left(\mathrm{J}_0^2 \left(k_{\text{cav}}^{r,m} R_{\text{cav}} \right) + \mathrm{J}_1 \left(k_{\text{cav}}^{r,m} R_{\text{cav}} \right) \right)}. \tag{A.24}$$

A.3 Linear system

The incident plane wave amplitude is fixed to $B_{\text{ext}}^0 = 1$. Therefore, the reflection coefficient is $R = A_{\text{ext}}^0$. To solve the linear system, we need to use the perfectly reflecting boundary condition on the back plate of the cavity, which leads to the following relation:

$$\forall m \in \mathbb{N} \quad A_{\text{ext}}^m = B_{\text{ext}}^m \mathrm{e}^{-\mathrm{j}k_{\text{cav}}^{z,m} L}. \tag{A.25}$$

We now have 5 equations ((A.8), (A.12), (A.18), (A.23), (A.25)) for 5 unknowns modal amplitudes in the case in which only the plane wave is matched in the exterior and the cavity domains. These 5 equations can be reduced to a linear system for the modal amplitudes B^m_{ext}, A^m_{cav}, B^m_{cav}, A_{neck} and B_{neck}. The size of the linear system is $5 + 3N$.

Appendix B

Weak formulations of the numerical models

B.1 LNSE plane wave derivations

On the upper boundary Γ_{in} of the computation domain, an incoming plane wave of the form $\mathrm{e}^{+\mathrm{j}\omega t+\mathrm{j}kz}$ is generated by using the following Robin boundary condition:

$$\nabla p' \cdot \boldsymbol{n} + \mathrm{j}kp' = 2\mathrm{j}kW\mathrm{e}^{\mathrm{j}kL_Z} \text{ on } \Gamma_{in}, \tag{B.1}$$

where $L_Z = L + h + L_T$ and W is the amplitude of the plane wave. The numerical implementation is formulated using the acoustic Reynolds number based on the sound speed Re_a instead of the shear number Sh which is used for the post-processing of the results. The wavenumber k remains to be determined together with the associated expression for the other variables of the linearized Navier–Stokes equations. To that end we use the fact that these variables are also of the form $\mathrm{e}^{+\mathrm{j}\omega t+\mathrm{j}kz}$ to modify equations (2.8), (2.9) and (2.10) and write:

$$\rho' = -\frac{k}{\omega}\boldsymbol{u}' \cdot \boldsymbol{n}\,, \quad p' = -\frac{\alpha}{k}\boldsymbol{u}' \cdot \boldsymbol{n}\,, \quad T' = -\frac{k}{\beta}\boldsymbol{u}' \cdot \boldsymbol{n}\,, \quad p' = [(\gamma-1)T' + \rho']/\gamma\,, \tag{B.2}$$

with

$$\alpha = \omega - \frac{\mathrm{j}k^2}{Re_a}\left(\mu_B + \tfrac{4}{3}\right)\,, \quad \beta = \omega - \mathrm{j}k^2\frac{\gamma}{Re_a Pr}\,.$$

From these relations, and assuming that thermal effects are small, one can recover the definition of the wavenumber (2.12) of the dispersion relation. One can also obtain the boundary conditions for the linearized Navier–Stokes equations corresponding to an incoming plane wave:

$$\nabla\rho' \cdot \boldsymbol{n} + \mathrm{j}k\rho' = \frac{2k^3}{\omega\alpha}\mathrm{j}W\mathrm{e}^{\mathrm{j}kL_Z}\,, \tag{B.3}$$

$$\nabla\left(\boldsymbol{u}' \cdot \boldsymbol{n}\right) \cdot \boldsymbol{n} + \mathrm{j}k\boldsymbol{u}' \cdot \boldsymbol{n} = \frac{-2k^2}{\alpha}\mathrm{j}W\mathrm{e}^{\mathrm{j}kL_Z}\,, \tag{B.4}$$

$$\nabla T' \cdot \boldsymbol{n} + \mathrm{j}kT' = \frac{2k^3}{\alpha\beta}\mathrm{j}W\mathrm{e}^{\mathrm{j}kL_Z}\,. \tag{B.5}$$

These expressions are used below in the variational formulation of the LNSE.

B.2 LNSE weak formulations

B.2.1 Mass equation

The weak formulation of the mass conservation equation is

$$\int_\Omega q\frac{\partial \rho'}{\partial t}\,\mathrm{d}\Omega = \int_\Omega \boldsymbol{u}'\cdot\nabla q\,\mathrm{d}\Omega - \int_\Gamma q\boldsymbol{u}'\cdot\boldsymbol{n}\,\mathrm{d}\Gamma\,, \tag{B.6}$$

where q is a test function. Incorporating the plane-wave boundary condition (B.4) in equation (B.6) yields

$$\int_\Omega q\frac{\partial \rho'}{\partial t}\,\mathrm{d}\Omega = \int_\Omega \boldsymbol{u}'\cdot\nabla q\,\mathrm{d}\Omega + \frac{1}{\mathrm{j}k}\int_{\Gamma_{\text{in}}} q(\boldsymbol{n}\cdot\nabla)(\boldsymbol{u}'\cdot\boldsymbol{n})\,\mathrm{d}\Gamma + \frac{2k}{\alpha}We^{\mathrm{j}kL_Z}\int_{\Gamma_{\text{in}}} q\,\mathrm{d}\Gamma\,. \tag{B.7}$$

B.2.2 Momentum equation

The boundary including the axis and the free-slip boundaries is written $\Gamma_s = \Gamma_{\text{axis}}\cup\Gamma_{\text{ext,lat}}\cup\Gamma_{\text{cav,lat}}$. The weak formulation of the momentum equation reads

$$\begin{aligned}\int_\Omega \boldsymbol{v}\cdot\frac{\partial \boldsymbol{u}}{\partial t}\,\mathrm{d}\Omega = {}& \frac{1}{\gamma}\int_\Omega (\nabla\cdot\boldsymbol{v})\left[(\gamma-1)T'+\rho'\right]\mathrm{d}\Omega \\ & - \frac{1}{Re_a}\int_\Omega \nabla\boldsymbol{v}:\left[\nabla\boldsymbol{u}'+\left(\nabla\boldsymbol{u}'\right)^{\mathrm{T}}\right] + \left(\mu_B-\tfrac{2}{3}\right)(\nabla\cdot\boldsymbol{v})\left(\nabla\cdot\boldsymbol{u}'\right)\,\mathrm{d}\Omega \\ & - \frac{1}{\gamma}\int_\Gamma (\boldsymbol{v}\cdot\boldsymbol{n})\left[(\gamma-1)T'+\rho'\right]\mathrm{d}\Gamma \\ & + \frac{1}{Re_a}\int_\Gamma \boldsymbol{v}\cdot\left[\nabla\boldsymbol{u}'+\left(\nabla\boldsymbol{u}'\right)^{\mathrm{T}}\right]\boldsymbol{n} + \left(\mu_B-\tfrac{2}{3}\right)\boldsymbol{v}\cdot\boldsymbol{n}\left(\nabla\cdot\boldsymbol{u}'\right)\,\mathrm{d}\Gamma\end{aligned} \tag{B.8}$$

where $\boldsymbol{v}$ is a test function. Using the boundary conditions (B.3) to (B.5), we find

$$\begin{aligned}\rho_0\int_\Omega \boldsymbol{v}\cdot\frac{\partial \boldsymbol{u}}{\partial t}\,\mathrm{d}\Omega = {}& \frac{1}{\gamma}\int_\Omega (\nabla\cdot\boldsymbol{v})\left[(\gamma-1)T'+\rho'\right]\mathrm{d}\Omega \\ & - \frac{1}{Re_a}\int_\Omega \nabla\boldsymbol{v}:\left[\nabla\boldsymbol{u}'+\left(\nabla\boldsymbol{u}'\right)^{\mathrm{T}}\right] + \left(\mu_B-\tfrac{2}{3}\right)(\nabla\cdot\boldsymbol{v})\left(\nabla\cdot\boldsymbol{u}'\right)\,\mathrm{d}\Omega \\ & + \frac{1}{\mathrm{j}\gamma k}\int_{\Gamma_{\text{in}}} (\boldsymbol{v}\cdot\boldsymbol{n})(\boldsymbol{n}\cdot\nabla)\left[(\gamma-1)T'+\rho'\right]\mathrm{d}\Gamma \\ & - \left[2We^{ikL_Z} - \frac{2Wik^2e^{ikL_Z}}{\alpha}\left(\frac{\mu_B+\frac{4}{3}}{Re_a}\right)\right]\int_{\Gamma_{in}} \boldsymbol{v}\cdot\boldsymbol{n}\,\mathrm{d}\Gamma \\ & - \frac{ik}{Re_a}\left(\mu_B+\tfrac{4}{3}\right)\int_{\Gamma_{\text{in}}} (\boldsymbol{v}\cdot\boldsymbol{n})\left(\boldsymbol{u}'\cdot\boldsymbol{n}\right)\,\mathrm{d}\Gamma\,.\end{aligned} \tag{B.9}$$

B.2.3 Energy equation

The weak formulation of the energy equation corresponds to

$$\int_\Omega \epsilon\frac{\partial T'}{\partial t}\,\mathrm{d}\Omega = -\int_\Omega \left(\nabla\cdot\boldsymbol{u}'\right)\epsilon - \frac{\gamma}{Re_aPr}\nabla\epsilon\cdot\nabla T'\,\mathrm{d}\Omega + \frac{\gamma}{Re_aPr}\int_\Gamma \epsilon\nabla T'\cdot\boldsymbol{n}\,\mathrm{d}\Gamma\,,$$

where ϵ is a test function. Replacing $\nabla T' \cdot \boldsymbol{n}$ by the plane-wave boundary condition (B.5) on Γ_{in}, the weak formulation become

$$\begin{aligned}\int_\Omega \epsilon \frac{\partial T'}{\partial t}\,\mathrm{d}\Omega = &-\int_\Omega \left(\nabla\cdot\boldsymbol{u}'\right)\epsilon - \frac{\gamma}{Re_a Pr}\nabla\epsilon\cdot\nabla T'\,\mathrm{d}\Omega \\ &-\mathrm{j}k\frac{\gamma}{Re_a Pr}\int_{\Gamma_{\text{in}}}\epsilon T'\,\mathrm{d}\Gamma \\ &+\frac{2W\mathrm{j}k^3\mathrm{e}^{\mathrm{j}kL_Z}}{\alpha\beta}\frac{\gamma}{Re_a Pr}\int_{\Gamma_{\text{in}}}\epsilon\,\mathrm{d}\Gamma.\end{aligned} \tag{B.10}$$

B.3 Weak formulation of the Helmholtz model

The variational formulation for the Helmholtz equation is as follows:

$$-\int_\Omega \nabla p\cdot\nabla\eta\,\mathrm{d}\Omega + \int_\Gamma \nabla p\cdot\boldsymbol{n}\eta\,\mathrm{d}\Gamma + \omega^2\int_\Omega p\eta\,\mathrm{d}\Omega = 0, \tag{B.11}$$

where η is a test function.

An incoming plane wave is implemented on the upper boundary of the domain:

$$\frac{\partial p}{\partial n} + \mathrm{j}\omega p = 2W\mathrm{j}\mathrm{e}^{\mathrm{j}\omega L_Z} \text{ on } \Gamma_{\text{in}}\ . \tag{B.12}$$

The boundary condition (2.20) is implemented on Γ_w.

These boundary conditions are introduced in (B.11) to give

$$\begin{aligned}&\int_\Omega -\nabla p\cdot\nabla\eta + \omega^2 p\eta\,\mathrm{d}\Omega + \int_{\Gamma_w} -\delta_V\frac{\mathrm{j}-1}{2}\nabla_T p\cdot\nabla_T\eta - \delta_T\omega^2\frac{(\mathrm{j}-1)(\gamma-1)}{2}p\eta\,\mathrm{d}\Gamma_w \\ &+\int_{\Gamma_{\text{in}}} -\mathrm{j}\omega p\eta + 2\mathrm{j}\omega\mathrm{e}^{\mathrm{j}\omega L_Z}\eta\,\mathrm{d}\Gamma_{\text{in}} = 0.\end{aligned} \tag{B.13}$$

Appendix C

Details on the measured samples in the non-linear regime

Table C.1 summarizes the geometrical parameters used to validate the non-linear resistance term from Ingard *et al.* (1967) with impedance tube measurements performed with a white noise source.

Porosity (%)	Radius (mm)	Thickness (mm)
1,4	0.15	0.6
1.8	0.15	0.6
2.1	1.5	4.0
2.8	0.15	0.6
2.9	0.15	1.2
4.1	1.5	4.0
4.2	0.15	0.6
4.6	0.25	0.6
4.9	0.15	1.2
6.0	1.0	2.1
6.0	0.8	2.1
6.0	0.4	2.1
6.0	0.8	1.5
6.0	1.0	1.5
6.0	0.4	1.5
6.0	0.6	1.5
6.0	1.0	0.9
8.0	0.4	0.9
8.0	0.8	0.9
8.0	0.8	2.1
10.0	1.0	1.5
10.0	0.8	1.5
10.0	0.8	2.1
10.0	0.8	0.9
10.0	0.4	1.5
12.0	0.4	0.9
12.0	0.8	2.1
14.0	0.8	2.1
14.0	0.8	0.9
16.0	0.8	2.1
16.0	0.8	0.9
16.0	0.8	1.5
18.0	1.0	1.5
18.0	0.8	1.5
20.0	0.8	2.1
20.0	0.8	0.9

TABLE C.1: List of the measured samples.

Appendix D

Results at $L_p = 130\,\mathrm{dB}$

For completeness, we include in this appendix the educed empirical parameters obtained at $L_p = 130\,\mathrm{dB}$ in figures D.1 and D.2. The trends remain the same as for $L_p = 150\,\mathrm{dB}$.

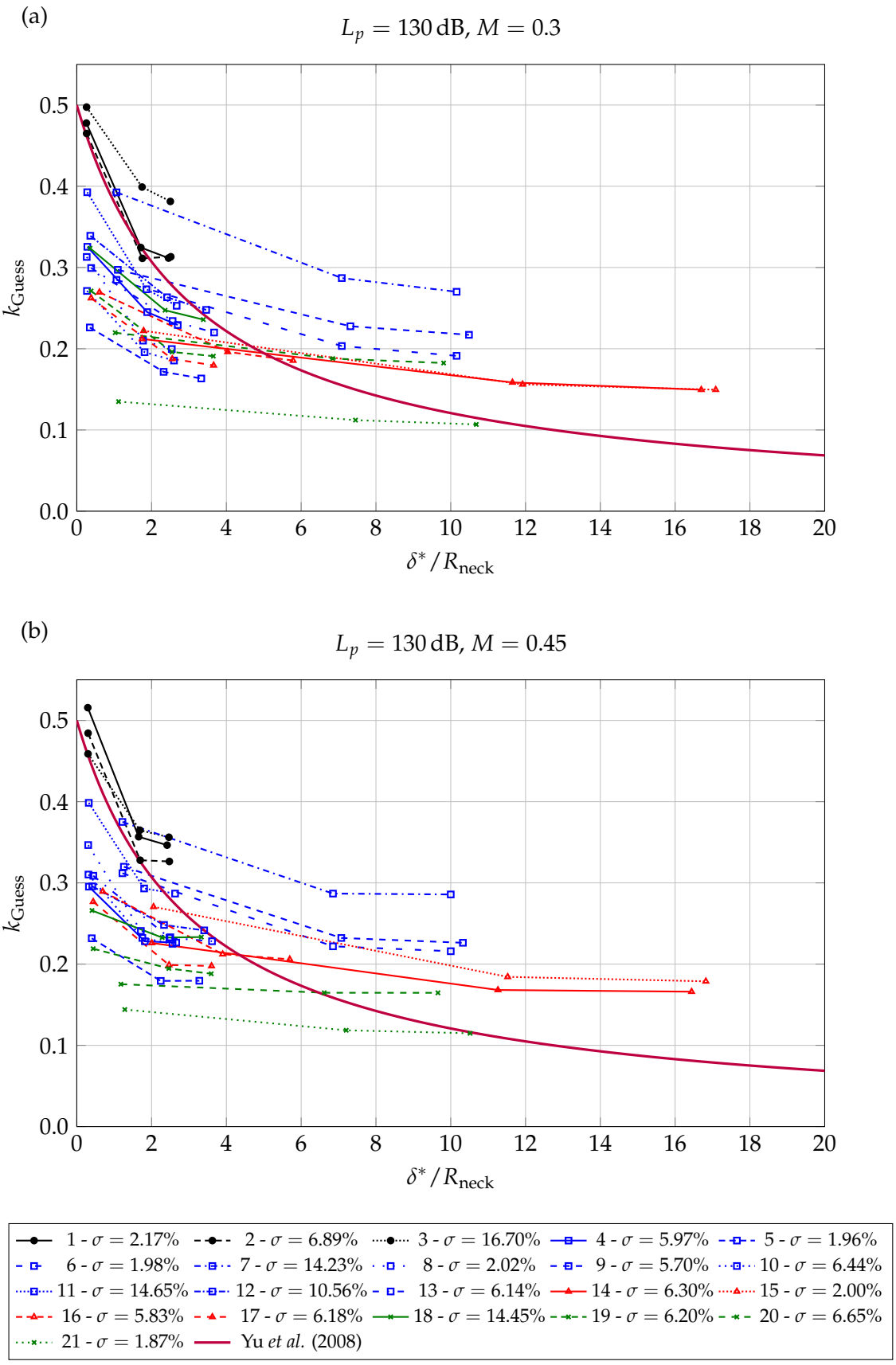

FIGURE D.1: Empirical parameter k_{Guess} as a function of $\delta^* / R_{\mathrm{neck}}$ for configuration 1 to 21.

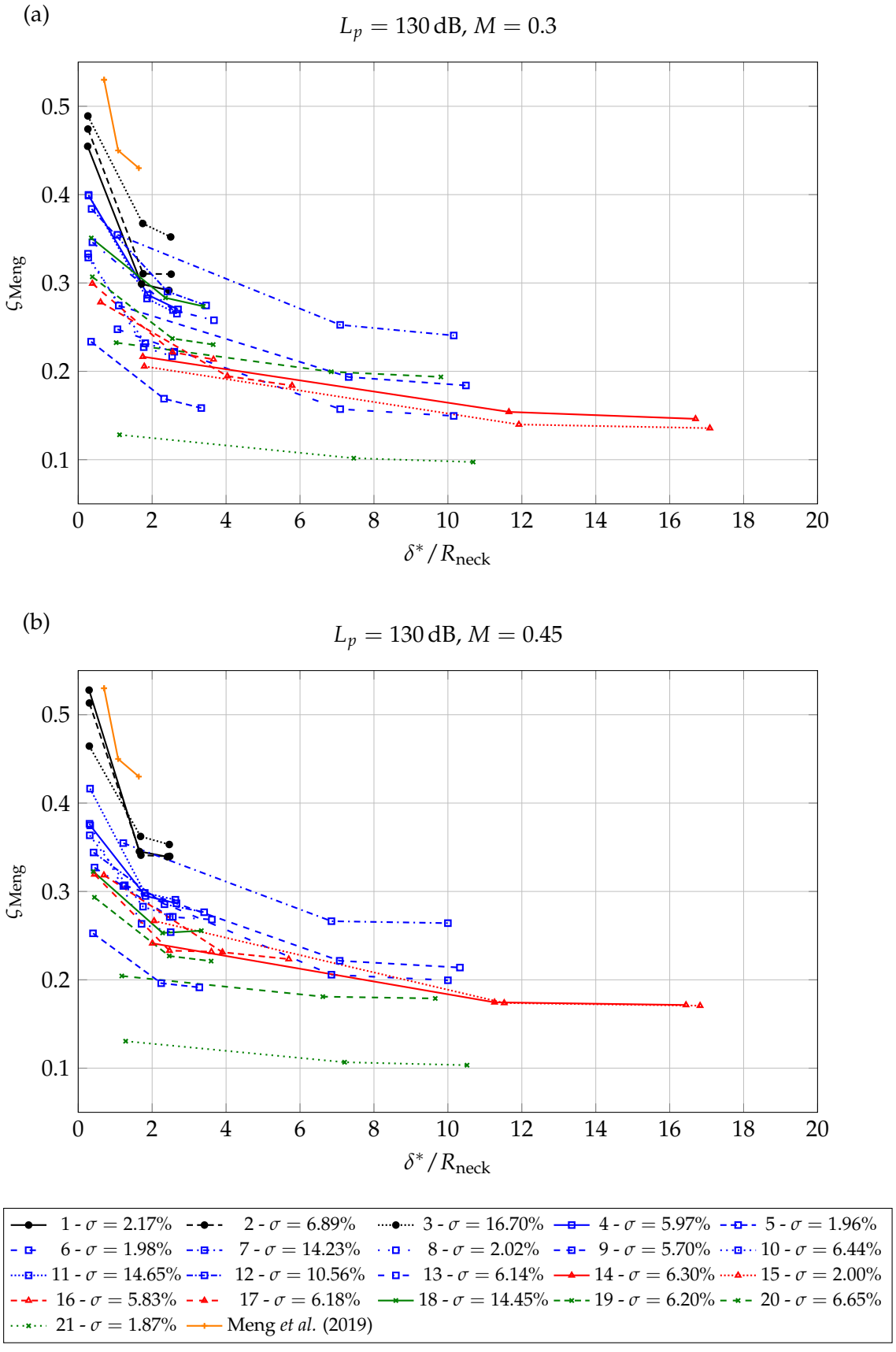

FIGURE D.2: Empirical parameter $\varsigma_{\mathrm{Meng}}$ as a function of $\delta^* / R_{\mathrm{neck}}$ for configuration 1 to 21.

Appendix E

Example of triadic interaction

Non-linear effects are known to occur for high sound pressure levels and to be the cause of harmonic distortion. In the work form Ingard *et al.* (1967), the resulting frequency interactions are not explicitly accounted for and it assumed that the first harmonic is dominating.

A more robust approximation of the interaction between frequencies can be found using the triadic interaction (Cavalieri *et al.* (2019), McKeon *et al.* (2010)). The triadic interaction accounts for the impact of two frequencies ω_1 and ω_2 whose the sum equals the frequency of interest. Hence, we shall have $\omega_1 + \omega_2 = \omega$. It is useful to define a non-linear forcing as in Chapter 5. It can be noted that this property is based on the orthogonality of the Fourier base.

An illustration of this approximation can be performed using the momentum conservation equation (2.4) in which the non-linear term $\rho\left(\mathbf{u}\cdot\nabla\right)\mathbf{u}$ is present.

First, we introduce the Fourier transform and its inverse

$$\hat{f}(\omega) = \int_{-\infty}^{+\infty} f(t)\mathrm{e}^{-\mathrm{j}\omega t}dt, \quad f(t) = \frac{1}{2\pi}\int_{-\infty}^{+\infty} \hat{f}(\omega)e^{+\mathrm{j}\omega t}d\omega. \tag{E.1}$$

Here, the quantities expressed in the frequency domain are denoted with a hat.

Secondly, in equation (2.4), we inject the inverse Fourier transform of the pressure and the velocity to obtain

$$\begin{aligned}\rho\frac{\partial}{\partial t}\left[\int_{-\infty}^{+\infty}\hat{\mathbf{u}}(\omega)e^{+\mathrm{j}\omega t}d\omega\right] + \frac{\rho}{2\pi}\int_{-\infty}^{+\infty}\int_{-\infty}^{+\infty}\left[\hat{\mathbf{u}}(\omega_1)\cdot\nabla\right]\hat{\mathbf{u}}(\omega_2)e^{\mathrm{j}(\omega_1+\omega_2)t}d\omega_1 d\omega_2 \\ = -\nabla\int_{-\infty}^{+\infty}\hat{p}(\omega)e^{+\mathrm{j}\omega t}d\omega + \nabla\cdot\int_{-\infty}^{+\infty}\underline{\tau}\left[\hat{\mathbf{u}}(\omega)\right]e^{+\mathrm{j}\omega t}d\omega.\end{aligned} \tag{E.2}$$

We apply the Fourier transform to the previous equation and we obtain for a time period T

$$\rho\frac{\partial\mathbf{u}}{\partial t} + \frac{1}{2T}\frac{\rho}{2\pi}\int_{-T}^{+T}\int_{-\infty}^{+\infty}\int_{-\infty}^{+\infty}\left[\hat{\mathbf{u}}(\omega_1)\cdot\nabla\right]\hat{\mathbf{u}}(\omega_2)e^{\mathrm{j}(\omega_1+\omega_2-\omega)t}d\omega_1 d\omega_2 dt = -\nabla p + \nabla\cdot\underline{\tau}(\mathbf{u}), \tag{E.3}$$

We now compute the limit of the previous equation (E.3) for $T\to+\infty$ and we use the relation

$$\lim_{T\to+\infty}\frac{1}{2T}\int_{-T}^{+T}e^{\mathrm{j}(\omega_1+\omega_2-\omega)t}dt = \delta(\omega_1+\omega_2-\omega). \tag{E.4}$$

Hence, the non-linear term is non-zero if $\omega = \omega_1 + \omega_2$ and become

$$\frac{\rho}{2\pi}\int_{\omega=\omega_1+\omega_2}\left[\hat{\mathbf{u}}(\omega_1)\cdot\nabla\right]\hat{\mathbf{u}}(\omega_2)d\omega. \tag{E.5}$$

The time convolution can be obtained by operating the change of variables such that $\omega_1 = \omega'$ and $\omega_2 = \omega - \omega'$, we get

$$\rho \frac{\partial \mathbf{u}}{\partial t} + \frac{\rho}{2\pi} \int_{\omega=\omega_1+\omega_2} \left[\hat{\mathbf{u}}(\omega') \cdot \nabla\right] \hat{\mathbf{u}}(\omega - \omega') d\omega = -\nabla p + \nabla \cdot \underline{\tau}(\mathbf{u}). \tag{E.6}$$

Equation (E.6) highlights that the non-linear term can be approximated by a convolution over all frequencies. This strategy is used implicitly when defining the non-linear optimal forcing in the sensitivity analysis presented in Chapter 5.

Bibliography

Abreu, L. I., A. V. Cavalieri, P. Schlatter, R. Vinuesa, and D. S. Henningson (2020). "Resolvent modelling of near-wall coherent structures in turbulent channel flow". In: *International Journal of Heat and Fluid Flow* 85, p. 108662.

Allam, S. and M. Åbom (2011). "A New Type of Muffler Based on Microperforated Tubes". In: *Journal of Vibration and Acoustics* 133(3), p. 031005.

Allard, J.-F. and N. Atalla (2009). *Propagation of sound in porous media: modelling sound absorbing materials*. 2nd. Wiley.

Atalla, N. and F. Sgard (2007). "Modeling of perforated plates and screens using rigid frame porous models". In: *Journal of Sound and Vibration* 303(1-2), pp. 195–208.

Avallone, F., P. Manjunath, D. Ragni, and D. Casalino (2019). "Lattice-Boltzmann Very Large Eddy Simulation of a Multi-Orifice Acoustic Liner with Turbulent Grazing Flow". In: *25th AIAA/CEAS Aeroacoustics Conference*. American Institute of Aeronautics and Astronautics: Delft, The Netherlands.

Batchelor, G. K. (1967). *An introduction to fluid dynamics*. Cambridge University Press: Cambridge.

Beck, B. S., N. H. Schiller, and M. G. Jones (2015). "Impedance assessment of a dual-resonance acoustic liner". In: *Applied Acoustics* 93, pp. 15–22.

Berggren, M., A. Bernland, and D. Noreland (2018). "Acoustic boundary layers as boundary conditions". In: *Journal of Computational Physics* 371, pp. 633–650.

Billard, R., G. Tissot, G. Gabard, and M. Versaevel (2021). "Numerical simulations of perforated plate liners: Analysis of the visco-thermal dissipation mechanisms". In: *Journal of the Acoustical Society of America*, pp. 16–27.

Bruneau, M. and T. Scelo (2006). *Fundamentals of acoustics*. ISTE: London.

Brynjell-Rahkola, M., L. S. Tuckerman, P. Schlatter, and D. S. Henningson (2017). "Computing Optimal Forcing Using Laplace Preconditioning". In: *Communications in Computational Physics* 22(05), pp. 1508–1532.

Cavalieri, A. V. G., P. Jordan, and L. Lesshafft (2019). "Wave-Packet Models for Jet Dynamics and Sound Radiation". In: *Applied Mechanics Reviews* 71(2), p. 020802.

Cops, M. J., J. G. McDaniel, E. A. Magliula, D. J. Bamford, and M. Berggren (2020). "Estimation of acoustic absorption in porous materials based on visco-thermal boundary layers modeled as boundary conditions". In: *The Journal of the Acoustical Society of America* 148(3), pp. 1624–1635.

Crandall, I. B. (1926). *Theory of Vibrating Systems and Sound*. van Nostrand Company: New York.

Cummings, A. (1986). "The Effects of Grazing Turbulent Pipe-Flow on the Impedance of an Orifice". In: *Acta Acustica united with Acustica* 61(4), pp. 233–242.

Cummings, A. and W. Eversman (1983). "High amplitude acoustic transmission through duct terminations: Theory". In: *Journal of Sound and Vibration* 91(4), pp. 503–518.

Cutanda-Henríquez, V. and P. M. Juhl (2013). "An axisymmetric boundary element formulation of sound wave propagation in fluids including viscous and thermal losses". In: *The Journal of the Acoustical Society of America* 134(5), pp. 3409–3418.

Dean, P. (1974). "An in situ method of wall acoustic impedance measurement in flow ducts". In: *Journal of Sound and Vibration* 34(1), pp. 97–130.

Dergham, G., D. Sipp, and J.-C. Robinet (2013). "Stochastic dynamics and model reduction of amplifier flows: the backward facing step flow". In: *Journal of Fluid Mechanics* 719, pp. 406–430.

Drevon, E. (2004). "Measurement Methods and Devices Applied to A380 Nacelle Double Degree-Of-Freedom Acoustic Liner Development". In: *10th AIAA/CEAS Aeroacoustics Conference*. American Institute of Aeronautics and Astronautics: Manchester, Great Britain.

Fabre, D., R. Longobardi, V. Citro, and P. Luchini (2020). "Acoustic impedance and hydrodynamic instability of the flow through a circular aperture in a thick plate". In: *Journal of Fluid Mechanics* 885, A11.

Feder, E. and L. W. Dean (1969). *Analytical and experimental studies for predicting noise attenuation in acoustically treated ducts for turbofan engines*. Tech. rep. NASA CR-1373.

Fok, V. A. (1941). "Theoretical research of the conductivity of a circular aperture in a partition across a pipe". In: *Doklady akademii nauk SSSR* 31(9), pp. 875–82.

Gabard, G. (2013). "A comparison of impedance boundary conditions for flow acoustics". In: *Journal of Sound and Vibration* 332(4), pp. 714–724.

Geuzaine, C. and J.-F. Remacle (2009). "Gmsh: a three-dimensional finite element mesh generator with built-in pre- and post-processing facilities". In: *International Journal for Numerical Methods in Engineering* 79(11), pp. 1309–1331.

Groeneweg, J. (1969). "Current Understanding of Helmholtz Resonator Arrays as Duct Boundary Conditions". In: *NASA Special Publication*, p. 357.

Guess, A. W. (1975). "Calculation of perforated plate liner parameters from specified acoustic resistance and reactance". In: *Journal of Sound and Vibration* 40(1), pp. 119–137.

Herrmann, B., P. J. Baddoo, R. Semaan, S. L. Brunton, and B. J. McKeon (2020). *Data-driven resolvent analysis*. arXiv: `2010.02181 [physics.flu-dyn]`.

Honzík, P., S. Durand, N. Joly, and M. Bruneau (2013). "On the Acoustic Transfer Function of Slowly Tapered Small Horns Filled With Thermo-Viscous Fluid". In: *Acta Acustica united with Acustica* 99(5), pp. 694–702.

Howe, M. (1979). "The influence of grazing flow on the acoustic impedance of a cylindrical wall cavity". In: *Journal of Sound and Vibration* 67(4), pp. 533–544.

Howe, M., M. Scott, and S. Sipcic (1996). "The Influence of Tangential Mean Flow on the Rayleigh Conductivity of an Aperture". In: *Proceedings of The Royal Society* 452, pp. 2303–2317.

Ingard, U. (1953). "On the Theory and Design of Acoustic Resonators". In: *The Journal of the Acoustical Society of America* 25(6), pp. 1037–1061.

Ingard, U. (1968). "Absorption Characteristics of Nonlinear Acoustic Resonators". In: *The Journal of the Acoustical Society of America* 44(4), pp. 1155–1156.

Ingard, U. and H. Ising (1967). "Acoustic Nonlinearity of an Orifice". In: *The Journal of the Acoustical Society of America* 42(1), pp. 6–17.

Ingard, U. and S. Labate (1950). "Acoustic Circulation Effects and the Nonlinear Impedance of Orifices". In: *The Journal of the Acoustical Society of America* 22(2).

Jing, X., X. Sun, J. Wu, and K. Meng (2001). "Effect of Grazing Flow on the Acoustic Impedance of an Orifice". In: *AIAA Journal* 39(8), pp. 1478–1484.

Joly, N. (2010). "Finite Element Modeling of Thermoviscous Acoustics on Adapted Anisotropic Meshes: Implementation of the Particle Velocity and Temperature Variation Formulation". In: *Acta Acustica united with Acustica* 96(1), pp. 102–114.

Joly, N., M. Bruneau, and R. Bossart (2006). "Coupled Equations for Particle Velocity and Temperature Variation as the Fundamental Formulation of Linear Acoustics in Thermo-Viscous Fluids at Rest". In: *Acta Acustica united with Acustica* 92, p. 8.

Kampinga, W. R. and Y. H. Wijnant (2010). "Performance of Several Viscothermal Acoustic Finite Elements". In: *Acta Acustica united with Acustica* 96, p. 10.

Kampinga, W. R. and Y. H. Wijnant (2011). "An Efficient Finite Element Model for Viscothermal Acoustics". In: *Acta Acustica united with Acustica* 97, p. 14.

Keefe, D. H. (1984). "Acoustical wave propagation in cylindrical ducts: Transmission line parameter approximations for isothermal and nonisothermal boundary conditions". In: *The Journal of the Acoustical Society of America* 75(1), pp. 58–62.

Kellogg, R. B. and B. Liu (1996). "A Finite Element Method for the Compressible Stokes Equations". In: *SIAM Journal on Numerical Analysis* 33(2), pp. 780–788.

Kinsler, L. E. and A. R. Frey (1950). *Fundamentals of Acoustics*. John Wiley and Sons.: New York.

Kirchhoff, G. (1868). "About the influence of heat conduction on the sound propagation in a gas". In: *Annual Review of Physical Chemistry* 134, pp. 177–193.

Komkin, A., A. Bykov, and M. Mironov (2020). "Experimental study of nonlinear acoustic impedance of circular orifices". In: *The Journal of the Acoustical Society of America* 148(3), pp. 1391–1403.

Laly, Z., N. Atalla, and S.-A. Meslioui (2018a). "Acoustical modeling of micro-perforated panel at high sound pressure levels using equivalent fluid approach". In: *Journal of Sound and Vibration* 427, pp. 134–158.

Laly, Z., N. Atalla, S.-A. Meslioui, and K. EL Bikri (2018b). "Modeling of acoustic lined duct with and without grazing air flow by an analytical method". In: *Noise Control Engineering Journal* 66(4), pp. 340–352.

Laurens, S., S. Tordeux, A. Bendali, M. Fares, and P. Kotiuga (2013). "Lower and upper bounds for the Rayleigh conductivity of a perforated plate". In: *ESAIM: Mathematical Modelling and Numerical Analysis* 47(6), pp. 1691–1712.

Lighthill, J. (1978). *Waves in Fluids*. Cambridge University Press: Cambridge.

Maa, D.-Y. (1994). "Microperforated panel at high sound intensity". In: *Proceedings of Inter Noise 94*. Japan, pp. 1511–1514.

Maa, D.-Y. (1998). "Potential of microperforated panel absorber". In: *The Journal of the Acoustical Society of America* 104(5).

Malinen, M., M. Lyly, P. Raback, A. Karkainen, and L. Karkkainen (2004). "A Finite element Method for the modeling of thermo-viscous effects in acoustics". In: *Proceedings of the 4th European Congress on Computational Methods in Applied and Engineering ECCOMAS*. Jyvaskyla, Finland.

Martini, E., A. V. G. Cavalieri, P. Jordan, A. Towne, and L. Lesshafft (2020a). "Resolvent-based optimal estimation of transitional and turbulent flows". In: *Journal of Fluid Mechanics* 900, A2.

Martini, E., D. Rodríguez, A. Towne, and A. V. G. Cavalieri (2020b). *Efficient computation of global resolvent modes*. arXiv: `2008.10904 [physics.flu-dyn]`.

Marx, D., Y. Aurégan, H. Bailliet, and J.-C. Valière (2010). "PIV and LDV evidence of hydrodynamic instability over a liner in a duct with flow". In: *Journal of Sound and Vibration* 329(18), pp. 3798–3812.

Mbailassem, F., E. Gourdon, Q. Leclère, E. Redon, and T. Cambonie (2019). "Sound absorption prediction of linear damped acoustic resonators using a lightweight hybrid model". In: *Applied Acoustics* 150, pp. 14–26.

McKeon, B. J. and A. S. Sharma (2010). "A critical-layer framework for turbulent pipe flow". In: *Journal of Fluid Mechanics* 658, pp. 336–382.

Melling, T. (1973). "The acoustic impendance of perforates at medium and high sound pressure levels". In: *Journal of Sound and Vibration* 29(1), pp. 1–65.

Meng, Y., B. Xin, X. Jing, X. Sun, H. Boden, and M. Åbom (2019). "Semi-empirical impedance model of perforated plate under grazing flow". In: *25th AIAA/CEAS Aeroacoustics Conference*. American Institute of Aeronautics and Astronautics: Delft, The Netherlands.

Moarref, R., A. S. Sharma, J. A. Tropp, and B. J. McKeon (2013). "Model-based scaling of the streamwise energy density in high-Reynolds-number turbulent channels". In: *Journal of Fluid Mechanics* 734, pp. 275–316.

Morse, P. M. and K. U. Ingard (1968). *Theoretical Acoustics*. McGraw-Hill Book Company: New York.

Peat, K. S., J.-G. Ih, and S.-H. Lee (2003). "The acoustic impedance of a circular orifice in grazing mean flow: Comparison with theory". In: *The Journal of the Acoustical Society of America* 114(6), pp. 3076–3086.

Pierce, A. D. (1981). *Acoustics: An Introduction to its Physical Principles and Applications*. McGraw-Hill Book Company: New York.

Popie, V. (2016). "Modélisation asymptotique de la réponse acoustique de plaques perforées dans un cadre linéaire avec études des effets visqueux". PhD thesis. Université de Toulouse.

Pryor, R. W. (2009). *Multiphysics modeling using COMSOL: a first principles approach.* Jones & Bartlett Publishers: Sudbury, Massachussetts.

Rayleigh (1878). *The Theory of Sound*. Vol. 2. MacMillan and Company, Ltd.: London.

Renard, Y. and K. Poulios (2020). "GetFEM: Automated FE modeling of multiphysics problems based on a generic weak form language". Working paper or preprint.

Ribeiro, J. H. M., C.-A. Yeh, and K. Taira (2020). "Randomized resolvent analysis". In: *Phys. Rev. Fluids* 5 (3), p. 033902.

Rice, E. (1971). "A model for the acoustic impedance of a perforated plate liner with mulltiple frequency excitation". In: *NASA Technical Memorandum, TM X-67950*.

Rienstra, S. W. and A Hirschberg (2018). *An Introduction to Acoustics*. Eindhoven.

Roberts, D. (1977). "Equivalent sand-grain roughness of perforated plate acoustic linings". In: *15th Aerospace Sciences Meeting*. American Institute of Aeronautics and Astronautics: Los Angeles, CA, U.S.A.

Roche, J.-M. (2011). "Simulation numérique de l'absorption acoustique de matériaux résonnants en présence d'écoulement." PhD thesis. Université du Mans.

Roche, J.-M., L. Leylekian, G. Delattre, and F. Vuillot (2009). "Aircraft Fan Noise Absorption: DNS of the Acoustic Dissipation of Resonant Liners". In: *15th AIAA/CEAS Aeroacoustics Conference (30th AIAA Aeroacoustics Conference)*. American Institute of Aeronautics and Astronautics: Miami, Florida.

Roche, J.-M., F. Vuillot, L. Leylekian, G. Delattre, E. Piot, and F. Simon (2010). "Numerical and Experimental Study of Resonant Liners Aeroacoustic Absorption Under Grazing Flow". In: *16th AIAA/CEAS Aeroacoustics Conference*. American Institute of Aeronautics and Astronautics: Stockholm, Sweden.

Scarpato, A. (2014). "Linear and nonlinear analysis of the acoustic response of perforated plates traversed by a bias flow". PhD thesis. École Centrale Paris.

Schlichting, H. (1979). *Boundary layer theory*. 7th ed. McGraw-Hill Book Company: New York.

Schmid, P and D. S. Henningson (2001). *Stability and Transition in Shear Flows*. Springer-Verlag: New York.

Sergent, P. (1996). "Optimisation géométrique du contrôle actif dans les gaines de ventilation". PhD thesis. École Nationale des Ponts et Chaussées.

Sipp, D., O. Marquet, P. Meliga, and A. Barbagallo (2010). "Dynamics and Control of Global Instabilities in Open-Flows: A Linearized Approach". In: *Applied Mechanics Reviews* 63(3), p. 030801.

Spillere, A. M. N. (2017). "Towards optimal design of acoustic liners in turbofan aero-engines". PhD thesis. Federal University of Santa Catarina.

Stinson, M. R. (1991). "The propagation of plane sound waves in narrow and wide circular tubes, and generalization to uniform tubes of arbitrary cross-sectional shape". In: *The Journal of the Acoustical Society of America* 89(2), pp. 550–558.

Symon, S., D. Sipp, and B. J. McKeon (2019). "A tale of two airfoils: resolvent-based modelling of an oscillator versus an amplifier from an experimental mean". In: *Journal of Fluid Mechanics* 881, pp. 51–83.

Tam, C. K., N. N. Pastouchenko, M. G. Jones, and W. R. Watson (2014). "Experimental validation of numerical simulations for an acoustic liner in grazing flow: Self-noise and added drag". In: *Journal of Sound and Vibration* 333(13), pp. 2831–2854.

Tam, C., K. Kurbatskii, K. Ahuja, and R. Gaeta (2001). "A numerical and experimental investigation of the dissipation mechanisms of resonant acoustic liners". In: *Journal of Sound and Vibration* 245(3), pp. 545–557.

Temiz, M. A., I. Lopez Arteaga, G. Efraimsson, M. Åbom, and A. Hirschberg (2015). "The influence of edge geometry on end-correction coefficients in micro perforated plates". In: *The Journal of the Acoustical Society of America* 138(6), pp. 3668–3677.

Temiz, M. A., J. Tournadre, I. L. Arteaga, and A. Hirschberg (2016). "Non-linear acoustic transfer impedance of micro-perforated plates with circular orifices". In: *Journal of Sound and Vibration* 366, pp. 418–428.

Tissot, G., R. Billard, and G. Gabard (2020). "Optimal cavity shape design for acoustic liners using Helmholtz equation with visco-thermal losses". In: *Journal of Computational Physics* 402, p. 109048.

Towne, A., O. T. Schmidt, and T. Colonius (2018). "Spectral proper orthogonal decomposition and its relationship to dynamic mode decomposition and resolvent analysis". In: *Journal of Fluid Mechanics* 847, pp. 821–867.

Vandemaele, S., H. Denayer, W. De Roeck, and W. Desmet (2019). "Numerical modeling of the flow acoustic behavior of sub-millimeter orifices in 3D using linearized Navier-Stokes equations". In: *25th AIAA/CEAS Aeroacoustics Conference*. American Institute of Aeronautics and Astronautics: Delft, The Netherlands.

Wu, G., Z. Lu, X. Xu, W. Pan, W. Wu, J. Li, and J. Ci (2019). "Numerical investigation of aeroacoustics damping performance of a Helmholtz resonator: Effects of geometry, grazing and bias flow". In: *Aerospace Science and Technology* 86, pp. 191–203.

Yu, J., M. Ruiz, and H.-W. Kwan (2008). "Validation of Goodrich Perforate Liner Impedance Model Using NASA Langley Test Data". In: *14th AIAA/CEAS Aeroacoustics Conference (29th AIAA Aeroacoustics Conference)*. American Institute of Aeronautics and Astronautics: Vancouver, British Columbia, Canada.

Zhang, Q. and D. J. Bodony (2012). "Numerical investigation and modelling of acoustically excited flow through a circular orifice backed by a hexagonal cavity". In: *Journal of Fluid Mechanics* 693, pp. 367–401.

Zhang, Q. and D. J. Bodony (2016). "Numerical investigation of a honeycomb liner grazed by laminar and turbulent boundary layers". In: *Journal of Fluid Mechanics* 792, pp. 936–980.

Zieliński, T. G., R. Venegas, C. Perrot, M. Červenka, F. Chevillotte, and K. Attenborough (2020). "Benchmarks for microstructure-based modelling of sound absorbing rigid-frame porous media". In: *Journal of Sound and Vibration* 483, p. 115441.

Zinn, B. (1970). "A theoretical study of nonlinear damping by helmholtz resonators". In: *Journal of Sound and Vibration* 13(3), pp. 347–356.

Zwikker, C. and C. W. Kosten (1949). *Sound absorbing materials*. Elsevier: New York.

Álamo, J. C. del and J. Jiménez (2006). "Linear energy amplification in turbulent channels". In: *Journal of Fluid Mechanics* 559, p. 205.

DOCTORAT BRETAGNE LOIRE SCIENCES POUR L'INGENIEUR

Le Mans Université

Titre : Étude de traitements acoustiques perforés pour l'aéronautique.

Mots clés : traitements micro-perforés, pertes visco-thermiques, non-linéarités, écoulement rasant, modèles numériques, analyse de sensibilité.

Résumé : Le principe du résonateur de Helmholtz, par sa simplicité et son efficacité, est la technologie la plus répandue pour jouer le rôle d'absorbant acoustique. Les revêtements perforés sont un moyen simple de fabriquer et d'intégrer ces résonateurs à l'échelle industrielle. Les revêtements micro-perforés, ayant un diamètre de perforation inférieur au millimètre, permettent d'atténuer les émissions sonores des turboréacteurs tout en réduisant leur trainée aérodynamique. Pourtant, les modèles existants échouent encore à la prédiction des performances de ces revêtements. Pour cette raison, l'auteur propose, dans cette thèse de doctorat, d'évaluer et d'enrichir ces modèles afin d'étendre leur domaine de validité aux traitements micro-perforés.

La thèse commence par l'étude des pertes visco-thermiques dans le régime linéaire sans écoulement en relâchant certaines hypothèses et en développant un modèle numérique précis et peu coûteux numériquement. Une analyse du taux de dissipation est également présentée. Par la suite, notre analyse s'étend au régime non-linéaire dans lequel le modèle de Guess est modifié avec une procédure itérative, qui s'avère être essentielle pour l'obtention d'une impédance précise. La fin de la thèse s'articule sur les effets non-linéaire en présence d'écoulement par une étude empirique cohérente avec la littérature. Finalement, une analyse de sensibilité permet de mettre en évidence les quantités effectives impactant le plus l'impédance en présence d'écoulement.

Title : Study of perforated liners for aeronautics.

Keywords : micro-perforated liners, visco-thermal losses, non-linearities, grazing flow, numerical models, sensitivity analysis.

Abstract : The Helmholtz resonator, through its simplicity and efficiency, is the most widespread technology employed in acoustic treatments. Perforated liners are a simple way to manufacture and integrate these resonators at an industrial scale. In this thesis, micro-perforated liners, allowing to reduce the sound emissions from a turbofan and its flow drag, are studied. The domain of validity of the existing models excludes these liners, with a perforation diameter below one millimeter. For this reason, the author proposes, in this doctoral thesis, both to evaluate and upgrade these models especially when it comes to micro-perforated treatments.

We start by studying the visco-thermal losses in the linear regime without flow, relaxing some hypotheses and developing an accurate numerical model, shown to be computationally efficient. In parallel, an analysis of the dissipation rate is presented. Then, our framework extends to the non-linear regime in which we modify the model from Guess with an iterative procedure, which is essential to obtain accurate impedance predictions. The last chapters focus on the non-linear regime with flow with an empirical investigation consistent with existing works. A sensitivity analysis is finally presented, which provides more insight on the quantities impacting the most the impedance in the presence of shear flow.